THE UNIVERSITY OF
SYDNEY

COPYRIGHT AND USE OF THIS THESIS

This thesis must be used in accordance with the provisions of the Copyright Act 1968.

Reproduction of material protected by copyright may be an infringement of copyright and copyright owners may be entitled to take legal action against persons who infringe their copyright.

Section 51 (2) of the Copyright Act permits an authorized officer of a university library or archives to provide a copy (by communication or otherwise) of an unpublished thesis kept in the library or archives, to a person who satisfies the authorized officer that he or she requires the reproduction for the purposes of research or study.

The Copyright Act grants the creator of a work a number of moral rights, specifically the right of attribution, the right against false attribution and the right of integrity.

You may infringe the author's moral rights if you:

- fail to acknowledge the author of this thesis if you quote sections from the work
- attribute this thesis to another author
- subject this thesis to derogatory treatment which may prejudice the author's reputation

For further information contact the University's Director of Copyright Services

sydney.edu.au/copyright

STRUCTURAL, MAGNETIC AND ELECTRICAL STUDIES ON SOME MIXED METAL PEROVSKITE OXIDES

by

Labib Ali Awin

A thesis submitted in partial fulfilment of the requirements for the degree of

Doctor of Philosophy

The University of Sydney

2013

ABSTRACT

This thesis describes crystallographic, magnetic and electrical studies of some mixed metal perovskites. In the first part, the charge distribution, magnetic and electrical properties of mixed metal rhodium-copper perovskite oxides were investigated. Various series with the general formula $Ln_{1-y}A_yRh_{1-2x}Cu_xB_xO_3$ in which (Ln = La^{3+}, Tb^{3+}; A = Ca^{2+}, Sr^{2+}, Pb^{2+}, Bi^{3+}; B = Sc^{3+}, Cu^{2+}, Zn^{2+} ; $y \leq 0.3$, $x \leq 0.25$), have been synthesised by solid state reaction, and characterised by X-ray diffraction, scanning electron microscopy and physical property measurements and, as available, neutron diffraction and X-ray absorption near edge structure measurements. Structures were invariably orthorhombic with space group *Pbnm* with the Rh and Cu ions disordered on the same site. X-ray diffraction measurements of selected samples showed that the orthorhombic structure persisted over a wide temperature range, 30 to 900 ºC. All the samples are semiconductors and paramagnetic over the temperature range 4-300 K.

Doping a divalent cation onto the *B* site appears to have a significant impact on charge delocalization between $Rh^{3+/4+}$ and $Cu^{2+/3+}$ ions due to the oxidation of Rh^{3+} to Rh^{4+} required to maintain the overall charge. That was most evident from the Rh L_3 XANES measurements of the $LaRh_{1-2x}Cu_{2x}O_3$ and $La_{1-x}Pb_xRh_{0.5}Cu_{0.5}O_3$ series. Powder neutron diffraction measurements of $La_{0.75}Pb_{0.25}Rh_{0.5}Cu_{0.25}Zn_{0.25}O_3$, $LaRh_{0.5}Cu_{0.25}Zn_{0.25}O_3$ and $La_{0.75}Pb_{0.25}Rh_{0.5}Cu_{0.5}O_3$ show no evidence for anion vacancies and it is postulated the oxides do not contain appreciable amount of oxygen vacancies. The magnetization curves show negative values for Weiss constants indicating weak antiferromagnetism may be present but there is no indication for long range coupling in the oxides.

There are several factors that may influence the magnitude of the cell volume, octahedral distortion, octahedral tilting, magnetic interactions and electronic properties. These include ionic size, effective charge, electron configuration and electronegativity. In addition the charge delocalization and local ordering effects can play a role. The present work has demonstrated that:

a) The changes in the unit cell volume and the octahedral distortion of the isovalent doped oxides such as $La_{0.75}A_{0.25}Rh_{0.7}Cu_{0.3}O_3$ where A = Ca^{2+}, Sr^{2+} and Pb^{2+} are consistent with the increase in the ionic radii, whereas the decrease in magnetic moments of these is correlated with the increase in the electronegativities of the

dopant cation. The unit cell volumes for the terbium oxides are somewhat smaller than found in the analogous lanthanum oxides reflecting the small ionic size of Tb^{3+}.

b) The divalent cation doped oxides $Ln Rh_{1-2x}Cu_{2x}O_3$ and $Ln Rh_{1-2x}Cu_xZn_xO_3$ display lower cell volumes and octahedral distortions but higher magnetic moments and electrical conductivities than the trivalent cation doped oxides $Ln Rh_{1-2x}Cu_xSc_xO_3$ as consequence of charge delocalization. The electrical conductivity of the oxides increases as the divalent dopant content increases possibly because of an increase in carrier concentration that occurs as consequences of the formation of ionic defects due to the oxidation of Rh^{3+} ($3d^6$) to Rh^{4+} ($3d^5$).

c) The electron configuration influences the spin coupling and the band gap and this is most evident in the Pb^{2+} and Bi^{3+} ($6s^2$) doped $LaRh_{1-2x}Cu_{2x}O_3$ oxides which exhibited the lowest magnetic moments and the highest activation energies among the oxides studied. Compared with the analogous lanthanum oxides, the magnetic susceptibilities of the terbium oxides increased as a consequence of the contribution of Tb^{3+} 4 f^8 electrons.

d) Changing the *A* site composition resulted in anomalous changes in the cell volumes, octahedral distortions, electrical resistivity and magnetic susceptibility of the $La_{1-x}Pb_xRh_{0.5}Cu_{0.5}O_3$ and $La_{1-x}Bi_xRh_{0.5}Cu_{0.5}O_3$ perovskites. This is likely a consequence of charge delocalization and short-range local ordering effects. Increasing the doping on the *B*-site resulted in either a decrease or increase in the cell volumes and the magnetic moments, depending on the dopant type cation.

The final part of this thesis describes the structure of some $Ba_{2-x}Sr_{1+x}BO_{5.5}$ (*B* = Nb^{5+} and Ta^{5+}) perovskites. These were characterised by scanning electron microscopy, thermogravimetric analysis, X-ray and neutron diffraction. The preparation of these used solid state methods but the initial reactions were conducted under different media. Four compounds were prepared and these all have a face centred cubic structure with space group $Fm\bar{3}m$. The two synthetic methods produce monophasic powders and these differ in color, particle size, and hardness. The cell edges of the oxides obtained by mixing the reactants with water are larger than these obtained when the mixing was conducted with acetone. The neutron diffraction profiles demonstrate that the *A* cation and oxygen ions are disordered in the $BaSr_2NbO_{5.5}$ and $BaSr_2TaO_{5.5}$ structures. The unusual thermal expansion of the unit cell is due to the presences of water and anion deficiency into the oxides structure. The oxides were found to absorb CO_2 atmosphere during storage.

LIST OF PUBLICATIONS

Parts of the results described in this thesis have been or will be published elsewhere in a different form. A list of papers is given below.

1) L. A. Awin**,** B. J. Kennedy and M. Avdeev, Structural and Magnetic Studies of Zn Doped $LaRh_{1-2x}Cu_{2x}O_3$, *Key Engineering Materials*, 547(2013)173-180.

2) L. A. Awin**,** B. J. Kennedy and M. Avdeev, Structural and Magnetic Studies of *A* site Doped $LaRh_{1-x}Cu_xO_3$ (*A*= Ca^{2+}, Sr^{2+}, $Pb^{2+}$and Bi^{3+}), *Ceramics International*, 39(2013)233-237.

قَالُوا سُبْحَانَكَ لَا عِلْمَ لَنَا إِلَّا مَا عَلَّمْتَنَا إِنَّكَ أَنتَ الْعَلِيمُ الْحَكِيمُ(32)

They said: "Glory be to You! we have no knowledge except what You have taught us. Verily, it is You, the All-Knower, the All-Wise."

Holy Quran - Al-Baqarah / القران الكريم - سورة البقرة

TO
Those who taught me since my youth
My Father and Mother

ACKNOWLODGMENTS

First and for most, I would like to express my sincere appreciation to my supervisor, Prof. Brendan. J. Kennedy for his generous guidance, patience and expert advice through all stages of this research. Appreciation is also extended for my co- supervisor, Chris. T. Ling for his assistance whenever needed.

I am grateful to Drs. Qingdi, Rene, Hank, Wojciech, Peter at the School of Chemistry for their help in the experimental works and data analysis. I would also thank Drs. Patrick and Yanyan at the Electronic Microscope Unit for their assistance in measuring the element compositions of the samples.

My thanks are also due to all my past and present labmates: Jimmy, Richard, Teckyee, William, Emily, Sam, Tom, Thomas, Jose and Dinessa for their help and friendships. Special thanks to Jimmy for advice on the synthesis method for the $LaRh_{0.5}Cu_{0.5}O_3$ compound. Also to Dr. Peter, William, Thomas, Sam, Andrew and my friend Nabeel for spending their precious time proofreading the whole chapters. I would thank Ilyas for his continues support.

I am also indebted to Libyan government for the scholarship. Many thanks to Mr. Omran, Yaser, Aatef, Adrease, Ali and all the people in Libyan embassy – Canberra for their cooperation. I wish also to acknowledge The University of Sydney for the PRSS scholarship 2012.

I am really grateful to my wife Eman for her support, patience and understanding during my research period. Thanks to my little daughters Khadeja and Raneem for being calm and nice. Thanks to my family for their prayers.

Labib Ali Mohamed Awin

2013

TABLE OF CONTENTS

Chapter 1

Chapter 2

Chapter 5

Chapter 6

LIST OF TABLES

Chapter 1

Chapter 2

Chapter 3

Chapter 4

Chapter 5

Chapter 6

LIST OF FIGURES

Chapter 1

Chapter 2

Chapter 3

Chapter 4

Chapter 5

Chapter 6

LIST OF EQUATIONS

Chapter 1

Chapter 2

Chapter 3

Chapter 4

LIST OF SYMBOLS AND ABBREVIATIONS

A, *B* or *M*	A metal Cation
FE	Ferroelectricity
PZT	Lead zirconate titanates
Ln	A lanthanoid cation
τ	Tolerance factor
R_A, R_x and R_B	The ionic radii of the larger, oxide and smaller ions
RT	Room temperature
a , b and c	Lattice parameters
u, v and w	A proportion of oxygen coordinates
φ and ψ	Tilt angles
JT	Jahn-Teller effect
Q_n	A degenerate vibration mode
L	Atomic displacements
d_i and d_{av}	Individual and average bond distance
Δd	The octahedral distortion
a_i and a_{av}	Individual and average converted lattice parameters
D	The distortion of lattice parameters
$V_O^{\bullet\bullet}$ and $h^{\bullet}$	Oxygen vacancy and electron hole
T_c	Curie temperature
P	Electrical displacement
E	Applied electrical field
σ_t	Electrical conductivity at certain temperature
ε_a	Activation energy
T	Temperature
S	The quantum spin number

SOFCs	Solid oxide fuel cells
SSR	Solid State Reaction
LSR	Liquid Solutions Reaction
GPR	Gas Phase Reaction
XRD	X-ray powder diffraction
SXRD	Synchrotron X-ray diffraction
ND	Neutron diffraction
SEM	Scanning electron microscopy
TGA	Thermo gravimetric analysis
PPMS	Physical Properties Measurement System
n	Order of reflection
λ	Wave length
d	Inter planar distance
Θ	Angle between incident and reflected beam
VT-XRD	Variable temperature- X-ray diffraction
VCM	Vertically collimating mirror
VFM	Vertically focusing mirror
DCM	Double crystal monochromators
h	Planck's constant
p	The momentum of a free particle
b_i	A neutron scattering length
f_m	A form factor
$F_{hkl}^{nuc^2}$ and $F_{hkl}^{mag^2}$	Factors of nuclear and magnetic structures
q	The magnetic interaction vector
XANES	X-ray absorption near edge structure
NSRRC	National Synchrotron Radiation Research Centre
EMU	Electronic Microscope Unit
EDX	Energy-dispersive X-ray

EHT	Electron high tension
R	Electrical resistance
ρ	Electrical resistivity
A	The cross sectional area of a material
L	The length of a material
DC	Direct current
χ	Magnetic susceptibility
H	Applied magnetic field
M	Magnetisation
N_A	Avogadro's number
K_B	Boltzmann constant
μ_B	Magnetic Bohar moment
μ_{eff}	The effective magnetic moment
g_J	Landé g-factor
J and L	Total angular and orbital angular momentums
T_N	Néel temperature
Θ	Weiss constant
Ms	Saturated magnetisation
Mr	Remnant magnetisation
Hc	The coercive field
VSM	Vibrating Sample Magnetometer
χ_m	Molar magnetic susceptibility
M_m	Molar mass
m	A mass of the sample
$y_{i\,(obs)}$	Observed intensity
$y_{i\,(background)}$	Background intensity
$y_{i\,(Bragg)}$	Bragg intensity

s	The scale factor
hkl	Miller indices reflection
L_{hkl}	Lorentz Factor
P_{hkl}	The preferred orientation function
R_p, R_{wp} and χ^2	R-pattern, R- Weight pattern and Goodness
U_{ij}	The widths of the peaks to the root mean square scatter
W. C	Water Content

Introduction

1.1 Motivation and Objectives of the Study

Perovskite type oxides with the general formula ABO_3 have been the focus of numerous studies. The major interest in such materials typically stems from their applications in the modern chemical industry such as catalysts, sensors and optical devices. The perovskite type oxides exist in a variety of compositions and structures each associated with unique electrical and magnetic properties [1].

Historically, $CaTiO_3$ oxide was the first perovskite type material discovered in nature in 1839 [2]. Since then, many investigations of perovskites have been made. Significant outcomes of this research were the synthesis of perovskite materials in the laboratory 1929 [3], the characterization of the crystal structure of $BaTiO_3$ using X- ray diffraction in 1946 [3]. The employment of modern techniques such as X-ray, electron and neutron diffraction enables scientists to explore the precise structural details of the compounds. The importance of collecting the structural data is to analyse and to understand the nature of the physical proprieties of the perovskites, such as ferroelectricity, colossal magnetoresistance and piezoelectricity. Ferroelectricity (FE) in perovskites was initially discovered in $BaTiO_3$ in 1944 [3, 4]. Subsequently, more oxides were investigated and revealed as FE materials. The lead zirconate titanates $Pb(Zr_{1-x}Ti_x)O_3$ (PZT) and the alkali niobates $ANbO_3$ were among those reported as FE solid solution systems [3]. Colossal magnetoresistance and the piezoelectricity were also first reported in the mixed valence perovskite manganites and the PZT compounds in 1950s [5, 6]. The mid 1980s saw the discovery of the photo-destructive effect in PZT oxides [7] and the superconductivity in Cu oxide systems [8]. Such fascinating discoveries have led to intensive exploration of the structural and electronic behaviour of perovskites. Subsequently, many contributions and findings have been published addressing different properties of these oxides [7].

Research in perovskites has benefited from scientific and technical developments in synthetic methods. For instance, the sol–gel techniques for preparing FE films, the integration of FE films to silicon technology and the growth of relaxor single-crystal materials for piezotransducers were developed in 1980s and

1990s [7]. Despite the enormous efforts deployed in recent years, there are still many aspects of perovskites that remain unexplored.

One of the promising approaches to understand the physical proprieties of the perovskites is to track and determine the modification in crystal structure upon the changes in solid solutions. Perovskites are capable of accommodating different combinations of cations, so long as the crystal charge is neutral. The present work investigates the influence of changing the chemical compositions on the electrical and magnetic properties of some mixed metal perovskite oxides with general formula: $Ln_{1-y}A_yRh_{1-2x}Cu_xB_xO_3$ and $AA^*(BB^*)O_{5.5}$ where Ln = La^{3+} and Tb^{3+}, A = Ca^{2+}, Sr^{2+}, Pb^{2+} and Bi^{3+}, B = Sc^{3+}, Cu^{2+} and Zn^{2+}; $y \leq 0.3$, $x \leq 0.25$; A, A^* & B = Sr^{2+} and Ba^{2+}, and B^* = Nb^{5+} and Ta^{5+}.

The aim of this study is summarised in the following general points:

a) The determination of Rh oxidation states in the series $La_{1-x}A_xRh_{1-2x}Cu_xB_xO_3$.
b) The study of the impact of charge delocalization between the *B* site cations on the physical properties such as crystal structure, electrical conductivity and magnetization.
c) Establishing the relationships between cation content and the changes in the perovskites properties.
d) Finding mathematical functions to link the values of these properties with the various potential differences, as well as to explore if any of the compounds may be suitable for use as semiconductors, selective electrode or in photoelectric cells industry.
e) The investigation of the doping effect on the oxidation state of Tb ions as well as the physical properties of the Tb oxides.
f) The characterization of the Nb and Ta oxide structures and studying the effect of water on them.

1.2 Thesis Outline

The structure of this thesis is outlined as followed:

- **Introduction:**

The chapter presents general background on the perovskite structure, derivatives, chemical synthesis, physical properties, applications and literature review for the relevant systems.

- **Experimental Section:**

In this section, details of the sample preparation methods, characterization techniques and the instrumentation are provided.

- **Results and discussion:**

In this part, experimental results and discussion for the different series studied are presented in four chapters:

a) $La_{0.75}A_{0.25}Rh_{1-x}Cu_xO_3$ and $La_{1-x}A_xRh_{0.5}Cu_{0.5}O_3$.

b) $LaRh_{1-2x}Cu_xB_xO_3$ and $La_{0.75}A_{0.25}Rh_{1-2x}Cu_xB_xO_3$.

c) $TbRh_{1-2x}Cu_xB_xO_3$ and $Tb_{0.75}A_{0.25}Rh_{0.6}Cu_{0.4}O_3$.

d) $AA^*(BB^*)O_{5.5}$.

1.3 General Background

In the present chapter, some general background and information on perovskite type oxides, including their chemical structure, derivates, distortions, defects and physical properties is introduced. In addition, a literature review for relevant papers of the study is present.

1.3.1 Perovskite Structure and Derivatives

Generally, perovskite type oxides contain two different cations, each surrounded by oxygen anions [9]. The larger cation which can be alkali, alkaline earth, or rare earth has, ideally, dodecahedral symmetry, whilst the smaller cation which can be a transition metal ion, is six coordinate [10]. The cubic structure cannot be formed if the Goldschmidt tolerance factor is not in the range of 0.8 to 1.0 [11]. Equation 1.1 defines the tolerance factor (τ) [12].

$$\tau = \frac{R_A + R_x}{\sqrt{2}(R_B + R_x)} \qquad 1.1$$

$^*R_A$, R_x and R_B are the ionic radii of the larger, oxide and smaller ions.

Despite the simplicity of the cubic perovskite crystal structure, this structure can tolerate significant non-stoichiometry and partial substitution. Consequently, perovskite compounds show a diversity of structural modifications and variants. These derivatives could be classified to three main types: cubic perovskites, double perovskites and layered perovskites.

1.3.1.1 Cubic Perovskites (ABO_3)

The ideal cubic perovskite has a symmetric structure and crystalline in space group $Pm\bar{3}m$. It is represented by the general formula ABO_3, in which *A* is the larger cation and *B* is the smaller. The *B* cations form BO_6 units in octahedral coordination, that are joined at the corners; while the *A* cations forming AO_{12} groups in dodecahedral coordination; these occupy the holes that were created by *B* cations in the framework. For instance, in $SrTiO_3$, the Sr ions occupy the 12 coordinate sites, while Ti ions sit in the six coordinate sites [10]. A representation of the $SrTiO_3$ cubic structure is shown in Figure 1.1. The equivalent positions of the *A* and *B* sites cations in the ideal unit cell are (0, 0, 0) and $(\frac{1}{2}, \frac{1}{2}, \frac{1}{2})$ respectively, and for the oxygen anions are $(\frac{1}{2}, 0, 0)$.

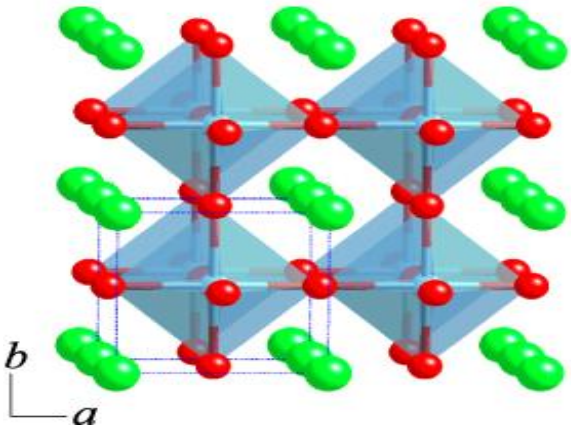

Figure 1.1 Representation of the ideal cubic perovskite $SrTiO_3$ with space group $Pm\bar{3}m$ [13]. The green, blue and red spheres are the Sr^{2+}, Ti^{4+} and O^{2-} ions. The blue octahedra show the 6- coordinate geometry of Ti^{4+} cations.

The variation of the *A* and *B* site cations, depending on the constituent properties such as ionic radius, valence and electronegativity, influences the local symmetry of the perovskite structure resulting in deviations from the ideal. Consequently, perovskite oxides with other structures are often encountered at room temperature (RT), although there are examples that transform to the cubic structure at high temperatures. For example, the perovskite oxide $CaTiO_3$ exhibits an orthorhombic structure with space group *Pbnm* below 1380 K. Increasing the temperature results in a series of transition phases, ultimately to the ideal cubic structure above 1580 K [2].

1.3.1.2 Double Perovskites ($AB_{1-x}B_xO_3$)

In the double perovskite structure, the unit cell length is twice of that of the cubic perovskite [14]. That is because the two different *B* type cations alternate at 6 coordinate sites in a NaCl type ordering, while the one type of *A* cation occupies the 12 coordinate site. The formation of such structures is described in *B*-cation arrangement in double perovskites by Poeppelmeier and co-workers [15]. The Sr_2FeMoO_6 oxide is an example of an ordered double perovskite where Fe and Mo ions occupy the *B* sites, and Sr the *A* site [16, 17]. Ordering of the octahedral cations is particularly common when x = 1/2, 1/3 and 1/4 and there is a large difference in the ionic radii and/or oxidation states of the octahedral cations [17]. Figure 1.2 shows a rock-salt type ordering in double perovskite structure. The ideal structure of double perovskites is cubic and belongs to space group $Fm\bar{3}m$. The positions of the atoms in the cubic double perovskite unit cell are (0, 0, 0) and $(\frac{1}{2}, \frac{1}{2}, \frac{1}{2})$ for the two *B* site atoms and $(\frac{1}{4}, \frac{1}{4}, \frac{1}{4})$ for the *A* site atom. The oxygen anions sit at (x, 0, 0) where $x \approx \frac{1}{4}$ [17].

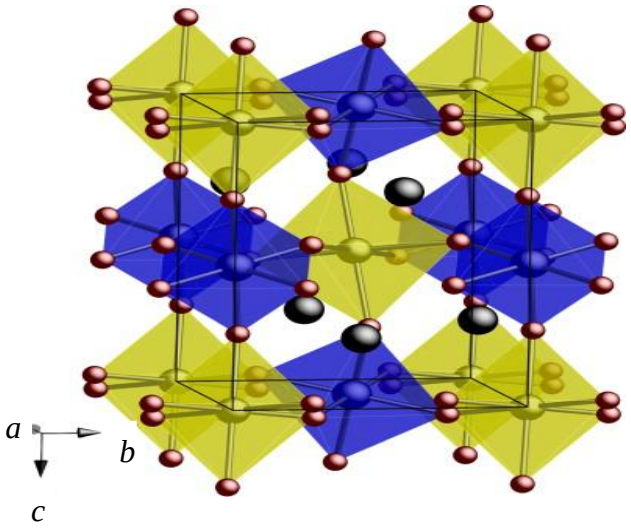

Figure 1.2 A rock salt ordering in double perovskite structure [18]. The black, gray and red spheres are the A site, B site and oxygen ions. The blue and yellow octahedra containing the two different B site cations are rock-salt ordered.

Oxides with general formula ABO_3 can also form double perovskites structure, if one type of the *B* site atom has two different oxidation states in the framework. For instance, $BaBiO_3$ forms a double perovskite structure due to the oxidation of Bi from

3+ to 5+. The two Bi ions share the corner of the octahedral site on the structure [19]. The materials reported in chapter 6 are double perovskites.

1.3.1.3 Layered Perovskites ($A_{(n-1)}B_{(n)}O_{(3n+1)}$)

The three most important classes of layered perovskites structure types are the Ruddleson-Popper, Aurivillius and Dion-Jacobson phases. In each case, a number of two dimensional (2D) slabs are inserted into the ABO_3 structure with different offsets creating layers. Generally, layered perovskites are represented by the formula $A_{(n+1)}B_{(n)}O_{(3n+1)}$ where n indicates to the size of 2D slab. If the slab is one, two or three BO_6 units thick, n will equal to 1, 2 or 3.... For instance, Sr_2RuO_4 is Ruddleson-Popper phase with a motif of SrO layer and $SrRuO_3$ slabs offset at a $(\frac{1}{2}, \frac{1}{2})$ translation [20, 21]. Bi_3TiNbO_9 perovskite is an example of an Aurivillius phase, the motif is a α-PbO type Bi_2O_2 layer and the slabs displace a $(\frac{1}{2}, \frac{1}{2})$ translation [22]; $KLaNb_2O_7$ is Dion-Jacobson phase is formed by a layer of potassium ions and $LaNb_2O_6$ slabs displacement at $(\frac{1}{2}, 0)$ [23]. Representatives of Sr_2RuO_4 and $Sr_3Ru_2O_7$ layered perovskite structures are shown in Figure 1.3.

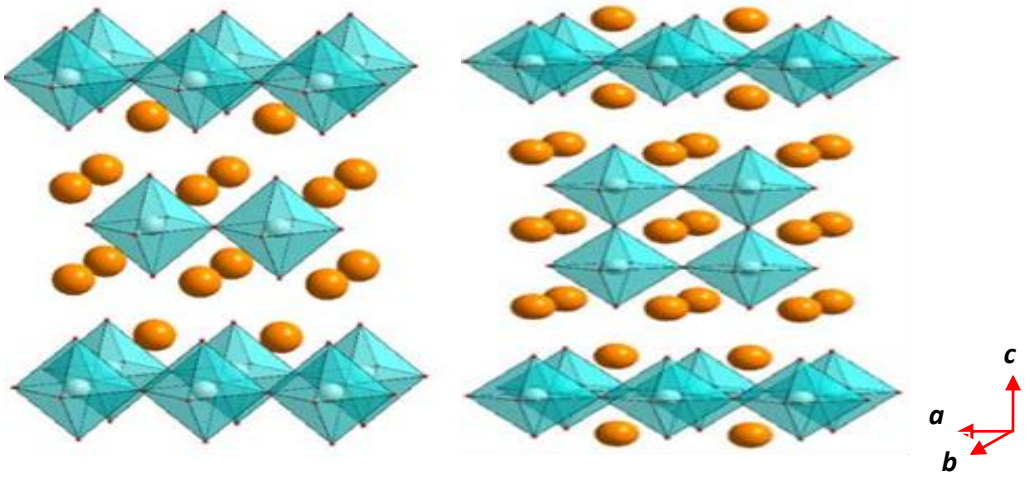

Figure 1.3 Representatives of Sr_2RuO_4 and $Sr_3Ru_2O_7$ layered perovskite structures [24]. The cyan, orange and red spheres are the strontium, ruthenium and oxygen ions.

$Sr_3Ru_2O_7$ structure consists of two layers of corner-sharing RuO_6 octahedra interleaved with SrO rock-salt layers, *i.e.*, $SrO(SrRuO_3)_n$ (n = 2) [25]. The Ru atoms are located in the centre of each octahedron and the crystallographic *c*-axis is shown in the vertical direction of Figure 1.3. There are two oxygen atoms in Sr_2RuO_4 at (0,

0, *z*), referred to as the apical O atoms and four oxygen atoms at (0, $\frac{1}{2}$, 0) and at equivalent positions, the equatorial O atoms [26].

1.3.2 Structural Distortions

Distortions in perovskites occur as a consequence of competition between cations. The deviation from the ideal cubic structure to orthorhombic, rhombohedral, tetragonal etc... represents a common distortion in perovskites [27]. As seen in Table 1.1, the variation in either *A* or *B* site type cations results in changes in the unit cell symmetry. For instance, the crystal structures of the titanates perovskites $CaTiO_3$ and $BaTiO_3$ are derived the high symmetry $Pm\bar{3}m$ structure as result of Ca and Ba substitutions on the *A* site respectively. The rare earth oxides La*B*O_3 (*B*= V, Cr, Fe and Rh…) also show the replacement of the *B* site cation, by either Al or Ni, lowers the crystal symmetry of these from orthorhombic to rhombohedral. Distortion mechanisms in perovskites can be described by octahedral tilting, octahedral distortion and lattice parameters distortion in the unit cells.

Table 1.1 Chemical formula, Crystal structure and Space group for some perovskites at RT.

Chemical formula	Crystal Structure	Space Group
$SrTiO_3$ [28], $KTaO_3$ [29], $BaSnO_3$ [30], $EuTiO_3$ [31]	Cubic	$Pm\bar{3}m$
$CaTiO_3$ [32], $ScAlO_3$ [33], $CeVO_3$ [34], $GdFeO_3$ [35], $LaRhO_3$ [36], $TbFeO_3$ [37]	Orthorhombic	$Pbnm$
$BiFeO_3$ [38], $LaAlO_3$ [39], $LaNiO_3$ [40], $NdAlO_3$ [41], $PrAlO_3$ [42]	Rhombohedral	$R\bar{3}c$
$PbTiO_3$ [43], $BaTiO_3$ [44]	Tetragonal	$P4mm$
$BaTbO_3$ [45], $CeAlO_3$ [46]	Tetragonal	$I4/mcm$
$BiCrO_3$ [47], $BiMnO_3$ [48]	Monoclinic	$C2$

1.3.2.1 Octahedral Tilting

Tilting in perovskites occurs when the *A* site cation is too small for the cavity formed by the corner sharing octahedral network [17]. Consequently the octahedra, formed by the oxygen surrounding *B*-site cations, rotate about the three axes (*x*, *y*, *z*) reducing the bond-distance mismatch, and lowering the unit cell symmetry. Octahedral tilting is characterized by two means: tilt system and tilt angle. The tilt system describes the orientation of the *B* site octahedra along the three lattice vector ($\vec{a}, \vec{b}, \vec{c}$) in the unit cell [49]. For instance, if the octahedra have the same tilts with equal magnitudes about the three axes, the tilt system, will be given as $a^+a^+a^+$ in Glazer's notation [50], where the superscript (+) and the parameter (a) refer to the sense and direction of tilting respectively. The system parameters for the octahedra with different angle magnitudes along either (010) or (001) axes can be described by (*b*) and (*c*) respectively. For the octahedra with either no tilting or tilting in the opposite sense, the parameters are superscripted by (0) and (-) respectively. According to a group theoretical analysis of octahedral tilting in perovskites, undertaken by Howard and Stokes, there are 15 possible structures derived from the cubic aristotype by the simple tilting of rigid octahedra [51]. The common tilt systems in perovskites are summarized in Table 1.2. The tilts result in a decrease in the distances between octahedral centres (and hence pseudocubic subcell edges) perpendicular to the tilt axis. The corresponding distance along the tilt axis is unchanged by the tilt operation[50]. Denoting the angles of tilt about [100], [010] and [001] by α, β and γ respectively (less than 15 °) the pseudocubic axial lengths are given by $a_p = \xi \cos\beta \cos\gamma$; $b_p = \xi \cos\alpha \cos\gamma$; and $c_p = \xi \cos\alpha \cos\beta$ [50]. Where ξ is the anion-anion distance through the centre of the octahedron. These equations show that three unequal tilts produce three unequal pseudocubic spacings, two equal tilts produce two equal spacings and one different and three equal tilts produce three equal spacings.

The tilt angle is the bond angle of the oxygen atoms linked between two adjacent octahedra. The magnitude of tilts is commonly estimated from the atomic coordinates for the BO_6 octahedra. For instance, the tilt system in (*Cmcm*) orthorhombic structural phase transition of $CaTiO_3$ comprises out-of-phase tilting of the oxygen octahedra around the *b*-axis and in-phase tilting around the *c*-axis. The coordinates of the oxygen atoms can be written as O1 $(\frac{1}{4} + u_1,\ 0,\ 0)$,

O2 (0, $\frac{1}{4}-v_2$, w_2) and O3 ($\frac{1}{4}+u_3$, $\frac{1}{4}-v_3$, $\frac{1}{4}$) where *u*, *v* and *w* are small and the tilt angles can be estimated using $\tan\varphi = 2(u_3 + w_2)$ and $\tan\psi = 2(u_1 + v_2)$[52]. Octahedral tilting plays an important role in structural, electrical and magnetic properties of perovskites. For example, $Sr_xCa_{1-x}RuO_3$ [53] and $Se_{1-x}Te_xCuO_3$ [54] exhibit changes in magnetism upon the increases in *x*. These changes are thought to be driven by the changes in the (Ru-O-Ru) and (Cu-O-Cu) bond angles. It is well established that both orbital and charge orderings are sensitive to the changes in octahedral tilting [55].

Table 1.2 Possible tilt systems in perovskite [51].

Type	Tilt System	Space Group	Relative Pseudocubic subcell parameters
No Tilt	$a^0a^0a^0$	$Pm\bar{3}m$	$a_p = b_p = c_p$
One Tilt	$a^0a^0c^+$	$P4/mbm$	$a_p = b_p < c_p$
	$a^0a^0c^-$	$I4/mcm$	$a_p = b_p < c_p$
Two Tilts	$a^0b^+b^+$	$I4/mmm$	$a_p < b_p = c_p$
	$a^0b^+c^-$	$Cmcm$	$a_p < b_p \neq c_p$
	$a^0b^-c^-$	$C2/m$	$a_p < b_p \neq c_p$, $\propto \neq 90^o$
	$a^0b^-b^-$	$Imma$	$a_p < b_p = c_p$, $\propto \neq 90^o$
Three Tilts	$a^+b^+c^+$	$Immm$	$a_p \neq b_p \neq c_p$
	$a^+a^+a^+$	$Im\bar{3}$	$a_p = b_p = c_p$
	$a^+a^+c^-$	$P4_2/nmc$	$a_p = b_p \neq c_p$
	$a^+b^-c^-$	$P2_1/m$	$a_p \neq b_p \neq c_p$, $\propto \neq 90^o$
	$a^+b^-b^-$	$Pnma$	$a_p \neq b_p = c_p$, $\propto \neq 90^o$
	$a^-b^-c^-$	$P\bar{1}$	$a_p \neq b_p \neq c_p$, $\propto \neq \beta \neq \gamma \neq 90^o$
	$a^-b^-b^-$	$C2/c$	$a_p \neq b_p = c_p$, $\propto \neq \beta \neq \gamma \neq 90^o$
	$a^-a^-a^-$	$R\bar{3}c$	$a_p = b_p = c_p$, $\propto = \beta = \gamma \neq 90^o$

The treatment of the perovskite materials at high temperatures and pressures typically results in a decrease or an increase in the octahedral tilting, respectively. For $CaTiO_3$ this implies that the thermo expansion of unit cells leads to decreasing in octahedral tilting which eventually increases the symmetry. The distribution in bond

angles *B*-O-*B* decreases as the bond distances *B*-O increases upon heating [2]. For different perovskite compositions, octahedral tilting decreases upon an increase in the tolerance factor. For instance, in the alkaline earth double perovskites A_2MnMO$_6$ where *M* =Ru, Sb, Nb and Ta, replacing Ca^{2+} (8 coordinate ionic radius, 1.12 Å) [56] with a larger cation such as Sr^{2+}(1.26 Å) [56] results in lowering the tilting from $(a^-b^+a^-)$ for Ca$_2$MnMO$_6$ to $(a^0b^0c^-)$ for Sr$_2$MnMO$_6$ [55]. The increase in the relative size of *A* site cations is consistent with a increase in tolerance factor according to the Goldschmidt equation.

1.3.2.2 Octahedral Distortion

The octahedral site distortion results in splitting the six *B*-O bonds into different lengths. It is commonly attributed to main cooperative factors; ionic size effects, electronic and magnetic effects, including the Jahn-Teller effect (JT). In all cases, a distortion in the ideal octahedral geometry is necessary to minimize energy changes associated with octahedron rotation, strains and electronic degeneracy. The energetic stabilization of perovskites becomes larger when the primary distortion mechanism is elongation of two bonds (trans to each other), and contraction of the remaining four. The mechanism of inverse distortion where four bonds are expanded and two bonds are contracted results in lower energetic stabilization [55]. In the example given above for alkaline earth mixed metal perovskites A_2MnMO$_6$, the replacement of Ca with Sr results in increases in octahedral distortion. This increase is thought to be driven, not only by the increase in tolerance factor (size effect), but also by the impact of the lattice symmetry, local cation ordering and the JT ions (Mn^{3+}) [55].

Octahedral distortion can be described by the degenerate vibration modes Q_n where Q is a vibration function of the displacements (*l*) originated from the split of the bond distances, and n = 1, 2, 3… [57]. For instance, the octahedral distortions in the ternary and ordered quaternary perovskites $LaMnO_3$ and Sr_2CuWO_6 are denoted as $Q_2 = [l_x - l_y]$ and $Q_3 = [(2l_z - l_x - l_y)/\sqrt{3}\ ]$ respectively. The vibration mode Q_2 describes a distortion where two *B*-*O* bonds shorten and two *B*-*O* bonds lengthen, whilst Q_3 describes a deformation with four bonds contract and two bonds expand[55]. The quantitative measurement of the distortion magnitude is given as Δd in Equation 1.2, in which d_i is the individual bond distance between the *B* site cations and the

oxygen anions, and d_{av} is the average of these distances [55]. The octahedral distortion can also be measured by the deviation of the bond angle O-*B*-O from 90°.

$$\Delta d = 1/6 \sum_i (d_i - d_{av})^2 / (d_{av})^2 \ * i = 1, 2, ..6. \qquad 1.2$$

Perovskites containing JT active ions on the octahedral site exhibit many significant properties like metal-insulator transitions, magnetic and structural phase changes, etc. depending on charge density, temperature and atomic structure. The cooperative JT distortion plays also a crucial role in charge and orbital orderings. The manganese perovskites $Ln_{1-x}A_xMnO_3$ and the ordered copper oxide A_2CuWO_6 where *Ln* is trivalent rare earth cation, *A* is alkaline earth ions exhibit charge and orbital orderings that can be attributed to cooperative JT distortion [55].

1.3.2.3 Lattice Parameters Distortion

The distortion of lattice parameters from pseudocubic symmetry can be quantified by Equation 1.3 where a_i is the individual lattice parameters converted to the length of the equivalent primitive unit cell and a_{av} is the average of the converted lattice parameter [55].

$$D = 1/3 \sum_i (a_i - a_{av}) / a_{av} \qquad 1.3$$

The distortion of lattice metric from the cubic is commonly attributed to strain effects on the structure. Strain in perovskites can be induced through several means including octahedral tilting, octahedral distortions and disorder. The cooperative JT distortion is expected to have the most significant effect on *D*. The lattice parameters for the 3*d* metal perovskite $LnMnO_3$ ($D > 2.0$ %) are more distorted than these for $LnFeO_3$ ($D \leq 2.0$ %) due to the cooperative JT distortion [55].

The increase in lattice parameters distortion frequently influences both the electrical and magnetic states in transition metal oxides. For example, the degeneracy of the Co 3*d* level ions in $LaCo_{1-x}Ti_xO_3$ [58] decreases as the distortion in lattice parameters decreases whilst in $Ln_{1-x}A_xMnO_3$ [59], the observed increase in the Curie temperature and decrease in colossal magnetic resistance effects are correlated with an increase in lattice parameters distortion.

1.3.3 Structural Defects

Perovskite oxides with different chemical compositions exhibit a wide range of ordered and disordered structures [60]. These structures often contain point defects induced by either internal effects such as nonstoichiometry or external effect including temperature, pressure and nuclear irradiation. The defect formation, structure and characteristics can play a crucial role in the optical, catalytic and transport properties of the oxides [27, 60]. The increase in oxygen non stoichiometry in $LnCoO_{3-\delta}$, for instance, is found to be consistent with a decrease in the activation energy for CO oxidation [61]. This correlation implies that the activity is more strongly related to the ease of oxygen removal rather than other factors such as adsorbed states. The ordered double perovskites $A_2A^*MO_{6-\delta}$ where A and A^* are alkaline earth and M = Sb, Nb and Ta exhibit a transition from non-ionic conductor to conductor as consequence of defect formation on the structure [62, 63].

Mechanisms of defect formation in nonstoichiometric crystals suggest lattices may have either excess charge or excess ions situated in the structure. Defects can be introduced in the perovskite structure by the substitution of similar sized cations with different formal valencies on both the A and B sites [64, 65]. Doping with either higher or lower valence cations on the B site produces nonstoichiometric compounds of the type $AB_{1-x}B'_xO_{3\pm\delta}$ with oxygen ion vacancies or interstitials in the structure. The substitution of the A site ions with higher valence cation results in A site vacancies with stoichiometry $A_{(1-x)}A_x'BO_3$, but doping with lower valence cations on the A site generates oxygen vacancies or electron holes on the $A_{(1-x)}A_x'BO_{3-\delta}$ structure [64, 65]. The reactions associated with the formation of structural defects are given in the Equations 1.4-7 [66] where $B_B^\times$, $O_O^\times$, $A_A^\times$ are B site, oxygen and A site atoms; $V_O^{\bullet\bullet}$, $h^\bullet$ are oxygen vacancy and electron hole; V_A'' and M_B'' are A site cation vacancy and divalent B site cation vacancy.

$$B_B^\times + O_O^\times \leftrightarrow M_B'' + V_O^{\bullet\bullet} + \frac{1}{2}O_2(\mathrm{g}) \qquad 1.4$$

$$V_O^{\bullet\bullet} + \frac{1}{2}O_2(\mathrm{g}) \leftrightarrow 2h^\bullet + O_O^\times \qquad 1.5$$

$$A_A^\times + O_O^\times \leftrightarrow V_A'' + V_O^{\bullet\bullet} + AO \qquad 1.6$$

$$O_O^\times \leftrightarrow V_O^{\bullet\bullet} + \frac{1}{2}O_2(\mathrm{g}) + 2\bar{e} \qquad 1.7$$

Examples of oxygen deficient perovskites are $(La, Sr)_2M_{1-x}Cr_xO_{6-\delta}$ where *M* = V, Mn, Fe, Co, Ni, and Cu, and for *A* site cation deficient compounds are $Cu_{0.5}TaO_3$ [27] and $La_{0.4}Sr_{0.4}TiO_3$ [67]. Excess oxygen anion nonstoichiometry can be found in $LaMnO_{3+\delta}$ and $EuTiO_{3+\delta}$ perovskites. This type of nonstoichiometry is less common than the oxygen deficiency because the introduction of oxygen interstitial in the structure is thermodynamically unfavourable.

The anion nonstoichiometry and defect concentrations are typically a function of partial oxygen pressure and temperature. Equations 1.5 and 1.7 illustrate that applying high oxygen pressures on the systems result in either an increase in the concentration of the electron holes (positive charge carriers) or decrease in the oxygen vacancy and free electron (negative charge carriers) contents. Consequently, the *p*-type conductivity at high oxygen pressure P_{O_2} is higher while *n*-type conductivity is lower. An increase in the number of vacant sites facilities oxygen transport through the crystals by increasing the concentration of potential carries. An increase in temperature is expected to increase the kinetic mobility of the ions. Therefore, more oxygen vacancies would be generated [27, 68]. Ordered anion vacancies are believed to be partly responsible for some important solid state phenomena, such as superconductivity, as well as unusual cation geometries [69]. In $YBa_2Cu_3O_7$, ordering of the cations, anions and oxygen vacancies results in an orthorhombic structure that contains copper-oxygen square planes and square pyramids. This arrangement is thought to be the source of its unusual electronic behaviour, where the superconducting planes (CuO square pyramids) are separated by insulating one dimensional chains (Cu-O planes) [69, 70].

1.3.4 Physical properties

The flexibility in the chemical structures and compositions enables perovskite materials to exhibit various physical properties including ferroelectricity, superconductivity, charge ordering and high thermopower. These properties are impacted by the interplay of structural, spin dependent transport, magnetic and transport properties.

1.3.4.1 Electrical Properties

As with other materials, the electrical behaviour of perovskites depends on the outermost electrons, which may be localized on a specific atomic site or may be

collective. Perovskite oxides are found to be ferroelectric, dielectric, metallic or even superconductive, but most are semiconductors. The ferroelectric materials (FE) are generally defined by the reversible spontaneous electrical polarization in absence of any electrical field [71]. The ferroelectricity usually appears at temperatures below the Curie temperature (T_c), the temperature where a transition from a non-polarized to polarized state occurs in the system. In the ferroelectric phase, the off centre displacement of the positive charges (cations) and the negative charges (oxygen anions) in the crystal do not coincide. A number of ABO_3 perovskites exhibit ferroelectric behaviour. $BiTiO_3$, $PbTiO_3$ and $PbZrO_3$ have been well studied and reported as FE materials [72]. The FE materials exhibit an electrical dipole moment in absence of an external electrical field. In addition, plots of the electrical displacement (P) against applied electrical field (E) show different hysteresis loops that are not seen in dielectric materials (Figure 1.4). The electrical displacement of dielectric compounds displays a linear relationship with the electrical field.

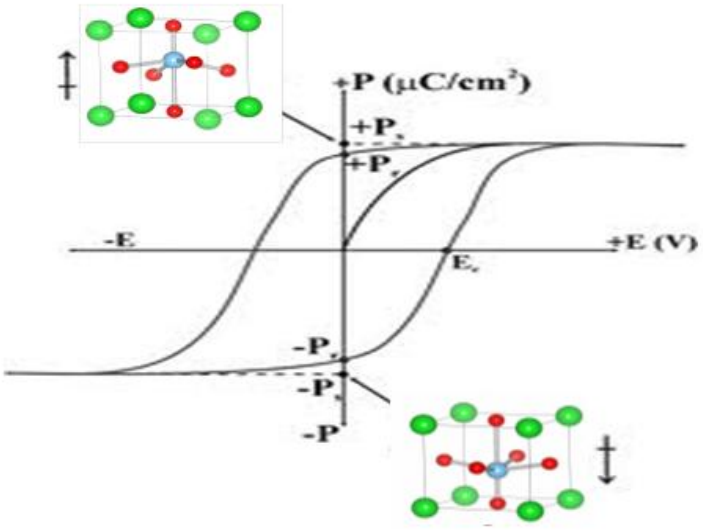

Figure 1.4 Applied electrical field versus polarization values for a FE material. The octahedra upper and down the hysteresis loop display the electrical displacement of B site cation toward the electrical field.

Ferroelectric crystals are composed of small regions called domains within which the polarisation is in same direction, but in adjacent domains the polarisation is in a different direction. The ferroelectric behaviour of poly crystalline and thin film materials differ from the single crystals due to the effects of grain boundary and

the surface on the orientation of the domain polarization. Perovskite materials can also be either pyroelectric or piezoelectric if the spontaneous polarization is temperature or pressure dependent. The perovskite oxides $PbZr_{1-x}Ti_xO_3$ are utilized in pyroelectric and piezoelectric applications. Materials with dielectric behaviour are, in fact, also polarized in an applied electrical field, but the displacements of the cations and the shift of oxygen anions toward the electrical field are in opposite directions to each other. This results in no impact on the property. The alkaline earth titanates $CaTiO_3$ and $SrTiO_3$ serve as examples of dielectric materials [6, 71].

A distinguishing feature between metallic and insulator materials is the ability of the electrical charges to flow corresponding to the electrical field. Insulators completely resist the flow of electrical charges whereas the metallic compounds respond to an electrical field. Perovskites with high dielectric constants such as $SrTiO_3$ [73] and $YBiO_3$ [74] are considered insulators. The mixed metal perovskite system $LaMn_{1-x}Ru_xO_3$ exhibits a metallic- insulator transition upon increasing *x* whereas $LaNiO_3$ [75] and $LaTiO_3$ [76] are metallic conductors. The superconductivity of cuprates oxides containing mixed valence Cu^{2+}/Cu^{3+} is another interesting character to the electrical properties of perovskites. Superconductivity exists in oxides such as $Tl_2Ba_2Ca_2Cu_3O_{9+\delta}$, $YBa_2Cu_3O_{7-\delta}$ and $HgBa_2Ca_2Cu_3O_{8+\delta}$ at a critical temperature higher than that found in conventional alloys [77].

Semiconductor behaviour is the most common electrical property of perovskites [78]. In semiconductor materials, the magnitude of electrical conductivity is in-between those for conductor and insulator. The mechanism of semiconducting is understood by two concepts: band gap and charge carrier. In such materials, electrons can be exited from the valence band to the conduction band, only if have sufficient energy to cross the band gap. The exited electrons in the conduction band leave behind an unoccupied state, creating electron holes in the valence band. The electrons in the two bands and the holes contribute to the electrical conductivity. Doping with electron acceptors or donors creates respectively positive (holes) or negative (electrons) charge carriers in the crystal structure and also generates higher electrical conductivity [79]. Based on that, semiconductors are classified to *p* and *n*-type materials indicating the positive and negative charge carriers respectively. The conductivity of semiconductor materials commonly follows the Arrhenius Equation 1.8 [80] where σ_t is the electrical conductivity at certain temperature and σ_o is the conductivity coefficient factor. ε_a is the activation energy (eV), k is Boltzmann

constant (8.617×10^{-5} eV. K^{-1}) and T is temperature (K). Examples of semiconductor perovskite are *Ln*RhO_3 [81] and $La_{1-x}Sr_xCrO_3$ [82].

$$\sigma_t = \sigma_o e^{-\varepsilon_a/kT} \qquad 1.8$$

1.3.4.2 Magnetic Properties.

Contrary to classical studies, magnetism is a purely quantum mechanical property. It is robust phenomenon that is yet not fully understood [83]. Perovskites have an enormous variety of intriguing electronic and magnetic properties. This variety is related not only to the chemical flexibility, but also to properties of the metal on the *B* site [1]. Perovskite oxides with transition metals exhibit magnetic properties that are mainly related to the quantum spin number (S) of the *d* orbital electrons of the metal ions. Oxides containing transition metal ions with unfilled *d* orbitals or only having paired electrons in the valence shell are diamagnetic (S = 0), where compounds with metals that have unpaired of electrons are generally paramagnetic.

The *B*-O-*B* angle of oxygen shared by two *B* site cations plays an important role in magnetization. In the ideal cubic double perovskites $A_2BB'O_6$ where the *B*-O-*B* bond angle is 180°, the superexchange interactions between the nearest neighbour *B* cations frequently results in antiparallel coupling of the spins. When the B^{3+} ions are in two sublattices ($A_2BB^*O_6$) other spin arrangements are possible. If the B^* cations are diamagnetic, the *B* cations will align antiferromagnetically, and the most important exchange mechanism is believed to be long range superexchange interaction through two oxygens of the type *B*-O-B^*-O-*B* [27]. The strength of the superexchange interaction is weakened as the bond angle decreases [27]. When the *B*-O-*B* bond angle is 90°, the superexchange via the overlap of metal *d* orbitals and two different *p* oxygen anions orbitals can result in ferromagnetic coupling. For instance, the *A*-site ordered perovskites $CaCu_3Ge_4O_{12}$ and $CaCu_3Sn_4O_{12}$ exhibit ferromagnetic behaviour although $CaCu_3Ti_4O_{12}$ (isostructural oxide) is antiferromagnetic. That is due to special alignments of the CuO_4 planes which influence the magnetic properties of Cu spins [84]. In the two first cases, direct exchange interactions give rise to the ferromagnetism, whereas the involvement of Ti-3*d* orbital produces antiferromagnetic superexchange interaction in the third oxide [84].

1.3.4.3 Charge, Orbital and Spin Ordering

The presence of mixed valent cations in perovskites may give rise to charge ordering, where the cations with different charge are ordered on either the *A*-site or *B*-site. When the charge ordering occurs below the transition temperature (*Tco*), the electron hopping between the cations is suppressed and the electrical resistivity is increased [85]. Doped manganites perovskites have been extensively studied due to charge ordering that results in different ground states and colossal magneto-resistance [85, 86]. For instance, doping with $x = 0.5$ in $La_{1-x}Ca_xMnO_3$ results in charge localization between Mn^{3+} and Mn^{4+} ions below T*co* [87]. A stripe model of charge ordered perovskite $La^{3+}_{0.5}Ca^{2+}_{0.5}Mn^{3+}_{0.5}Mn^{4+}_{0.5}O_3$ [88, 89] is shown in Figure 1.5. Charge orderings can also be observed in the undoped oxides $Ba^{2+}Bi^{3+}_{0.5}Bi^{5+}_{0.5}O_3$ [90], $Ca^{2+}Fe^{3+}_{0.5}Fe^{5+}_{0.5}O_3$ [91] and $Pr^{3+}Ni^{2+}_{0.5}Ni^{4+}_{0.5}O_3$ [92] where the instability of the oxidation states of *B* site cations leads to charge disproportion and ordering of two stable cations below the transition temperature.

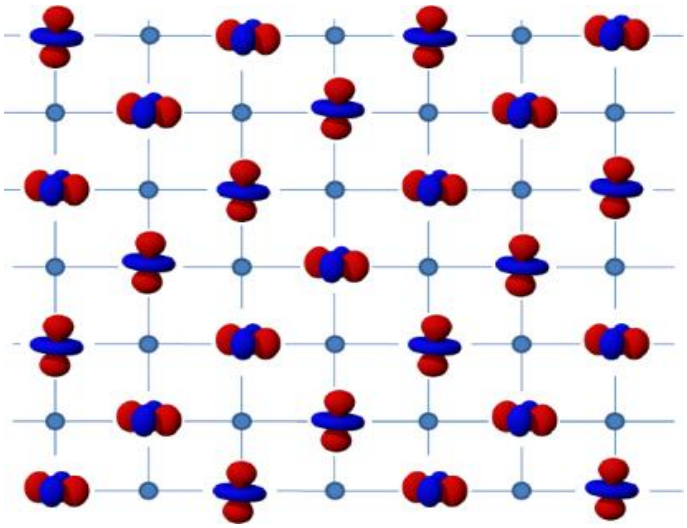

Figure 1.5 Charge and orbital ordering of Mn^{3+} and Mn^{4+} in $La^{3+}_{0.5}Ca^{2+}_{0.5}Mn^{3+}_{0.5}Mn^{4+}_{0.5}O_3$. The blue spheres are representative of the Mn^{4+} ions where the red and blue dumb bell shapes are the Mn^{3+} ions [93].

In transition metal perovskites ABO_3, the transition metal forms a BO_6 octahedra configuration, in which its d orbitals split into t_{2g} and e_g orbital groups. The t_{2g} orbitals are lower in energy while the e_g orbitals are higher in energy and point directly toward the ligands. This gives rise to two possible configurations of the *d* electron filling, the low spin (LS) and high spin (HS) states. In perovskite materials mainly the high spin configuration is observed for 3*d* transition metals.

When the t_{2g} or e_g orbitals are partially occupied, the elongation of the octahedra occurs usually giving two long and four short *B*O bonds, which is known as a Jahn-Teller (JT) distortion. The presence of JT active cations in perovskites can lead to the so called cooperative JT distortions, and long range orbital ordering [27]. The manner of the ordered orbitals may affect the magnetic ordering of a material, which is described by the Goodenough-Kanamori rules [94]. Magnetic properties are mainly exhibited by materials containing transition metals or lanthanides, owing to their partially filled *d* and *f* orbitals, respectively. When the moments in the material are oriented randomly, it is known as a paramagnet, in which the alignment of the moments can be achieved through the application of a magnetic field. Examples of paramagnetic materials are $SrIrO_3$ [95] and $LaRhO_3$ [96]. A spontaneous magnetic ordering can be observed, however, when the interaction between unpaired electrons lead to alignments of electron spins. If all the long *B*-O bonds are orientated in same direction, the cooperative distortion along single axis results in a ferrodistortive orbital ordering. This orbital ordering pattern is adopted by the ordered perovskites Ba_2CuWO_6 [97] and Ba_2CuTeO_6. Antiferrodistortive orbital ordering is observed in $LaMnO_3$ [86] where the orientation of the octahedral distortions is contracted in *ac* plane [98]. Orbital-ordering gives rise to the anisotropy of the electron-transfer interaction. This favours or disfavours the double-exchange interaction or superexchange interaction in an orbital direction-dependent manner and hence gives a complex spin-orbital coupled state. Figure 1.6 shows different types of orbital ordering occurring in manganese perovskites [86].

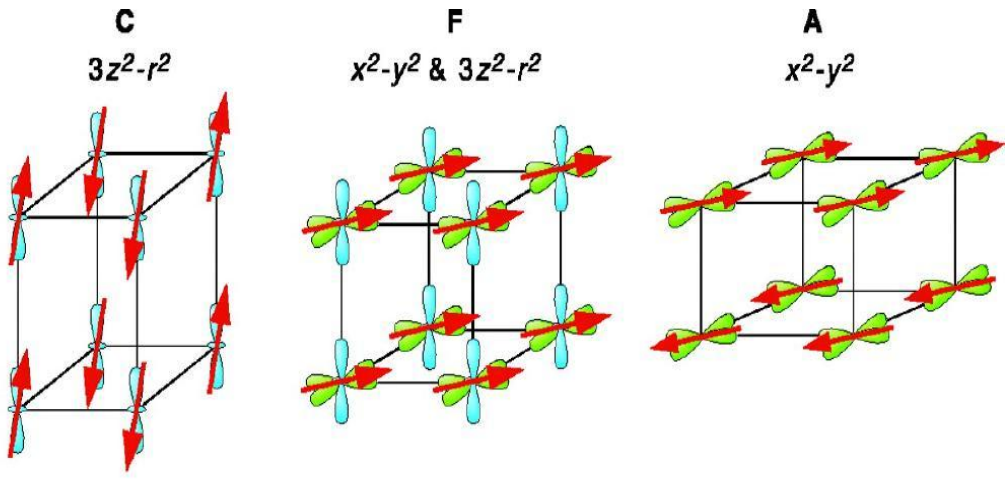

Figure 1.6 Different types of orbital ordering in manganese perovskite oxides. The A and C spin arrangements show two types of magnetic ordering in antiferromagnetic materials where F spin arrangement illustrates the ferromagnetic ordering [99].

The spontaneous spin (magnetic) ordering can be observed in perovskite oxides when the interaction between unpaired electrons leads to alignments of electron spins. If the spins are oriented parallel to each other and giving overall moments, the materials are ferromagnetic. Compounds containing multiple magnetic ions with different magnitude moments and antiparallel alignments could also exhibit ferromagnetic behaviour as the overall moments are not cancelled. For instance, the cation-disordered perovskite $La_{1.5}Sr_{0.5}RhMnO_6$ is shown to be a soft ferromagnetic with T_c = 105 K and an ordered magnetic moment of 3.65 μ_B per Mn [100]. In the antiferromagnetic ordering, the spin moments on the neighbouring cations are aligned antiparallel and the overall moments is cancelled. The spins in such ordering can be aligned with several different arrangements. These are classified in three types *A*, *C* and *G* illustrated in Figures 1.6 and 1.7 respectively. The *A*– type antiferromagnetic ordering, for example, is observed in $LaMnO_3$ where the *C* and *G* types are adopted by systems such as, $BiCoO_3$ [101] and $La_{1-x}Bi_xFe_{0.5}Mn_{0.5}O_3$ [102] respectively.

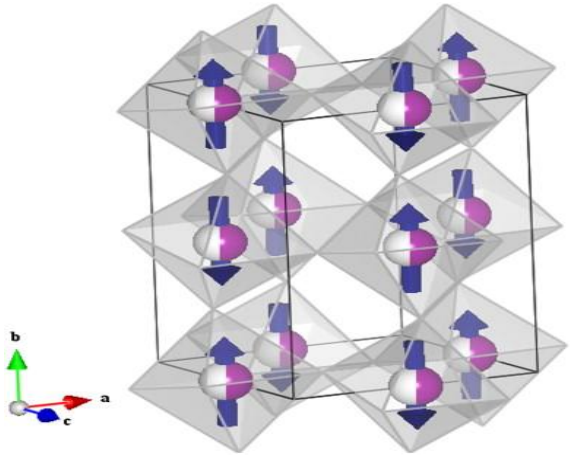

Figure 1.7 G -type antiferromagnetic ordering in double perovskites [103].

1.3.4.4 Optical Properties

Compounds with the perovskite structure have been used as model systems for spectroscopic studies in the infrared, visible, and ultraviolet regions [27]. Perovskite

oxides are particularly interesting since the effect of magnetic ordering of the transition metal ion in the *B*-site can be studied [27]. The optical properties of many perovskites containing transition metal ions with an empty or partially filled *d*-orbital, have been explored. For instance, for $SrTiO_3$ where the *d* orbitals of Ti^{4+} ion are empty, the emission spectrum shows a band maximum around 50 nm with low quenching temperature, 35 K and a small Stokes shift, 7000 cm^{-1} [27]. Such results are not seen for oxides with partial filled *d* orbitals such as $SrCrO_3$. The TiO_6 octahedra in $SrTiO_3$ are favourable for energy band formation [104]. It is possible to sensitize an $SrTiO_3$ electrode for visible light by doping with other transition metals such as Nb^{3+}, Cr^{3+} and Rh^{3+} [105-107].

1.3.4.5 Adsorption Properties

Gas adsorption on the perovskite surfaces has frequently been investigated because of the importance of these compounds as catalysts [27]. The extent of gas adsorption on La*B*O_3 perovskites, where *B* is transition metal, at 298 K was found to be dependent on the electron configuration of the transition metal cation. The $CO_{(g)}$ adsorption on La*B*O_3 reaches a maximum when *B* = Fe^{3+}, whereas $NO_{(g)}$ adsorption shows maximum for Co^{3+} and Mn^{3+} [27]. The NO adsorption over the wide range of temperature 273-673 K is independent of the temperature on substrates such as $LaFeO_3$ and $LaNiO_3$ [27]. A thermodynamic study on gases adsorption on $LaCrO_3$ demonstrated that NO has higher adsorption enthalpy and lower adsorption entropy than CO. It is stated that gases could be adsorbed on different sites of the perovskite surface [27]. O_2 adsorption on doped perovskites such as $La_{1-x}Sr_xCoO_3$ display two adsorption peaks (α and β). These peaks are attributed to adsorbed oxygen at low temperature and lattice oxygen at high temperature respectively [27]. The amount of O_2 adsorption and the intensity of α type adsorption peak are related to nonstoichiometry and structural defects, where the decrease in α type adsorption temperature is consistent with the increasing number of *d* electrons of the transition metal. The β type adsorption peaks is associated with *B* site cations [27].

1.3.5 Applications

Perovskite oxides are used in many electrical, magnetic and optical devices. For instance, $BaTiO_3$ is used in multi-layer capacitors, $BaZrO_3$ in dielectric resonators, $GdFeO_3$ in magnetic bubble memory and $YAlO_3$ as a laser host [1].

Manganese perovskites are widely utilized in ferromagnetic materials and photochemical catalysts [10]. Lead zirconate titanates and lanthanum lead zirconate titanate oxides are employed in piezoelectric transducers and electro optical modulators [10]. Semiconducting Pt and Sr doped $LaNiO_3$ perovskites are effective electro-catalysts for the oxygen generation reactions in strong basic solutions [27]. Some perovskites display good performance as cathodes in high temperature solid oxide fuel cells (SOFCs). For example, the electronic conducting perovskites $La_{1-x}Sr_xMnO_3$ have been extensively used as cathodes in ZrO_2 based SOFCs [1]. Oxide ionic conductors such as Sr and Mg doped $LaGaO_3$ are important electrolyte materials with high oxide ion conduction over wide range of oxygen pressure for CeO_2 based SOFCs [1]. Sr doped $LaCr_{1-x}M_xO_3$ oxides, where M = Mn, Fe, Co, Ni, are also used as anodes for SOFCs [1]. Perovskites are also useful materials in gas sensors. Oxygen, humidity and alcohol gas sensors can be built from $SrTiO_3$, $BaSnO_3$, and $GdCoO_3$ [1].

1.4 Literature Review

This section gives a very brief overview of the topics related to the materials studied. It describes the literature relevant to *A* site and *B* site doped $LnRh_{1-x}Cu_xO_3$ and $AA^*(BB^*)O_{5.5}$ perovskites. It reviews experimental results, discussion and conclusions for a number of papers related to these oxides.

1.4.1 Studies on the structural, electrical and magnetic properties of the *A* site and *B* site doped $Ln_{1-y}A_yRh_{1-x}Cu_xB_xO_3$ (*Ln* = La^{3+}, Tb^{3+}; *A*= Ca^{2+}, Sr^{2+}, Pb^{2+} and Bi^{3+}; *B* = Sc^{3+} and Zn^{2+})

Perovskite oxides containing transition metals with a high oxidation state have been extensively investigated, since the number of *d*-electrons is critical in determining the electronic and magnetic properties of such systems [96, 108]. For example, Cu is generally found as Cu^{2+} in most perovskites although in oxides prepared under strongly oxidising conditions Cu^{3+} can be realized. The structural studies of $LaCuO_3$ illustrated that the copper trivalent state can be stabilized in six fold coordination and revealed both Cu^{2+} and Cu^{3+} can coexist within a remarkable wide range of the oxygen stoichiometry. The correlation between the covalency of the metal oxygen bond and the copper valance state increased with the increase in the oxidation value. The trivalent copper state can adopt different electronic

configurations [109, 110]. The importance of controlling the oxidation state is clearly evident in both the cuprate superconductors and manganate CMR materials [111, 112]. An interesting question, and one we have been addressing, is what happens when two or more transition metals, that are capable of existing in different oxidation states, are incorporated on the *B*-site in perovskites oxides? Electron delocalization between these is likely to have a significant impact on properties of such oxides. For instance, the Curie temperature of the ruthenates $SrRu_{1-x}Cr_xO_3$, increases with x as consequence of a double exchange interaction involving Cr^{3+} and Cr^{4+} [113]. This behaviour is contrary to that seen for all other the 3*d* transition metal substituted compounds such as $SrRu_{1-x}Mn_xO_3$ where doping reduces the Curie temperature [114, 115].

The variation of the *A* site doping may also have enormous impact on the oxides properties. The substitution of Ca on the *A* site in $ARu_{1-x}Cr_xO_3$ results in robust ferromagnetic behaviour and two transition steps are now seen in the Sr doped oxide due to the spin-orbital coupling [116]. The alkaline earth oxide A_2FeMoO_6 serves as another example where the effects of both the *A*-site cation character and the charge delocalization between the *B*-site cations results in unpredictable ferromagnetic behaviours [117]. The percentage of the *A* and *B* site compositions is considered to be important as well. The studies on $SrRu_{1-x}Cr_xO_3$ illustrated that the magnetic behaviours of the oxides are depended on x content. In $La_{1-x}Pb_xFeO_3$, where the oxidation state of Fe^{3+} ion is fixed, the decrease in the electrical resistivity is not linearly related with Pb content. A decline in the resistance is obtained up to $x > 0.2$ due to a point defect of doped Pb^{2+} ions, which increases the mobility of the charge carriers on the La^{3+} site. In contrast, the resistivity increases of the range $0.2 < x < 0.32$ as a result of an increase in the oxygen vacancies of La site, which leads to an electronic neutralization of some holes in the materials. Above $x = 0.32$, the resistance declines against an increase in the free electrons concentration of the oxygen vacancies [118]. It is worth recalling that when $x = 1$ the majority of Pb doped perovskites exhibit a stronger ferroelectric stability than other doped earth alkali materials [119].

Various systems of the type $Ln_{1-y}A_yRh_{1-x}B_xO_3$ (*Ln* = lanthanoid ions, *A* = alkali or alkali earth ions, and *B* = transition metal ions) have been reported [120, 121]. The desirable physical properties of these compounds make them attractive for use in catalysis or as magnetic sensors [122, 123]. The compounds are typically stable to high

temperature and can exhibit interesting magnetic and crystallographic properties [124, 125]. It has been established that complex magnetic interactions can occur in systems with the mixed valences [111, 126]. The Rh ions, which favour the low spin state, can exist as a mixture of Rh^{3+} and Rh^{4+} creating disordered structures with unpredictable charge distributions [96, 126]. It is well known that 4*d* electrons have a large spatial extent; then, a very strong spin-orbit coupling, small coulomb interaction between *d* electrons, and a large ligand-field effect, that results in a low spin state, are expected [127]. Generally, the magnetic and structural properties are sensitive to the ionic radii of the *A* site and *B* site cations. Therefore, the size limitation, doping concentration and mechanical strains will influence the electrical and magnetic properties [128, 129]. Perovskite-type Rh oxides seem interesting; however, there are a few of systematic studies on these oxides [96]. This likely because the trivalent rhodium ion with six 4*d* electrons is expected to have no appreciable magnetic moment of in the low spin state. Hence, it seems important to investigate the magnetic and electrical properties of these materials.

The family of the lanthanoid rhodium oxides is found to be isostructural with $GdFeO_3$ [81, 96, 130], and has an orthorhombic structure with space group *Pbnm*. Recall that perovskites having sufficiently small *A*-site ions (a small tolerance factor) often allow for a distorted perovskite structure that has a rotated framework of oxygen octahedra and displaced *A* site ions [49]. This lowers the space group symmetry from cubic $Pm\bar{3}m$ to orthorhombic *Pbnm*, and the number of ABO_3 formula units per primitive cell increases from Z = 1 to Z = 4 [50]. The rotations of the octahedra in the *Pbnm* space group can be decomposed into two steps [50]. The first step is the rotation around the [110] direction of the original cubic frame (the cubic frame is rotated by 45° around the *c* axis with respect to the *Pbnm* frame). The second step is a rotation around [001] direction. The rotations minimize distortions of the octahedra. The pattern of neighboring octahedral rotations is denoted by $a^-a^-c^+$ in Glazer notation [50]. These rotations also allow for the displacement of *A*-site ions in the *x*-*y* plane without further lowering of the space-group symmetry. It is well know that a tilt-distorted ABO_3 perovskite can be empirically expressed as a decoupled combination of changes of the *B*-O bond length and the tilting angle of BO_6 octahedral framework[131]. The crystal structure of $LnRhO_3$ is in contrast with the $BiRhO_3$ oxide, which generally forms pyrochlore structures at atmospheric pressure [132]. The

perovskite-type structure is favored for $BiRhO_3$ by high pressure, since it consists of close-packed BiO_3 layers having Rh^{3+} cations occupying all the octahedral sites, which share common corners because of cubic stacking of the BiO_3 layers [132].

The distortion in the lanthanoid compounds is mainly attributed to size effects [81, 130], but charge delocalization and other effects can also be important [111, 133]. The structure of the oxides can distort by modifying the chemical compositions. For instance, the orthorhombicity of the alkaline earth oxide $La_{1-x}A_xRhO_3$, at x = 0.05, decreases from 1.530×10^{-2} for undoped $LaRhO_3$ to 1.529, 1.375 and 1.282×10^{-2} for Ca, Sr and Ba doped ions respectively as consequence of the ionic size effect. The unitless orthorhombicity is given as $(b-a)/a$ where a and b are lattice parameters [96]. The increases in the A content from 0.05 to 0.1 leads to a decline in the orthorhombicity at 1.484 and 1.291×10^{-2} for Ca and Sr respectively. The orthorhombicity decreases as both the relative size and the ionic content of the doped cations increases [129]. Consequently, phase transitions are expected to occur at high doping concentrations. The doped oxide $La_{1-x}Sr_xRhO_3$, for example, exhibits a phase transition from orthorhombic to tetragonal at x = 0.4. Doping with Mn^{2+} in $LaMn_{0.9}Rh_{0.1}O_3$ results in orthorhombic-pseudocubic- rhombohedral phase transitions at high temperature [111].

The $Ln_{1-y}A_yRh_{1-x}B_xO_3$ oxides are either n or p type semiconductors with a band gap around 2.2 eV [123]. For instance, the substitution of La^{3+} with divalent cations acts as hole-doping [129, 134] and results in lower resistivity and thermopower for the perovskites. The paramagnetic oxide $La_{1-x}Sr_xRhO_3$ exhibits transitions from semiconducting to metallic at $x \geq 0.3$ as consequence of the hole mobility effect on the structure [128, 134]. Doping with the transition metals ions Mn^{2+}, Cu^{2+} and Ni^{2+} on the B-site introduces holes in the electronic structure [125, 133]. The electrical conductivity of the ferromagnetic perovskite $LaRh_{1-x}Mn_xO_3$ increases with x indicating the materials are p type semiconductors [111]. The undoped oxide $LuRhO_3$ serves, also, an example for p type semiconductor behavior, but it may be doped n-type by the introduction of Th^{4+} during the synthesis [123]. The Fermi level of $LuRhO_3$ is pinned to that of the electrolyte, in photocatalytic cells, and the potential is independent of whether the oxide is a p or n-type semiconductor [123]. Unlike the 3*d* Co perovskites, doped $LnRhO_3$ oxides have large values of thermo-power at high temperatures [135]. The region of the valence band in the proximity of Fermi level is believed to be dominated by Rh-derived states [136]. In $CuRh_{0.9}Mg_{0.1}O_2$, the Rh states

are located in the proximity of forbidden band level suggesting the importance of the electronic structure of the Rh ions for the large thermoelectric power at high temperature [136].

The 3*d*-4*d* mixed metal oxide $LaRh_{0.5}Cu_{0.5}O_3$ has been prepared and is reported to have an orthorhombic perovskite structure in space group *Pbnm*, where the Rh and Cu are disordered at the octahedral site with $\Delta d = 1.1\times10^{-4}$. The substitution of the Jahn-Teller active Cu^{2+} ion increases the distortion of the BO_6 octahedra, but the effect was less than what expected for 50 % Cu^{2+} content. X-ray spectroscopy showed Rh in $LaCu_{0.5}Rh_{0.5}O_3$ to have a valence state of around +3.5 as a consequence of charge delocalisation between the Cu and Rh cations. This delocalisation increases the formal valency of the Cu to close to 2.5, which reduces the impact of the Jahn-Teller distortion. Furthermore, $LaRh_{0.5}Cu_{0.5}O_3$ exhibits semiconducting and paramagnetic behavior in the temperature range 4-300 K[133, 137].

The partial substitution of the *A* site is expected to influence the extent of electron delocalization between the two transition metals on the *B* site that have been described as $Rh^{3.5+}$ and $Cu^{+2.5}$, leading to changes in the physical properties. These changes could be influenced, not only by the differences in the effective charges, but also by the differences in the ionic radii and the electron configurations of both the *A* and *B*-site cations. The Pb^{2+} and Bi^{3+} doped oxides are found to exhibit electrical and magnetic behavior different to that of the alkaline earth doped oxides. That is believed to be a consequence of the sterochemical influence of the $6s^2$ lone pair electrons [119, 138, 139]. On the other hand, both the effective charges of the ($4s^0$ $3d^0$) Sc^{3+} and ($4s^0$ $3d^{10}$) Zn^{2+} ions and the strong overlap of the unfilled and filled 3*d* orbitals with sp^2 oxygen orbital [140] are also expected to effect the formal valency of Rh ions leading to changes in the magnetic and electronic properties of the perovskites.

This study focuses on the influence of the *A* and *B* site doping on $LnRh_{1-x}Cu_xO_3$ oxides characteristics. The series was targeted due to the lack of research on Rh-Cu perovskite oxides, which exhibited interesting structural, electrical and magnetic behavior upon the changes in composition. Doping with different valent cations, either on *A* or *B* site influences the charge delocalization of the system. The doped cations have been selected based on their effective charge, ionic size and electron configuration. The impact of the replacing of La^{3+} with Tb^{3+} has been addressed to establish the role of the *A*-site cation in controlling the structure and

valence distribution of the cations. The rare earth oxide $TbRhO_3$ exhibits physical properties similar to those for $LaRhO_3$ oxide, but the latter oxide has much lower magnetic susceptibility and conductivity due to the absence of the 4*f* orbital electrons[96].

1.4.2 Influence of water on the structure of anion deficient perovskites $AA^*(BB^*)O_{5.5}$ (A, A^* and B = Sr^{2+} or Ba^{2+}, B^*= Nb^{5+} or Ta^{5+})

A major barrier to the wide-scale utilization of solid oxide fuel cells (SOFCs) is the development of an anode material that has low electrode over-potentials and ohmic losses at relatively low temperatures and that will operate with a range of fuels, and in particular natural gas [1, 141]. Several mixed oxides with the perovskite structure are candidates for use as SOFC components [142] depending on the type of conductivity exhibited: purely ionic conduction for electrolytes, electronic for interconnect materials, and mixed ionic-electronic conduction for electrodes. Anion deficient perovskite-type oxides of the type $ABO_{3-\delta}$ are currently amongst the most promising materials for such applications, and considerable effort is being directed to the study of such oxides [143]. Recent work in this area has included studies of a number of oxygen deficient double perovskites of the type $A_2BB'O_{5.5-\delta}$ were two different cation exhibit a rock-salt like ordering in the octahedral lattice [144]. In addition to oxide ion conductivity the same anion deficient perovskites can exhibit proton conductivity at lower temperatures under wet atmospheres as a consequence of their ability to incorporate water [143, 145]. $Sr_{4.5}Nb_{1.5}O_{8.25}$ is reported to become a proton conductor after absorbing water at moderate temperatures [146]. Anion deficient double perovskites also show promise as photo catalysts for water splitting[147].

Niobium and tantalum both form a series of double perovskites that can described by the general formula $Sr_{6-2x}B_{2+2x}O_{11+3x}$ (B = Nb^{5+}, Ta^{5+}) that simplifies to $Sr_3BO_{5.5}$ when x = 0. These oxides are structurally related to the rare mineral cryolite Na_3AlF_6 in which the Na^+ cation occupies both the *A* and half the *B*-sites of the perovskite [148]. Stoichiometric analogues such as Sr_3ReO_6 are also known [149]. Levin and co-workers have demonstrated that $Sr_4Nb_2O_9$, the x = 1/3 member of the series $Sr_{6-2x}Nb_{2+2x}O_{11+3x}$ exhibits a cryolite like structure with Sr and Nb ordering on the perovskite *B*-sites [150]. These workers concluded that the materials exhibit a complicated local structure with disorder of both the anion and perovskite *A*-type Sr

cations. They also noted that the precise composition of $Sr_4Nb_2O_9$ was sensitive to annealing conditions suggesting that there may be anion and/or *A*-site vacancies [150]. Li and Hong explored this suggestion and these authors established both that the oxygen anions partially occupy interstitial sites in the perovskite, and that the distribution of the anions was dependent on the precise stoichiometry [151].

Many studies on the electronic structures of alkaline earth antimonite, niobates and tantalates oxides with general formula $A(B^*B)O_3$ have been done [62, 63]. These are in face-centred cubic symmetry with space group $Fm\bar{3}m$. The highly polarizing cations Sr^{2+} and Ba^{2+} can occupy the octahedral site obtaining a rocked salt ordering in the structure [141]. The ordered-cation distribution is mainly attributed to both the ionic size and the bonding character of the *B*-site cations [141]. The double perovskites have also a large concentration of oxygen vacancies in their cubic structures. For instance, the earth alkali oxides $Ba_6Nb_2O_{11}$ and $Sr_{5.92}Ta_{2.08}O_{11.12}$ contain a large concentration of oxygen vacancies [62, 152]. It is assumed that the vacancies promote proton defects in the crystals following to the reaction illustrated in Equation 1.9, resulting in a high ionic conductivity [62]. The total oxygen ion conductivity and proton conductivity is very sensitive to atmosphere conditions [152]. The conductivity is significantly impacted by changes to the oxygen superlattice structure due to the differences in coordination tendencies of *A* and *B* cations [62]. The perovskites related oxides, under saturated atmospheric water vapour, possibly uptake maximum one mole water per formula unit, exhibiting high-temperature proton transportation [153]. These properties are favourable for many applications in the industry such as, photovoltaic cells and solid oxide fuel cells [154, 155].

$$H_2O + V_0^{**} + O_0 \leftrightarrow 2(OH^*)_0 \qquad 1.9$$

The main features of the interaction of water with niobates and tantalates perovskites are: (1) the interaction process functionally depends on the temperature and water vapour activity; and (2) the initial matrix structure of the oxides totally sustains ordering at low contents of the water uptake [152]. The increase in water uptake of the oxides associated with both lowering in the cell symmetry and forming of new hydrated phases in the crystal structure [153]. There are different methods for creating oxygen vacancies in the oxides structure such as, acceptor doping, a stoichiometry shift and structural disorder in the oxygen sub lattice [63, 154]. The importance of creating oxygen vacancies is to develop characteristics of the

materials that may be used in devices such as solid oxide fuel cells [10]. The influence of the dry and wet atmosphere environments on the electronic structure of such materials has been particularly undertaken in major studies. The total conductivity of the oxides was found to be a functional of the vapour pressure and temperature. In the $Sr_6Ta_2O_6$ oxide, the conductivity in wet environment is higher than in the dry environment, indicating the contribution of the ion conductivity [152].

The defect ordered oxides $Sr_3MO_{5.5-\delta}$, $Sr_2CaMO_{5.5-\delta}$ and $Sr_2BaMO_{5.5-\delta}$ where M = Sb^{5+}, Nb^{5+} or Ta^{5+} are isostructral with $(NH_4)_3FeF_6$ and have also an ideal cubic double perovskite structure with space group $Fm\bar{3}m$ [156-158]. They exhibit a large amount of diffuse scattering in their neutron powder diffraction patterns [156]. This diffuse scattering associated with absence of long range ordering for both the octahedral tilting and vacancies on the structure [156, 158]. Increasing the lattice parameter (a) influences the physical properties of the compounds, resulting in high conductivity at high temperatures [156]. For instance, the electrical conductivity for $Sr_3NbO_{5.5-\delta}$ (a = 8.271 Å), $Sr_2CaTaO_{5.5-\delta}$ (8.232 Å) and $Sr_2CaNbO_{5.5-\delta}$ (8.172 Å) increases in order consistently with the increase in the lattice parameter, a, at temperatures above 650 $^{\circ}$C [156]. The increase in lattice parameter is thought to result in more open structure which implies higher ion mobility due to lower energy path for ion immigration, and thus the conductivity increases [156]. Doping on the A site can change the structural properties of the perovskites. For example, Rietveld refinement of the powder X-ray diffraction data for $A_2MnB'O_6$ (A = Ca, Sr; B = Sb, Ta) indicated significant ordering of Mn and Sb at the B-site in Sr_2MnSbO_6 while all other phases showed mostly a random distribution of the B-site cations [159]. Doping with rare earth ions as La^{3+} in Sr_2LaSbO_6 results in a distorted structure and lower symmetry [160].

In this work attempts were made to prepare compounds with $AA^*(BB^*)O_{5.5}$ structures using two general methods. The methods were both solid state reactions but used different slurry media, namely acetone and ionized water. The purpose of the solvents is to enhance the homogeneity of the mixtures, and to create dry and wet media for the reaction. Four oxides have been successfully obtained and structurally characterized. The morphology and the microstructure of the oxides are found to be dependent on the synthetic methods. The oxides form a cation ordered double perovskite structure (space group $Fm\bar{3}m$) where both the A cations and oxygen

anions are disordered into the two sites. The identifications of anion disorder and water structure demonstrate the possibility of oxygen and proton conductance for the materials.

1.5 References

[1] T. Ishihara, Structure and Properties of Perovskite Oxides, 2009, Springer, US.

[2] L. S. Cavalcante, V. S. Marques, J. C. Sczancoski, M. T. Escote, M. R. Joya, J. A. Varela, M. R. M. C. Santos, P. S. Pizani and E. Longo, *Chemical Engineering* 143 (2008) 299-307.

[3] L. E. Cross and R. E. Newnham, *The American Ceramic Society*, 3 (1986) 289-305 .

[4] K. M. Rabe, C. H. Ahn and J.-M. Triscone, Physics of ferroelectrics: a modern perspective, 2007, Springer, New York, .

[5] G. H. Jonker and J. H. Van Santen, *Physica*, 16 (1950) 337-349.

[6] A. von Hippel, *Zeitschrift für Physik A Hadrons and Nuclei*, 133 (1952) 158-173.

[7] G. H. Haertling, *Journal of the American Ceramic Society*, 82 (1999) 797-818.

[8] Y.-M. Li, *Solid State Communications*, 62 (1987) 677-680.

[9] H. R. Wenk and A. G. Bulach, Minerals: Their Constitution and Origin, 2005, Cambridge University Press, Cambridge, .

[10] L. G. Tejuca and J. L. G. Fierro, Properties and Applications of Perovskite-Type Oxides, 1993, Marcel Dekker, New York, .

[11] A. S. Bhalla, R. Guo and R. Roy, *Materials Research Innovations*, 4 (2000) 3-26.

[12] V. M. Goldschmidt, *Naturwissenschaften*, 14 (1926) 477-485.

[13] N. A. Marks, D. J. Carter, M. Sassi, A. L. Rohl, K. E. Sickafus, B. P. Uberuaga and C. R. Stanek, *Journal of Physics: Condensed Matter*, 25 (2013) 065504.

[14] M. C. Knapp, Investigations Into the Structure and Properties of Ordered Perovskites, Layered Perovskites, and Defect Pyrochlores, 2006, The Ohio State University, .

[15] M. T. Anderson, K. B. Greenwood, G. A. Taylor and K. R. Poeppelmeier, *Progress in Solid State Chemistry*, 22 (1993) 197-233.

[16] Y. Tomioka, T. Okuda, Y. Okimoto, R. Kumai, K. I. Kobayashi and Y. Tokura, *Physical Review B*, 61 (2000) 422-427.

[17] M. W. Lufaso, P. W. Barnes and P. M. Woodward, *Acta Crystallographica Section B*, 62 (2006) 397-410.

[18] S. J. Mugavero Iii, W. R. Gemmill, I. P. Roof and H.-C. zur Loye, *Journal of Solid State Chemistry*, 182 (2009) 1950-1963.

[19] G. Thornton and A. J. Jacobson, *Acta Crystallographica Section B*, 34 (1978) 351-354.

[20] J. J. Neumeier, M. F. Hundley, M. G. Smith, J. D. Thompson, C. Allgeier, H. Xie, W. Yelon and J. S. Kim, *Physical Review B*, 50 (1994) 17910-17916.

[21] L. Walz and F. Lichtenberg, *Acta Crystallographica Section C*, 49 (1993) 1268-1270.

[22] J. G. Thompson, A. D. Rae, R. L. Withers and D. C. Craig, *Acta Crystallographica Section B*, 47 (1991) 174-80.

[23] M. Sato, J. Abo, T. Jin and M. Ohta, *Solid State Ionics*, 51 (1992) 85-89.

[24] Perovskite Structure and Derivatives, http://www.princeton.edu, 2012.

[25] Q. Huang, J. W. Lynn, R. W. Erwin, J. Jarupatrakorn and R. J. Cava, *Physical Review B*, 58 (1998) 8515-8521.

[26] B. J. Kennedy and T. Vogt, *Journal of Physics and Chemistry of Solids*, 63 (2002) 2093-2100.

[27] M. A. Pena and J. L. G. Fierro, *Chemical Reviews*, 101 (2001) 1981-2017.

[28] S. Fuentes, R. Zarate, E. Chavez, P. Muñoz, D. Díaz-Droguett and P. Leyton, *Journal of Materials Science*, 45 (2010) 1448-1452.

[29] E. A. Zhurova, Y. Ivanov, V. Zavodnik and V. Tsirelson, *Acta Crystallographica Section B*, 56 (2000) 594-600.

[30] A. S. Deepa, S. Vidya, P. C. Manu, S. Solomon, A. John and J. K. Thomas, *Journal of Alloys and Compounds*, 509 (2011) 1830-1835.

[31] T. Wei, Q. J. Zhou, X. Yang, Q. G. Song, Z. P. Li, X. L. Qi and J. M. Liu, *Applied Surface Science*, 258 (2012) 4601-4606.

[32] X. Liu and R. C. Liebermann, *Physics and Chemistry of Mineral*, 20 (1993) 171-175.

[33] N. L. Ross, *Physics and Chemistry of Mineral*, 25 (1998) 597-602.

[34] M. Reehuis, C. Ulrich, P. Pattison, M. Miyasaka, Y. Tokura and B. Keimer, *The European Physical Journal B - Condensed Matter and Complex Systems*, 64 (2008) 27-34.

[35] G. C. Kostogloudis and C. H. Ftikos, *Journal of Materials Science*, 34 (1999) 2169-2173.

[36] R. B. Macquart, M. D. Smith and H.-C. Zur Loye, *Crystal Growth & Design*, 6 (2006) 1361-1365.

[37] Y. H. Zou, W. L. Li, S. L. Wang, H. W. Zhu, P. G. Li and W. H. Tang, *Journal of Alloys and Compounds*, 519 (2012) 82-84.

[38] F. Kubel and H. Schmid, *Acta Crystallographica Section B*, 46 (1990) 698-702.

[39] H. Lehnert, H. Boysen, P. Dreier and Y. Yu, *Zeitschrift für Kristallographie*, 215 (2000) 145.

[40] G. Gou, I. Grinberg, A. M. Rappe and J. M. Rondinelli, *Physical Review B*, 84 (2011) 144101.

[41] C. J. Howard, B. J. Kennedy and B. C. Chakoumakos, *Journal of Physics: Condensed Matter*, 12 (2000) 349.

[42] S. M. Moussa, B. J. Kennedy, B. A. Hunter, C. J. Howard and T. Vogt, *Journal of Physics: Condensed Matter*, 13 (2001) L203.

[43] A. Khalal and D. Khatib, *Ferroelectrics Letters Section*, 26 (1999) 91-98.

[44] D. S. Keeble and P. A. Thomas, *Journal of Applied Crystallography*, 42 (2009) 480-484.

[45] W. T. Fu, D. Visser and D. J. W. Ijdo, *Journal of Solid State Chemistry*, 165 (2002) 393-396.

[46] W. T. Fu and D. J. W. Ijdo, *Journal of Solid State Chemistry*, 177 (2004) 2973-2976.

[47] S. Niitaka, M. Azuma, M. Takano, E. Nishibori, M. Takata and M. Sakata, *Solid State Ionics*, 172 (2004) 557-559.

[48] H. Yang, Z. H. Chi, J. L. Jiang, W. J. Feng, Z. E. Cao, T. Xian, C. Q. Jin and R. C. Yu, *Journal of Alloys and Compounds*, 461 (2008) 1-5.

[49] P. Woodward, *Acta Crystallographica Section B*, 53 (1997) 32-43.

[50] A. Glazer, *Acta Crystallographica Section B*, 28 (1972) 3384-3392.

[51] C. J. Howard and H. T. Stokes, *Acta Crystallographica Section B*, 54 (1998) 782-789.

[52] B. J. Kennedy, C. J. Howard and B. C. Chakoumakos, *Journal of Physics: Condensed Matter*, 11 (1999) 1479.

[53] I. I. Mazin and D. J. Singh, *Physical Review B*, 56 (1997) 2556-2571.

[54] A. Villesuzanne, M. H. Whangbo, M. A. Subramanian and S. F. Matar, *Chemistry of Materials*, 17 (2005) 4350-4355.

[55] M. W. Lufaso and P. M. Woodward, *Acta Crystallographica Section B*, 60 (2004) 10-20.

[56] R. D. Shannon, *Acta Crystallographica Section A*, 32 (1976) 751-767.

[57] J. S. Zhou and J. B. Goodenough, *Physical Review B*, 77 (2008) 132104.

[58] I. Álvarez-Serrano, G. J. Cuello, M. L. López, A. Jiménez-López, C. Pico, E. Rodríguez-Castellón, E. Rodríguez and M. L. Veiga, *Journal of Physics D: Applied Physics*, 41 (2008) 195001.

[59] N. C. Yeh, C. C. Fu, J. Y. T. Wei, R. P. Vasquez, J. Huynh, S. M. Maurer, G. Beach and D. A. Beam, *Journal of Applied Physics*, 81 (1997) 5499-5501.

[60] D. M. Smyth, *Annual Review of Materials Science*, 15 (1985) 329-357.

[61] I. D. Seymour, A. Chroneos, J. A. Kilner and R. W. Grimes, *Physical Chemistry Chemical Physics*, 13 (2011) 15305-15310.

[62] I. Animitsa, A. Neiman, A. Sharafutdinov and S. Nochrin, *Solid State Ionics*, 136–137 (2000) 265-271.

[63] P. Colomban, F. Romain, A. Neiman and I. Animitsa, *Solid State Ionics*, 145 (2001) 339-347.

[64] N. L. Ross, R. J. Angel, L. W. Finger, R. M. Hazen and C. T. Prewitt, *Journal of American Chemical Society*, 351 (1987) 164-172.

[65] W. Wunderlich, *Journal of Nuclear Materials*, 389 (2009) 57-61.

[66] J. L. G. Fierro, Metal Oxides: Chemistry and Applications, 2005, Taylor & Francis, .

[67] D. Neagu and J. T. S. Irvine, *Chemistry of Materials*, 22 (2010) 5042-5053.

[68] J. W. Fergus, *Sensors and Actuators B: Chemical*, 123 (2007) 1169-1179.

[69] S. E. Dann, Reactions and Characterization of Solids, 2002, Royal Society of Chemistry, UK, .

[70] G. Calestani and C. Rizzoli, *Nature*, 328 (1987) 606.

[71] R. E. Cohen, *Nature*, 358 (1992) 136-138.

[72] A. Sternberg, M. Antonova, M. Livinsh, M. Dambekalne, K. Kundzins, W. Haessler, R. Bittner and H. Weber, *Ferroelectrics*, 298 (2004) 283-288.

[73] S. De Gendt, S. F. Bent, A. Delabie, J. W. Elam, S. B. Kang, A. Londergan and O. van der Straten, Atomic Layer Deposition Applications 5, 2009, Electrochemical Society, USA, .

[74] H. Jin, S. H. Rhim, J. Im and A. J. Freeman, *Scientific Reports*, 3 (2013).

[75] K. Sreedhar, J. M. Honig, M. Darwin, M. McElfresh, P. M. Shand, J. Xu, B. C. Crooker and J. Spalek, *Physical Review B*, 46 (1992) 6382-6386.

[76] F. J. Wong, S.-H. Baek, R. V. Chopdekar, V. V. Mehta, H.-W. Jang, C.-B. Eom and Y. Suzuki, *Physical Review B*, 81 (2010) 161101.

[77] A. M. Luiz, Room Temperature Superconductivity, 2011, .

[78] L. G. Tejuca and J. L. G. Fierro, Properties and Applications of Perovskite-Type Oxides, 1992, Taylor & Francis, .

[79] A. R. West, Solid State Chemistry and Its Applications, 1991, Wiley, UK, .

[80] S. R. Logan, *Journal of Chemical Education*, 59 (1982) 279.

[81] R. B. Macquart, M. D. Smith and H. C. zur Loye, *Crystal Growth & Design*, 6 (2006) 1361-1365.

[82] D. P. Karim and A. T. Aldred, *Physical Review B*, 20 (1979) 2255-2263.

[83] W. Nolting and A. Ramakanth, Quantum Theory of Magnetism, 2008, Springer-Verlag, Berlin Heidelberg, .

[84] H. Shiraki, T. Saito, T. Yamada, M. Tsujimoto, M. Azuma, H. Kurata, S. Isoda, M. Takano and Y. Shimakawa, *Physical Review B*, 76 (2007) 140403.

[85] C. Zener, *Physical Review*, 82 (1951) 403-405.

[86] J. B. Goodenough, *Physical Review*, 100 (1955) 564-573.

[87] Z. Jirák, E. Hadová, O. Kaman, K. Knížek, M. Maryško, E. Pollert, M. Dlouhá and S. Vratislav, *Physical Review B*, 81 (2010) 024403.

[88] P. G. Radaelli, D. E. Cox, M. Marezio and S. W. Cheong, *Physical Review B*, 55 (1997) 3015-3023.

[89] S. Mori, C. H. Chen and S. W. Cheong, *Nature*, 392 (1998) 473-476.

[90] D. E. Cox and A. W. Sleight, *Acta Crystallographica Section B*, 35 (1979) 1-10.

[91] P. M. Woodward, D. E. Cox, E. Moshopoulou, A. W. Sleight and S. Morimoto, *Physical Review B*, 62 (2000) 844-855.

[92] J. B. Torrance, P. Lacorre, A. I. Nazzal, E. J. Ansaldo and C. Niedermayer, *Physical Review B*, 45 (1992) 8209-8212.

[93] A. Singh and D. K. Singh, *Journal of Physics: Condensed Matter*, 24 (2012) 086003.

[94] J. B. Goodenough, Magnetism and the Chemical Bond, 1963, John Wiley & Sons, US.

[95] J. G. Zhao, L. X. Yang, Y. Yu, F. Y. Li, R. C. Yu, Z. Fang, L. C. Chen and C. Q. Jin, *Journal of Applied Physics*, 103 (2008) 103706-5.

[96] T. Taniguchi, W. Iizuka, Y. Nagata, T. Uchida and H. Samata, *Journal of Alloys and Compounds*, 350 (2003) 24-29.

[97] M. Gateshki and J. M. Igartua, *Journal of Physics: Condensed Matter*, 15 (2003) 6749.

[98] P. D. Battle, S. J. Blundell, J. B. Claridge, A. I. Coldea, E. J. Cussen, L. D. Noailles, M. J. Rosseinsky, J. Singleton and J. Sloan, *Chemistry of Materials*, 14 (2001) 425-434.

[99] Orbital Ordering, http://folk.uio.no, 2013.

[100] B. Bakowski, P. D. Battle, E. J. Cussen, L. D. Noailles, M. J. Rosseinsky, A. I. Coldea and J. Singleton, *Chemical Communications*, (1999) 2209-2210.

[101] A. A. Belik, I. Satoshi, K. Katsuaki, I. Naoki, S. Shin-Ichi, N. Seiji, A. Masaki, S. Yuichi, T. Mikio, I. Fujio and T. M. Eiji, *Chemistry of Materials*, 18 (2006) 6.

[102] C. A. Bridges, A. S. Sefat, E. A. Payzant, L. Cranswick and M. P. Paranthaman, *Journal of Solid State Chemistry*, 184 (2011) 830-842.

[103] Y. Long and Y. Shimakawa, *New Journal of Physics*, 12 (2010) 063029.

[104] S. Saha, T. P. Sinha and A. Mookerjee, *Journal of Physics: Condensed Matter*, 12 (2000) 3325.

[105] X. G. Guo, X. S. Chen and W. Lu, *Solid State Communications*, 126 (2003) 441-446.

[106] J. W. Liu, G. Chen, Z. H. Li and Z. G. Zhang, *Journal of Solid State Chemistry*, 38 (2007) 3704–3708.

[107] S. Kawasaki, K. Nakatsuji, J. Yoshinobu, F. Komori, R. Takahashi, M. Lippmaa, K. Mase and A. Kudo, *Applied Physics Letters*, 101 (2012) 033910-4.

[108] V. V. Bannikov, I. R. Shein, V. L. Kozhevnikov and A. L. Ivanovskii, *Journal of Structural Chemistry*, 49 (2008) 781-787.

[109] M. Karppinen, H. Yamauchi, T. Ito, H. Suematsu and O. Fukunaga, *Materials Science and Engineering B-Solid State Materials for Advanced Technology*, 41 (1996) 59-62.

[110] H. Falcon, M. J. Martinez-Lope, J. A. Alonso and J. L. G. Fierro, *Applied Catalysis B-Environmental*, 26 (2000) 131-142.

[111] M. T. Haque, H. Satoh and N. Kamegashira, *Materials Research Bulletin*, 39 (2004) 375-388.

[112] J. Liu, Z. Zhao, C. M. Xu, A. J. Duan and G. Y. Jiang, *Journal of Physical Chemistry C*, 112 (2008) 5930-5941.

[113] B. Dabrowski, S. Kolesnik, O. Chmaissem, T. Maxwell, M. Avdeev, P. W. Barnes and J. D. Jorgensen, *Physical Review B*, 72 (2005) 054428.

[114] B. J. Kennedy and Q. Zhou, *Solid State Communications*, 147 (2008) 208-211.

[115] G. Cao, S. Chikara, X. N. Lin, E. Elhami, V. Durairaj and P. Schlottmann, *Physical Review B*, 71 (2005) 035104.

[116] V. Durairaj, S. Chikara, X. N. Lin, A. Douglass, G. Cao, P. Schlottmann, E. S. Choi and R. P. Guertin, *Physical Review B*, 73 (2006) 214414.

[117] R. K. Kotnala, V. Pandey, M. Arora, V. Verma, R. P. Aloysius, A. Malik and G. L. Bhalla, *Solid State Communications*, 151 (2011) 415-419.

[118] P. Song, H. Qin, L. Zhang, K. An, Z. Lin, J. Hu and M. Jiang, *Sensors and Actuators B: Chemical*, 104 (2005) 312-316.

[119] S. Takagi, A. Subedi, D. J. Singh and V. R. Cooper, *Physical Review B*, 81 (2010) 134106.

[120] A. Martínez-Juárez, L. Sánchez, E. Chinarro, P. Recio, C. Pascual and J. R. Jurado, *Solid State Ionics*, 135 (2000) 525-528.

[121] S. Shibasaki, Y. Takahashi and I. Terasaki, *Journal of Electronic Materials*, 38 (2009) 1013-1016.

[122] R. von Helmolt, J. Wecker, B. Holzapfel, L. Schultz and K. Samwer, *Physical Review Letters*, 71 (1993) 2331-2333.

[123] H. S. Jarrett, A. W. Sleight, H. H. Kung and J. L. Gillson, *Journal of Applied Physics*, 51 (1980) 3916-3925.

[124] H. Usui, K. Kuroki and R. Arita, *Journal of Physics: Conference Series*, 150 (2009) 022095.

[125] S. Shibasaki, Y. Takahashi and I. Terasaki, *Journal of Physics: Condensed Matter*, 21 (2009) 115501.

[126] W. C. Sheets, A. E. Smith, M. A. Subramanian and W. Prellier, *Journal of Applied Physics*, 105 (2009) 023915-6.

[127] J. H. Van Vleck, The Theory of Electric and Magnetic Susceptibilities, 1965, Oxford University Press, Oxford.

[128] T. A. Mary and U. V. Varadaraju, *Journal of Solid State Chemistry*, 110 (1994) 176-179.

[129] T. Nakamura, T. Shimura, M. Itoh and Y. Takeda, *Journal of Solid State Chemistry*, 103 (1993) 523-527.

[130] A. Wold, R. J. Arnott and W. J. Croft, The Reaction of Rare Earth Oxides with a High Temperature Form of Rhodium (iii) Oxide, 1963, Defense Technical Information Center, US, .

[131] Y. Zhao, J. B. Parise, Y. Wang, K. Kusaba, M. T. Vaughan, D. J. Weidner, T. Kikegawa, J. Chen and O. Shimomura, *American Mineralogist*, 79 (1994) 615-621.

[132] J. M. Longo, P. M. Raccah, J. A. Kafalas and J. W. Pierce, *Materials Research Bulletin*, 7 (1972) 137-146.

[133] J. Ting, B. J. Kennedy, Z. Zhang, M. Avdeev, B. Johannessen and L.-Y. Jang, *Chemistry of Materials*, 22 (2010) 1640-1646.

[134] T. Shimura, M. Shikano, M. Itoh and T. Nakamura, *Physica C: Superconductivity*, 190 (1991) 104-106.

[135] I. Terasaki, S. Shibasaki, S. Yoshida and W. Kobayashi, *Materials*, 3 (2010) 786-799.

[136] P. Vilmercati, E. Martin, C. P. Cheney, F. Bondino, E. Magnano, F. Parmigiani, T. Sasagawa and N. Mannella, *Physical Review B*, 87 (2013) 125103.

[137] A. E. Smith, A. W. Sleight and M. A. Subramanian, *Materials Research Bulletin*, 45 (2010) 460-463.

[138] T. He, J. Chen, T. G. Calvarese and M. A. Subramanian, *Solid State Sciences*, 37 (2006) 467-469.

[139] S. Takagi, A. Subedi, V. R. Cooper and D. J. Singh, *Physical Review B*, 82 (2010) 134108.

[140] Z. L. Gong, X. O. Yin and L. A. Hong, *Journal of the Electrochemical Society*, 157 (2010) 129-134.

[141] E. Chinarro, G. C. Mather, A. Caballero, M. Saidi and E. Moran, *Solid State Sciences*, 10 (2008) 645-650.

[142] B. Rambabu, S. Ghosh, W. Zhao and H. Jena, *Journal of Power Sources*, 159 (2006) 21-28.

[143] R. Glöckner, M. S. Islam and T. Norby, *Solid State Ionics*, 122 (1999) 145-156.

[144] T. Norby, *Journal of Materials Chemistry*, 11 (2001) 11-18.

[145] E. Kendrick, K. S. Knight, M. S. Islam and P. R. Slater, *Solid State Ionics*, 178 (2007) 943-949.

[146] R. Glöckner, A. Neiman, Y. Larring and T. Norby, *Solid State Ionics*, 125 (1999) 369-376.

[147] K. Yoshioka, V. Petrykin, M. Kakihana, H. Kato and A. Kudo, *Journal of Catalysis*, 232 (2005) 102-107.

[148] Q. Zhou and B. J. Kennedy, *Journal of Solid State Chemistry*, 177 (2004) 654-659.

[149] B. L. Chamberland and G. Levasseur, *Materials Research Bulletin*, 14 (1979) 401-407.

[150] I. Levin, J. Y. Chan, J. H. Scott, L. Farber, T. A. Vanderah and J. E. Maslar, *Journal of Solid State Chemistry*, 166 (2002) 24-41.

[151] M. R. Li and S. T. Hong, *Chemistry of Materials*, 20 (2008) 2736-2741.

[152] I. Animitsa, T. Norby, S. Marion, R. Glöckner and A. Neiman, *Solid State Ionics*, 145 (2001) 357-364.

[153] I. Animitsa, A. Neiman, N. Kochetova, D. Korona and A. Sharafutdinov, *Solid State Ionics*, 177 (2006) 2363-2368.

[154] N. Jalarvo, C. Haavik, C. Kongshaug, P. Norby and T. Norby, *Solid State Ionics*, 180 (2009) 1151-1156.

[155] J. Yin, Z. Zou and J. Ye, *The Journal of Physical Chemistry B*, 107 (2002) 61-65.

[156] K. W. Browall, O. Muller and R. H. Doremus, *Materials Research Bulletin*, 11 (1976) 1475-1481.

[157] Q. Zhou, B. J. Kennedy and M. Avdeev, *Journal of Solid State Chemistry*, 184 (2011) 2559-2565.

[158] G. King, K. J. Thomas and A. Llobet, *Inorganic Chemistry*, 51 (2012) 13060-13068.

[159] T. Mandal, V. Poltavets, M. Croft and M. Greenblatt, *Journal of Solid State Chemistry*, 181 (2008) 2325 - 2331.

[160] X. Yin, Y. Wang, F. Huang, Y. Xia, D. Wan and J. Yao, *Journal of Solid State Chemistry*, 184 (2011) 3324-3328.

Experimental

In this chapter, the details of the sample preparation techniques and experimental instrumentation used during the research are described and discussed. A brief introduction to different methodology and characterization techniques is also presented.

2.1 Chemical Synthesis

The synthesis of a material is the first and foremost essential step during the experiment research in chemical crystallography. The quality of samples depends to a great extent on the preparation method used. Furthermore, the proper selection of synthesis parameters aids optimizing the desirable properties of the samples. Chemical structure, surface morphology, grain growth, electron transport and magnetic properties are all dependent on the synthesis methods. There are various methods available for the synthesis of polycrystalline perovskite materials like the Solid State Reaction (SSR) route, Liquid Solutions Reaction (LSR) route and Gas Phase Reaction (GPR) route.

2.1.1 Solid State Reaction (SSR)

The solid state reaction can be done by the calcination of homogenous mixtures in the solid state. The reactants which are typically mixtures of metal oxides, carbonates or nitrites, are subjected to repeated grinding and sintering at high temperatures, to complete the reaction, and to obtain a pure phase [1]. There are two factors which considered to be important in solid state reaction: thermodynamic and kinetic [2]. The former predicts the possibility that any chemical reaction may occur where the later determines the rate at which the reaction occurs [3,4]. Therefore, during synthesis, the parameters such as temperature, pressure, gas flow and time for the reaction must be varied according to the targeted phase requirements. One disadvantage of the method is that the samples are obtained as powders often with irregular grain sizes and shapes. In addition, intermediate regrinding after each heating stage is needed due to the low surface of the reaction. Consequently, the solid state method often requires long times (sometimes several days) for preparing a pure sample [1].

2.1.2 Liquid Solution Reaction (LSR)

Due to the disadvantages of low surface area and limited control of micro structure in the high temperature process, techniques such as sol–gel preparations and co-precipitation of metal ions are utilized [1]. These improve the homogeneity plus the reactivity [5]. According to the method of solvent removal, liquid solutions reactions are classified to two types. The first technique is the precipitation with filtration or centrifugation etc... The second is the thermal processing which is based on evaporation, combustion and calcination. In both techniques, the starting materials must be dissolved in a volatile, generally, organic solvent. These methods are applicable for the low temperature reactions where the solubility in the solutions is high and the toxicity of the solvents is very low [1,6]. The wet chemical preparation method is utilized to produce samples in both film and powder forms. The general procedure for liquid- phase synthesis method is shown in Figure 2.1.

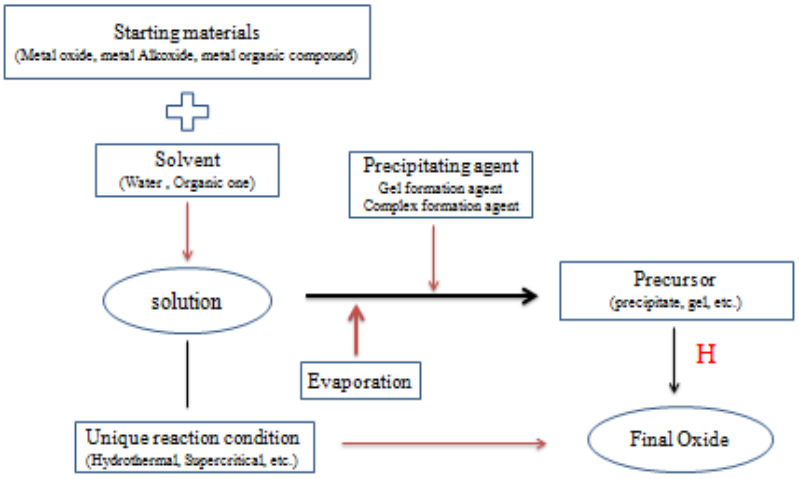

Figure 2.1 General procedure for liquid- phase synthesis method [7].

2.1.3 Gas Phase Reaction (GPR)

This reaction is generated by many physical techniques, such as laser ablation, molecular beam epitaxy, dc sputtering, magnetron sputtering and electron beam evaporation etc... It allows perovskite films with specific thickness and compositions to be obtained. In addition, it can be a good method for the preparation of metal catalysts; it can reduce the combined problems in perovskite synthesis in liquid solutions. However, the technique is comparatively expensive, because of the high

cost of the instruments which generate the atoms in the gas phase. Generally this is limited to the growth of thin films [1].

GPR techniques are divided to two categories based on the targeted materials. The first type uses separate targets where the different speed of deposition for each element has to be determined. For instances, thin films of $YBa_2Cu_3O_7$ can be made by co-evaporation of Y, Cu, and BaF_2, and subsequent annealing in a wet oxygen atmosphere [8]. The second category uses a performed perovskite material as target and its stoichiometry phase is transported to the substrate by sputtering or ablation techniques. Thin films of lead zirconate titanates can be deposited by radio frequency magnetron sputtering of a multi element metal target [9]. Gas phase depositions use a low substrate temperature followed by a post annealing at elevated temperatures, deposition at an intermediate temperature around (600- 800 $^{\circ}C$) followed by a post annealing treatment, and deposition at crystallization temperature at a controlled atmosphere [1].

2.1.4 Experimental Routes

To prepare the samples studied in this thesis the conventional solid state synthesis was utilized. This method is a relatively simple and low cost procedure and often produces samples with the appropriate physical properties. The details of the method and the different conditions of the sample preparation are described below. The perovskite type oxides are typically prepared from stoichiometric amounts of the required elements in their oxide or carbonate forms. The high-purity starting materials are ground using, a mortar and pestle, until a homogeneous mixture is obtained. The powders are heated in an alumina crucible within a commercial furnace usually between 800 and 1100 °C. After a certain period of heating, the products are quenched from high temperature in order to ensure homogeneity. The progress of each reaction is monitored with laboratory X-ray powder diffractometer (XRD) after each firing stage. Several intermediate regrinds are applied in the synthesis to ensure the homogeneity of the required material and the completeness of reaction. The repetition is halted when a single phase product is confirmed by XRD.

2.1.4.1 Synthesis of the Mixed Metal Oxides $Ln_{1-y}A_yRh_{1-2x}Cu_xB_xO_3$

Commercially available materials, La_2O_3, Bi_2O_3, PbO, $CaCO_3$, $SrCO_3$ and CuO (Aldrich ≥ 99.9%), Rh (Althaca 99.95%), Sc_2O_3 (Althaca 99.99%), ZnO

(Merck, ≥ 99%) and $Tb(NO_3)_3.5H_2O$ were utilized in the synthesis. Except for the $LaRh_{1-2x}Cu_{2x}O_3$ series which was prepared in an atmosphere of pure oxygen within a furnace (Tetlow tube furnace, Figure 2.2), all the rhodium copper perovskite oxides were synthesized in the air by standard solid state methods using muffle furnaces (Tetlow laboratory furnace). The raw materials, according to the targeted compositions listed in Table 2.1, were mixed with appropriate stoichiometric amounts, using a mortar and pestle, and then heated in several steps with intermittent regrinding. Samples were initially heated for 24 h at 850 °C followed by reheating at 950 °C for 24 h, and then 1000 °C for 48 h and 1050 °C for 48 h. The samples were finally annealed at 1100 °C for 48 h, at which time the X-ray diffraction pattern no longer change. Small increases in heating conditions, rather than prolonged heating at high temperatures, were used due to the high cost of the Rh. In some cases, the temperature was increased to 1250 °C to obtain higher quality samples such as $LaRhO_3$, whereas in others the higher temperature limited at 1050 °C such as $La_{0.75}Bi_{0.25}Rh_{1-x}Cu_xO_3$. As appropriate the final annealing conditions for the individual members of each series were identical. In general, in the chemical synthesis, standard conditions of temperature and pressure are required to minimize the derivations on the means of the oxides properties. The samples containing Pb and Bi were pressed into pellets to avoid the volatilization of elements during heating by enhancing intimate content of reactants and minimizing contact with crucible. All the prepared samples had black colour at the final heating stage. Intermediate changes to the colours also were observed at the range 850-1000 °C for Tb and La doped Zn oxides. These colours are golden and reddish brown for Tb oxides at 850 and 1000 °C. The colour of La doped Zn oxides developed in the range 850-1000 °C.

Figure 2.2 A photograph of a Tetlow Tube Furnace.

Table 2.1 Chemical formulas and mixtures for the prepared rhodate oxides.

Chemical Formula	Mixture	Temperature of Annealing
$LaRh_{1-x}Cu_xO_3$ ($x \leq 0.5$)	La_2O_3, Rh, CuO	1100 ºC , 1250 ºC (x = 0)
$LaRh_{1-2x}Cu_xZn_xO_3$ ($x \leq 0.25$)	La_2O_3, Rh, CuO, ZnO	1100 ºC
$LaRh_{1-2x}Cu_xSc_xO_3$ ($x \leq 0.25$)	La_2O_3, Rh, CuO, Sc_2O_3	1100 ºC
$La_{0.75}Ca_{0.25}Rh_{1-x}Cu_xO_3$ ($x = 0.3$)	La_2O_3, Rh, CuO, $CaCO_3$	1100 ºC
$La_{0.75}Sr_{0.25}Rh_{1-x}Cu_xO_3$ ($x = 0.3$)	La_2O_3, Rh, CuO, $SrCO_3$	1100 ºC
$La_{0.75}Pb_{0.25}Rh_{1-x}Cu_xO_3$ ($x = 0.3$)	La_2O_3, Rh, CuO, PbO	1100 ºC
$La_{0.75}Bi_{0.25}Rh_{1-x}Cu_xO_3$ ($x = 0.3$)	La_2O_3, Rh, CuO, Bi_2O_3	1050 ºC
$La_{1-x}Pb_xRh_{0.5}Cu_{0.5}O_3$ ($x \leq 0.3$)	La_2O_3, Rh, CuO, PbO	1100 ºC
$La_{1-x}Bi_xRh_{0.5}Cu_{0.5}O_3$ ($x \leq 0.3$)	La_2O_3, Rh, CuO, Bi_2O_3	1050 ºC, 1100 ºC (x = 0.3)
$TbRh_{1-2x}Cu_{2x}O_3$ ($x \leq 0.2$)	$Tb(NO_3)_3.5H_2O$, Rh, CuO	1100 ºC
$TbRh_{1-2x}Cu_xZn_xO_3$ ($x \leq 0.2$)	$Tb(NO_3)_3.5H_2O$, Rh, CuO, ZnO	1100 ºC
$TbRh_{1-2x}Cu_xSc_xO_3$ ($x \leq 0.2$)	$Tb(NO_3)_3.5H_2O$, Rh, CuO, Sc_2O_3	1100 ºC
$Tb_{0.75}Ca_{0.25}Rh_{1-x}Cu_xO_3$ ($x = 0.3$)	$Tb(NO_3)_3.5H_2O$,Rh,CuO,$CaCO_3$	1100 ºC
$Tb_{0.75}Sr_{0.25}Rh_{1-x}Cu_xO_3$ ($x = 0.3$)	$Tb(NO_3)_3.5H_2O$, Rh, CuO, $SrCO_3$	1100 ºC
$Tb_{0.75}Pb_{0.25}Rh_{1-x}Cu_xO_3$ ($x = 0.3$)	$Tb(NO_3)_3.5H_2O$,Rh,CuO, PbO	1100 ºC
$Tb_{0.75}Bi_{0.25}Rh_{1-x}Cu_xO_3$ ($x = 0.3$)	$Tb(NO_3)_3.5H_2O$, Rh, CuO, Bi_2O_3	1100 ºC
$Tb_{1-x}Pb_xRh_{0.6}Cu_{0.4}O_3$ ($x \leq 0.3$)	$Tb(NO_3)_3.5H_2O$, Rh, CuO, PbO	1100 ºC, 1250 ºC (x = 0.3)

2.1.4.2 Synthesis of the anion deficient perovskites $AA^*BB^*O_{5.5}$

Attempts were made to prepare compounds with a $AA^*BB^*O_{5.5}$ structure using two general methods. Only four oxides have been successfully obtained as single phases. These are $Sr_3NbO_{5.5}$, $BaSr_2NbO_{5.5}$, $Ba_2SrNbO_{5.5}$ $BaSr_2TaO_{5.5}$.The methods were both solid state reactions but used different slurry medium, namely acetone and ionized water. The purpose of the solvents is to enhance the homogeneity of the mixtures, and to create dry and wet media for the reaction. The preparation of samples involved different stoichiometric compositions of Nb_2O_5 or Ta_2O_5 (Aldrich, 99.99%) added to $SrCO_3$ or $BaCO_3$ (Aithaca, 99.98-99.99%). Initially, the mixtures were ground with the solvent and preheated at 850 $^{\circ}$C for 12 h, and then reground and heated at 1100 $^{\circ}$C for 48 h.

2.2 Characterization

In order to characterize the polycrystalline materials, techniques such as X-ray diffraction (XRD), synchrotron X-ray diffraction (SXRD), neutron diffraction (ND) and scanning electron microscopy (SEM) and thermo gravimetric analysis (TGA) are employed. The electrical and magnetic measurements were carried out using a Physical Properties Measurement System (PPMS). The following section gives a brief explanation about various characterization techniques and the Rietveld analysis of the diffraction data.

2.2.1 X-ray Powder Diffraction (XRD)

X-ray analysis is powerful non-destructive method for determining a range of physical and chemical characteristics of solid materials. The technique is widely utilized in many scientific, medical and industrial applications. In crystallography, X-ray powder diffraction is used to determine the type and quantities of phases present in the sample, the crystallographic unit cell and crystal structure, crystallographic texture, crystalline size, macro-stress and microstrain. X-ray diffraction results from the interaction between X-rays and the electrons of the targeted atoms. According to the atomic arrangement, interference between the scattered rays becomes constructive when the path difference between two diffracted rays differs by an integral number of wavelengths. This selective condition is described by the Bragg Equation 2.1; the wavelength of the incident beam has to be with same order of the magnitude of the lattice plane separations (see Figure 2.3). Solving Bragg's Equation gives the d-spacing between the crystal lattice planes of atoms that produce the constructive interference. The collection of reflections of the lattice planes is utilized to identify unknown structures. Crystals with high symmetry have relatively few atomic planes, whereas crystals with low symmetry tend to have a large number of possible atomic planes in their structures. X-rays have wavelengths of the order of 1 Å, the same as typical interatomic distances in crystalline solids. Therefore, the rays can interact with atoms and can yield information on the atomic arrangement [10,11,12].

$$n\lambda = 2d\sin\theta \qquad 2.1$$

n is order of reflection (integer value), λ is wave length of X-ray, d is inter planar distance, and θ is the angle between incident and reflected beam.

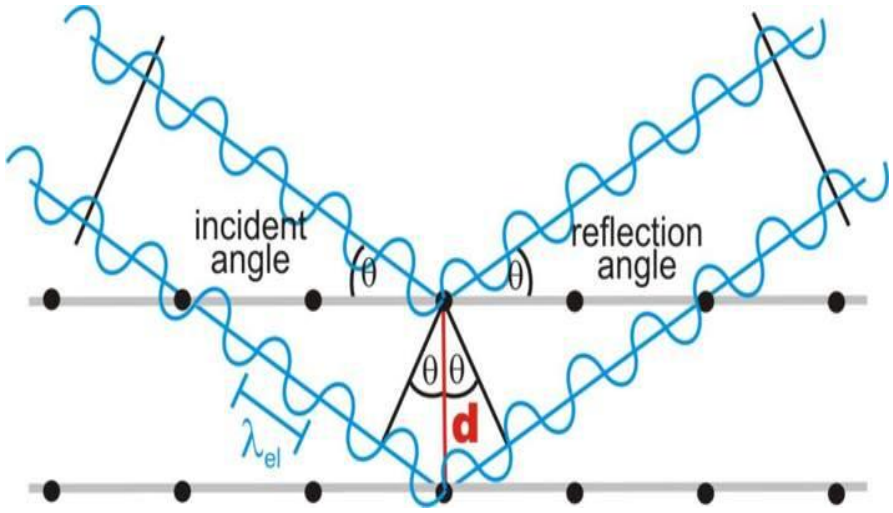

Figure 2.3 Bragg's Law reflection. The diffracted X-rays exhibit constructive interference when the distance between paths ABC and A'B'C' differs by an integer number of wavelengths (λ) [13] .

Table 2.2 Selected crystal structure, unit cell shape, formula and unit cell volume [14].

Crystal Structure	Unit Cell Shape	*d*- spacing ($1/d^2$)	Cell Volume
Monoclinic	$a \neq b \neq c$ $\alpha = \beta = 90^o \neq \gamma$	$1/\sin^2(\beta)\ [(h^2/a^2) + (\sin^2(\beta)\ k^2/b^2) + (l^2/c^2) - (2hl\cos(\beta)/ac)]$	$abc\ \sin(\beta)$
Cubic	$a = b = c$ $\alpha = \beta = \gamma = 90^o$	$(h^2+k^2+l^2)/a^2$	a^3
Tetragonal	$a = b \neq c$ $\alpha = \beta = \gamma$	$(h^2+k^2)/a^2 + (l^2/c^2)$	a^2c
Orthorhombic	$a \neq b \neq c$ $\alpha = \beta = \gamma$	$(h^2/a^2)+(k^2/b^2)+ (l^2/c^2)$	Abc
Hexagonal	$a = b \neq c$ $\alpha = \beta = 90^o, \gamma = 120^o$	$4/3(h^2+hk+k^2)/a^2+(l^2/c^2)$	$(\sqrt{3}a^2c)/2$

Crystalline materials are described by their unit cells which are the smallest units reflecting the structure. The unit cell is repeated in all directions, resulting in planes of atoms at certain intervals. The *d*-spacing of set of planes as the perpendicular distance between any pair of adjacent planes is correlated with unit cell parameters shown in Table 2.2. The essential features of X-ray diffractometer

are shown in Figure 2.4. X-ray from the tube is incident on a sample which is placed on a sample holder. The diffracted X-ray passes through a filter to the detector. The sample is positioned so that its diffracting planes make some particular angle θ with the incident beam and the detector is set at the corresponding angle 2θ. The detector records the intensity of the diffracted beams and these can be plotted out as a function of 2θ. Each crystalline substance has its own characteristic diffraction pattern which may be used for its identification [15].

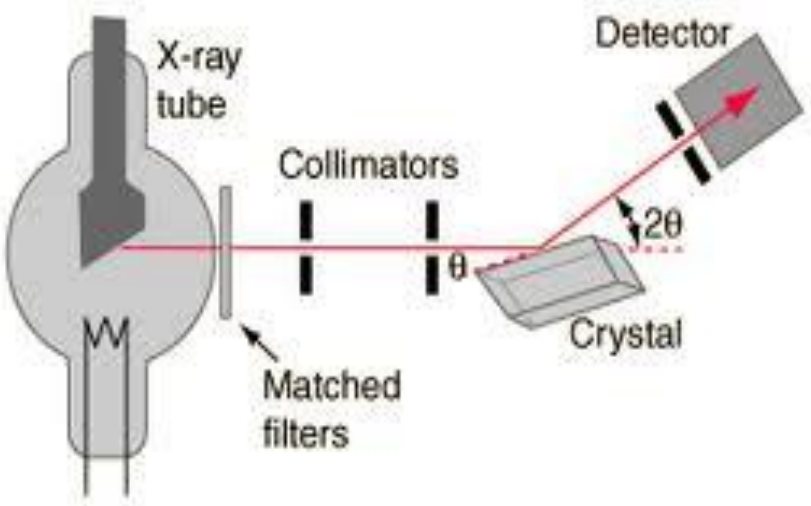

Figure 2.4 The essential features of X-ray diffractometer [16].

2.2.1.1 Preparation the samples for XRD measurements

The phase composition and purity of each sample was initially determined from X-ray diffraction. The XRD instrument used was a PANalytical's X'Pert Powder diffractometer located at the University of Sydney, Sydney, Australia equipped with a copper tube (Cu-K α_1 radiation), having a wavelength of 1.5406 Å. The operating voltage was 40 kV and the current was 20 mA. All samples were measured in flat plate mode at room temperature, and for some samples, variable temperature data (VT-XRD) were also recorded under evacuated atmosphere from 30 to 800 $^{\circ}$C. A scan range of $10° < 2\theta < 100°$ and a scan length of 10 minutes were used. Diffraction patterns obtained from the ICSD (Inorganic Crystal Structure Database) were used for the comparison with obtained products, and as the starting models for the refinements.

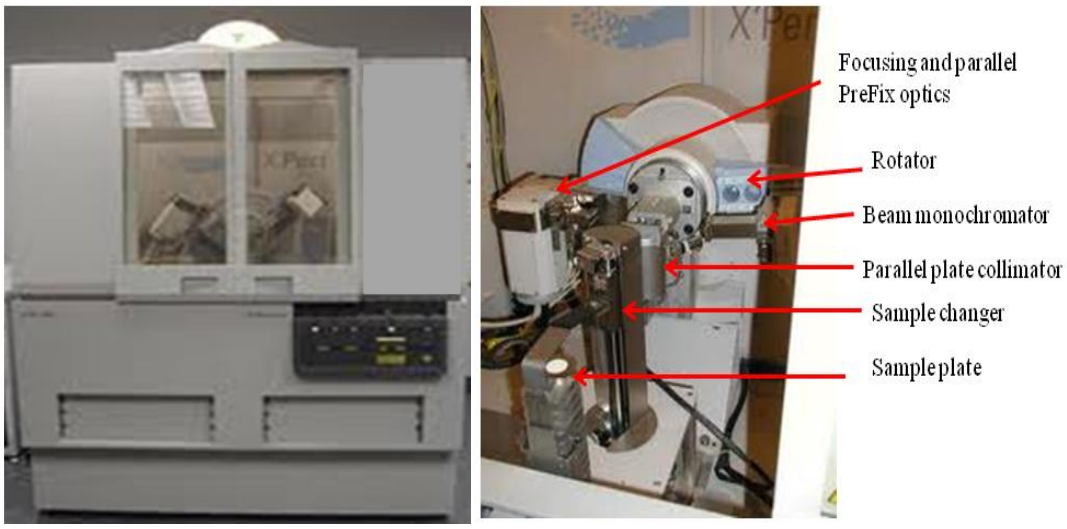

Figure 2.5 A photograph of PANalytical's X'Pert powder X-ray diffractometer.

2.2.2 Synchrotron X-ray Diffraction (S-XRD)

A synchrotron radiation source produces high coherence electromagnetic waves with high brilliance of the beam. It generates very intense X-rays compare to those obtained from a conventional X-ray source. The main constituents of a synchrotron radiation source are illustrated in Figure 2.6. The electrons are accelerated from a linear accelerator and then by a booster ring. When the electrons reach certain energy and velocity (approaching the speed of light), the electron beam will be injected into the storage ring which is operated under ultrahigh vacuum conditions. Then will be confined in a circular orbit, with a large radius by a succession of magnets without gaining any further energy. The beam is deflected from a straight path by some degrees when passing through a magnet. Through bending magnets, consequently synchrotron radiation will be emitted tangentially to the electron orbit. The emitted radiation has not only extremely high brilliance but also a very broad spectral range with high intensity which easily allows a desired wavelength to be selected for different experiment requirements. In addition, insertion devices such as undulators, wigglers and focusing magnets, which consist of periodically arranged magnets, can be employed at the straight sections of the ring to improve the intensity and brilliance of the radiation [15].

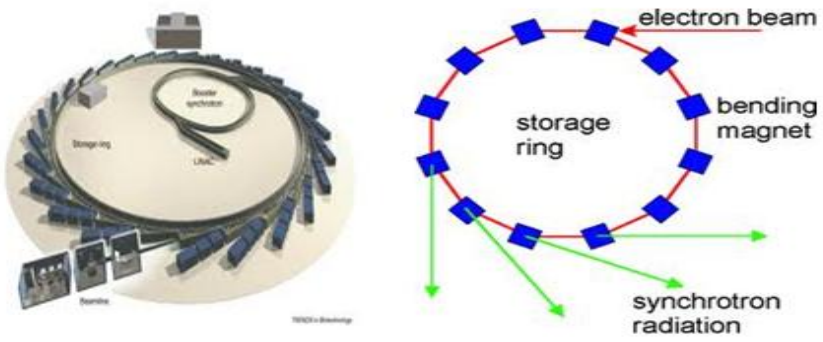

Figure 2.6 A construction of synchrotron radiation source.

2.2.2.1 Australian Synchrotron Radiation Facility

The Australian Synchrotron is a third generation facility producing light ranging from infrared to hard X-rays. The high resolution powder diffraction beamline (10-BM-1) is located on a bending magnet source and has been designed to operate over the energy range 5-30 keV (0.41-2.4 Å). The beam line consists of three hutches and a user cabin (Figure 2.7). The first hutch contains the optics, including mirrors and double crystal monochromators (DCM). The centre hutch houses the primary end station where the powder diffraction experiments are undertaken. Finally, the third hutch contains a large optical table which allows a variety of alternative configurations, primarily centred on engineering applications [17].

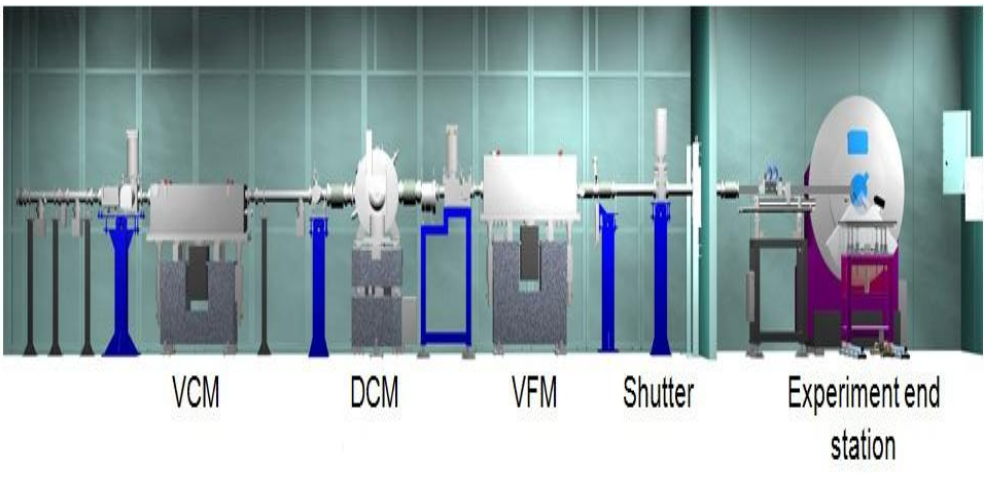

Figure 2.7 Schematic layout of the 10-BM-1 Powder Diffraction beamline [17]. VCM and VFM are vertically collimating and focusing mirrors.

The beam is monochromated by double-crystal Si (111) monochromators. In this work, diffractions data were collected for samples housed in narrow diameter capillaries that were rotated continuously during the measurements. The detector consists of an array of 16 MYTHEN microstrip detectors. The detector channels are offset approximately 2° from each other thus the movement of the detector arm needs no more than about 2-3° to measure an angular range of 80° in 2θ. The primary end station has been designed such that it is capable of accommodating a wide variety of experiments, particularly those utilising non-standard sample stages and cells. The range of studies carried out at the station include: structural and physical property studies of solid metal oxides, examination of minerals and minerals processing products, particularly under non-ambient conditions, phase identification and quantification of pharmaceuticals, *ab* initio structure solution and variable temperature studies [17].

2.2.2.2 Preparation the samples for S-XRD measurements

The synchrotron diffraction data presented in this thesis was collected at the Australian Synchrotron high resolution powder diffraction beamline (10-BM-1), using a spinning glass capillary of 0.3 mm diameter with a wavelength of 0.82554 Å. The data were recorded at room temperature over an angular range of $5^{\circ} < 2\theta < 85^{\circ}$. The wavelength was calibrated using LaB_6, as a standard.

2.2.3 Neutron Diffraction (ND)

Neutron diffraction can also be used to study the structure of crystalline materials. The weak interactions of neutrons with atom nuclei provide a highly penetrating and non-destructive probe, which enable experimental configurations with complex sample environments such as cryostats, furnaces and pressure cells to be used. According to the de Broglie Equation ($\lambda = h/p$) where h is Planck's constant, the wavelength of neutrons (λ) is dependent on the momentum of a free particle (p). Therefore, thermal neutrons which have an approximate velocity of 2.2 km/s can be a useful crystallographic probe since its wavelength is comparable to interatomic distances [18,19].

Unlike X-rays, neutrons interact with the nuclei rather than electrons, and the scattering power of the nuclei is approximately constant for all elements [20]. The scattering power, which is represented by neutron scattering length (b_i) is generally

independent of scattering angle and as consequence, strong reflections can be observed at both long and short *d*-spacings. Furthermore, neutron scattering lengths (b_i) vary as an irregular function of atomic number (see Figure 2.8). Consequently, the neutron diffraction technique can distinguish not only neighbouring atoms in the periodic table from each other, but can also detect light atoms in the presence of heavier atoms. The ability to scatter both light and heavy atoms in solid materials plays an important role, for instance, in the completion of metal oxide structure determinations [21].

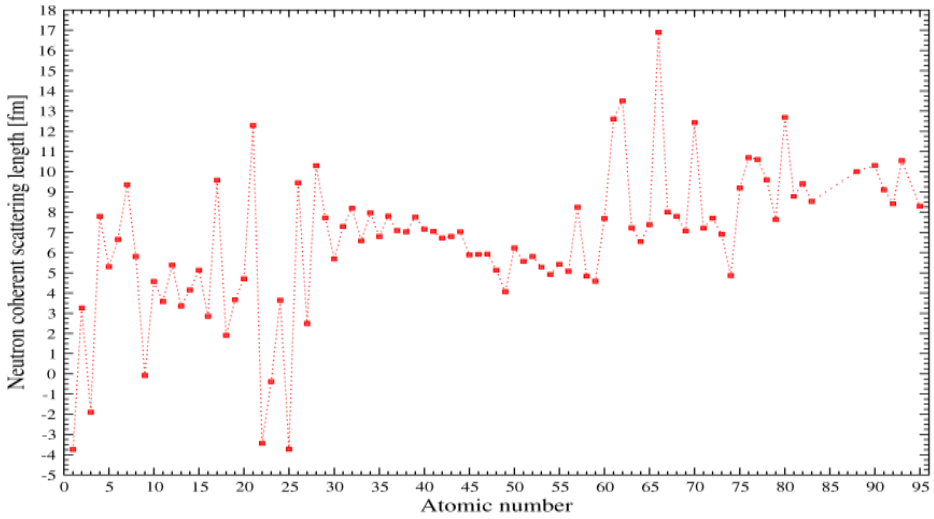

Figure 2.8 The irregular function of neutron scattering length against atomic number [21].

The neutron has a spin quantum number (1/2), and the possession of a magnetic moment and this allows the neutron to interact with unpaired electron spin. Consequently, neutron diffraction can also be a powerful tool to determine magnetic structures of materials. The magnetic scattering power of neutron diffraction, which can be termed as a form factor (f_m), is similar to the X-ray scattering factor. The total intensity scattered by unpolarised neutrons which contain all directions of spins will be the sum of both nuclear and magnetic scattering, as shown in Equation 2.2 where $F_{hkl}^{nuc^2}$ and $F_{hkl}^{mag^2}$ are factors of nuclear and magnetic structures respectively.

$$F_{hkl}^{Tot^2} = F_{hkl}^{nuc^2} + F_{hkl}^{mag^2} \qquad 2.2$$

The structure factor $F_{hkl}^{mag^2}$ is defined in Equation 2.3 where q is the magnetic interaction vector which depends on magnetic moment and scattering vector of atom i, and p is the magnetic scattering length which is calculated from the magnitude of the magnetic moment and the magnetic form factor f_m.

$$F_{hkl}^{mag^2} = \sum_{i=1}^{n} q_i \, p_i e^{2\pi i \, (hx_i + ky_i + lz_i)} \qquad 2.3$$

When a compound possesses magnetic moments which are orientated in all directions, the incident neutron is scattered incoherently, and the background intensity consequently increases. The magnetic Bragg reflections can only be detected if magnetic ordering appears in the structure. For ferromagnetic materials, the magnetic ordering and the nuclear cell have the same periodicity; hence the reflections of nuclear and magnetic structure are superimposed. For antiferromagnetic materials, extra reflections from magnetic ordering will also be observed. That is due to the supercell of the magnetic structure, which has a periodicity greater than that of the nuclear cell in one or more directions [18,19].

Comparing to XRD techniques, ND examinations require relatively large amounts of sample due to the weak interaction and the low intensity generated by neutron sources. Sufficient neutron flux can be conventionally generated from a nuclear reactor where fast neutrons are produced continuously by nuclear fission. In order to maintain the process of nuclear fission and also to have a suitable range of wavelengths to study atomic structure, a moderator which normally contains a large amount of low mass nuclei is used to slow down the produced fast neutrons. The moderated thermal neutrons have a wide range of energy such as white spectrum; hence a monochromator is required to select neutrons with a desired constant wavelength for the experiments [10].

2.2.3.1 Echidna, the high resolution powder diffractometer at Australian Neutron Source OPAL

Echidna (Figure 2.9) is one of the world's best reactor based high resolution powder diffractometers, located on neutron-guide hall, thermal guide TG-1 at the Australian Neutron Source OPAL, near Sydney. The diffractometer is designed to achieve high resolution using a single wavelength. The optimum neutron flux on the sample is enabled by both vertical and horizontal focussing of the monochromator

and the monochromator has a variable take-off angle between 90° and 140°. The neutron flux at the sample position is up to 10^7 $ncm^{-2}s^{-1}$. A range of neutron wavelengths from 1 to 3 Å is available by using different (*h k l*) orientations of a Ge crystal monochromator. The detector array consists of high resolution collimators and 128 sensitive detectors that are 300 mm in height. The typical scans take around 2-3 hours. A choice of cryostat, cryofurnace or vacuum furnace allows sample temperature to be as low as 1.8 K or as high as 2073 K [22].

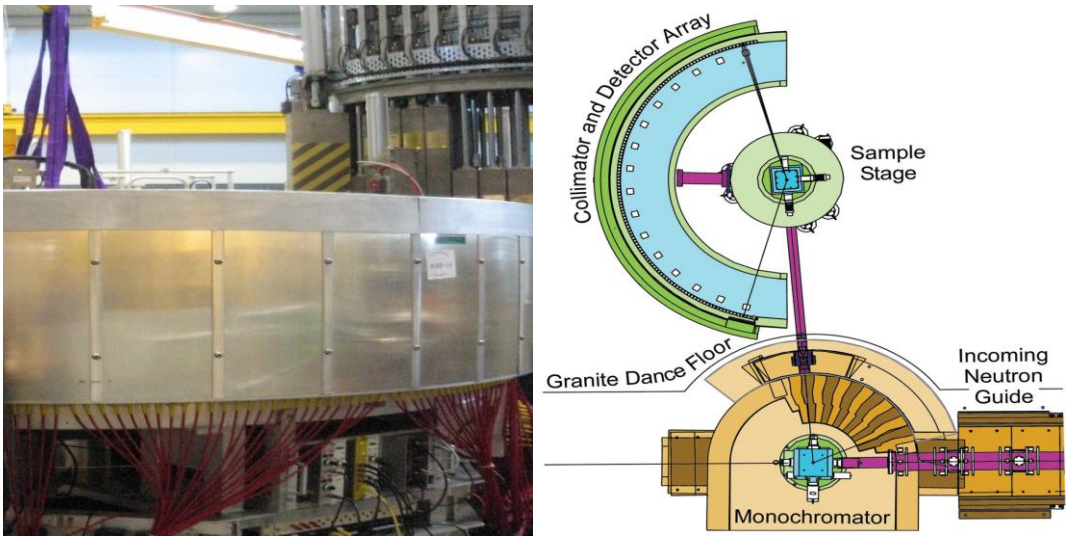

Figure 2.9 A photograph and layout of the Echidna diffractometer [22].

2.2.3.2 Preparation the samples for ND measurements

In this work, neutron powder diffraction data for some samples were measured using the high resolution powder diffractometer, Echidna [23], at the OPAL facility (Australian Nuclear Science and Technology Organization) at a wavelength of 2.4395 Å. For these measurements the sample was contained in a 8 mm cylindrical vanadium can. The scanning angular range was $10° < 2\theta < 160°$.

2.2.4 X-ray Absorption near Edge Structure (XANES) Spectroscopy

X-ray absorption near edge structure (XANES) spectroscopy is a non-destructive analytical technique which reveals information about the local structure, chemical composition, and physical properties of materials [20]. The technique is based on observing the scattered intensity of an X-ray beam hitting a sample as a function of the energy. XANES data are typically observed as absorption peaks

when protons are absorbed within a specific energy region [24]. As seen in Figure 2.10, the fundamental phenomenon of the XANES technique is derived from the absorption of an X-ray photon by a core level of an atom in a solid and the consequent emission of a photoelectron (step 1). The resulting core hole is filled either via an Auger process or by capture of an electron from another shell followed by emission of a fluorescent photon (step 2).

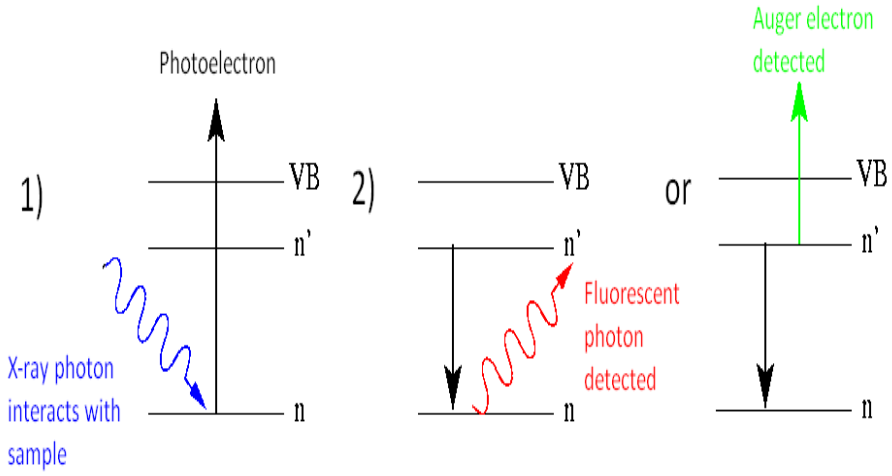

Figure 2.10 The fundamental processes which contribute to XANES spectra [25].

Unlike the photoemission technique where the final state of the emitted electron captured in the detector must be extended, the final state of the photoelectron in XANES may be a bound state since the photoelectron need not be detected. When the X-ray photon energy resonantly connects a core level with a narrow final state in a solid, readily identifiable characteristic peaks will appear in the spectrum. The absorption peaks of XANES spectra are determined by multiple scattering resonances of the photoelectron excited at the atomic absorption site and scattered by neighbouring atoms. The local character of the final states is determined by the short photoelectron mean free path which is strongly reduced to about 0.3 nm at 50 eV. The typical energy range allows inelastic scattering of the photoelectron by electron-hole excitations and collective electronic oscillations of the valence electrons called plasmons [25,26].

In the XANES region, starting energy is about 5 eV beyond the absorption threshold. The photoelectron backscattering amplitude by neighbor atoms is very

large so that multiple scattering events become dominant in the XANES spectra. Synchrotron radiation has a natural polarization that can be utilized to great advantage in XANES studies. The commonly studied molecular adsorbates have sigma and pi bonds that may have a particular orientation on a surface. The angle dependence of the X-ray absorption tracks the orientation of resonant bonds due to dipole selection rules [25,27].

2.2.4.1 Preparation the samples for XANES measurements

Rh $L_{3,2}$-edge X-ray absorption spectra were recorded for $LaRh_{1-x}Cu_xO_3$ and $La_{1-x}Pb_xRh_{0.5}Cu_{0.5}O_3$, from powder samples dispersed on Kapton tape, in fluorescence mode on beam line BL-16A1 at the National Synchrotron Radiation Research Centre (NSRRC) in Hsinchu, Taiwan using a Lytle detector [28]. Energy steps as small as 0.2 eV were employed near the absorption edges with a counting time of 2 s per step. The spectra were normalized to the incident photon current. The energy scale of the Rh $L_{3,2}$- edge spectra was calibrated using the L_2-edge of a Mo foil. $LaRhO_3$ and Sr_2RhO_4 were used as the Rh^{3+} and Rh^{4+} standards respectively.

2.2.5 Scanning Electron Microscope (SEM)

The scanning electron microscope used in this work was a Intellection Quemscan located on the Electronic Microscope Unit (EMU) at the University of Sydney (Figure 2.11). The SEM technique consists of an energetically focused beam of electrons. This highly focused beam is obtained using a series of magnetic lenses. The beam hits the sample releasing secondary electrons that are then counted by a detector and amplified to obtain a reasonable signal. A set of scanning coils moves the beam across the specimen in order to obtain an image of the area under study. The image can be gathered at various magnifications generally from 1 to 20000 times. Low-count energy-dispersive X-ray spectra (EDX) are also generated and provide information on the elemental composition at each measurement point. The instrument has four EDS detectors and can analyse up to 200 points per second. The focused beam of electrons excited the atoms, which release characteristic X-rays. The total intensity gives the relative concentration of each element in the zone under study.

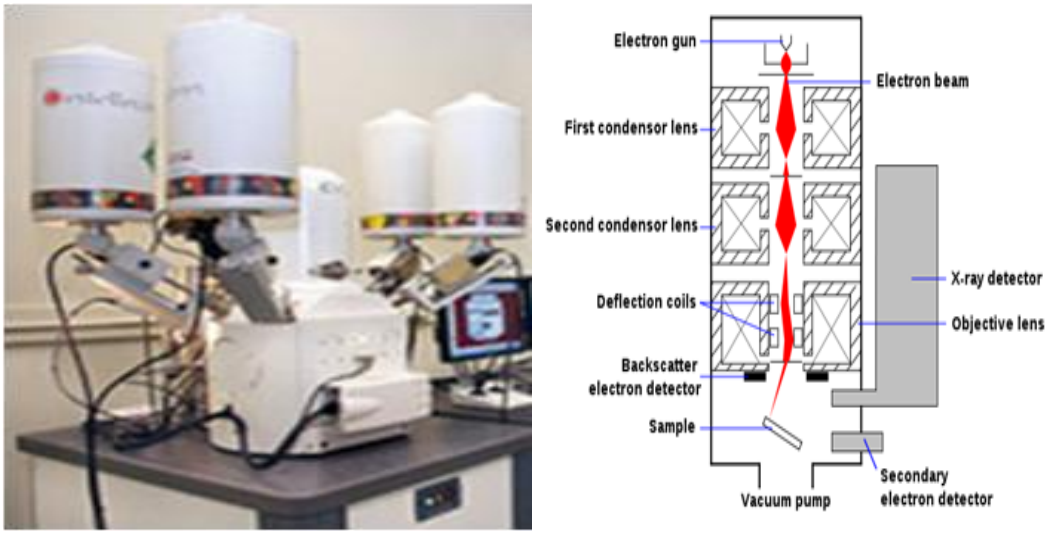

Figure 2.11 A photograph and Schematic diagram for a Quemscan SEM.

2.2.5.1 Preparation the samples for SEM measurements

Powder samples were dispersed on double sided Kapton tape attached to aluminium samples plates. The samples were then coated by carbon to roughly 2 mm thickness. The samples were placed in the chamber which was purged, sealed and evacuated. The microstructure and EDX analysis was carried out using a Intellection Quemscan with electron high tension (EHT= 20.0 KV), filament current (Fil I = 2.394), gun vacuum (5.66 e^{-7} mbar) and system vacuum (3.46 e^{-6} mbar). Phoenix software was used for the element analysis.

2.2.6 Resistivity Measurements

The electrical resistivity of a material varies over many orders of magnitude and depends upon many factors, including chemical composition and structure [29]. The electrical resistance is defined as the opposition to the flow of electrical current through the material. It scales with the dimensions of the sample (length and cross sectional area). Thus, a more meaningful property of a material is the resistivity. Resistivity is an intrinsic quantity independent on the sample size [29]. The resistance and resistivity (ρ) are related by:

$$R = \rho . (L/A) \qquad 2.4$$

Where, A is the cross sectional area of the material and L is the length.

The electrical conductivity (σ) is defined as the reciprocal of the electrical resistivity and is given SI units ($S.m^{-1}$). The property is strongly correlated with the

atomic number and electron configuration of the elements. Materials, based on the magnitude of electrical conductivity, are classified as metallic, semiconductor and insulator [10,29]. Electrons in an atom cannot have an arbitrary energy value, but rather have fixed energy levels. These energy levels split to two bands (valence and conduction), determining the conducting type. In insulators and semiconductors, a forbidden gap between the energy levels which the electrons cannot occupy also exists. Thus, in order for a current to flow, a relatively large amount of energy must be applied to enable an electron to leap across the gap into the conduction band [10,29]. In metals, the resistance is too small due to either the overlap (Figure 2.12) between the valance and conduction bands, or the occupation of nonbonding electrons in a band with states just above the excitation level [10,29].

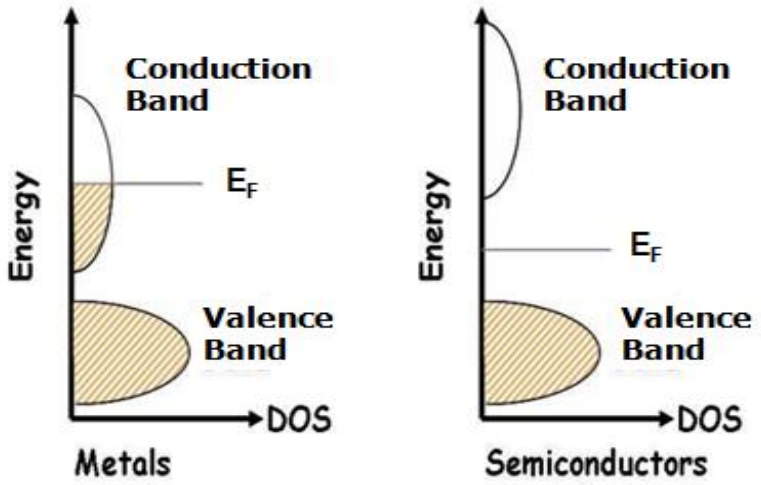

Figure 2.12 A scheme of electronic band structures in metals and semiconductors materials. Where E_F is a forbidden band energy (less than 2.0 eV for semiconductors), and DOS is density of states. The band gap of insulators is much greater than in semiconductors [29].

Experimentally, the thermal behaviour of the conducting type materials is understood by Arrhenius's law. Metals conduct down to the lowest attainable temperature, and become less conducting upon increasing temperature. That is as consequence of lattice vibrations which cause barriers for the movement of carriers. Insulators and semiconductors become more conducting upon increasing temperatures

(Figure 2.13) due to thermal excitations of electrons into the empty conduction band [10,29]. The temperature effect on the conductivity is much more significant in semiconductors than in insulators. Insulators tend to be ionic or strongly covalent, and thus the valence electrons are tightly bound to the atom (high electron localization) where semiconductors are predominately covalent and have valence electrons that are weakly bound to the atoms, thus they are free to move upon some thermal excitation [10,29].

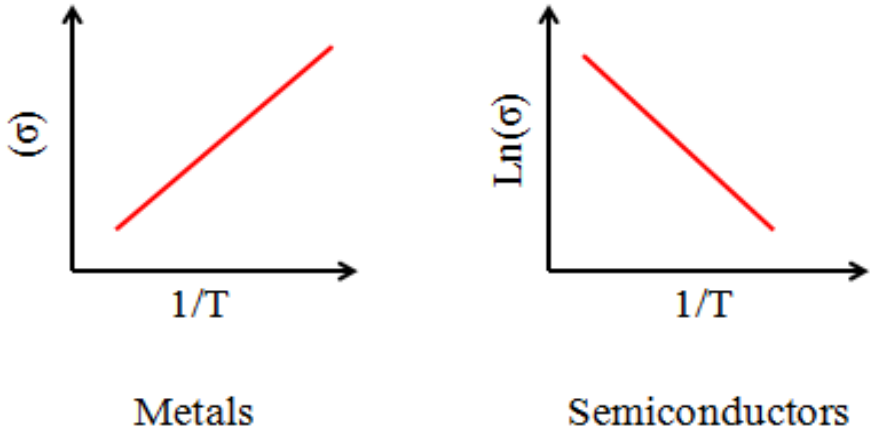

Figure 2.13 The temperature dependence of the electrical conductivity for metals and semiconductor.

2.2.6.1 Physical Properties Measurement System (PPMS)

The electrical and magnetic measurements were performed using a Physical Properties Measurement System (PPMS) manufactured by Quantum Design. The PPMS is liquid helium cooled, temperature and variable system capable of doing a number of electrical, thermal and magnetic measurements [30]. The system can generate magnetic fields between 7 Tesla and temperatures between 1.9 and 400 K. The PPMS is composed of a standard dewar with a liquid helium bath in which a probe is immersed [30]. The probe (Figure 2.14) is capable of temperature control and is composed of a superconducting magnet, a sample puck connector and electrical connections. A vacuum pump continuously pumps the sample chamber [30].

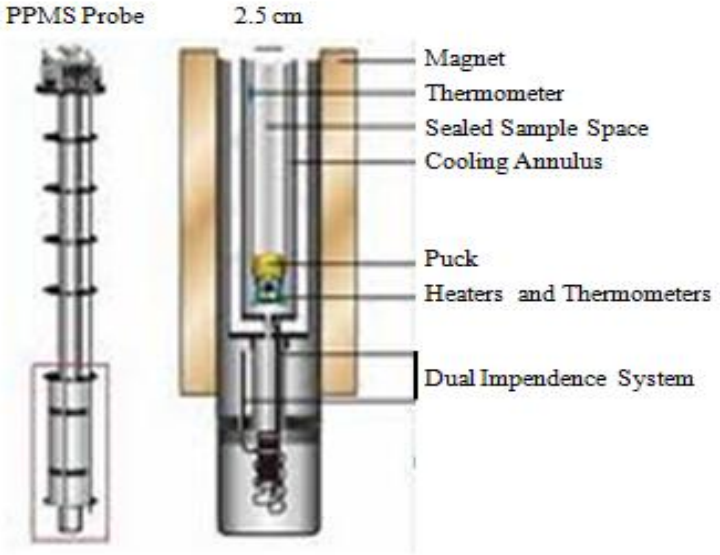

Figure 2.14 Layout of the PPMS Probe [30].

2.2.6.2 Preparation the samples for Resistivity Measurement

Sintered samples with 0.5-1 mm thickness were cut into rectangular pieces approximately 3 × 4 mm for four wire direct current (DC) resistivity measurements. Each sample was glued onto a Kapton tape attached to the sample puck. The puck (Figure 2.15) is a copper, gold-plated disk with a 2.3 cm diameter designed to measure four probe resistivity on 3 samples independently. Four contacts were painted onto the sample and attached to the sample puck using silver paste and copper wires. The puck was set on 12-pin connector at the base of the chamber near the thermometer and heater. Current was fed through two electrical leads placed at the very ends of the sample and the two inner leads measured the potential drop across the sample. The input impedance of the voltmeter allowed for a high degree of accuracy. Proper electrical connections were verified using a digital voltmeter before the sample was installed into the chamber. Once the puck was installed, the sample chamber was purged and sealed and resistivity measurements were taken at zero field over the temperature range 5- 300 K. The current, power and voltage limits were set at 999.0 μ A, 1000 μ W and 95 mV respectively. Using the geometry of the samples, the data were processed to obtain resistivity values as discussed in the results.

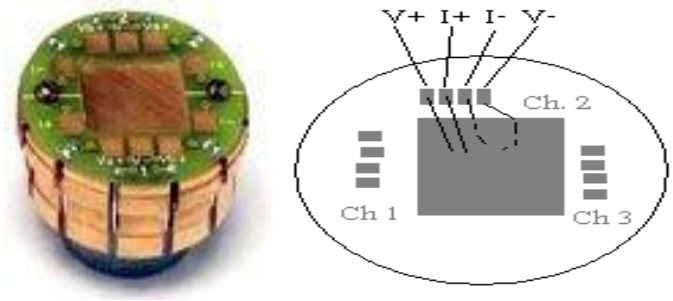

Figure 2.15 The front view of DC resistivity puck, and the four probe technique connection.

2.2.7 Magnetic measurements

Magnetism as a macroscopic phenomenon is attributed to nearest neighbour interactions on the atomic scale [31]. A simple two particle interaction is the key ingredient to account for large scale, observed magnetic states. When the magnetic field *H* is applied to a substance, a linear magnetisation response *M* is induced [31], and the magnetic susceptibility can be defined as:

$$\chi = M/H \qquad 2.5$$

The magnetic susceptibility χ represents the response of a material to an applied magnetic field at certain temperature. The paramagnetic materials, in which there is no interaction between moments, follow the Curie law Equation 2.6. Where *C* is the Curie constant, *T* is temperature in K, N_A is Avogadro's number, K_B is Boltzmann constant, μ_{eff} is the effective magnetic moment and g_J is the Landé g-factor, $J = (S + L)$ is the total angular momentum quantum number, S and L are spin and orbital angular momentum respectively; μ_B is the Bohr magneton.

$$M = \left(\frac{C}{T}\right).\ H = \chi.\ H \qquad 2.6$$

$$C = \left(\frac{N_A\,\mu_B}{3K_B}\right)\mu_{eff}{}^2 \qquad 2.7$$

$$\mu_{eff} \approx g_J\sqrt{J(J+1)}\,\mu_B, \quad g_J = \frac{3}{2} + \frac{S(S+1)-L(L+1)}{2J(J+1)} \qquad 2.8$$

Curie's law is derived from a thermodynamical approach to the Hamiltonian of a collection of ions with no interactions [31]. At low temperatures, entropy cannot

disrupt the spins and consequently spins will be aligned to the applied magnetic field, lowering the energy of the system. As the temperature increases, entropy dominates and the spins will rotate causing disorder [31]. When the spontaneous interaction between neighbouring unpaired electrons exists, the magnetic properties of the material become more complex and the Curie law will be no longer valid. Curie's law explains the magnetism of transition metal ions and rare earth ions in the presence of a magnetic field. These elements tend to have valence electrons in the *d* and *f* orbital, and the paramagnetic behaviour is associated with the presence of those electrons [31]. The quantum state of an atom can be characterized by the total spin S, total orbital angular momentum L and total angular momentum J. These values can be calculated using Hund's rules. The contribution of orbital angular momentum is often ignored since there is normally quenched by crystal field effects for the first row transition metals [31].

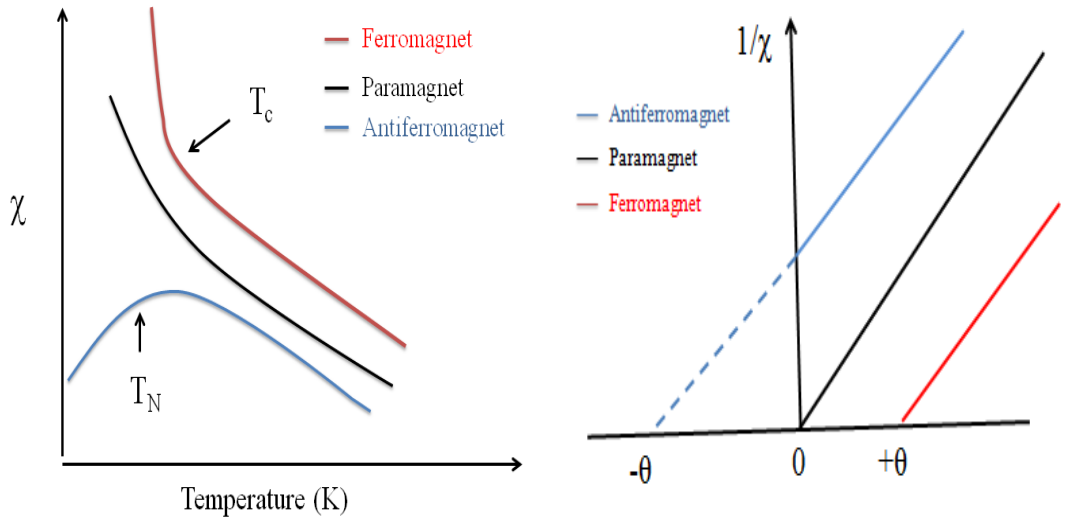

Figure 2.16 The temperature dependence of magnetic susceptibility and inverse susceptibility curves for paramagnetic, ferro and antiferromagnetic materials.

Magnetic materials are classified to paramagnetic, ferromagnetic, and antiferromagnetic [32]. Figure 2.16 demonstrates the temperature dependence of magnetic susceptibility and inverse susceptibility curves for paramagnetic, ferro and antiferromagnetic materials. The materials with positive magnetic susceptibilities and only exhibit magnetism in the presence of an applied magnetic field are

paramagnetic. The ferromagnetic materials show a sharp increase in the susceptibility below a transition temperature, called the Curie temperature, T_C. Conversely, antiferromagnets exhibit a decrease in susceptibility below a transition temperature, known as the Néel temperature, T_N. Above the transition temperature, the paramagnetic behaviour of ferro and antiferromagnetic materials can be described with the Curie-Weiss law where θ is the Weiss constant. The Weiss constant is generally positive for ferromagnets and negative for antiferromagnets [32]. For ferromagnetic materials, a characteristic hysteresis loop can also be observed (Figure 2.17). The ferromagnetic material is magnetised in one direction with an increasing field. Thus, the saturated magnetisation (*Ms*) can be found when the magnetisation reaches a maximum [33]. The magnetisation will not relax to zero when the field is removed and the application of an opposite direction field is necessary to relax the magnetisation. If a cyclic magnetic field is applied, the magnetisation of the material will trace out a loop. The hysteresis loop results from the existence of magnetic domains in the material. With the application of the opposite field, a remnant magnetisation (*Mr*) occurs showing the remaining magnetisation at zero fields, while the coercive field (*Hc*) is the opposite field applied when the magnetisation is relaxed to zero. A large hysteresis area is the property of a hard magnetic material, while a small area indicates a soft magnetic material [32].

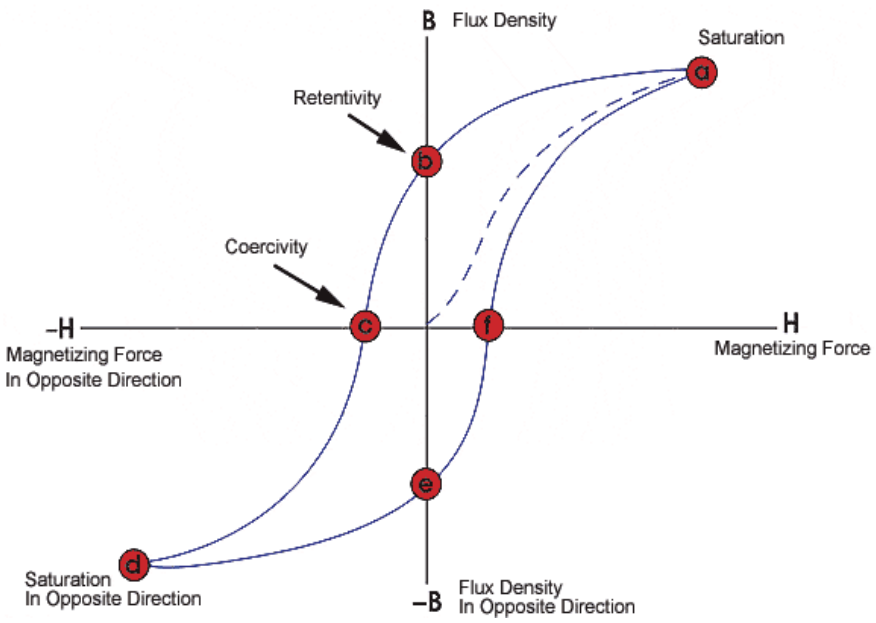

Figure 2.17 A typical hysteresis loop of a ferromagnetic material [33].

2.2.7.1 Vibrating Sample Magnetometer option (VSM- PPMS)

The Quantum Design Vibrating Sample Magnetometer (VSM) option for the Physical Property Measurement System (PPMS) is a fast and sensitive DC magnetometer [30]. The basic measurement is accomplished by oscillating the sample near a detection (pickup) coil and synchronously detecting the voltage induced. By using a compact gradiometer pickup coil configuration, relatively large oscillation amplitude (1.3 mm peak) and a frequency of 40 Hz, the system is able to resolve magnetization changes of less than 10-6 emu at a data rate of 1 Hz [30]. The VSM option for the PPMS consists primarily of a VSM linear motor transport head for vibrating the sample, a coil-set puck for detection, electronics for driving the linear motor transport and detecting the response from the pickup coils, and a copy of the Multi-Vu software application for automation and control [30].

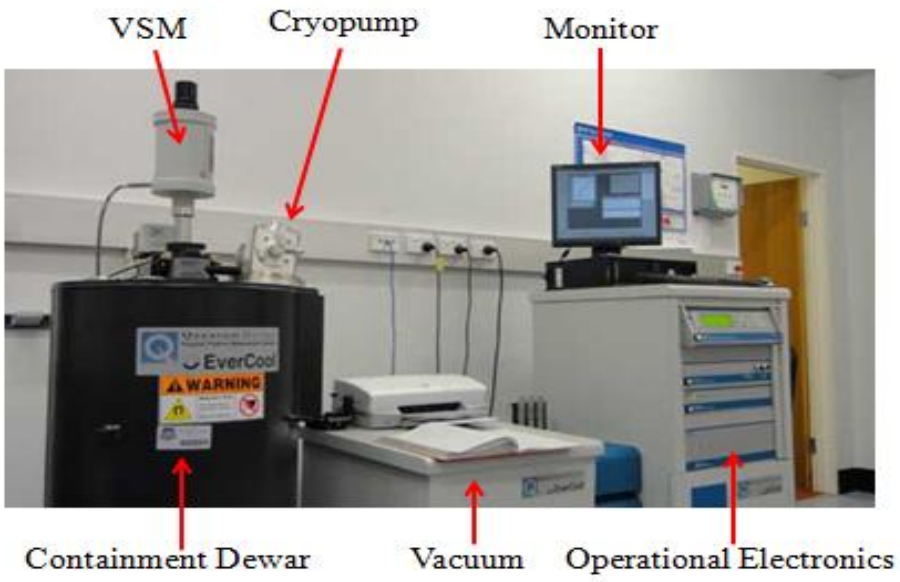

Figure 2.18 Quantum Design Physical Properties Measurement System set up for VSM.

2.2.7.2 Preparation the samples for magnetic measurements

The magnetic measurements were also performed using the PPMS employing the vibrating sample magnetometer feature (VSM). The studied powder samples with approximate mass 30-40 mg were placed in a clean dry sample capsule container which was mounted in a special sample holder. The sample holder was rigged onto a centering unit, ‘‘sample mounting station’’ to place the sample at the

correct position in relation to the detection coil inside of the magnetometer. The sample in the holder was attached to the end of a sinusoidally driven sample rod. The centre of oscillation is positioned at vertical centre of gradiometer pick up. The signal from the interaction of the sample with the pickup coil was used to determine whether the sample was the correct position for reliable measurements to be taken. Once the chamber was purged and sealed, certain magnetic fields 5 kOe were applied to study temperature-dependent behaviour at a temperature range of 5-300 K, and variations in the applied magnetic field of ±10, 50 and 90 kOe were adopted for the hysteresis studies. Scaling the magnetic moment by the sample mass and molar mass, and then the magnetization was divided by the applied field to obtain the molar magnetic susceptibility (Equation 2.9). Magnetism is due to the magnetic moments of electrons given in units of Bohr Magnetons (μ_{eff}):

$$\chi_m = (M \times M_m)/(H \times m) \qquad 2.9$$

Where (χ_m) is the molar magnetic susceptibility (emu.mole^{-}), M_m is molar mass (g. mole^{-}) and *m* is the mass of the sample (g).

2.2.8 Thermogravimetric Analysis (TGA)

Thermogravimetric analysis (TGA) is an analytical tool that measures weight changes in a material treated thermally [34,35]. It is commonly employed to examine characteristics of materials, to determine degradation temperatures, absorbed moisture content, level of inorganic and organic components, purity, and decomposition points for different materials [34,35]. The analysis is carried out by raising the temperature of the sample gradually and plotting weight (percentage) against temperature. A derivative weight loss curve can identify the point where weight loss is most apparent.

TGA analyser usually consists of a high-precision balance with a platinum pan loaded with the sample. That pan resides in a furnace and is heated or cooled during the experiment. The sample is placed in a small electrically heated oven with a thermocouple to accurately measure the temperature [34,35]. The atmosphere may be purged with an inert gas such nitrogen to prevent oxidation or other undesired reactions.

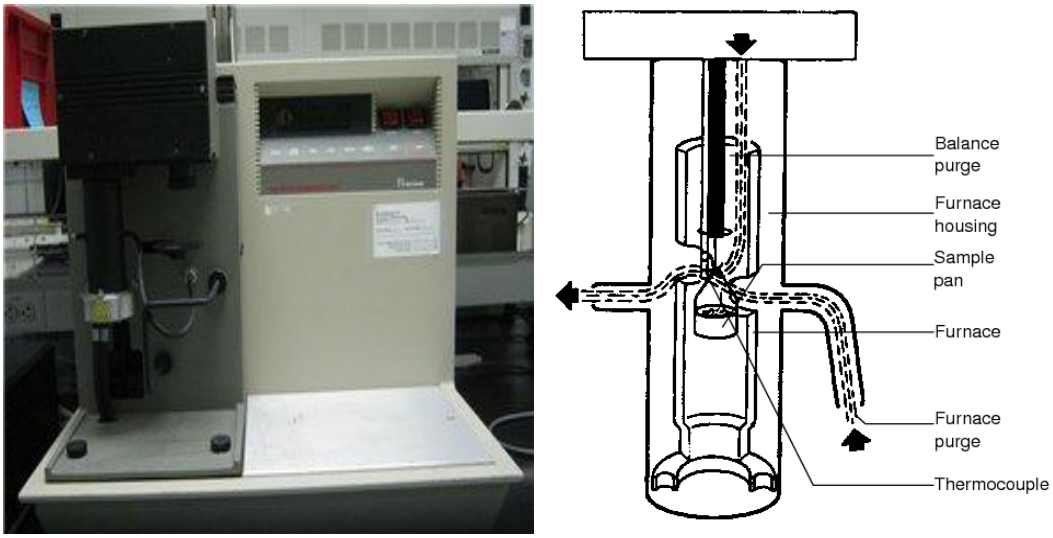

Figure 2.19 A photograph and layout of TGA 2950 furnace.

2.2.8.1 Preparation the samples for TGA analysis

The instrument used in this work was a TGA 2950 Thermal Analyser. Generally, a small mass of powder samples (~ 10-50 mg) was placed on a pre-dried platinum pan which is attached to a high precision balance. The sample's mass is constantly weighed as the sample is heated at a standard rate in a pure nitrogen atmosphere in order to examine weight loss under inert condition. Samples for antimonite, niobate and tantalate oxides were analysed up to a maximum temperature of 800 $^{\circ}$C using a heating rate of 10 $^{\circ}$C per minute. The calculations of weight lost were performed using the Universal Analysis 2000 (Version 4.2E) programme.

2.2.3 Data Analysis

The major software and programmes used in this work are RIETICA for structure refinements and IFEFFIT Athena programme for XANES spectra normalization.

2.3.1 The Rietveld Analysis

The Rietveld method is utilized to refine crystal and magnetic structures from obtained X-ray or neutron powder diffraction patterns [36]. It refines various metrics including lattice parameters, peak width and shape, and preferred orientation to derive a calculated diffraction pattern. In most powder diffraction patterns, overlap between Bragg reflections occurs particularly for lower-symmetry materials due to the polycrystalline nature. As an alternative for analysing each individual reflection

or resolving the reflection overlap, the Rietveld analysis performs a curve fitting method by considering the observed intensity $y_{i\,(obs)}$ of each equal spaced step over the entire pattern. That includes the background intensity $y_{i\,(background)}$ and the sum of the contribution of reflections close to the powder pattern step $y_{i\,(Bragg)}$ [36].

$$y_{i\,(obs)} = y_{i\,(background)} + \sum_i y_{i\,(Bragg)} \qquad 2.10$$

The Rietveld method is a least-square fit that minimises the residual between the observed intensity $y_{i\,(obs)}$ and the calculated intensity $y_{i\,(calc)}$ at all the steps. Once the derived pattern is nearly identical to an unknown sample data, various properties pertaining to that sample can be obtained including: accurate quantitative information, crystallite size, and site occupancy factors. The method basically requires some information related to initial structural model, space group, unit cell lattice parameters, atomic positions and instrumental details. The calculated intensity $y_{i\,(calc)}$ of each step as expressed in Equation 2.11 can be calculated by a mathematical expression that includes the factors related to both the structure and the non-diffraction terms [36].

$$y_{i\,(calc)} = s \sum_{hkl} L_{hkl} |F_{hkl}|^2 \, \emptyset\,(2\theta_i - 2\theta_{hkl}) P_{hkl} A + y_{i\,(background)} \qquad 2.11$$

Where s is the scale factor, L_{hkl} contains the Lorentz, polarisation and multiplicity factors, F_{hkl} is the structure factor which includes nuclear and magnetic structure factors if applicable, $\emptyset\,(2\theta_i - 2\theta_{hkl})$ is the peak shape function which describes the effects of the instrument and the sample on the reflection profile, P_{hkl} is the preferred orientation function, and A is the absorption factor [36].

To improve the match between observed and calculated diffraction patterns during the refinement process, each of structural and functional parameters must be cycled and varied. The fitting results can be estimated by the examinations of a plot of the difference between observed and calculated patterns, or by referring to the reliability factors R_p, R_{wp} and χ^2 [36]. The residual values R-pattern, R- Weight pattern and Goodness of fit are defend in the following Equations:

$$R_p = \sum \left| \left(y_{i\,(obs)}\right) - \left(y_{i\,(calc)}\right) \right| / \sum y_{i\,(obs)} \,. \qquad 2.12$$

$$R_{wp} = \left| \sum w_i \left(y_{i\,(obs)} - y_{i\,(calc)}\right)^2 / \sum w_i \left(y_{i\,(obs)}\right)^2 \right|^{1/2}. \qquad 2.13$$

$$\chi^2 = \sum w_i \, (y_{i\,(obs)} - y_{i\,(calc)})^2/(n - p + c). \qquad 2.14$$

Where n is the number of observations, p is the number of parameters and c is the number of constrains in the definition of goodness of fit. A good fit with the refined structure model should have a low residual value. The χ^2 value is directly proportional to S_y and is ideally unity [36].

The Rietveld Method has an advantage, over conventional quantitative analysis, that no standards are required to achieve accurate results. Before this approach, an accurate and standardless quantitative phase analysis of complex materials using powder diffraction was almost impossible. All refinements of perovskite structures from X-rays and neutrons powder diffraction patterns in this thesis were carried out with Rietveld method using the programme RIETICA [36].

2.3.2 IFEFFIT programme

IFEFFIT is an interactive program for X-ray absorption fluoresce spectroscopy analysis (XAFS). It combines the high-quality analysis algorithms of AUTOBK and FEFFIT with graphical display of XAFS data and general data manipulation [37,38]. IFEFFIT comes as a command-line program, but the underlying functionality is available as a programming library. The IFEFFIT library can be used from C, Fortran, Tcl, Perl, and Python [37,38]. It includes ATHENA, ARTEMIS, and SIXPACK softwares. The programme includes a feature of generalized minimization routine for fitting non-XAFS data, including XANES fitting to combinations of model spectra or pre-defined functions [37,38]. In this work, Athena software programme was utilized to estimate the ionic ratio $Rh^{3+/4+}$ in the $La_{1-x}Pb_xRh_{0.5}Cu_{0.5}O_3$ and $LaRh_{1-x}Cu_xO_3$ series. The method is based on XANES fitting to combination of model spectra.

2.3.3 General Calculations

To calculate the actual masses needed to synthesize the samples, physical means include activation energy, effective magnetic moments and water content in the samples, the following Equations were utilized.

a) Mass of starting materials (m_s)

$$m_s = \frac{n_t}{n_s} \times \frac{M_s}{M_t} \times m_t \qquad 2.15$$

Where *m* and *M* are the mass (g) and the molar mass (g/mole), *s* and *t* refer to starting and targeted materials, $\frac{n_t}{n_s}$ is a stoichiometry factor for an element in the compounds.

b) Activation Energy

$$\epsilon_a = -b \times 8.617 \times 10^{-5}. \quad 2.16$$

Where ϵ_a is activation energy (eV) and *b* is a slope of the straight line of an Arrhenius plot where natural logarithm of electrical conductivity is plotted against inverse temperature (K^{-1}), 8.617×10^{-5} is Boltzmann constant (eV/K).

c) Effective Moment (μ_{eff}), Weiss constant (θ) and Curie constant (C).

$$\mu_{eff} = 2.82/\sqrt{b} \quad 2.17$$

$$\theta = -a/b \quad 2.18$$

$$C = -T_c/b \quad 2.19$$

Where *a* and *b* are the intercept with *x* axis and the slope of a straight line for a Curie-Weiss plot (inverse molar magnetic susceptibility against temperature).

d) Water Content in a sample (W. C).

$$\text{W. C} = \frac{whight\ loss\ (mg) \times molar\ mass\ of\ the\ compound(mg/mmole)}{residul\ mass\ (mg) \times molar\ mass\ of water(mg/mmole)} \quad 2.20$$

In the following chapters observations, results and discussion for studied perovskite material will be presented.

2.4 References

[1] L.G. Tejuca, J.L.G. Fierro, Properties and Applications of Perovskite-Type Oxides, 1993, Marcel Dekker, New York.

[2] R.R. Chromik, W.K. Neils, E.J. Cotts, *Journal of Applied Physics*, 86 (1999) 4273-4281.

[3] H. Yokokawa, N. Sakai, T. Kawada, M. Dokiya, *Solid State Ionics*, 52 (1992) 43-56.

[4] J. Šesták, G. Berggren, *Thermochimica Acta*, 3 (1971) 1-12.

[5] D. Sporn, S. Merklein, W. Grond, S. Seifert, S. Wahl, A. Berger, *Microelectronic Engineering*, 29 (1995) 161-168.

[6] V. Kozhukharov, M. Machkova, N. Brashkova, C. Trapalis, *Journal of Sol-Gel Science and Technology*, 26 (2003) 753-757.

[7] T. Ishihara, Structure and Properties of Perovskite Oxides, 2009, Springer, US.

[8] R. Feenstra, L.A. Boatner, J.D. Budai, D.K. Christen, M.D. Galloway, D.B. Poker, *Applied Physics Letters*, 54 (1989) 1063.

[9] C.C. Chang, C.S. Tang, *Journal of Applied Physics*, 87 (2000) 3931-3936.

[10] A.R. West, Solid State Chemistry and Its Applications, 1991, Wiley, UK.

[11] R.E. Dinnebier, S.J.L. Billinge, Principles of Powder Diffraction: Theory and Practice, 2008, The Royal Society of Chemistry, UK.

[12] R. Jenkins, X-Ray Techniques: Overview, 2006, John Wiley & Sons, USA.

[13] X-ray reflection in accordance with Bragg's Law, http://serc.carleton.edu; 2012

[14] A.R. West, Basic Solid State Chemistry, 1999, John Wiley & Sons, USA.

[15] V.K. Pecharsky, P.Y. Zavalij, Fundamentals of Powder Diffraction and Structural Characterization of Materials, 2009, Springer, US.

[16] Bragg's Law http://hyperphysics.phy-astr.gsu.edu; 2012

[17] The Powder Diffraction Beamline, Australian Synchrotron, http://www.synchrotron.org.au; 2012

[18] T. Chatterji, Neutron Scattering from Magnetic Materials, 2005, Elsevier Science, France.

[19] K. Sköld, D.L. Price, Neutron Scattering, 1987, Elsevier Science, USA.

[20] S.E. Dann, Reactions and Characterization of Solids, 2002, Royal Society of Chemistry, UK.

[21] V.F. Sears, *Neutron News*, 3 (1992) 26-37.

[22] Echinda- High-Resolution Powder Diffractomete, Australian Nuclear Science and Technology Organisation, http://www.ansto.gov.au; 2012

[23] K.D. Liss, B. Hunter, M. Hagen, T. Noakes, S. Kennedy, *Physica B-Condensed Matter*, 385-86 (2006) 1010-1012.

[24] D. Norman, *Journal of Physics C: Solid State Physics*, 19 (1986) 3273.

[25] T. Hemraj-Benny, S. Banerjee, S. Sambasivan, M. Balasubramanian, D.A. Fischer, G. Eres, A.A. Puretzky, D.B. Geohegan, D.H. Lowndes, W. Han, J.A. Misewich, S.S. Wong, *Small*, 2 (2006) 26-35.

[26] A. Bianconi, *Applications of Surface Science*, 6 (1980) 392-418.

[27] P. Behrens, *TrAC Trends in Analytical Chemistry*, 11 (1992) 237-244.

[28] T.E. Dann, S.C. Chung, L.J. Huang, J.M. Juang, C.I. Chen, K.L. Tsang, *Journal of Synchrotron Radiation*, 5 (1998) 664-666.

[29] S.L. Kakani, Material Science, 2006, New Age International, India.

[30] Physical Property Measurement System, PPMS, http://www.qdusa.com; 2012

[31] A. Aharoni, Introduction to the Theory of Ferromagnetism, 2001, Oxford University Press, USA.

[32] S. Chikazumi, Physics of Ferromagnetism, 2009, Oxford University Press, USA.

[33] The Hysteresis Loop and Magnetic Properties, http://www.ndt-ed.org; 2012

[34] R.B. Prime, H.E. Bair, S. Vyazovkin, P.K. Gallagher, A. Riga, Thermogravimetric Analysis (TGA), 2008, John Wiley & Sons, USA.

[35] M.E. Brown, Thermogravimetry (TG): Introduction to Thermal Analysis, 2004, Springer, Netherlands.

[36] B.A. Hunter, C.J. Howard, RIETICA. A Computer Program for Rietveld Analysis of X-Ray and Neutron Powder Diffraction Patterns, (1998)

[37] IFEFFIT: Interactive XAFS Analysis, http://cars.uchicago.edu; 2012

[38] M. Newville, *Journal of Synchrotron Radiation*, 8 (2001) 322-324.

Structural, Electrical and Magnetic Studies of the *A* site Doped Oxides $LaRh_{0.5}Cu_{0.5}O_3$ (*A*= Ca^{2+}, Sr^{2+}, Pb^{2+} and Bi^{3+})

3.1 Introduction

The electrical and magnetic properties of many double perovskites remain controversial and enormous efforts are ongoing in the search for an improved understanding of these properties [1, 2]. One extensively studied system is the alkaline earth 3*d*-4*d* mixed metal perovskite Sr_2FeMoO_6 [3]. While the effect of varying the *A*-site doping on the ferromagnetism is still open to discussion, it appears that chemical ordering between the 3*d* (Fe) and 4*d* (Mo) cations plays a key role [4]. Even when such ordering does not exist complex magnetic and electronic behaviour results, as illustrated by the mixed Ru-Mn perovskites of the type $ARu_{1-x}Mn_xO_3$ where *A* = Ca, Sr or a mixture of these [5, 6].

The incorporation of a cation with a stereochemically active lone pair of electrons onto the *A*-site is known to have a significant effect on the structure and properties of perovskites. This has been explored in the complex manganites $La_{1-x}A_xMnO_3$ (*A* = Pb^{2+}, Bi^{3+}) [7-9]. The substitution of La^{3+} by Pb^{2+} reduces the amount of Jahn-Teller (JT) active Mn^{3+} present, inducing changes in the crystal structure, resistivity and magnetic ordering [7, 8], reflecting the importance of the JT effect. It is postulated that the $6s^2$ electrons from the Pb^{2+} ions also influence the structure and properties [10]. Similarly, the substitution of Bi^{3+} for La^{3+} in $LaMnO_3$ has a significant effect on the magnetoresistance. This has been attributed to the influence of the lone pair electrons on Bi^{3+} on the superexchange interactions between adjacent Mn cations [9, 11].

The structure of the Rh containing perovskite $LaRh_{0.5}Cu_{0.5}O_3$ [12] has been recently described. X-ray spectroscopy showed the Rh and Cu in $LaRh_{0.5}Cu_{0.5}O_3$ to have valence states of around +3.5 and +2.5 respectively, as a consequence of extensive charge delocalisation between the Rh and Cu cations. Although this increase in the formal valency of the Cu would reduce the impact of the JT distortion of the BO_6 octahedra, the structural distortion is noticeably larger in $LaCu_{0.5}Rh_{0.5}O_3$ ($\Delta d \sim 11 \times 10^{-5}$) [12] than in $LaRhO_3$ ($\Delta d \sim 2.5 \times 10^{-5}$) [13], suggesting that a JT-type distortion remains significant.

3.1.1 Aims and Objectives

In the present work, the influence of *A*- site doping on the structure, electrical and magnetic properties of the perovskite oxide, $La_{0.75}A_{0.25}Rh_{1-x}Cu_xO_3$ where *A* = Ca^{2+}, Sr^{2+}, Pb^{2+} and Bi^{3+}, were investigated. The *A*- site cations were selected based on their size, charge and electron configuration. The partial substitution of the *A*- site was expected to influence the extent of electron delocalization between the two transition metals on the *B*- site, which have been described as $Rh^{3.5+}$ and $Cu^{+2.5}$ [12], leading to changes in the physical properties. These physical properties can be influenced by the differences in the effective charges, the ionic radii and the electron configurations of both the *A* and *B*- site cations. In addition, changes to electrical and magnetic behaviour can be induced by the stereochemical influence of $6s^2$ lone pair electrons. For example, the Pb^{2+} and Bi^{3+} doped oxides are found to exhibit electrical and magnetic behaviour different to that of the alkaline earth doped oxides [14, 15].

3.1.2 Methodology

Commercially available materials, La_2O_3, CuO, Bi_2O_3, PbO, $CaCO_3$ and $SrCO_3$ (Aldrich ≥ 99.9 %), Rh (Althaca 99.95 %) were utilized in the synthesis. The appropriate stoichiometric amounts were mixed, using a mortar and pestle, and then heated in several steps with further intermittent regrinding. Samples were initially heated for 24 h at 850 °C followed by reheating at 950 °C for 24 h, 1000 °C for 48 h and 1050 °C for 48 h. The samples were finally annealed at 1100 °C for 48 h. Samples containing Pb and Bi were pressed into pellets to minimize the volatilization of the elements at high temperatures.

Neutron powder diffraction data were collected using the high resolution powder diffractometer, Echidna [16], at the OPAL facility (Australian Nuclear Science and Technology Organization) at a wavelength of 2.4395 Å. For these measurements the sample was contained in a cylindrical vanadium can. Synchrotron X-ray powder diffraction data were collected over the angular range $5 < 2\theta < 85°$, using X-rays of wavelength 0.82554 Å on the powder diffraction beamline at the Australian Synchrotron [17]. For these measurements the samples were housed in 0.3 mm diameter capillaries. The structures were refined using the program RIETICA[18]. The peak shapes were modelled using a pseudo Voigt function. The microstructure of the powder samples was examined by scanning electron microscopy (SEM) using an Intellection Quemscan**.**

Magnetic measurements were carried out using a Quantum Design, PPMS. The temperature dependence of the magnetic susceptibilities was measured under both zero- field cooled (ZFC) and field cooled (FC) conditions in an applied field of 5 kOe over the temperature range 4-300K. The temperature dependence of the resistivity was measured using a DC four probe technique with the same measurement system. For the resistivity measurements the sintered samples were cut into pieces of approximately 3 × 4 mm onto which four contacts were painted using silver paste.

Rh $L_{3,2}$ edge X-ray absorption spectra were recorded from, powder samples dispersed on Kapton tape, in fluorescence mode on beam line BL-16A1 at the National Synchrotron Radiation Research Centre (NSRRC) in Hsinchu, Taiwan using a Lytle detector [19]. Energy steps as small as 0.2 eV were employed near the absorption edges with a counting time of 2 s per step. The spectra were normalized to the incident photon current. The energy scale of the Rh $L_{3,2}$ edge spectra was calibrated using the L_2 edge of a Mo foil. $LaRhO_3$ and Sr_2RhO_4 were used as the Rh^{3+} and Rh^{4+} standards respectively.

3.2 Results and discussion: $La_{0.75}A_{0.25}Rh_{1-x}Cu_xO_3$

Eight members of the *A*- site doped Rh perovskites with general formula $La_{0.75}A_{0.25}Rh_{0.7}Cu_{0.3}O_3$ and $La_{0.75}A_{0.25}Rh_{0.5}Cu_{0.5}O_3$ (*A* = Ca^{2+}, Sr^{2+}, Pb^{2+} and Bi^{3+}) were synthesised by solid-state methods and their crystallographic, magnetic, and electric properties investigated. Each of these samples has an orthorhombic perovskite-type structure in space group *Pbnm*. Initially, the synthetic attempts focused on $La_{0.75}A_{0.25}Rh_{0.5}Cu_{0.5}O_3$ oxides where *A* = Ca^{2+}, Sr^{2+}, Pb^{2+} and Bi^{3+}, however only for Pb^{2+} and Bi^{3+} were single phase samples obtained. Subsequently, the $La_{0.75}A_{0.25}Rh_{0.7}Cu_{0.3}O_3$ series was also prepared.

3.2.1 Visual Inspection

The heating regime described above produced crystalline, black coloured, samples. The colour of the samples changed from gray, for the raw material, to black for samples heated above 950 °C. SEM measurements (Figure 3.1) demonstrated the samples to be well sintered and free of any obvious impurities.

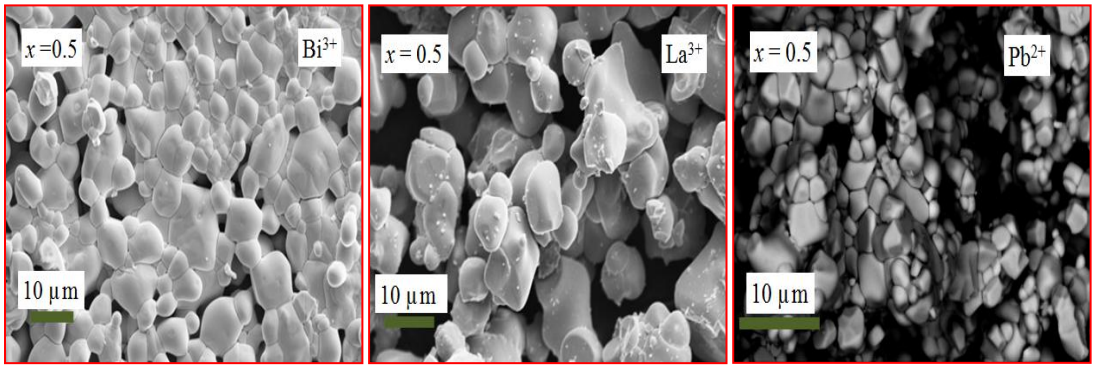

Figure 3.1 Scanning Electron Micrograph images for $La_{0.75}Bi_{0.25}Rh_{0.5}Cu_{0.5}O_3$, $LaRh_{0.5}Cu_{0.5}O_3$ and $La_{0.75}Pb_{0.25}Rh_{0.5}Cu_{0.5}O_3$.

The Pb doped oxides are much more crystalline than the undoped and Bi doped oxides. Decreasing the Cu content did not lead to any changes in the shape and sizes of the particles. However, it was found that Ca and Sr are more soluble in the $La_{0.75}A_{0.25}Rh_{0.7}Cu_{0.3}O_3$ solid solutions than in $La_{0.75}A_{0.25}Rh_{0.5}Cu_{0.5}O_3$. Doping with Ca and Sr results in smaller particle sizes than what was observed for the Pb doped compounds. In addition, $La_{0.75}Ca_{0.25}Rh_{0.7}Cu_{0.3}O_3$ and $La_{0.75}Sr_{0.25}Rh_{0.7}Cu_{0.3}O_3$ are more crystalline than $La_{0.75}Pb_{0.25}Rh_{0.7}Cu_{0.3}O_3$ (Figure 3.2).

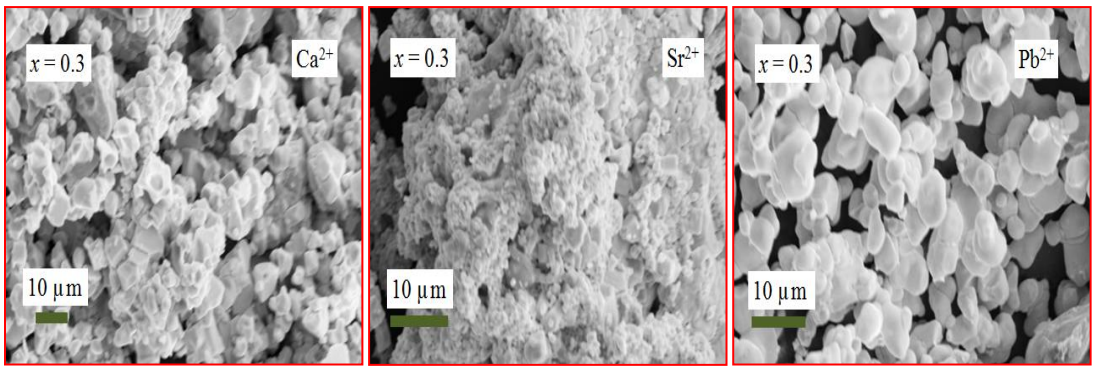

Figure 3.2 Scanning Electron Micrograph images for $La_{0.75}Ca_{0.25}Rh_{0.7}Cu_{0.3}O_3$, $La_{0.75}Sr_{0.25}Rh_{07}Cu_{0.3}O_3$ and $La_{0.75}Pb_{0.25}Rh_{0.7}Cu_{0.3}O_3$.

EDX measurements provide qualitative and quantitative information about the elemental compositions of the materials. In the present case overlap of the characteristic X- ray lines limited the accuracy of such measurements. There was no evidence for the loss of any element from the samples during heating. The mass ratios of the elements agree with the nominal stoichiometry.

3.2.2 Crystal Structure

X-ray diffraction measurements showed the oxides were isostructural with undoped $LaRhO_3$ [20] and have an orthorhombic *Pbnm* structure. The position of both the Rh and Cu ions in the unit cell is (0, 0, 0). The orthorhombic structure was identified by conventional XRD patterns and then confirmed by Synchrotron-XRD. Figure 3.3 illustrates the Rietveld refinement profiles for $LaRh_{0.5}Cu_{0.5}O_3$. The lattice parameters were determined to be a = 5.55285(3), b = 5.69054(3) and c = 7.83210(3) Å; the reliablity factors R_p = 5.39, R_{wp} = 8.26, χ^2 = 20.89.

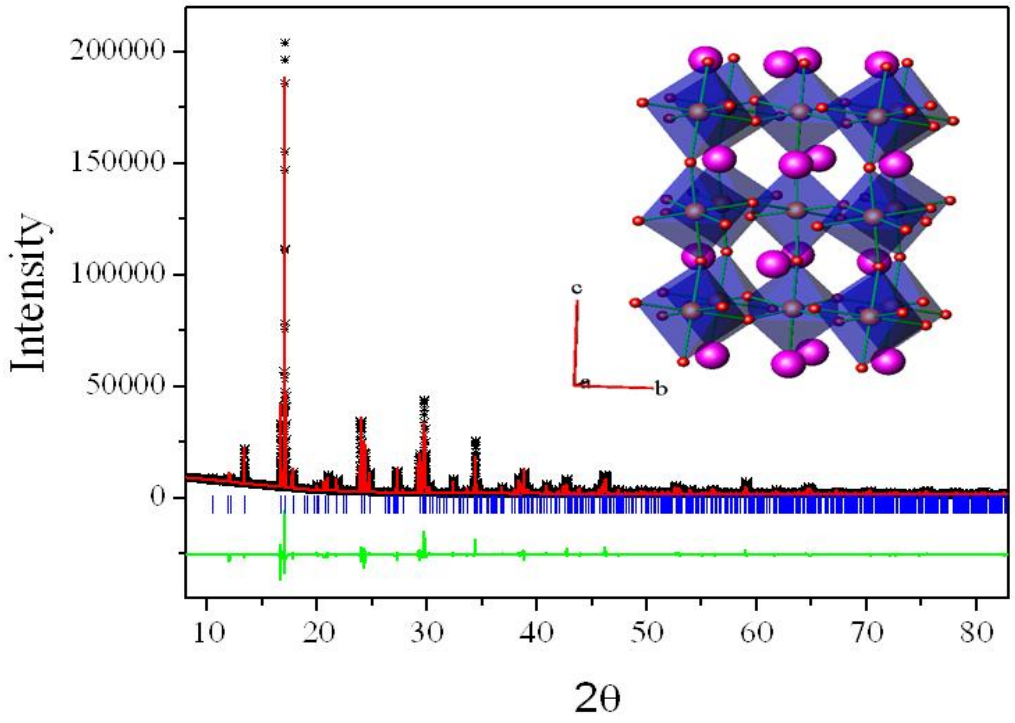

Figure 3.3 Synchrotron X-ray diffraction profiles for $LaRh_{0.5}Cu_{0.5}O_3$. The data are represented by the crosses and the solid lines are the calculated and difference profiles. The positions of the space group allowed reflections are shown by the vertical markers immediately below the observed profile. A representation of the $LaRh_{0.5}Cu_{0.5}O_3$ structure is also included.

The protocol used in the Rietveld refinements was to initially estimate the background, lattice parameters and diffractometer zero-point errors using typical peak shape parameters for the diffractometer, obtained from fitting of a standard material. Next the variable positional parameters for the heavy and oxygen atoms

were sequentially refined, followed by the atomic displacement parameters. Finally the instrumental peak shape parameters were refined. The quality of the fit was judged from both visual examination of the profile, and consideration of the various R-factors. The validity of the structural model was established through examination of the refined bond distances and angles. The X-ray diffraction measurements showed no evidence for ordering of the Cu and Rh cations. Subsequently, powder neutron diffraction data were obtained for $La_{0.75}Pb_{0.25}Rh_{0.5}Cu_{0.5}O_3$ and this was analysed using a model in the orthorhombic space group *Pbnm* where the Cu and Rh were disordered at the octahedral sites. The results of Rietveld refinement are presented in Figure 3.4 and summarised in Table 3.1. The structural refinement provided no evidence for any anion vacancies in the structure, attempts to refine the anion occupancies resulted in values within two esds of full occupancy. This conclusion is also supported by the values of the refined displacement parameters which were normal.

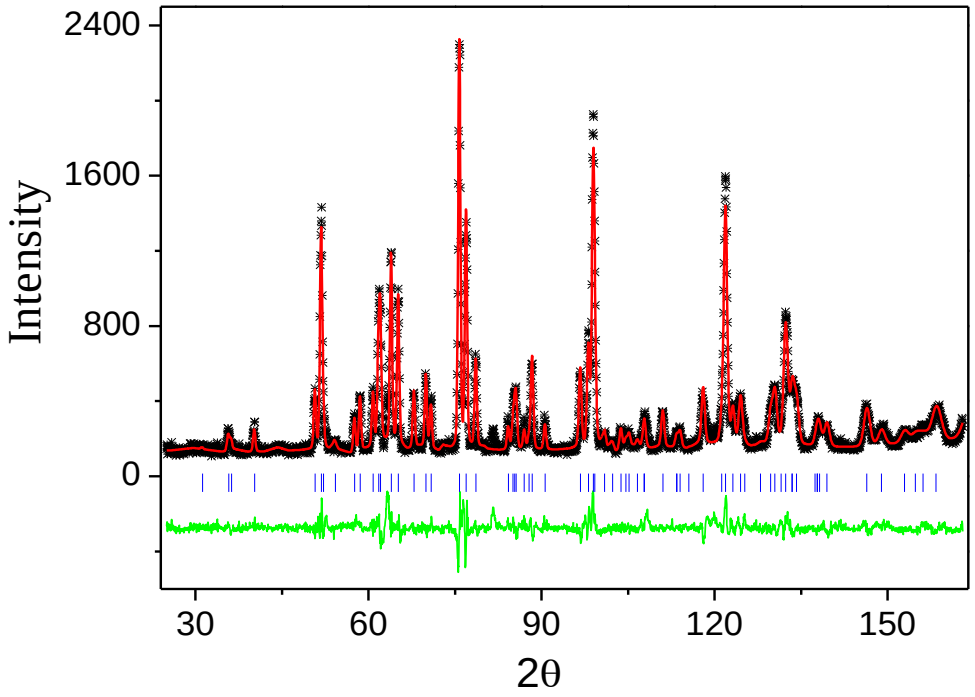

Figure 3.4 Neutron diffraction profiles for $La_{0.75}Pb_{0.25}Rh_{0.5}Cu_{0.5}O_3$ at room temperature. The data are represented by the crosses and the solid lines are the calculated and difference profiles. The positions of the space group allowed reflections are shown by the vertical markers immediately below the observed profile.

Table 3.1 Results of the structural refinement for $La_{0.75}Pb_{0.25}Rh_{0.5}Cu_{0.5}O_3$ using neutron powder diffraction data at room temperature. The bond distances for *M*-O_1, *M*-O_2 and *M*-O_2^* are 2.024(1), 2.047(2), and 2.061(2) Å respectively.

Atom	*Site*	*x*	*y*	*z*	B_{iso} (Å^2)	*Occ*
La/Pb	4(*c*)	0.4900(5)	-0.0499(4)	0.25	1.66(10)	0.75/0.25
Cu/Rh	4(*b*)	0	0	0	1.61(09)	0.5/0.5
O(1)	4(*c*)	0.5875(6)	0.5222(6)	0.25	0.85(13)	1.0
O(2)	8(*d*)	0.2992(4)	0.2014(4)	0.0443(3)	1.73(07)	1.0
Parameters	*a* = 5.5483(4), *b* = 5.6929(3) and *c* = 7.8447(3) Å					
R- factors	R_p = 7.07, R_{wp} = 9.11, and χ^2 = 2.09					

Bond Valence Sums (BVS) are a powerful method to probe the stability of ions in crystal structures. These are calculated from the refined bond distances using Equation 3.1 where R_i is the observed bond distance to an individual atom, R_0 and *b* are tabulated constants, and *N* is the coordination number of the central atom within a preset cut-off distance [21]. Accurate bond valence parameters, R_0, for Rh^{4+} were not available, and we have thus estimated the value to be 1.84, based on the structure of $SrRhO_3$ [22]. Using this and the tabulated value for Cu^{2+}, bond valences for Cu and Rh were estimated from the refined structure to be 2.24 and 3.41 respectively, with the average site valence being marginally lower than the anticipated value, 2.83. These values suggest partial electron transfer between the two cations. The weighted average BVS for the *A*- site in $La_{0.75}Pb_{0.25}Rh_{0.5}Cu_{0.5}O_3$ is 3.03 although the BVS for the Pb^{2+} cations, at 2.68, is unusually high suggesting considerable overbonding. Such overbonding can be relieved by disorder of the Pb cations as seen in oxides such as $PbZrO_3$ [23]. The BVS for the La^{3+} cation, 3.15, is unexceptional since the La ($6s^2\,5d^1$) atom has only three valence electrons in its outer shell.

$$BVS = \sum_{i=1}^{N}\left[exp\left(\frac{R_0 - R_i}{b}\right)\right] \qquad 3.1$$

The orthorhombic *Pbnm* structure is derived from the aristotype $Pm\bar{3}m$ cubic structure by tilting of the octahedra. Octahedra in adjacent unit cells may tilt either in-phase or out-of-phase, and the magnitude of these tilts can be estimated from the refined atomic coordinates as described by Kennedy *et al* [24]. Both the in-phase (+)

and out-of-phase (-) tilts are appreciable in $La_{0.75}Pb_{0.25}Rh_{0.5}Cu_{0.5}O_3$, 10.9° and 14.1° respectively. X-ray diffraction measurements showed that the orthorhombic structure persisted over a wide temperature range, 30 to 900 °C, for the various oxides. The temperature dependence of the lattice parameters for a representative sample is illustrated in Figure 3.5. The failure to observe any structural phase transitions below 900 °C in the XRD studies is consistent with the size of the tilts. At room temperature the tilts in $CaTiO_3$ are 9.1° and 12.2° respectively and the compound does not undergo any structural transitions below 1200 °C, where the smaller in-phase tilts are lost [24]. A feature of the temperature dependence of the lattice parameters is the contraction along the *b*-axis upon heating, whereas both the *a* and *c* parameters show simple thermal expansion. The anisotropy in the lattice parameters is a consequence of the tilting of the octahedra and it is believed that the negative thermal expansion of *b* reflects the reduction in the tilting upon heating. This behaviour is reminiscent of that seen in a number of other perovskites including some hole-doped manganites of the type $Sr_{1-x}Ce_xMnO_3$ [25]. The thermal expansion in the volume is unexceptional, as expected given the lack of any structural phase transitions.

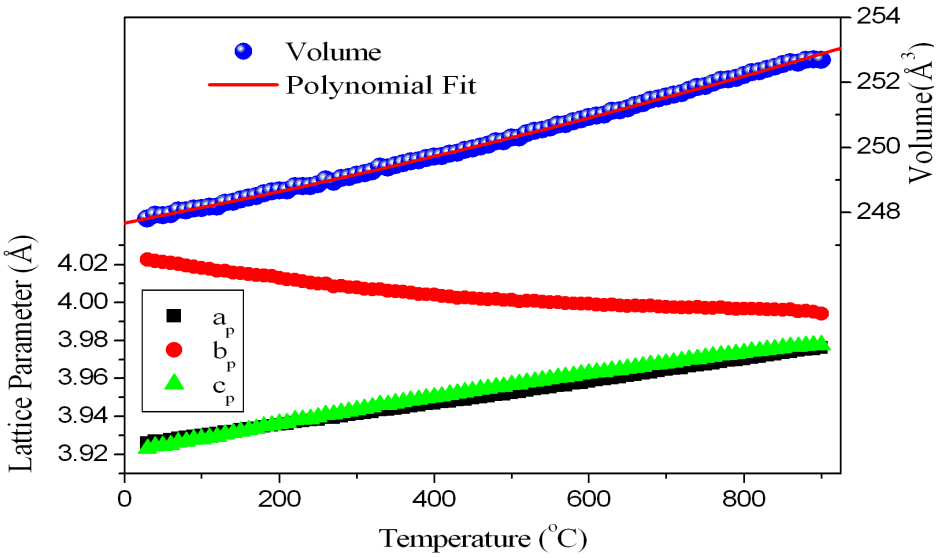

Figure 3.5 The temperature dependence of lattice parameters for $La_{0.75}Pb_{0.25}Rh_{0.5}Cu_{0.5}O_3$ estimated by Rietveld refinement using X-ray diffraction data. a_p, b_p and c_p are the individual lattice parameters converted to the length of the equivalent primitive unit cell ($\frac{a}{\sqrt{2}}$, $\frac{b}{\sqrt{2}}$, $\frac{c}{2}$). The temperature dependent variation of the cell volume is fitted to $V_{(t)} = 247.68(1) + 4.58(7)\times10^{-3}\,T + 1.32(7)\times10^{-6}\,T^2$.

The composition dependence of the unit cell volumes estimated from the synchrotron diffraction data for the two series $La_{0.75}A_{0.25}Rh_{0.7}Cu_{0.3}O_3$ and $La_{0.75}A_{0.25}Rh_{0.5}Cu_{0.5}O_3$ is illustrated in Figure 3.6. Doping with divalent metals, such as Ca and Sr, significantly reduces the cell volume. This is likely driven by the partial oxidation of the Rh^{3+} (6 coordinate ionic radius, 0.67 Å) to Rh^{4+} (0.60 Å) [26] necessary to maintain charge neutrality. Despite the impact of such oxidation, the Pb doped oxide exhibits an increase in the cell volume due to the large ionic size of the Pb^{2+} cation (8 coordinate ionic radius, 1.29 Å). Doping with trivalent metals such as Bi^{3+} is expected to have little impact on the charge delocalization in the system. The similarity in formal valency for both La^{3+} and Bi^{3+} ions means there is no change in the overall charge of the perovskites system. The small increase in cell volume of $La_{0.75}Bi_{0.25}Rh_{0.7}Cu_{0.3}O_3$ is consistent with the relative ionic size of the Bi^{3+} (8 coordinate ionic radius, 1.17 Å) and La^{3+} (1.16 Å) cations [26].

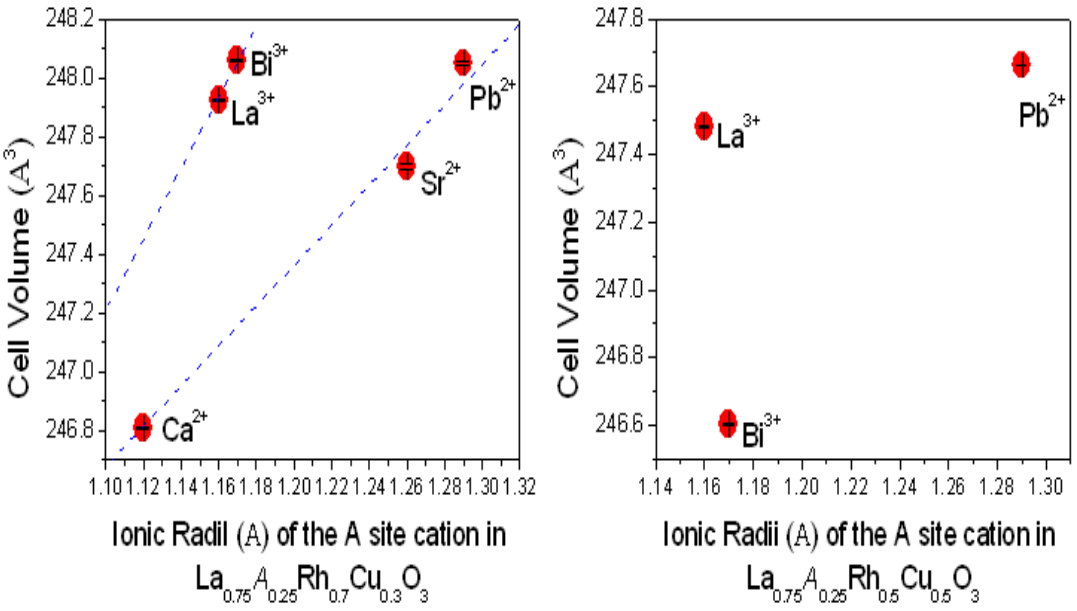

Figure 3.6 Composition dependence of the cell volume for $La_{0.75}A_{0.25}Rh_{0.7}Cu_{0.3}O_3$ and $La_{0.75}A_{0.25}Rh_{0.5}Cu_{0.5}O_3$ estimated by Rietveld refinement using synchrotron X-ray diffraction data. Where not obvious the error bars are smaller than the symbols.

The $La_{0.75}A_{0.25}Rh_{0.5}Cu_{0.5}O_3$ oxides have lower cell volumes than the corresponding $La_{0.75}A_{0.25}Rh_{0.7}Cu_{0.3}O_3$ oxides, presumably due to charge delocalization between the $Rh^{3.5+}$and $Cu^{2.5+}$ cations. As described above, partial

change transfer involving Rh^{4+} to Rh^{3+} and Cu^{2+} (6 coordinate ionic radius, 0.73 Å) to Cu^{3+} (0.53 Å) is possible [12]. Unexpectedly, $La_{0.75}Bi_{0.25}Rh_{0.5}Cu_{0.5}O_3$ displayed the lowest cell volume in the series, possibly as a consequence of local order effects. Similar effects have been reported for $La_xSr_{1-3x/2}TiO_3$ [27] and $Pr_{0.5}Ba_{0.5}Mn_2O_6$ [28]. It is postulated that the balance between the long range Coulomb energy and the short range ionic repulsion in the lattice is modified by local ordering of the *A*- site cations resulting in a decrease in the average cell volume. The decrease in the unit cell volume of $La_{0.75}Bi_{0.25}Rh_{0.5}Cu_{0.5}O_3$ could also be attributed to the high covalent bonding character of Bi ions, with small displacement of the *A*- site cations enhanced by the covalency [15, 23]. That the contraction in the cell volume was seen in $La_{0.75}Bi_{0.25}Rh_{0.5}Cu_{0.5}O_3$ rather than in $La_{0.75}Bi_{0.25}Rh_{0.7}Cu_{0.3}O_3$ possibly also reflects the solubility limit of Cu ions in the compound at $x = 0.5$. It is thought that local clustering of the doped ions is more likely to occur near the solubility limit. It was not possible to prepare single phase samples with $x > 0.5$.

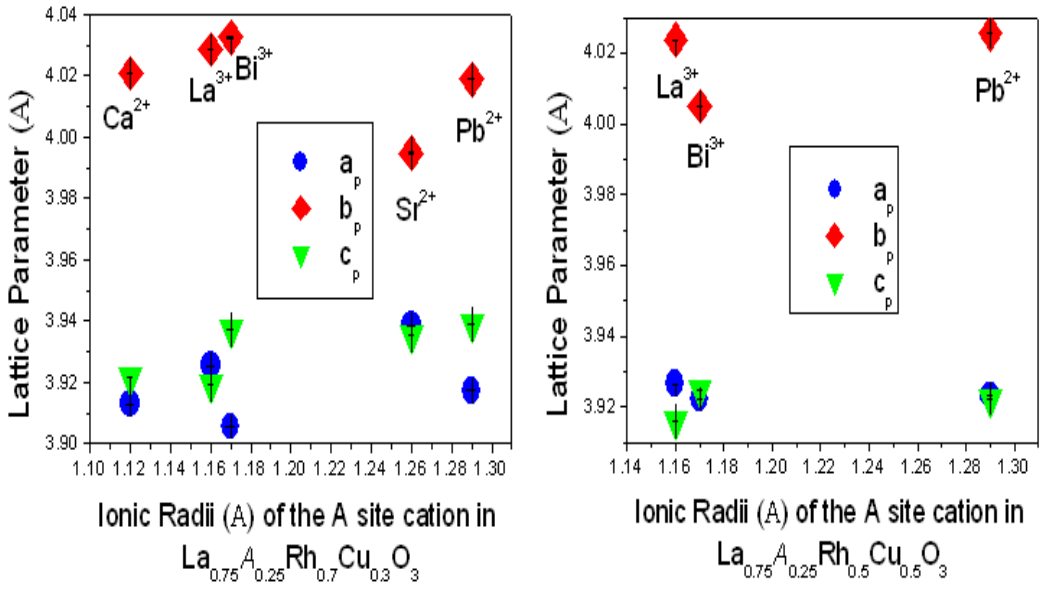

Figure 3.7 Lattice parameters a_p, b_p and c_p for $La_{0.75}A_{0.25}Rh_{0.7}Cu_{0.3}O_3$ and $La_{0.75}A_{0.25}Rh_{0.5}Cu_{0.5}O_3$ estimated by Rietveld refinement using synchrotron X-ray diffraction data. Where not obvious the error bars are smaller than the symbols.

The lattice parameters for the $La_{0.75}A_{0.25}Rh_{0.7}Cu_{0.3}O_3$ and $La_{0.75}A_{0.25}Rh_{0.5}Cu_{0.5}O_3$ series are illustrated in Figure 3.7. The lattice parameter

distortion (D) can be quantified as $D = (1/3)\sum_i 100\,[\frac{a_i - a_{av}}{a_{av}}]$ [29] where a_i is the individual lattice parameter converted to the length of the equivalent primitive unit cell ($a/\sqrt{2}$, $b/\sqrt{2}$, $c/2$), and a_{av} is the average lattice parameter. $La_{0.75}Sr_{0.25}Rh_{0.7}Cu_{0.3}O_3$ has the most symmetrical arrangement (lowest D value 0.65%), whereas $La_{0.75}Bi_{0.25}Rh_{0.7}Cu_{0.3}O_3$ has the most distorted lattice among the series (D = 1.25 %). The D value decreases as x increases in the trivalent metal doped oxides, but increases in the divalent metal doped oxides. This suggests, again, the importance of the charge delocalization. The distortion in lattice parameters of such Jahn-Teller systems is commonly attributed to strain effects on the structure. Strain in perovskites can be induced through several means including Jahn-Teller distortions, octahedral tilting, and disorder [30]. The increase in lattice parameter distortion frequently influences both the electrical and magnetic states in transition metal oxides. For example, the degeneracy of the Co 3d level ions in $LaCo_{1-x}Ti_xO_3$ decreases as the distortion in lattice parameter decreases [31], whilst in $Ln_{1-x}A_xMnO_3$ (Ln is a lanthanoid and A an alkaline earth cation), the observed increase in the Curie temperature and decrease in colossal magnetic resistance effects are correlated with an increase in lattice parameter distortion [32].

The diffraction studies demonstrate that both Cu and Rh cations were disordered at the octahedral sites of the perovskite structure. The distortion of this site can be quantified by $\Delta d = \sum_i (d_i - d_{av})^2 / (d_{av})^2$ where d_i is the individual bond distance between the B site cations and the oxygen anions, and d_{av} is the average of these distances. Δd was estimated to be 1.67×10^{-4} for $La_{0.75}Pb_{0.25}Rh_{0.5}Cu_{0.5}O_3$. This value is higher than found for $LaRhO_3$ ($\Delta d = 0.25 \times 10^{-4}$) [13]. The external structural distortion D and the internal structural distortion Δd for oxides compostions are summrised in Table 3.2. There is a strong negative correlation ($r = -0.95$) between the lattice parameter distortion and the octahedral distortion of both the divalent metal doped oxides $La_{0.75}A_{0.25}Rh_{0.7}Cu_{0.3}O_3$ and the trivalent metal doped oxides $La_{0.75}A_{0.25}Rh_{0.5}Cu_{0.5}O_3$. The correlation is positive for $LaRh_{0.7}Cu_{0.3}O_3$ and $La_{0.75}Bi_{0.25}Rh_{0.7}Cu_{0.3}O_3$. Doping with divalent cation, whether on A or B site, seems to have the same impact on the perovskites structure.

Table 3.2 Lattice parameter distortion D, octahedral distortion Δd, bond angles *M*-O(1)-*M* and *M*-O(2)-*M* for $La_{0.75}A_{0.25}Rh_{1-x}Cu_xO_3$ oxides.

Compositions	D (%)	$\Delta d \times 10^{-4}$	*M*-O(1)-*M*	*M*-O(2)-*M*
$LaRhO_3$ [33]	1.13	0.25	150.5º	149.1º
$LaRh_{0.7}Cu_{0.3}O_3$	1.19	5.33	145.3(5)º	150.4(3)º
$La_{0.75}Ca_{0.25}Rh_{0.7}Cu_{0.3}O_3$	1.17	0.65	154.4(5)º	155.8(4)º
$La_{0.75}Sr_{0.25}Rh_{0.7}Cu_{0.3}O_3$	0.65	9.30	158.4(7)º	152.7(4)º
$La_{0.75}Pb_{0.25}Rh_{0.7}Cu_{0.3}O_3$	1.02	0.87	155.5(7)º	154.0(5)º
$La_{0.75}Bi_{0.25}Rh_{0.7}Cu_{0.3}O_3$	1.25	7.07	152.5(6)º	151.6(4)º
$LaRh_{0.5}Cu_{0.5}O_3$	1.15	2.24	148.1(4)º	152.5(3)º
$La_{0.75}Pb_{0.25}Rh_{0.5}Cu_{0.5}O_3$	1.15	1.67	151.3(3)º	150.6(12)º
$La_{0.75}Bi_{0.25}Rh_{0.5}Cu_{0.5}O_3$	0.91	8.76	151.2(6)º	154.7(5)º

Examination of the structures, refined from synchrotron X-ray diffraction data, show that increasing the Cu content from 0.3 to 0.5 in $La_{0.75}A_{0.25}Rh_{1-x}Cu_xO_3$ significantly increases the octahedral distortion. The octahedral distortions in both $La_{0.75}Bi_{0.25}Rh_{0.5}Cu_{0.5}O_3$ ($\Delta d = 8.76 \times 10^{-4}$) and $La_{0.75}Pb_{0.25}Rh_{0.5}Cu_{0.5}O_3$ ($\Delta d = 1.67 \times 10^{-4}$) are higher than in $La_{0.75}Bi_{0.25}Rh_{0.7}Cu_{0.3}O_3$ ($\Delta d = 7.07 \times 10^{-4}$) and $La_{0.75}Pb_{0.25}Rh_{0.7}Cu_{0.3}O_3$ ($\Delta d = 0.87 \times 10^{-4}$). Surprisingly, Δd is lower in $LaRh_{0.5}Cu_{0.5}O_3$ ($\Delta d = 2.24 \times 10^{-4}$) than in $LaRh_{0.7}Cu_{0.3}O_3$ ($\Delta d = 5.33 \times 10^{-4}$). These changes are believed to result from partial oxidation of the Cu^{2+} to Cu^{3+}. The Cu^{2+} ($3d^9$) cations are susceptible to Jahn-Teller distortion and hence the presence of Cu^{2+} is expected to increase the octahedral distortion. To maintain charge balance, oxidation of Cu^{2+} must be accompanied by reduction of Rh^{4+} to give a mixed valent $Rh^{3+/4+}$, as observed in $LaRh_{0.5}^{(4+/3+)}Cu_{0.5}^{(2+/3+)}O_3$ [12]. As discussed in the following section cooperative tilting of octahedra is also likely to be important. The differences in the distortion between the various doped samples suggest a shift in the balance of the Cu and Rh redox states. The octahedral distortion is also dependent on the relative sizes of doped cations. For example, the increase in Δd for $La_{0.75}Ca_{0.25}Rh_{0.7}Cu_{0.3}O_3$ ($\Delta d = 0.65 \times 10^{-4}$) and $La_{0.75}Sr_{0.25}Rh_{0.7}Cu_{0.3}O_3$ ($\Delta d = 9.30 \times 10^{-4}$) mimics the change in the (8- coordinate) ionic radii of Ca^{2+} (1.12 Å) and Sr^{2+}

(1.26 Å) [26]. This trend is not seen in the Pb doped oxides; Δd in $La_{0.75}Pb_{0.25}Rh_{0.7}Cu_{0.3}O_3$ is lower than in $La_{0.75}Sr_{0.25}Rh_{0.7}Cu_{0.3}O_3$, possibly as a consequence of the stereochemical impact of Pb 6*s* electrons.

The *M*-O(1)-*M* and *M*-O(2)-*M* bond angles, as obtained from the structural refinements, reflect the octahedral tilting. It is well established that both orbital and charge ordering are sensitive to the changes in octahedral tilting [29]. These are smaller in $LaRh_{0.7}Cu_{0.3}O_3$ and $LaRh_{0.5}Cu_{0.5}O_3$ than in other *A* site doped oxides (see Table 3.2). Unlike the octahedral distortions, there was no obvious correlation between the bond angles and Cu content. The tilting of the corner sharing MO_6 octahedra for $La_{0.75}Pb_{0.25}Rh_{0.5}Cu_{0.5}O_3$ is similar to that reported for $LaRhO_3$ (150.5°and 149.1°) [13]. The similarity in both the bond angles and octahedral distortions for $La_{0.75}Ca_{0.25}Rh_{0.7}Cu_{0.3}O_3$ and $La_{0.75}Pb_{0.25}Rh_{0.7}Cu_{0.3}O_3$, where Pb^{2+} is more covalent and has a similar ionic size to Ca^{2+} (low electron negativity), suggests that the decrease in the covalency of the *A*- site cation also reduces the Jahn-Teller distortion effect. The correlation between the octahedral distortion, due to the Jahn-Teller effect and the tilting of the octahedra was described by Woodward [29] who showed that tilting could suppress cooperative Jahn-Teller ordering. It is possible that the decrease in Δd for $LaRh_{1-x}Cu_xO_3$ with increasing *x* can also be attributed to this effect. Octahedral tilting may also play an important role in magnetic properties of perovskites. For instance, $Sr_xCa_{1-x}RuO_3$ [34] and $Se_{1-x}Te_xCuO_3$ [35] exhibit changes in magnetism upon the increase in *x*. These changes are thought to be driven by the changes in the (Ru-O-Ru) and (Cu-O-Cu) bond angles.

3.2.3 Magnetization

The temperature dependent variation of the magnetic susceptibility for the $La_{0.75}A_{0.25}Rh_{1-x}Cu_xO_3$ oxides under both zero- field cooling (ZFC) and field cooling (FC) conditions is illustrated in Figure 3.8. In ZFC measurements, the samples were cooled from RT to 5 K in absence of any magnetic field. A field of 5 kOe was then applied at 5 K and magnetization measurements were carried out in the heating cycle. In the case of FC, the sample was first cooled from RT to 5 K in the presence of 5 kOe field and then magnetization was measured with increasing temperature. The magnetization curves of all the oxide show reversible field dependence suggesting paramagnetism at 5 K. Subsequently, the inverse molar susceptibility was fitted in the temperature region (5-300 K) using the Curie-Weiss equation.

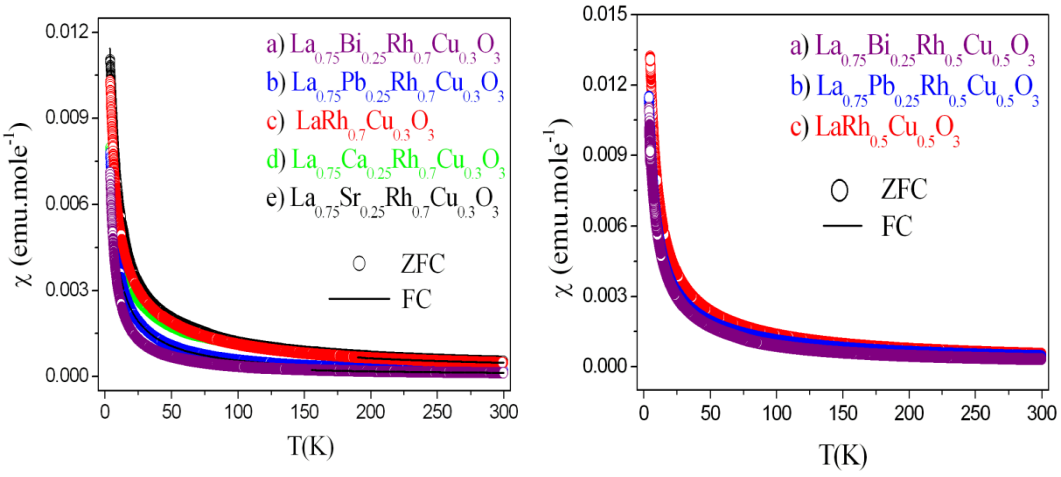

Figure 3.8 The temperature dependence of the molar magnetic susceptibility for $La_{0.75}A_{0.25}Rh_{0.7}Cu_{0.3}O_3$ and $La_{0.75}A_{0.25}Rh_{0.5}Cu_{0.5}O_3$ recorded under zero field cooling and field cooling conditions with an applied field of 5 kOe.

The inverse susceptibility plots (Figure 3.9) demonstrate that in $La_{0.75}A_{0.25}Rh_{1-x}Cu_xO_3$, the susceptibility decreased follow doping with Pb and Bi, but increased upon doping with Ca and Sr. The best linear fits to the inverse magnetization curves showed that the effective magnetic moments (μ_{eff}) for the oxides were negatively correlated with the Weiss constants. Hysteresis loop measurements (Figure 3.10) showed the absence of any long range magnetic ordering in the various oxides, although the non-linear behaviour demonstrates these are not simple paramagnets, suggesting weak magnetic interactions.

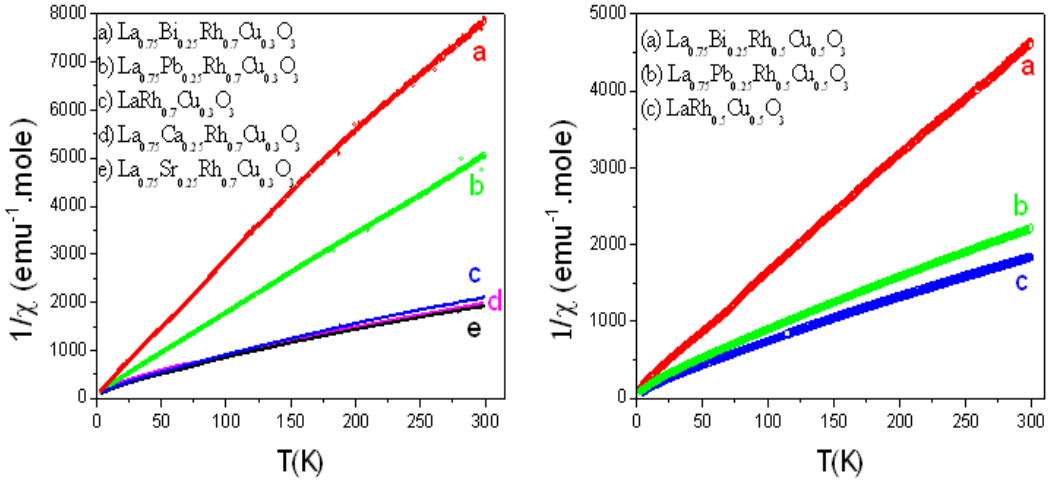

Figure 3.9 The temperature dependence of the inverse susceptibility for $La_{0.75}A_{0.25}Rh_{0.7}Cu_{0.3}O_3$ and $La_{0.75}A_{0.25}Rh_{0.5}Cu_{0.5}O_3$ recorded under zero field cooling conditions with an applied field of 5 kOe.

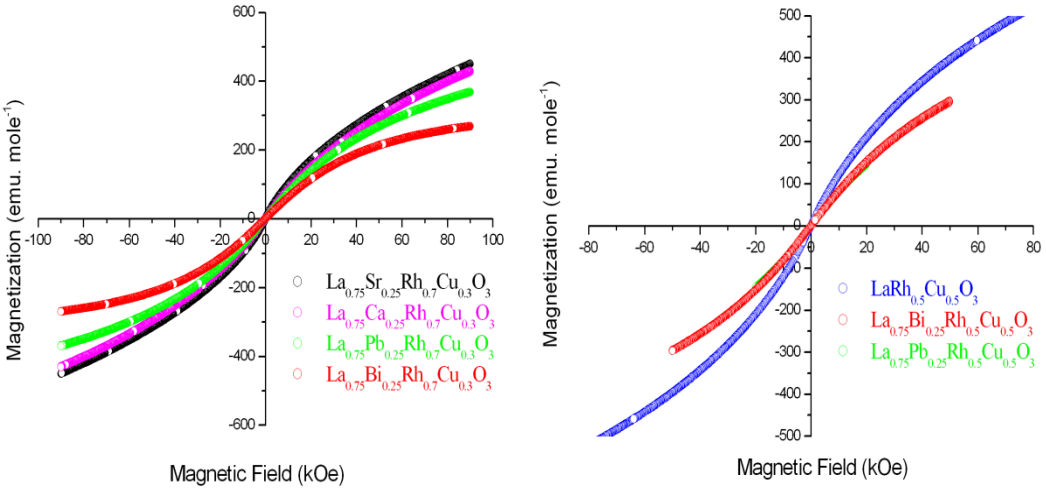

Figure 3.10 Magnetization hysteresis loops for $La_{0.75}A_{0.25}Rh_{0.7}Cu_{0.3}O_3$ and $La_{0.75}A_{0.25}Rh_{0.5}Cu_{0.5}O_3$ at 5 K.

As summarized in Table 3.3, the effective magnetic moments for the Ca^{2+} and Sr^{2+} doped oxides (1.15 and 1.16 μ_B) are similar to those for $LaRh_{0.5}Cu_{0.5}O_3$ (1.17 μ_B), indicating that doping with divalent metals, whether on the *A* site or *B* site, has a similar impact on the electron configuration of the transition metals. The decrease in magnetic moments of the divalent doped oxides was consistent with the ranking of electronegativities of the cations, $Sr^{2+}(0.95) < Ca^{2+}(1.00) < La^{3+}(1.10) < Pb^{2+}(1.87) < Bi^{3+}(2.02)$ [36]. Consequently, μ_{eff} for the Sr doped compound was greater than that observed for the Ca and Pb doped oxides. In the Bi^{3+} doped oxides, the magnetic moments were approximately 50 % lower than those found for $LaRh_{0.7}Cu_{0.3}O_3$ (1.11 μ_B) and $LaRh_{0.5}Cu_{0.5}O_3$ (1.17 μ_B). This decrease is thought to be driven, not only by the electronegativity of the cation but also by the effect of the $6s^2$ lone pair electrons, although the mechanism of this is unclear. The magnetic moments of the alkaline earth and undoped oxides are low spin states and that affects such as spin orbit coupling and/or weak exchange are also present. The Weiss constants (Θ) exhibited negative values, lower than seen in the weak paramagnetic oxide $LaRhO_3$ (-2.74 K, 0.295 μ_B) [37], indicating the importance of spin-orbit coupling and/or that the materials are weakly antiferromagnetic [38].

Table 3.3 Curie constant *C*, Weiss constant Θ, magnetic susceptibly coefficient factor χ_o and effective magnetic moment μ_{eff} for $La_{0.75}A_{0.25}Rh_{1-x}Cu_xO_3$.

Formula	Θ (K)	χ_o (10^{-3} emu.mole$^-$)	C (emu.mole$^-$)	μ_{eff} (μ_B)
$LaRh_{0.7}Cu_{0.3}O_3$	-33.9	4.564	5.258	1.11
$La_{0.75}Ca_{0.25}Rh_{0.7}Cu_{0.3}O_3$	-44.5	3.742	7.424	1.15
$La_{0.75}Sr_{0.25}Rh_{0.7}Cu_{0.3}O_3$	-34.2	4.923	5.761	1.16
$La_{0.75}Pb_{0.25}Rh_{0.7}Cu_{0.3}O_3$	-6.9	8.575	0.422	0.70
$La_{0.75}Bi_{0.25}Rh_{0.7}Cu_{0.3}O_3$	-8.3	4.595	0.319	0.55
$LaRh_{0.5}Cu_{0.5}O_3$	-23.5	7.337	4.057	1.17
$La_{0.75}Pb_{0.25}Rh_{0.5}Cu_{0.5}O_3$	-24.4	3.550	2.108	0.83
$La_{0.75}Bi_{0.25}Rh_{0.5}Cu_{0.5}O_3$	-5.9	10.965	0.388	0.72

3.2.4 Electrical conductivity

Electrical conductivity measurements show that *A*-site doping by either divalent or trivalent metals lowers the conductivity, suggesting an increase in the band gap occurs as a result of the interaction between the valence shell of the *A*- site cations and the 3*d* and 4*d* orbitals of the *B*- site cations. This was evident from the electrical conductivity (σ) for $LaRh_{0.7}Cu_{0.3}O_3$ (17.24×10^3 S.m^{-1}) which is ~ 5 to 20 times higher than that estimated for the Ca, Sr, Pb and Bi doped oxides at 300 K (1.75, 3.08, 1.22 and 0.75×10^3 S.m^{-1}). Also σ_{300K} for $LaRh_{0.5}Cu_{0.5}O_3$ (4.35×10^3 S.m^{-1}) was much higher than for $La_{0.75}Pb_{0.25}Rh_{0.5}Cu_{0.5}O_3$ (0.59×10^3 S.m^{-1}) and $La_{0.75}Bi_{0.25}Rh_{0.5}Cu_{0.5}O_3$ (1.16×10^3 S.m^{-1}). The Arrhenius plot in Figure 3.11 gave activation energy for $LaRh_{0.5}Cu_{0.5}O_3$ of 0.049 eV that is in good agreement with reported values (0.055 eV) [12], the small difference can be attributed to the different heating regimes used to prepare the samples. It was found doping with Pb^{2+} and Bi^{3+} resulted in a small increase in the activation energy from 0.049 eV to 0.071 and 0.055 eV respectively. Likewise in $La_{0.75}A_{0.25}Rh_{0.7}Cu_{0.3}O_3$, the activation energy is slightly increased from 0.040 eV for $LaRh_{0.7}Cu_{0.3}O_3$ to 0.047 and 0.067 eV for the

Pb and Bi doped oxides, but decreased to 0.035 and 0.033 eV for the Ca and Sr doped oxides respectively. The last three values were negatively correlated with Δd. The activation energies of the oxides, in general, are in the range of (0.007 - 0.06 eV) for $La_{0.75}Sr_{0.25}RhO_3$ and $LaRhO_3$[33], suggesting the materials are *p*- type semiconductors. The increase in the activation energy of the oxides is consistent with the electronegativity of the *A*- site cations (increasing the covalency).

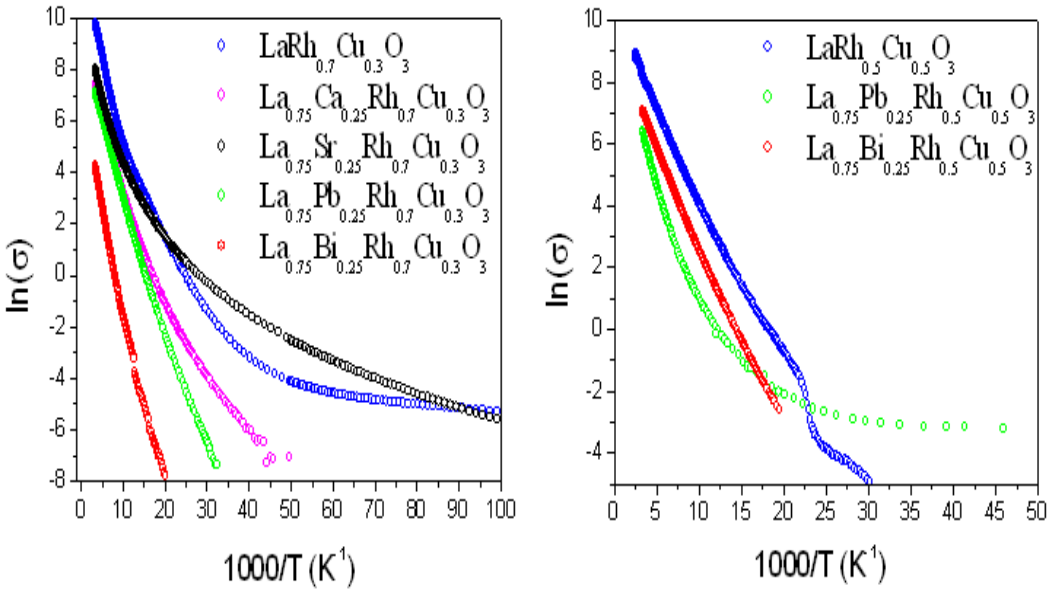

Figure 3.11 The Arrhenius plots of Ln (σ) verses inverse temperature for $La_{0.75}A_{0.25}Rh_{0.7}Cu_{0.3}O_3$ and $La_{0.75}A_{0.25}Rh_{0.5}Cu_{0.5}O_3$ series.

3.2.5 Summary

The impact of the *A*- site doping in $La_{0.75}A_{0.25}Rh_{0.7}Cu_{0.3}O_3$ and $La_{0.75}A_{0.25}Rh_{0.5}Cu_{0.5}O_3$ has been investigated. Differences in unit cell volumes, structural distortions and magnetization are attributed mainly to the effect of the charge delocalization between the Rh and Cu cations. The trivalent cation doped oxides display higher cell volumes and octahedral distortions but lower magnetic moments than the divalent cation oxides. In general, the observed changes in the unit cell volume and the octahedral distortion are consistent with the increase in ionic radii, whereas the decrease in magnetic moments is correlated with the increase in electronegativity. One exception is $La_{0.75}Bi_{0.25}Rh_{0.5}Cu_{0.5}O_3$ where the contraction in the unit cell volume is likely related to local ordering effects. The electron

configuration influences the spin coupling and the band gap. This is most evident in the Pb^{2+} and Bi^{3+} ($6s^2$) doped oxides which exhibited the lowest magnetic moments and the highest activation energies among the series. Magnetization measurements show the materials are weakly antiferromagnetic, whereas the electrical measurements demonstrate that doping with Ca, Sr, Pb and Bi cations decreases the conductivity of the oxides.

3.3 Results and discussion: $La_{1-x}A_xRh_{0.5}Cu_{0.5}O_3$

A balance between the Rh and Cu redox states was evident from the study of $LaRh_{0.5}Cu_{0.5}O_3$ [12]. Here we sought to further tune the properties by partially replacing the trivalent La^{3+} cation with divalent and trivalent cations to form oxides of the type $La_{1-x}A_xRh_{0.5}Cu_{0.5}O_3$. Initial synthetic attempts focussed on the alkaline earth cations Ca^{2+} and Sr^{2+}, however only small amounts of the divalent cations were incorporated and it was not possible to obtain single phase samples at $x > 0.1$. Subsequently we tested the possibility of partially substituting the La^{3+} with Pb^{2+} and Bi^{3+}, and single phase samples were apparently obtained for $0 \leq x \leq 0.3$.

3.3.1 Visual Inspection

All the prepared samples $La_{1-x}A_xRh_{0.5}Cu_{0.5}O_3$ were black coloured powders. SEM measurements (Figure 3.12) demonstrated the $La_{1-x}A_xRh_{0.5}Cu_{0.5}O_3$ samples. $La_{1-x}Bi_xRh_{0.5}Cu_{0.5}O_3$ showed more crystalline and smaller particles than $La_{1-x}Pb_xRh_{0.5}Cu_{0.5}O_3$ at $x = 0.1$ and 0.3. The shape of the particles and the grain boundary of the two oxides are homogeneous at $x = 0.2$. In general, the particle size of the oxides increases as x increased. In order to investigate the composition of the oxides, EDX measurements were performed. The measured mass ratios of Pb and Bi are consistent with the targeted compositions.

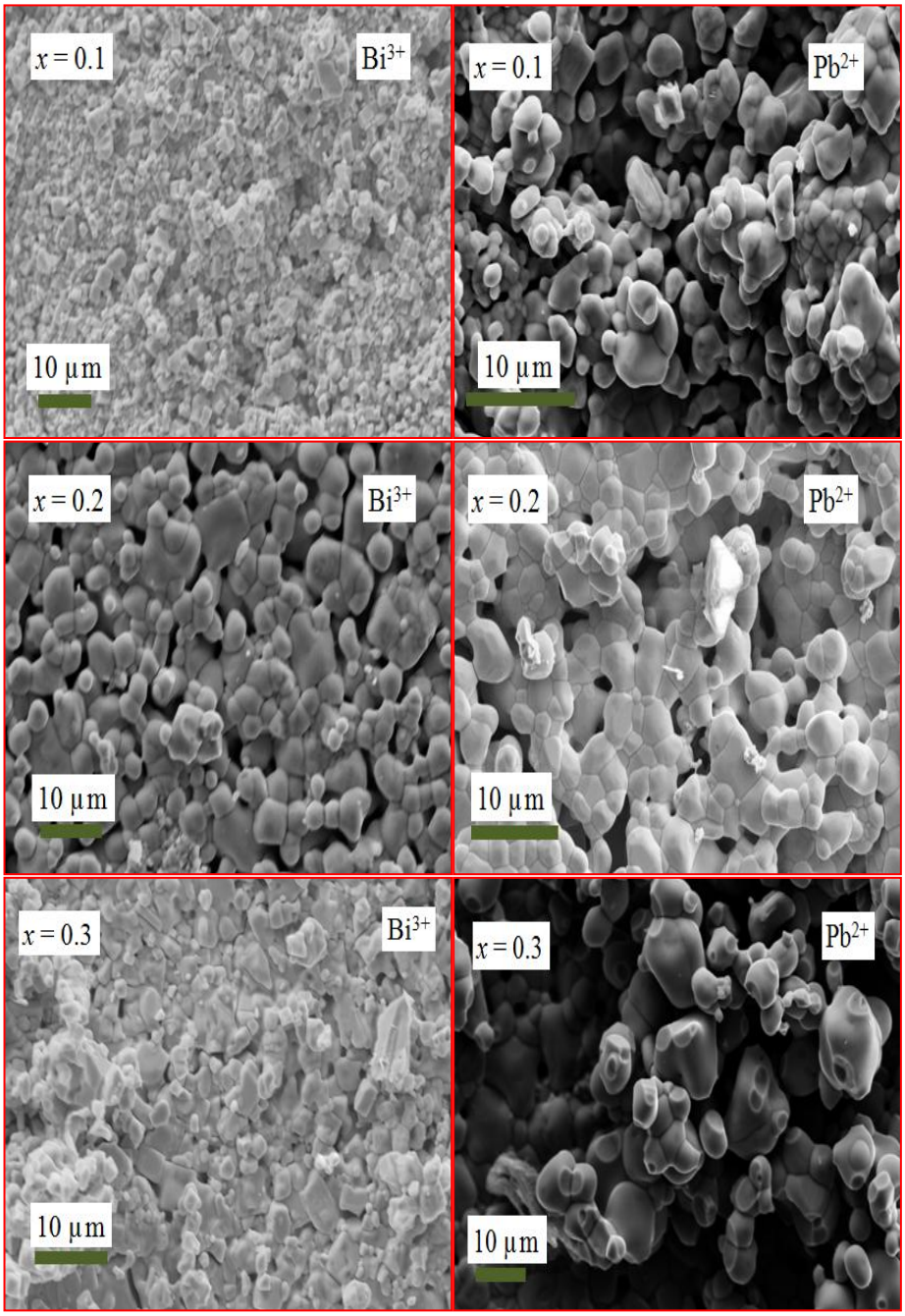

Figure 3.12 Scanning Electron Micrograph images for $La_{1-x}A_xRh_{0.5}Cu_{0.5}O_3$.

3.3.2 Crystal Structure

The structures for the various oxides were refined from S-XRD data. These data verified the samples to be highly crystalline and showed that the $La_{1-x}A_xRh_{0.5}Cu_{0.5}O_3$ oxides all have an orthorhombic, *Pbnm*, structure, there being no evidence for ordering of the Cu and Rh cations. Figure 3.13 illustrates the observed and calculated synchrotron X-ray diffraction profiles for $La_{1-x}A_xRh_{0.5}Cu_{0.5}O_3$.

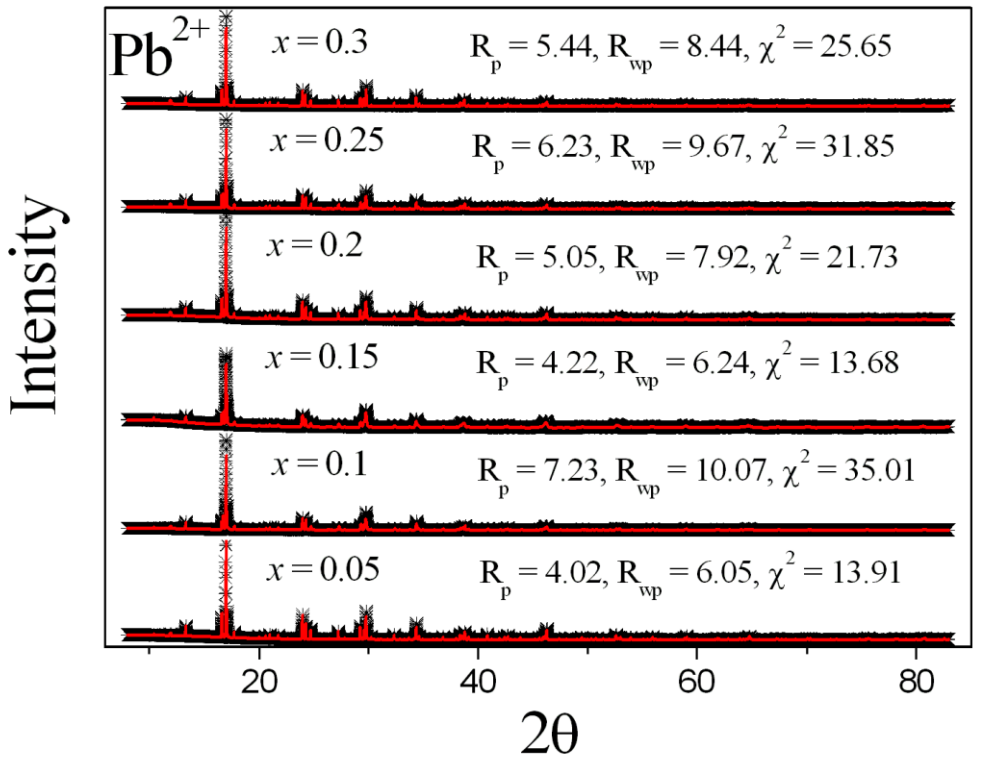

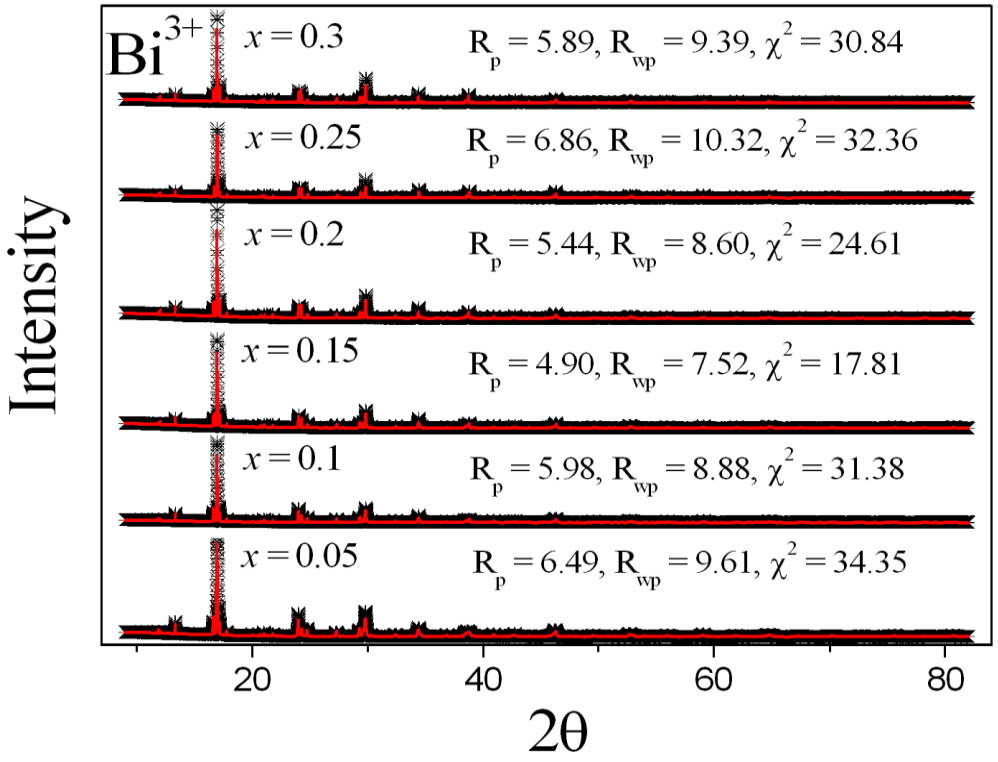

Figure 3.13 Observed and calculated synchrotron X-ray diffraction profiles for $La_{1-x}A_xRh_{0.5}Cu_{0.5}O_3$.

The composition dependence of the unit cell volumes estimated from the synchrotron diffraction data for the series $La_{1-x}A_xRh_{0.5}Cu_{0.5}O_3$ is illustrated in Figure 3.14. Doping with divalent metals such as Pb^{2+} is expected to result in partial oxidation of the Rh^{3+} (6 coordinate ionic radius, 0.67 Å) to Rh^{4+} (0.60 Å) [26] in order to maintain charge neutrality, which should reduce the cell volume. Despite such oxidation, the cell volume tends to increase upon doping with Pb as a consequence of the large ionic size of the Pb^{2+} cation (8 coordinate ionic radius, 1.29 Å) [26]. Doping with trivalent metals such as Bi is expected to have little impact on the charge delocalization in the system. Likewise since Bi^{3+} has a similar ionic size to La^{3+} (1.17 Å versus 1.16 Å) [26], it may be expected that the cell volume will be essentially independent of Bi content.

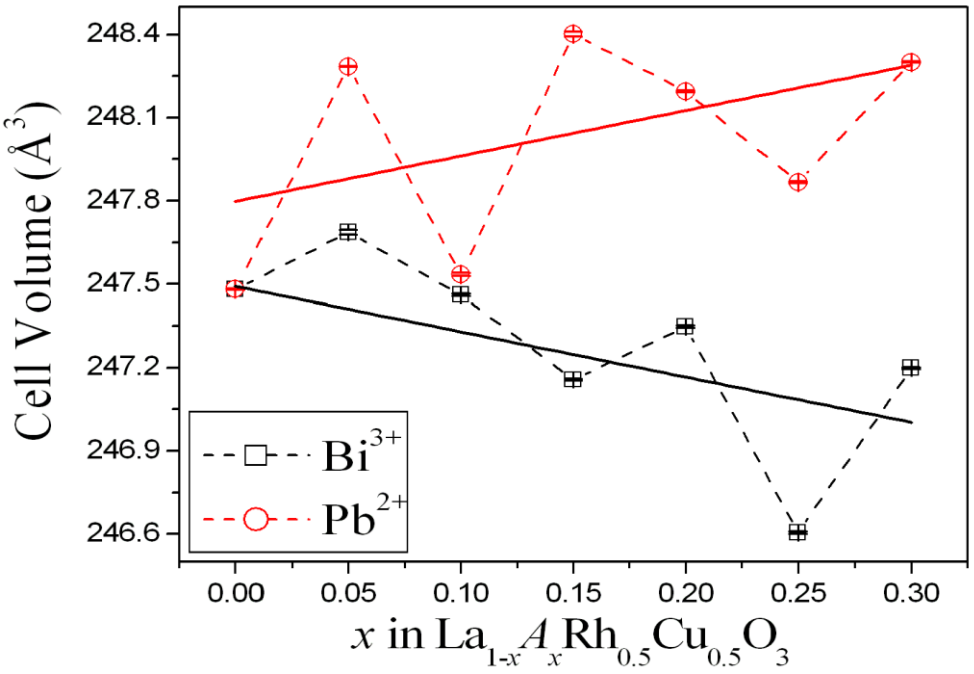

Figure 3.14 Composition dependence of the cell volume for $La_{1-x}A_xRh_{0.5}Cu_{0.5}O_3$ estimated by Rietveld refinement using synchrotron X-ray diffraction data, where not obvious the error bars are smaller than the symbols.

As evident from Figure 3.14, the cell volumes do not vary systemically upon doping. It was not possible to prepare single phase samples with Cu content greater than 0.5 and we believe part of the variation reflects the proximity to the Cu solubility limit at the *B*-site. In general physical properties of the oxides are more sensitive to the changes in compositions near the solubility limit possibly reflecting

local scale inhomogenities [39]. The fluctuations in the cell volumes may also reflect changes in the oxidation states of the constituent atoms and local ordering. Firstly, as noted above partial charge transfer involving oxidation of Cu^{2+} must be accompanied by reduction of Rh^{4+} to give a mixed valent $Rh^{3+/4+}$. The extent of this disorder may not vary linearly with composition as seen in other perovskite series, such as $Sr_{1-x}Ce_xMnO_3$[40] and $Ca_{1-x}Sr_xRu_{0.5}Mn_{05}O_3$ [41]. Secondly the observed structure reflects a balance between the long range Coulomb energy and the short range ionic repulsion in the lattice and this can be modified by local ordering of the *A* site cations resulting in a decrease in the average cell volume. Similar effects have been reported for $La_xSr_{1-3x/2}TiO_3$ [27] and $Pr_{0.5}Ba_{0.5}Mn_2O_6$ [28]. There is now an extensive literature demonstrating that ordering in mixed valence oxides occurs at specific ratios [42] and this may be significant for the Pb $x = 0.1$ and Bi $x = 0.25$ samples, where the largest deviations from Vegards Law are observed.

The effect of disorder in perovskites is well documented. Disorder of the *B*-type cations possibly reduces the entropic energy of the compounds increasing the stability and lowering the volumes. In the solid solutions (1-*x*) $Pb(Mg_{1/3}Nb_{2/3})O_3$ - (*x*) $Pb(Sc_{1/2}Nb_{1/2})O_3$ where $x \geq 0.1$, the random distribution of metal cations on the *B* sublattice introduces a significant entropic contribution to the free energy of the random-site structure producing large changes in bulk stability [43]. The thermal stability of the 1:1 ordered mixed-metal perovskite such as $Pb(Sc_{1/2}Nb_{1/2})O_3$ is derived from the valence difference and the difference in the average bond lengths of the *B* site cations [44]. The changes in the cell volumes could also be attributed to the high covalent character of the ions, with small displacements of the *A* site cations enhanced by the covalency. Both Pb^{2+} and Bi^{3+} are stereochemical active cations with high covalent character and $6s^2$ lone pair electrons [45, 46].

The structural refinements provide relatively accurate lattice parameters and atomic coordinates that describe the distortion of the unit cell *(D*) and BO_6 octahedra (Δd). The distortion parameters for the various oxides are summarised in Table 3.4. The lattice distortion in the Bi oxides generally decreases as the Bi content increases, whereas the octahedral distortion Δd appears independent of this. Conversely in the Pb doped oxides D appears to be relatively insensitive to increasing amounts of Pb, but this results in a small reduction in Δd. The octahedral distortion is noticeably smaller in the Pb doped oxides, as expected since these contain less JT active Cu^{3+}

cations. In all cases there is appreciable tilting of the corner sharing MO_6 octahedra as reflected in the *M*-O(1)-*M* and *M*-O(2)-*M* bond angles. These are similar to that seen in $LaRhO_3$ (150.5 and 149.1°) [47].

Table 3.4 Lattice parameter distortion D, octahedral distortion Δd , bond angles *M*-O(1)-*M* and *M*-O(2)-*M* for $La_{1-x}A_xRh_{0.5}Cu_{0.5}O_3$.

X	$La_{1-x}Bi_xRh_{0.5}Cu_{0.5}O_3$				$La_{1-x}Pb_xRh_{0.5}Cu_{0.5}O_3$			
	D (%)	$\Delta d\times10^{-4}$	*M(O1)M º*	*M(O2)M º*	*D (%)*	$\Delta d\times10^{-4}$	*M(O1)M º*	*M(O2)M º*
0.0	1.15	2.24	148.1(4) º	152.5(3) º	1.15	2.24	148.1(4) º	152.5(3) º
0.05	1.10	8.62	137.5(9) º	152.5(4) º	1.17	2.74	150.5(3) º	151.6(3) º
0.10	1.11	4.94	146.0(5) º	152.4(4) º	1.02	5.21	147.8(5) º	155.2(4) º
0.15	1.05	7.14	146.0(5) º	152.6(4) º	1.02	1.46	149.3(5) º	150.6(4) º
0.20	1.00	5.57	146.2(6) º	151.4(4) º	1.16	1.18	148.0(4) º	151.9(4) º
0.25	0.91	8.87	151.2(9) º	154.7(4) º	1.15	1.39	151.3(3) º	150.6(12) º
0.30	1.06	10.98	149.6(6) º	151.8(4) º	1.13	5.10	151.1(4) º	151.3(4) º

In the above discussion, it was postulated that the Cu and Rh are mixed valent as a consequence of electron transfer between these. To confirm this, XANES data at the Rh L-edge were collected for the $La_{1-x}Pb_xCu_{0.5}Rh_{0.5}O_3$ series. It is thought that the addition of Pb^{2+} will have a greater effect on oxidation states than doping with Bi^{3+}. The normalized Rh L_3 XANES spectrum for members in the series $La_{1-x}Pb_xCu_{0.5}Rh_{0.5}O_3$, and Rh^{3+}, $LaRhO_3$, and Rh^{4+}, Sr_2RhO_4, standards are presented in Figure 3.15. The Rh L-edge absorption spectra originates from dipole allowed transitions of the Rh 2*p* core electrons into the unoccupied Rh 4*d* states in the conduction band, which consist of the t_{2g} and e_g orbitals in octahedral symmetry. The splitting of the L-edge into L_3 and L_2 peaks is a consequence of spin-orbit coupling. The Rh L_2-edge spectra were also examined, and these show similar features to those of the L_3-edge. The normalized L_3-edge spectra of the Rh^{3+} ($4d^6$) standard $LaRhO_3$, the Rh^{4+} ($4d^5$) oxide Sr_2RhO_4 and the various Pb doped oxides all display sharp peaks near 3005.0 eV. The first derivative of these shows that the peaks are actually doublets due to transitions into the t_{2g} and e_g states. The spectra of $LaRhO_3$ contains a single peak since the t_{2g} orbitals are filled so that only transitions from the $2p_{3/2}$ core levels to the e_g states are possible [48].

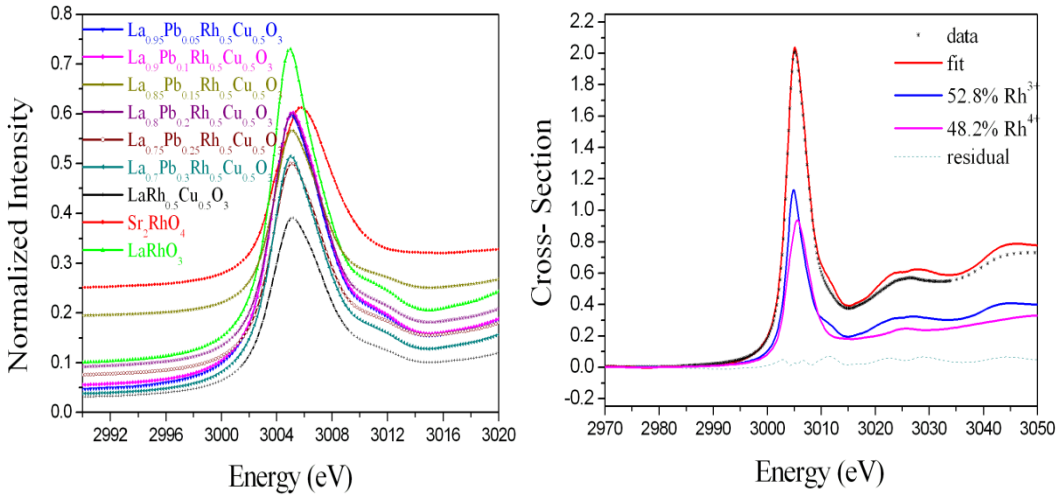

Figure 3.15 Normalised Rh L_3-edge XANES spectra for members in the series $La_{1x}Pb_xCu_{0.5}Rh_{0.5}O_3$, Rh^{3+} ($LaRhO_3$) and Rh^{4+} (Sr_2RhO_4) standards. The corresponding fit for $LaCu_{0.5}Rh_{0.5}O_3$ and the individual components Rh^{3+} and Rh^{4+} are presented on the right hand side. The data have been offset vertically for clarity.

The L_3-edge XANES spectra of the various $La_{1-x}Pb_xRh_{0.5}Cu_{0.5}O_3$ samples were fitted with a linear combination of the two standards ($LaRhO_3$ and Sr_2RhO_4) over the energy range of 2970- 3050 eV. The quantitative analysis was performed using a least-squares refinement program (Athena) within the IFEFFIT software package [49, 50]. The Rh L_3- edge XANES spectrum of $LaRh_{0.5}Cu_{0.5}O_3$ is very similar to that found previously [12], and is indicative of charge delocalization between the Cu and Rh cations. The Rh has average valence around 3.5 with the fitting giving 52.8 % Rh^{3+} and 48.2 % Rh^{4+}. This suggests partial charge transfer involving Rh^{4+} to Rh^{3+} and Cu^{2+} has occurred. Unexpectedly, and as illustrated in the Table 3.5, increasing the amount of Pb present in $La_{1-x}Pb_xRh_{0.5}Cu_{0.5}O_3$ reduces the average Rh oxidation states. This requires either formation of oxygen vacancies or more facile oxidation of the Cu^{2+} ions in order to maintain the overall charge balance. It is not believed that oxidation of the Pb^{2+} at the *A*-type sites will occur. Since the neutron diffraction measurements of the x = 0.25 sample provided no evidence for oxygen vacancies (Section 3.2.2), partial oxidation of the Cu^{2+} is the most likely mechanism of charge balance. That more Cu^{3+} is present in the Pb rich oxides accounts for the reduction in the octahedral distortion and the general trends in cell volume. Note that the effective oxidation state does not vary linearly with composition, and this is expected to impact on the cell volumes.

Table 3.5 The Rh^{3+}, Rh^{4+} and the average Rh oxidation states (Q_{av}) in $La_{1-x}Pb_xRh_{0.5}Cu_{0.5}O_3$. The activation energies (eV) calculated from Arrhenius plot for both Pb and Bi doped oxides are also given.

X	0.00	0.05	0.10	0.15	0.20	0.25	0.30
% Rh^{3+}	52.80	58.95	55.4	59.90	57.02	56.83	60.93
% Rh^{4+}	48.20	41.05	45.6	40.10	42.98	43.17	39.07
Q_{av}	3.51	3.41	3.48	3.40	3.36	3.37	3.06
E_{Pb} (eV)	0.049	0.040	0.043	0.055	0.040	0.066	0.040
E_{Bi} (eV)	0.049	0.054	0.053	0.046	0.063	0.054	0.051

3.3.3 Magnetization

The magnetization curves of the two series $La_{1-x}Bi_xCu_{0.5}Rh_{0.5}O_3$ and $La_{1-x}Pb_xCu_{0.5}Rh_{0.5}O_3$ are shown in Figure 3.16. The magnetic susceptibilities do not show a defined maximum, and the inverse susceptibilities of all the oxides display Curie–Weiss type behaviour without anomalies. This suggests that no long range magnetic ordering occurs. Below 100 K there is a slight deviation from Curie-Weiss behavior as a result of crystal-field effects [51], and only data above this temperature was used in the Curie-Weiss fitting.

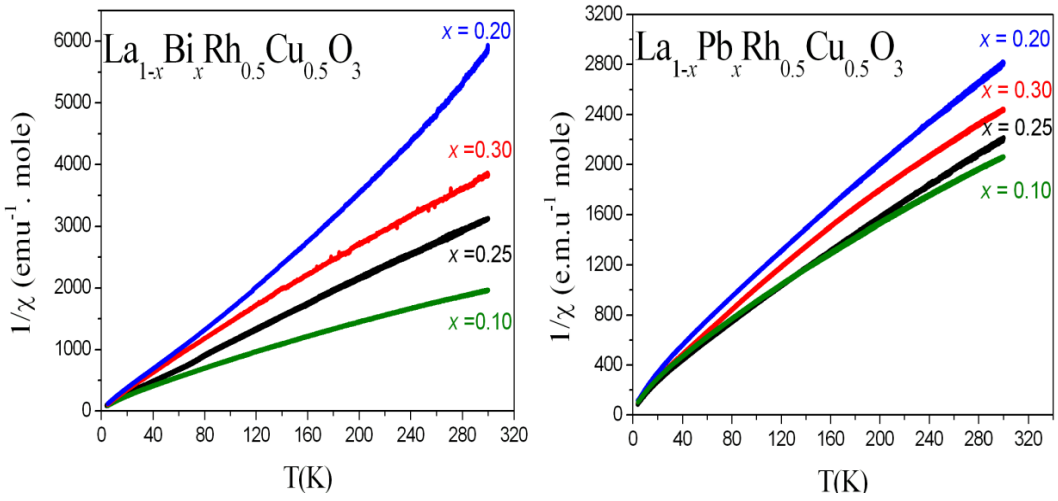

Figure 3.16 The temperature dependence of the inverse susceptibility for $La_{1-x}Bi_xCu_{0.5}Rh_{0.5}O_3$ and $La_{1-x}Pb_xCu_{0.5}Rh_{0.5}O_3$ recorded under zero field cooling conditions with an applied field of 5 kOe at temperatures between 5 and 300 K.

The magnetic susceptibilities of $La_{1-x}Bi_xCu_{0.5}Rh_{0.5}O_3$ and $La_{1-x}Pb_xCu_{0.5}Rh_{0.5}O_3$ are sensitive to doping. For the two series, the magnetic susceptibilities (χ) have the lowest value at x = 0.2 and have the highest value at x = 0.1. The magnetic susceptibilities for $La_{1-x}Pb_xCu_{0.5}Rh_{0.5}O_3$ are approximately two times higher than those for $La_{1-x}Bi_xCu_{0.5}Rh_{0.5}O_3$, indicating that doping with Pb^{2+} influences the electron configuration of the transition metals presumably via oxidation of Cu^{2+}. The best linear fits to the inverse magnetization curves showed that the effective magnetic moments (μ_{eff}) for both the Bi and Pb doped oxides are negatively correlated with Weiss constants (Θ). That means Bi and Pb substitutions enhances antiferromagnetic coupling.

Table 3.6 Curie constant C (emu. mole$^-$), Weiss constants Θ (K), magnetic susceptibly coefficient factor χ_o (10^{-3} emu. mole$^-$) and effective magnetic moment μ_{eff} (μ_B) for $La_{1-x}A_xCu_{0.5}Rh_{0.5}O_3$.

x	$La_{1-x}Bi_xRh_{0.5}Cu_{0.5}O_3$				$La_{1-x}Pb_xRh_{0.5}Cu_{0.5}O_3$			
	Θ	χ_o	C	μ_{eff}	Θ	χ_o	C	μ_{eff}
0.0	-23.5	7.337	4.057	1.17	-23.5	7.337	4.057	1.17
0.1	-29.8	5.433	4.820	1.13	-42.5	4.177	6.716	1.12
0.2	9.6	-5.378	-0.494	0.64	-25.8	4.409	2.943	0.95
0.25	-6.0	10.965	0.388	0.72	-24.4	3.550	2.108	0.83
0.3	-5.2	14.626	0.398	0.78	-27.6	4.693	3.576	1.02

As summarized in Table 3.6, the effective magnetic moments for the $La_{0.9}Pb_{0.1}Rh_{0.5}Cu_{0.5}O_3$ (1.12 μ_B) and $La_{0.9}Bi_{0.1}Rh_{0.5}Cu_{0.5}O_3$ (1.13 μ_B) are similar to that for $LaRh_{0.5}Cu_{0.5}O_3$ (1.17 μ_B), indicating that doping by Pb or Bi at x = 0.1, has no obvious impact on the electron configuration of the transition metals. This is consistent with the near constant average Rh oxidation state seen in the XANES studies. When $x > 0.1$, the oxides show magnetic moments approximately 50 % lower than $LaRh_{0.5}Cu_{0.5}O_3$, suggesting spin coupling may occur as a consequence of the $6s^2$ lone pair electrons. With the exception $La_{0.8}Bi_{0.2}Rh_{0.5}Cu_{0.5}O_3$ where Θ = + 9.6 K, the Weiss constant exhibited negative values, lower than seen in the weak paramagnetic oxide $LaRhO_3$ (-2.74 K, 0.295 μ_B) [37], indicating the materials are weakly antiferromagnetic [38].

3.3.4 Electrical conductivity

Electrical conductivity measurements show that *A*- site doping, by either divalent or trivalent metals, lowers the conductivity. This indicates that there is an increase in the band gap presumably as a result of the interaction between the valence shell of the *A* site cations and the 3*d* and 4*d* orbitals of the *B* site cations. The electrical conductivity for $LaRh_{0.5}Cu_{0.5}O_3$ ($\sigma = 4.35 \times 10^3$ $S.m^{-1}$) is ~5 to 10 times higher than that estimated for the Pb and Bi doped oxides at 300K. The activation energy for $LaRh_{0.5}Cu_{0.5}O_3$, estimated from the Arrhenius plot in Figure 3.17, is 0.049 eV. Doping with Bi^{3+} generally results in a small increase in the activation energy whereas the Pb doping decreases this. There is, however, considerable scatter in the data (see Table 3.5) presumably reflecting grain boundary effects and other sample inhomogeneities. These variations preclude more detailed discussion of these results.

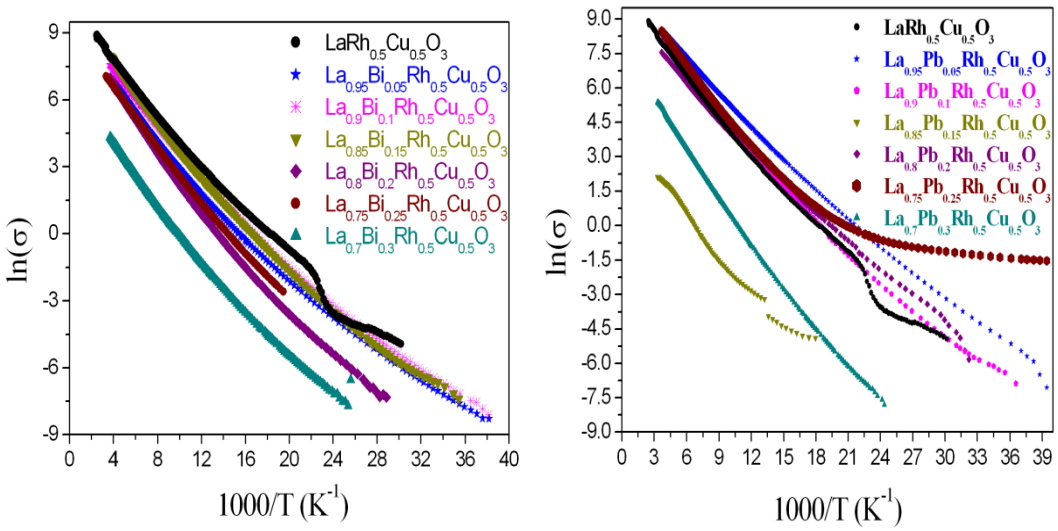

Figure 3.17 The Arrhenius plots of ln (σ) verses inverse temperature for $La_{1-x}Bi_xRh_{0.5}Cu_{0.5}O_3$ and $La_{1-x}Pb_xRh_{0.5}Cu_{0.5}O_3$ series.

3.3.5 Summary

Doping at the *A* site in the mixed metal perovskites $La_{1-x}A_xRh_{0.5}Cu_{0.5}O_3$ (*A* = Pb^{2+}, Bi^{3+} influences the magnetic and electronic properties of these compounds. Diffraction measurements show no evidence for either cation ordering or the formation of anion vacancies. Nevertheless, changing the *A*-site composition resulted in anomalous changes in the cell volumes, octahedral distortions, electrical resistivity and magnetic susceptibility of these complex perovskites. Rh L_3 XANES

measurements suggest this is a consequence of charge delocalisation between the Rh and Cu cations. Short-range local ordering effects are also believed to be important. The majority of the samples are non-metallic and display, very weak, antiferromagnetic coupling.

3.4 References

[1] J. B. Philipp, P. Majewski, L. Alff, A. Erb, R. Gross, T. Graf, M. S. Brandt, J. Simon, T. Walther, W. Mader, D. Topwal and D. D. Sarma, *Physical Review B*, 68 (2003) 144431.

[2] M. García-Hernández, J. L. Martínez, M. J. Martínez-Lope, M. T. Casais and J. A. Alonso, *Physical Review Letters*, 86 (2001) 2443-2446.

[3] R. S. Liu, T. S. Chan, S. Mylswamy, G. Y. Guo, J. M. Chen and J. P. Attfield, *Current Applied Physics*, 8 (2008) 110-113.

[4] R. K. Kotnala, V. Pandey, M. Arora, V. Verma, R. P. Aloysius, A. Malik and G. L. Bhalla, *Solid State Communications*, 151 (2011) 415-419.

[5] K. Hirofumi, N. Asumi, Y. Makoto, B. Hiroshi and N. Yoshikazu, *Journal of Physics: Conference Series*, 200 (2010) 032033.

[6] H. Kawanaka, M. Yokoyama, A. Noguchi, H. Bando and Y. Nishihara, *Journal of Physics: Condensed Matter*, 21 (2009) 296002.

[7] A. Chuchmala, R. J. Wiglusz, B. Macalik, P. Gluchowski, B. Mazurek and W. Strek, *Journal of Rare Earths*, 27 (2009) 646-650.

[8] M. Markina, K. Zakharov, A. Vasil'ev, I. Balasz, I. Deac and E. Burzo, *Bulletin of the Russian Academy of Sciences: Physics*, 75 (2011) 190-192.

[9] Y. Q. Lin, Y. J. Wu, S. P. Gu and X. M. Chen, *Ferroelectrics*, 388 (2009) 133-139.

[10] E. Burzo, I. Balasz, M. Isobe and Y. Ueda, *Journal of Alloys and Compounds*, 535 (2012) 129-137.

[11] T. Ogawa, A. Sandhu, M. Chiba, H. Takeuchi and Y. Koizumi, *Journal of Magnetism and Magnetic Materials*, 290–291 (2005) 933-936.

[12] J. Ting, B. J. Kennedy, Z. Zhang, M. Avdeev, B. Johannessen and L. Y. Jang, *Chemistry of Materials*, 22 (2010) 1640-1646.

[13] R. B. Macquart, M. D. Smith and H. C. zur Loye, *Crystal Growth & Design*, 6 (2006) 1361-1365.

[14] T. He, J. Chen, T. G. Calvarese and M. A. Subramanian, *Solid State Sciences*, 37 (2006) 467-469.

[15] S. Takagi, A. Subedi, V. R. Cooper and D. J. Singh, *Physical Review B*, 82 (2010) 134108.

[16] K. D. Liss, B. Hunter, M. Hagen, T. Noakes and S. Kennedy, *Physica B-Condensed Matter*, 385-86 (2006) 1010-1012.

[17] K. S. Wallwork, B. J. Kennedy and D. Wang, *AIP Conference Proceedings*, 879 (2007) 879-882.

[18] B. A. Hunter and C. J. Howard, RIETICA. A Computer Program for Rietveld Analysis of X-Ray and Neutron Powder Diffraction Patterns, 1998, Lucas Heights Research Laboratories Sydney.

[19] T. E. Dann, S. C. Chung, L. J. Huang, J. M. Juang, C. I. Chen and K. L. Tsang, *Journal of Synchrotron Radiation*, 5 (1998) 664-666.

[20] A. Wold, R. J. Arnott and W. J. Croft, *Inorganic Chemistry*, 2 (1963) 972-974.

[21] I. D. Brown and D. Altermatt, *Acta Crystallographica Section B*, 41 (1985) 244-247.

[22] B. J. Kennedy, K. Yamaura and E. Takayama-Muromachi, *Journal of Physics and Chemistry of Solids*, 65 (2004) 1065-1069.

[23] D. L. Corker, A. M. Glazer, W. Kaminsky, R. W. Whatmore, J. Dec and K. Roleder, *Acta Crystallographica Section B*, 54 (1998) 18-28.

[24] B. J. Kennedy, C. J. Howard and B. C. Chakoumakos, *Journal of Physics: Condensed Matter*, 11 (1999) 1479.

[25] B. J. Kennedy, P. J. Saines, Q. Zhou, Z. Zhang, M. Matsuda and M. Miyake, *Journal of Solid State Chemistry*, 181 (2008) 2639-2645.

[26] R. D. Shannon, *Acta Crystallographica Section A*, 32 (1976) 751-767.

[27] B. S. Thomas, N. A. Marks and P. Harrowell, *Physical Review B*, 74 (2006) 214109.

[28] S. Trukhanov, *Journal of Experimental and Theoretical Physics*, 101 (2005) 513-520.

[29] M. W. Lufaso and P. M. Woodward, *Acta Crystallographica Section B*, 60 (2004) 10-20.

[30] M. A. Carpenter and C. J. Howard, *Acta Crystallographica Section B*, 65 (2009) 134-146.

[31] I. Álvarez-Serrano, G. J. Cuello, M. L. López, A. Jiménez-López, C. Pico, E. Rodríguez-Castellón, E. Rodríguez and M. L. Veiga, *Journal of Physics D: Applied Physics*, 41 (2008) 195001.

[32] N. C. Yeh, C. C. Fu, J. Y. T. Wei, R. P. Vasquez, J. Huynh, S. M. Maurer, G. Beach and D. A. Beam, *Journal of Applied Physics*, 81 (1997) 5499-5501.

[33] T. A. Mary and U. V. Varadaraju, *Journal of Solid State Chemistry*, 110 (1994) 176-179.

[34] I. I. Mazin and D. J. Singh, *Physical Review B*, 56 (1997) 2556-2571.

[35] A. Villesuzanne, M. H. Whangbo, M. A. Subramanian and S. F. Matar, *Chemistry of Materials*, 17 (2005) 4350-4355.

[36] A. L. Allred, *Journal of Inorganic and Nuclear Chemistry*, 17 (1961) 215-221.

[37] T. Taniguchia, W. Iizukaa, Y. Nagataa, T. Uchidab and H. Samatac, *Journal of Alloys and Compounds*, 350 (2003) 24-29.

[38] T. Ohnishia, T. Taniguchia, A. Ikoshia, S. Mizusakia, Y. Nagataa, S. H. Lai, M. D. Lanb, Y. Noroc, T. C. Ozawad, K. Kindoe, A. Matsuoe and S. Takayanagif, *Journal of Alloys and Compounds*, 506 (2010) 27-32.

[39] S. Malo and A. Maignan, *Materials Research Bulletin*, 47 (2012) 974-979.

[40] Z. Zhang, B. J. Kennedy, C. J. Howard, L.-Y. Jang, K. S. Knight, M. Matsuda and M. Miyake, *Journal of Physics: Condensed Matter*, 22 (2010) 445401.

[41] R. A. Ricciardo, H. L. Cuthbert, P. M. Woodward, Q. Zhou, B. J. Kennedy, Z. Zhang, M. Avdeev and L.-Y. Jang, *Chemistry of Materials*, 22 (2010) 3369-3382.

[42] C. N. R. Rao and A. K. Cheetham, *Advanced Materials*, 9 (1997) 1009-1017.

[43] L. Farber, M. Valant, M. A. Akbas and P. K. Davies, *Journal of the American Ceramic Society*, 85 (2002) 2319-2324.

[44] C. G. F. Stenger and A. J. Burggraaf, *Physica Status Solidi (a)*, 61 (1980) 275-285.

[45] T. He, J. Chen, T. G. Calvarese and M. A. Subramanian, *Solid State Sciences*, 8 (2006) 467-469.

[46] S. Takagi, A. Subedi, D. J. Singh and V. R. Cooper, *Physical Review B*, 81 (2010) 134106.

[47] R. B. Macquart, M. D. Smith and H.-C. Zur Loye, *Crystal Growth & Design*, 6 (2006) 1361-1365.

[48] T. Burnus, Z. Hu, H. Wu, J. C. Cezar, S. Niitaka, H. Takagi, C. F. Chang, N. B. Brookes, H. J. Lin, L. Y. Jang, A. Tanaka, K. S. Liang, C. T. Chen and L. H. Tjeng, *Physical Review B*, 77 (2008) 205111.

[49] IFEFFIT: Interactive XAFS Analysis, http://cars.uchicago.edu, 2012.

[50] M. Newville, *Journal of Synchrotron Radiation*, 8 (2001) 322-324.

[51] C. Cascales, R. Sáez-Puche and P. Porcher, *Journal of Solid State Chemistry*, 114 (1995) 52-56.

Structural, Electrical and Magnetic Studies of the *B* Site Doped Oxides $LaRh_{1-2x}Cu_xB_xO_3$ (*B* = Sc^{3+}, Cu^{2+} and Zn^{2+})

4.1 Introduction

The *3d-4d* mixed metal perovskites of composition $LaRh_{1-x}B_xO_3$ have recently received great attention owing to the coexistence of ferromagnetic, thermoelectric and semiconducting properties [1,2]. The study of *B* site doping has been of interest, since the number of *d*-electrons is critical in determining the electronic and magnetic properties of these oxides [3,4]. For instance, the polycrystalline compounds $LaMn_{1-x}Rh_xO_3$ are ferromagnetic in the region $0.1 \leq x \leq 0.9$, but the substitution of Rh^{3+} ($4d^6$) for Mn^{3+} ($3d^4$) suppresses the ferromagnetism, which consequently reduces the Curie temperature [5]. The solid solutions $LaRh_{1-x}Co_xO_3$ and $LaRh_{1-x}Ni_xO_3$ exhibit high Seebeck coefficients and low electrical resistivity indicating the materials are thermoelectric [6,7]. This thermoelectric behavior is mainly attributed to the high-temperature stability of the low-spin state of the Rh^{3+}/Rh^{4+} ions [6,8]. In the rare earth oxide $LaRh_{0.5}Cu_{0.5}O_3$ (the targeted material of the study), there is extensive electron delocalization between the Rh and Cu. This delocalisation increases the formal valency of the Cu to close to 2.5, which reduces the impact of the Jahn-Teller distortion [9,10].

4.1.1 Aims and Objectives

Since a balance between the Rh and Cu redox states was evident in the study of $LaRh_{0.5}Cu_{0.5}O_3$ [9] and the work described in Chapter 3, we sought to further tune the properties of this oxide by replacing the ($4s^0 3d^9$) Cu^{2+} cations with ($4s^0\ 3d^0$) Sc^{3+} and ($4s^0 3d^{10}$) Zn^{2+} cations in the two series; $LaRh_{1-2x}Cu_xSc_xO_3$ and $LaRh_{1-2x}Cu_xZn_xO_3$. Both the effective charges of the Sc^{3+} and Zn^{2+} ions and the strong overlap of the unfilled and filled 3*d* orbitals with the sp^2 oxygen orbitals [11] are expected to impact on the formal valency of Rh ions leading to changes in the magnetic and electronic properties of the perovskites. Sc^{3+} and Zn^{2+} are both diamagnetic and have ionic sizes similar to that of Cu^{2+} [12]. The oxides compositions are limited to $0 \leq x \leq 0.25$ due to the solubility limit of Cu. It was not possible to prepare single phase samples with $x > 0.25$. The change in the formal oxidation

states of Rh and Cu can effectively be controlled by doping Sc^{3+} and Zn^{2+} into the structure.

This chapter also examines the effects of the *B*-site doping on the structural, electrical and magnetic properties of $LaRh_{1-2x}Cu_xB_xO_3$ and $La_{0.75}A_{0.25}Rh_{1-2x}Cu_xB_xO_3$ where B = Sc^{3+}, Cu^{2+} and Zn^{2+}; A = Pb^{2+} and Bi^{3+}. The series were targeted due to the lack of research on Rh-Cu perovskites. One of the aims was to understand the factors influence electron transfer in the system.

4.1.2 Methodology

The samples were prepared from stoichiometric mixtures of La_2O_3 (Aldrich ≥ 99.9%), Sc_2O_3, Bi_2O_3, PbO (Aldrich ≥ 99.99%), CuO, ZnO (Merck, ≥ 99%), and Rh (Althaca 99.95%). Except for the $LaRh_{1-x}Cu_xO_3$ series, which were prepared in an atmosphere of pure oxygen, all samples were synthesized in the air by conventional solid state methods. The preparation began with mixing and grinding the raw materials, and then heating these in several steps, before every step the materials were reground. The materials were heated at 800 $^{\circ}$C for 12 h followed by 950 $^{\circ}$C for 24 h, 1000 $^{\circ}$C for 48 h, 1050 $^{\circ}$C for 48 h, and 1100 $^{\circ}$C for 48 h. In some cases, the temperature was increased at 1250 $^{\circ}$C to obtain a pure structure. Neutron powder diffraction data were measured at 4 and 293 K using the high resolution powder diffractometer, Echidna [13], at the OPAL facility (Australian Nuclear Science and Technology Organization) at a wavelength of 2.4395 Å. For these measurements the sample was contained in a cylindrical vanadium can. Synchrotron X-ray powder diffraction data were collected over the angular range $5 < 2\theta < 85°$, using X-rays of wavelength 0.82554 Å on the powder diffractometer at the Australian Synchrotron [14]. For these measurements the sample was housed in a 0.3 mm diameter capillary. The structures were refined using the program RIETICA [15]. The peak shapes were modelled using a pseudo Voigt function.

The magnetic measurements were carried out using a Quantum Design, PPMS. The temperature dependence of the magnetic susceptibilities was measured under both zero-field cooled (ZFC) and field cooled (FC) conditions in an applied field of 5 kOe over the temperature range 4-300 K. The temperature dependence of the resistivity was measured using a DC four probe technique with the same measurement system. The sintered samples were cut into pieces of approximately 3x5 mm. Four contacts were painted onto the samples using silver paste. The

microstructure of the powder samples was examined by scanning electron microscopy (SEM) using a Intellection Quemscan**.**

Rh $L_{3,2}$- edge X-ray absorption spectra were recorded, from powder samples dispersed on Kapton tape, in fluorescence mode on beam line BL-16A1 at the National Synchrotron Radiation Research Centre (NSRRC) in Hsinchu, Taiwan using a Lytle detector [16]. Energy steps as small as 0.2 eV were employed near the absorption edges with a counting time of 2 s per step. The spectra were normalized to the incident photon current. The energy scale of the Rh $L_{3,2}$- edge spectra was calibrated using the L_2- edge of a Mo foil. $LaRhO_3$ and Sr_2RhO_4 were used as the Rh^{3+} and Rh^{4+} standards respectively.

4.2 Results and discussion: $LaRh_{1-2x}Cu_xB_xO_3$

New members of $LaRh_{1-2x}Cu_xSc_xO_3$, $LaRh_{1-2x}Cu_{2x}O_3$ and $LaRh_{1-2x}Cu_xZn_xO_3$ ($0 \geq x \leq 0.25$) series were successfully prepared, and their crystallographic, magnetic, and electric properties investigated.

4.2.1 Visual Inspection.

The heating regime described above produced crystalline, black coloured, samples. After heating to 950 $^{\circ}$C, the colour of samples turns from wine to black for the Sc doped oxides, and from brown to black for the Cu doped oxides whereas in Zn doped oxides, the colour changes from gray to black. This suggests that the three oxides compositions have taken different initial steps in the reaction leading to a variation in oxidation states of the *d* metal ions. The appearance of black colour as the temperature increases is an indication of completion of the reaction.

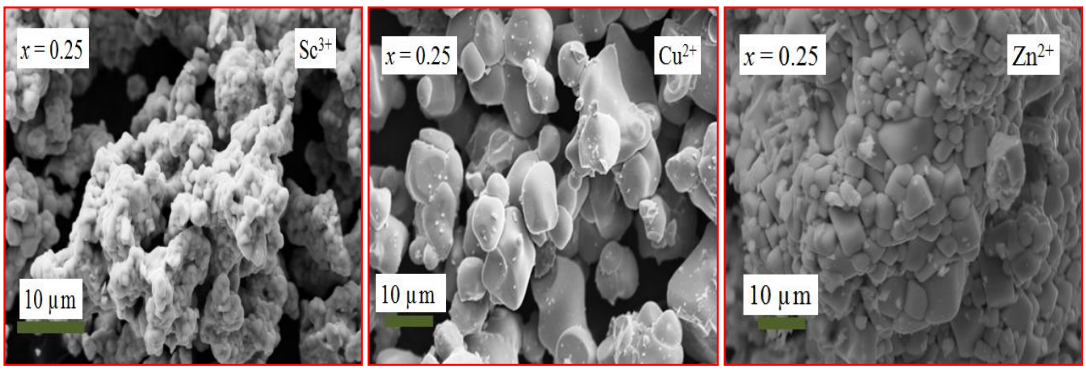

Figure 4.1 Scanning Electron Micrograph images for $LaRh_{0.5}Cu_{0.25}Sc_{0.25}O_3$, $LaRh_{0.5}Cu_{0.5}O_3$ and $LaRh_{0.5}Cu_{0.25}Zn_{0.25}O_3$.

SEM measurements (Figure 4.1) demonstrated the samples to be well sintered and free of any obvious impurities. The differences in the particles size and their shape are consistent with differences in compositions. Doping with Sc^{3+} results in well sintered rectangular shaped samples with small particle size whereas doping with Cu or Zn forms well crystalline samples with large particles. The Zn doped samples are more crystalline than the corresponding Cu doped oxides. Increasing *x* leads to no obvious change in the shape of the particles, but results in larger grain boundaries. Figure 4.2 exhibits the increase in particle size as *x* increases. EDX measurements showed the determined mass ratios of Sc and Zn with Cu are consistent with the targeted compositions.

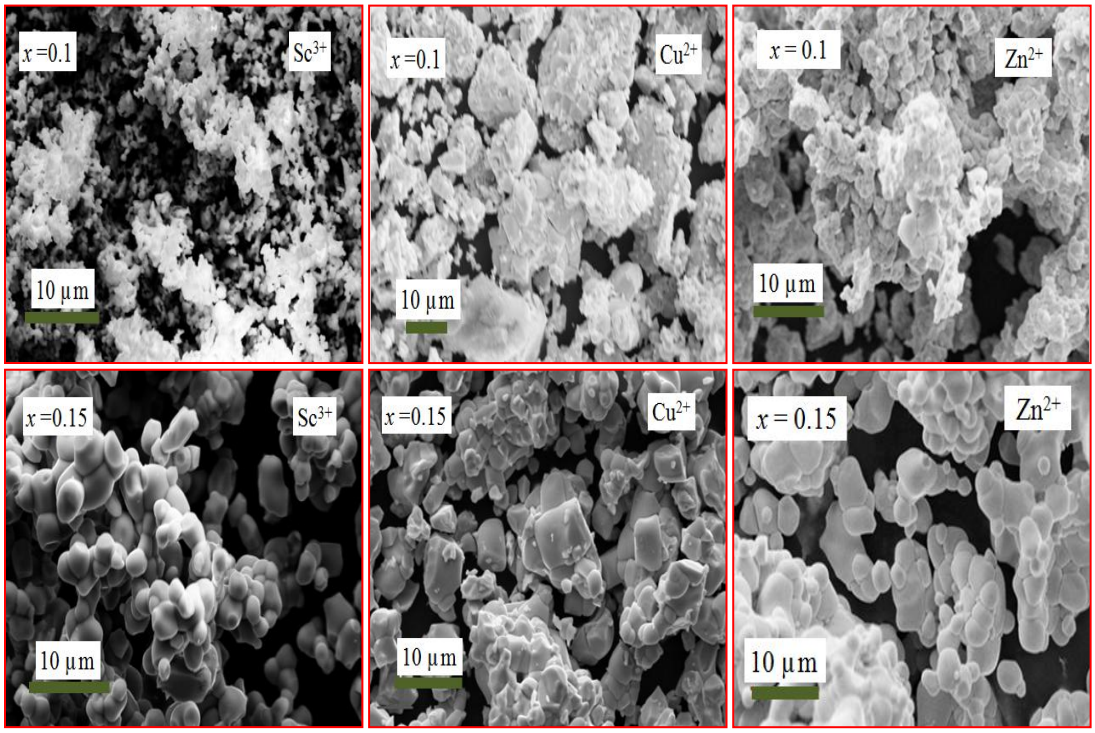

Figure 4.2 Scanning Electron Micrograph images for $LaRh_{1-2x}Cu_xSc_xO_3$, $LaRh_{1-2x}Cu_{2x}O_3$ and $LaRh_{1-2x}Cu_xZn_xO_3$ where x = 0.1 and 0.15.

4.2.2 Crystal Structure

Diffraction measurements illustrate that the $LaRh_{1-2x}Cu_xB_xO_3$ compounds are orthorhombic with space group *Pbnm*. In this structure, the Rh and Cu ions are at (0, 0, 0). The maximum value of *x* which allows a pure single phase of orthorhombic structure to be obtained is 0.25. The orthorhombic structure was initially identified by conventional powder XRD and then confirmed by synchrotron-XRD. Figure 4.3

illustrates the Rietveld refinement profiles for $LaRh_{0.5}Cu_{0.25}Zn_{0.25}O_3$. The refined lattice parameters *a* = 5.56043 (7), *b* = 5.66937 (8), and *c* = 7.88330 (9) Å; R_p = 6.13 % R_{wp} = 8.84 %, χ^2 = 24.29.

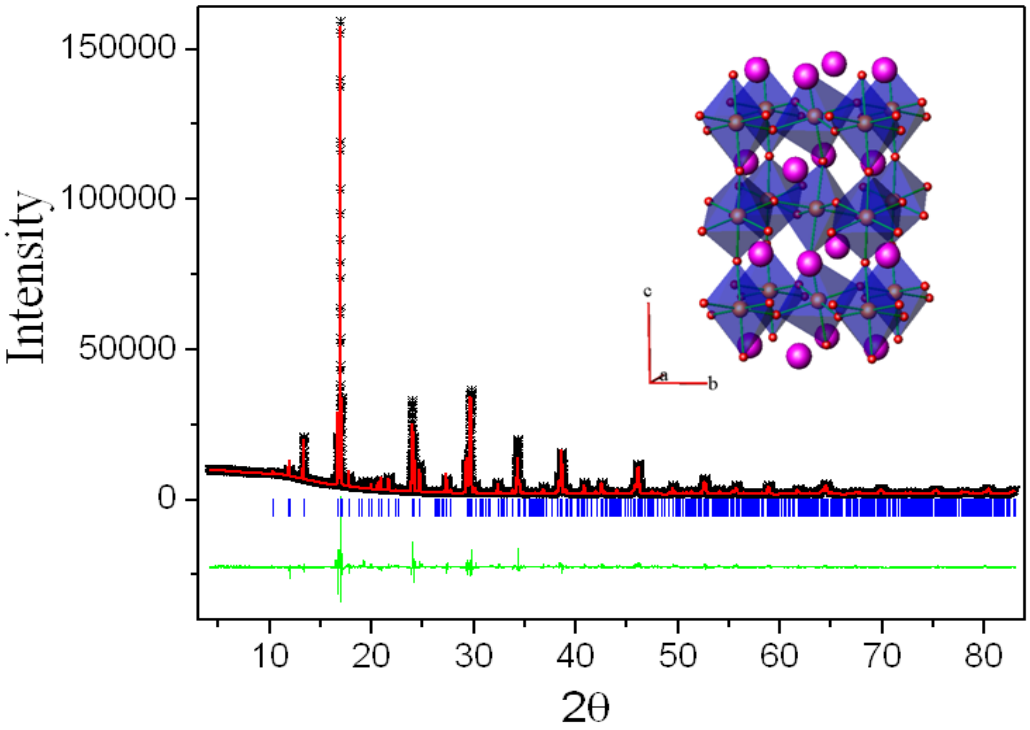

Figure 4.3 Synchrotron X-ray diffraction profiles for $LaRh_{0.5}Cu_{0.25}Zn_{0.25}O_3$. The data are represented by the crosses and the solid lines are the calculated and difference profiles. The allowed reflections of the space group are shown by the vertical markers immediately below the observed profile. A representation of the $LaRh_{0.5}Cu_{0.25}Zn_{0.25}O_3$ structure is included.

Structural refinements from the synchrotron diffraction data provided precise lattice parameters, however the presence of the very heavy La cation limited the accuracy of the refined structures. Consequently neutron diffraction data were also collected for $LaRh_{0.5}Cu_{0.25}Zn_{0.25}O_3$ and these results are summarised in Table 4.1. Neutron diffraction data were collected at 4 and 293 K to investigative the possibility of magnetic ordering. From the structural refinements, we found no evidence for any anion vacancies, and subsequently it is assumed such vacancies were absent in the $LaRh_{1-2x}Cu_xB_xO_3$ series. It is thought that oxygen vacancies are less likely to occur in samples with lower contents of the divalent cations in $LaRh_{0.5}Cu_{0.25}Zn_{0.25}O_3$.

Table 4.1 Results of the structural refinements for $LaRh_{0.5}Cu_{0.25}Zn_{0.25}O_3$ using neutron powder diffraction data. The *B* site cations are at (0, 0, 0).

Structural parameters	4 K	293K
a (Å)	5.5535(4)	5.5707(3)
b (Å)	5.6647(4)	5.6639(4)
c (Å)	7.8693(6)	7.8936(4)
V (Å^3)	247.56(3)	249.08(2)
La *x*	0.4891(9)	0.4907(8)
La *y*	-0.0502(6)	-0.0468(5)
La *z*	1/4	1/4
La B_{iso} (Å^2)	0.54(11)	0.99(11)
B/Rh B_{iso} (Å^2)	1.37(13)	1.73(12)
O1 *x*	0.5878(12)	0.5873(11)
O1 *y*	0.5226(9)	0.5224(9)
O1 *z*	1/4	1/4
O1 B_{iso} (Å^2)	1.20(12)	1.64(12)
O2 *x*	0.2960(7)	0.2968(6)
O2 *y*	0.2026(6)	0.2026(6)
O2 *z*	0.0451(5)	0.0449(5)
O2 B_{iso} (Å^2)	1.17(11)	1.56(10)
M-(O1)-M (º)	151.24(35)	151.42(34)
M-(O2)-M (º)	150.99(20)	150.91(19)
B/ Rh-O1 (Å)	2.0309(1)	2.0364(1)
B/ Rh-O2 (Å)	2.0360(1)	2.0434(1)
B/ Rh-O*2 (Å)	2.0610(1)	2.0603(1)
B/ Rh-O(av) (Å)	2.0426	2.0467
R_P (profile) (%)	8.99	8.36
R_{wp}(weighted profile) (%)	11.92	11.11
χ^2	3.96	3.54
Tilt angle (º)		
ψ (in phase)	10.6	10.7
φ (out of phase)	14.3	14.3

From the neutron diffraction studies, Δd was estimated to be 7.35×10^{-5} for $LaRh_{0.5}Cu_{0.25}Zn_{0.25}O_3$. This is higher than that seen in $LaRhO_3$ ($\Delta d = 2.5 \times 10^{-5}$) [17], but lower than for $LaRh_{0.5}Cu_{0.5}O_3$ ($\Delta d = 11 \times 10^{-5}$) [9]. Cu^{2+} cations are susceptible to a Jahn-Teller type distortion where the degeneracy of the six *M*-O bond lengths is removed, resulting in a distortion of the MO_6 octahedra [18]. Cooling the samples to 4K did not result in noticeable changes in the neutron profiles indicative of long range magnetic ordering. No systematic change in *M*-O(1)-*M* and *M*-O(2)-*M* angles was observed, these being (151.4(4)º and 151.0(2)º) in $LaRh_{0.5}Cu_{0.25}Zn_{0.25}O_3$. These angles are similar to those found for $LaRhO_3$, 150.5° and 149.1° [17].

The angles of the in-phase (ψ) and anti-phase (φ) oxygen octahedra rotations in $LaRh_{0.5}Cu_{0.25}Zn_{0.25}O_3$ were calculated from the refined atomic coordinates using the formulae given in the literature [19]. The displacements of the O(2) oxygen atoms from $(\frac{1}{4},\ \frac{1}{4},\ 0)$ to $(\frac{1}{4}-u,\ \frac{1}{4}+v,\ w)$ of $LaRh_{0.5}Cu_{0.25}Zn_{0.25}O_3$ are found to be almost identical ($u \cong v \cong 0.047$), suggesting rigidity of the octahedral tilts [19]. The variations in the octahedral tilt angles ψ and φ were small (less than 0.1°) and essentially temperature independent over the range 4-293 K. In perovskites, the tilt angles of the BO_6 octahedra are related in the inverse ratio of the *B*-O bond lengths [19]. Thus the change in tilt angles is governed by change in the *B*-O bond lengths. The *B*-O^*(2) bond length in $LaRh_{0.5}Cu_{0.25}Zn_{0.25}O_3$ is found to be temperature independent (see Table 4.1). This is in agreement with the reported structural studies of $CaRuO_3$ and $CaRu_{0.85}Cr_{0.15}O_3$ in which the octahedral tilts of these oxides are very rigid and do not vary significantly upon heating to 1300 °C [20,21], similar results were reported for the temperature evolution of the crystal structures in the $LaMg_{0.5}Ti_{0.5}O_3$ [22] and $LaZn_{0.5}Ti_{0.5}O_3$ [23] where the variations of the metal oxygen distances in the BO_6 octahedra and the octahedral tilt angles were both temperature independent. The thermal stability of the $LaRh_{0.5}Cu_{0.25}Zn_{0.25}O_3$ structure was examined by XRD between 30 and 900 °C. The perovskite oxides show high stability across the temperature range. The temperature dependence of the lattice parameters for $LaRh_{0.5}Cu_{0.25}Zn_{0.25}O_3$ is illustrated in Figure 4.4.

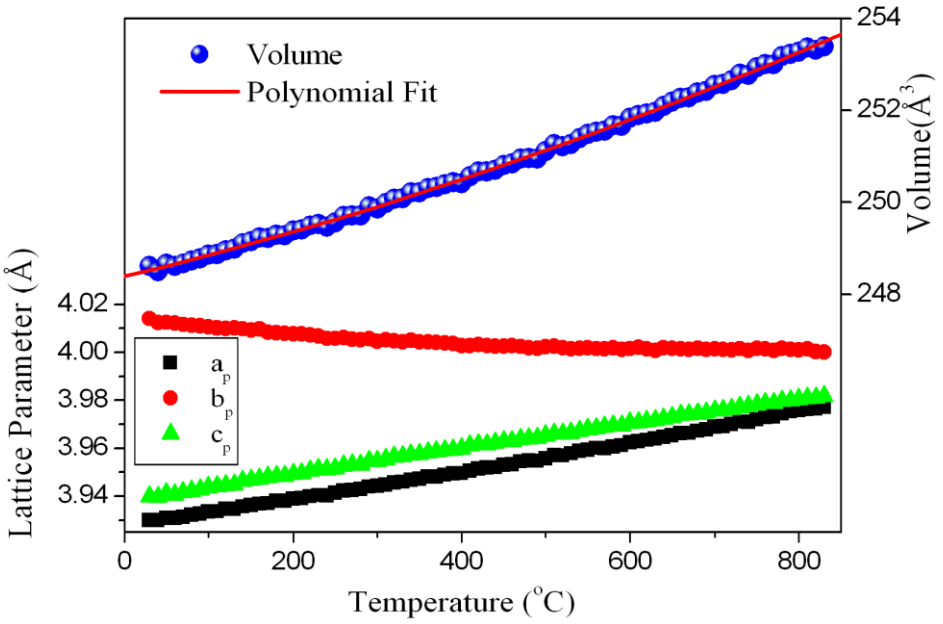

Figure 4.4 The temperature dependence of lattice parameters for $LaRh_{0.5}Cu_{0.25}Zn_{0.25}O_3$ estimated by Rietveld refinement using X-ray diffraction data. The temperature dependent variation of the cell volume is fit to the equation $V_{(t)} = 248.38(2) + 4.46(9)\times10^{-3}\,T + 2.1(1)\times10^{-6}\,T^2$.

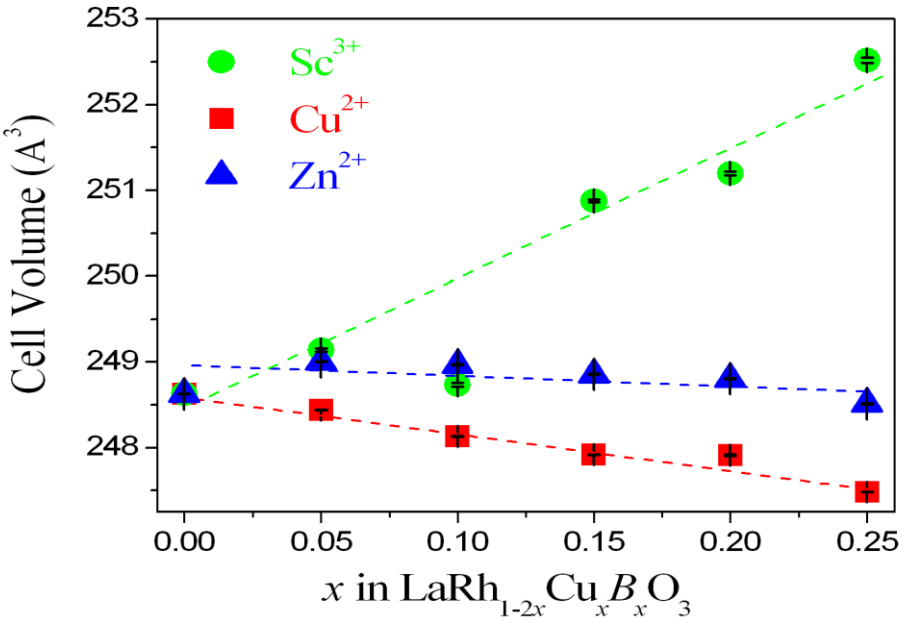

Figure 4.5 Composition dependence of the cell volume for $LaRh_{1-2x}Cu_xB_xO_3$ estimated by Rietveld refinement using synchrotron X-ray diffraction data. Where not obvious the error bars are smaller than the symbols.

The composition dependence of the unit cell volumes estimated from the synchrotron diffraction data for the $LaRh_{0.5}Cu_{0.25}B_{0.25}O_3$ series is illustrated in Figure 4.5. Doping with either Sc or Zn initially results in an increase in the cell volume. This is consistent with the relative sizes of the cations; Sc^{3+} (6-coordinate ionic radius, 0.745 Å) [12], Zn^{2+} (0.74 Å) [12] and Cu^{2+}(0.73 Å) [12] are considerably larger than Rh^{3+} (0.665 Å) [12]. This neglects the impact of electron transfer between the ions, and the possibility of partial oxidation of the Rh^{3+} to Rh^{4+} (0.60 Å) [12] and Cu^{2+} to Cu^{3+} (0.54 Å) [12] must also be considered because such oxidation is required to maintain charge neutrality. The decrease in the ionic radii of the *B* site cations with increasing *x* is believed to drive the observed reduction in cell volumes of the Cu and Zn doped samples. Doping with trivalent metals, such as Sc, is expected to have little impact on the charge delocalization in the system. As mentioned previously, the presence of Cu introduces the possibility of a partial charge transfer involving Rh^{4+} to Rh^{3+} and Cu^{2+} to Cu^{3+} [9]. Neither Zn nor Sc have alternate oxidation states. The Sc doped oxides have larger cell volumes than their Zn analogues at high doping levels and much larger volumes than the Cu doped oxides at all doping levels. The similarity in the cell volumes for $LaRh_{1-2x}Cu_xSc_xO_3$ and $LaRh_{1-2x}Cu_xZn_xO_3$ at x = 0.05 suggests that the oxidation states of Cu in these is 2+ whereas the decrease in cell volume for $LaRh_{0.8}Cu_{0.1}Sc_{0.1}O_3$ suggests that the formal valency of Cu must be higher than 2+. Equations 4.1, 4.2 and 4.3 describe the expected ionic volumes (T_v) for the $LaRh_{1-2x}Cu_xSc_xO_3$, $LaRh_{1-2x}Cu_{2x}O_3$ and $LaRh_{1-2x}Cu_xZn_xO_3$ series at room temperature.

$$T_v = \alpha_1(V_{(La^{3+})} + (1-3n)V_{(Rh^{3+})} + nV_{(Rh^{x+})} + nV_{(Cu^{z+})} + nV_{(Sc^{3+})} + 3\,V_{(O^{2-})} \quad 4.1$$

$$T_v = \alpha_2(V_{(La^{3+})} + (1-4n)V_{(Rh^{3+})} + 2nV_{(Rh^{x+})} + 2nV_{(Cu^{z+})} + 3\,V_{(O^{2-})} \quad 4.2$$

$$T_v = \alpha_3(V_{(La^{3+})} + (1-4n)V_{(Rh^{3+})} + nV_{(Rh^{x+})} + nV_{(Rh^{4+})} + nV_{(Cu^{z+})} + nV_{(Zn^{2+})} + 3\,V_{(O^{2-})} \quad 4.3$$

Where V_i is the ionic sphere volume given by $V_i = \frac{4}{3}\pi {r_i}^3$ [24] and r_i is the ionic radius of each ion, n is the number of mole of Sc, Cu and Zn ions, x and z are the average valence states of Rh and Cu ions (3.5+, 2.5+) respectively, α_1, α_2 and α_3 are the multiplicity factors that are defined as the observed unit cell volume of the oxides divided by the sum of V_i per formula. These are estimated to be around 6.

The ionic volume (T_v) is a function of the ionic sphere volumes (V_i) and the number of moles (n) of each ion in a given composition. This describes the change in the unit cell volume as the formal oxidation of the constituent ions changes. When *x* moles of Cu and Zn ions doped into the system, an equivalent number of moles of Rh^{3+} ions will be oxidized either partially or totally to Rh^{4+} causing a decrease in the total number of moles of Rh^{3+}. The oxidation states of the Rh ions are estimated to be on average 3.5+ (0.632Å) per mole unit of Cu ions, 3+ per mole unit of Sc^{3+} and 4+ per mole unit of Zn^{2+}. The average valency for Cu ions is considered to be 2.5+ with an effective ionic radius of the 0.635Å otherwise the cell volume for Cu and Zn doped oxides should increase at all doping levels. Assuming the multiplicity factor α is constant for each series, we found the correlation factors (*r*) between the experimental data and the calculated cell volumes from the equation for Sc, Cu and Zn doping to be 0.947, 0.979 and 0.945 respectively, indicating a strong correlation. T_v for the $LaRh_{0.9}Cu_{0.05}Sc_{0.05}O_3$ and $LaRh_{0.9}Cu_{0.05}Zn_{0.05}O_3$ was calculated using the ionic radii for Rh^{3+} and Cu^{2+}.

To establish the valence states of the constituent cations XANES data were collected for the $LaRh_{1-2x}Cu_{2x}O_3$ series. XANES spectra are commonly used as a direct probe of the formal valency, spin state and coordination environment of the transition metal cations [25,26]. The normalized Rh L_3 XANES spectra for members in the series $LaRh_{1-2x}Cu_{2x}O_3$, and Rh^{3+} ($LaRhO_3$) and Rh^{4+} (Sr_2RhO_4) standards are presented in Figure 4.6. The first derivative for the Rh^{4+} standard Sr_2RhO_4 and the various Cu doped oxides show the peaks are doublets corresponding to transitions from the t_{2g} and e_g states. The spectra for $LaRhO_3$ contains a single peak since the t_{2g} orbitals are completely filled and only transitions from the $2p_{3/2}$ core levels to the e_g states are possible [27]. The Rh L_3- edge XANES spectrum at $x = 0.25$ is similar to that seen in the literature [9], and is indicative of the coexistence of charge delocalization between the Cu and Rh cations. This is confirmed by quantitative analysis using least-squares refinement [28]. The L_3-edge XANES spectra from $LaRh_{1-2x}Cu_{2x}O_3$ was fitted with a linear combination of the two standards, $LaRhO_3$ and Sr_2RhO_4 over the energy range 2970 - 3050 eV. The Rh has average valence around 3.5 with a combination of mass ratios 52.8 % for Rh^{3+} and 48.2 % for Rh^{4+} ions. As illustrated in the table 4.2, increasing *x* in $LaRh_{1-2x}Cu_{2x}O_3$ results in average Rh oxidation states higher than 3+, indicating charge delocalization between the Cu

and Rh ions occurs. The absence of anion vacancies in the structure was evident from the neutron diffraction study of $LaRh_{0.5}Cu_{0.25}Zn_{0.25}O_3$ where the content of the doped divalent cations is similar to that in $LaRh_{0.5}Cu_{0.5}O_3$ oxides. The similarity in the average Rh oxidation states for $LaRh_{0.7}Cu_{0.3}O_3$ and $LaRh_{0.6}Cu_{0.4}O_3$ can be attributed to the preparation conditions. The $LaRh_{1-2x}Cu_{2x}O_3$ perovskites were synthesized under an atmosphere of pure oxygen and were, possibly, oxidized efficiently due to small differences in the surface morphologies. The decrease in the Rh^{4+} content was found to be positively correlated with the decrease in the cell volumes.

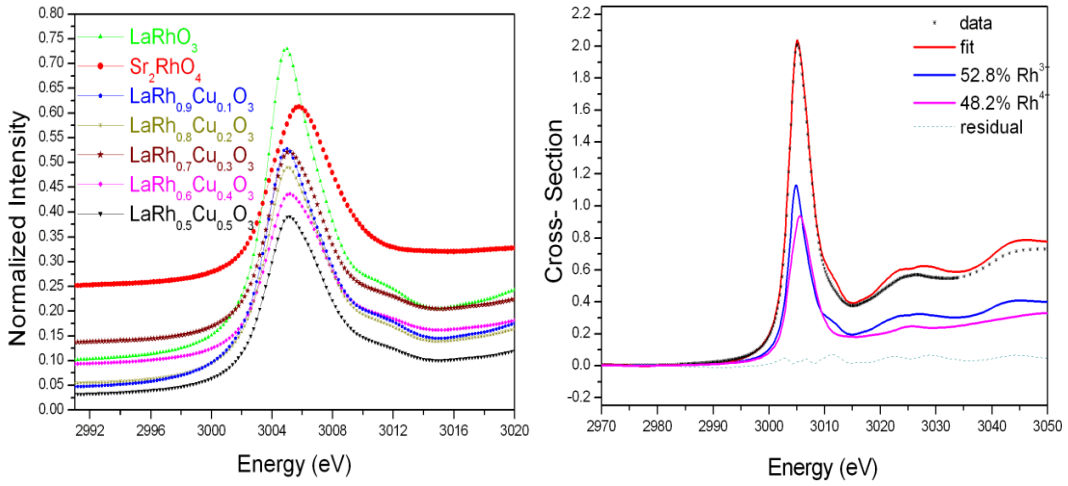

Figure 4.6 Normalized Rh L_3-edge XANES spectra for members in the series $LaRh_{1-2x}Cu_{2x}O_3$, Rh^{3+} ($LaRhO_3$) and Rh^{4+} (Sr_2RhO_4) standards. The corresponding fit for $LaRh_{0.5}Cu_{0.5}O_3$ and the individual components Rh^{3+} and Rh^{4+} are also presented on the right hand side. The data have been offset vertically for clarity.

Table 4.2 The Rh^{3+}, Rh^{4+} and the average Rh oxidation states (Q_{av}) in $LaRh_{1-2x}Cu_{2x}O_3$ estimated from XANES data.

X	0.05	0.10	0.15	0.20	0.25
% Rh^{3+}	91.2	86.2	64.0	68.1	52.8
% Rh^{4+}	8.8	13.8	36.0	31.9	48.2
n. moles of Rh^{3+}	0.821	0.690	0.448	0.409	0.264
n. moles of Rh^{4+}	0.079	0.110	0.252	0.191	0.236
Q_{av}	3.09	3.14	3.36	3.32	3.51

The external structural distortion *D* and the internal structural distortion Δd for $LaRh_{1-2x}Cu_xB_xO_3$ series are summrised in Table 4.3. The addition of Zn^{2+} into the *B* site results in smaller octahedral distortions compared to the substitution by Sc^{3+}. The distortions of the octahedra are in part due to the Jahn-Teller effect of the Cu^{2+} ions. The octahedral distortions for the Zn doped oxides were decreased, possibly due to the oxidation of Cu^{2+} to Cu^{3+}. As Zn^{2+} is added to the system, an equivalent quantity of Rh^{3+} is expected to be oxidized to Rh^{4+}. Consequently, the charge balance between $Rh^{3+/4+}$ and $Cu^{2+/3+}$ will shift toward Rh^{4+}/Cu^{3+} resulting in a smaller distortion. $LaRh_{1-2x}Cu_{2x}O_3$ shows a higher octahedral distortion than $LaRh_{1-2x}Cu_xZn_xO_3$ due to the higher Cu content. The $LaRh_{1-2x}Cu_xSc_xO_3$ oxides have the most symmetrical arrangement (lowest *D* value), whereas $LaRh_{1-2x}Cu_{2x}O_3$ oxides have the most distorted lattice among the three series. That is consistent with increases in the cell volumes and suggests, again, the importance of the charge delocalization. Distortion of the lattice parameters in Jahn-Teller systems is commonly attributed to strain effects due to Jahn-Teller distortions, octahedral tilting, and disorder [29,30]. The *M*-O(1)-*M* and *M*-O(2)-*M* bond angles (Table 4.4), as obtained from the structural refinements, reflect the octahedral tilting. The bond angles are somewhat smaller in $LaRh_{1-2x}Cu_xSc_xO_3$ and $LaRh_{1-2x}Cu_{2x}O_3$ than in $LaRh_{1-2x}Cu_xZn_xO_3$ which shows the lowest bond angle anisotropy. There is no obvious correlation between the bond angles and Cu content.

Table 4.3 Lattice parameter distortion *D* and octahedral distortion Δd for $LaRh_{1-2x}Cu_xB_xO_3$

x	$LaRh_{1-2x}Cu_xSc_xO_3$		$LaRh_{1-2x}Cu_{2x}O_3$		$LaRh_{1-2x}Cu_xZn_xO_3$	
	D (%)	$\Delta d\times10^{-4}$	*D (%)*	$\Delta d\times10^{-4}$	*D (%)*	$\Delta d\times10^{-4}$
0.05	1.08	5.56	1.22	0.73	1.12	0.73
0.10	1.09	16.73	1.26	1.14	0.94	1.41
0.15	0.90	13.93	1.19	5. 33	1.00	1.32
0.20	0.77	20.31	0.81	2.01	0.78	1.31
0.25	0.55	0.63	1.15	2.27	0.81	0.73

Table 4.4 Bond angles *M*-O(1)-*M* and *M*-O(2)-*M* for $LaRh_{1-2x}Cu_xB_xO_3$.

X	$LaRh_{1-2x}Cu_xSc_xO_3$		$LaRh_{1-2x}Cu_{2x}O_3$		$LaRh_{1-2x}Cu_xZn_xO_3$	
	M(O1)M º	*M(O2)M º*	*M(O1)M º*	*M(O2)M º*	*M(O1)M º*	*M(O2)M º*
0.05	147.99 (64)	148.80 (31)	150.08(29)	149.73(21)	152.50(47)	151.39(29)
0.10	145.99 (53)	150.06 (29)	147.39(30)	150.37(22)	149.22(67)	149.12(29)
0.15	149.39 (41)	150.45 (23)	145.34(54)	150.40 (28)	150.17(70)	150.11(31)
0.20	146.91 (46)	151.03 (24)	148.93(91)	146.86(26)	150.63(72)	150.29(26)
0.25	150.66 (31)	152.32 (17)	148.08(38)	152.54 (24)	151.36(34)	150.95(19)

4.2.3 Magnetization

The inverse susceptibility plots for the $LaRh_{1-2x}Cu_xSc_xO_3$ and $LaRh_{1-2x}Cu_xZn_xO_3$ series are illustrated in Figure 4.7. In both series, the susceptibility increases as the Cu content increases. Doping with Zn resulted in higher magnetic susceptibilities than doping with Sc. The increase in the magnetic susceptibility is mainly attributed to the increase in Rh^{4+} ($4d^5$) content. The deviation from simple Curie-Weiss type behaviour at low temperature for the Zn doped oxides suggests there are weak antiferromagnetic interactions. The noisy data for $LaRh_{0.9}Cu_{0.05}Sc_{0.05}O_3$ at high temperature reflects the sensitivity limits of the instrument at lower susceptibility values.

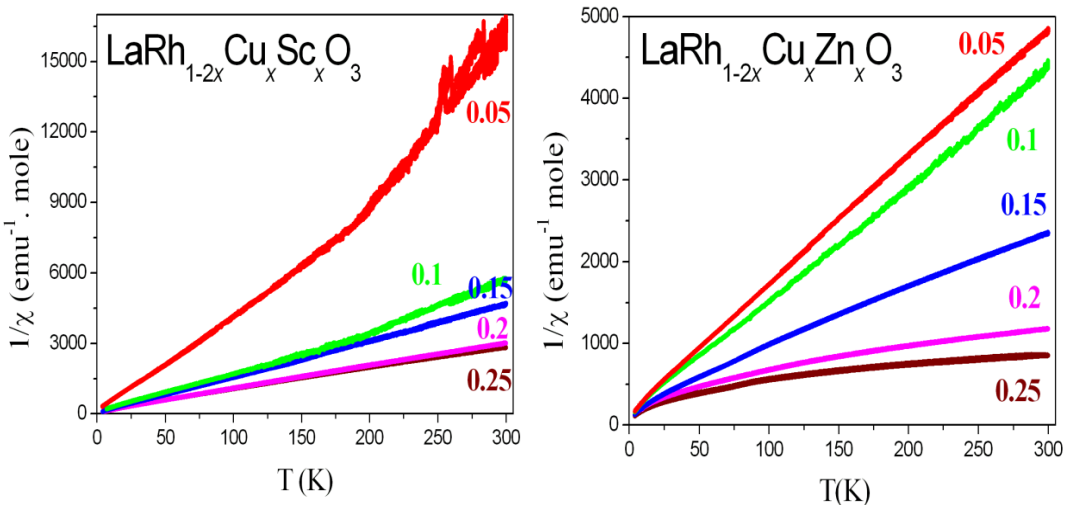

Figure 4.7 The temperature dependence of the inverse susceptibility for $LaRh_{1-2x}Cu_xSc_xO_3$ and $LaRh_{1-2x}Cu_xZn_xO_3$ recorded under zero field cooling conditions with an applied field of 5 kOe.

Hysteresis loop measurements, as illustrated in Figure 4.8, showed the absence of any long range magnetic ordering, also evident from the neutron diffraction measurements. The plot of the magnetization against the applied field displays no hysteresis loop at range of ± 90 kOe. Neutron diffraction profiles for $LaRh_{0.5}Cu_{0.25}Zn_{0.25}O_3$ show no systematic change in the *M*-O(1)-*M* and *M*-O(2)-*M* bond angles at 4 and 293 K. There were no additional peaks in ND patterns demonstrating the absence of long range magnetic ordering.

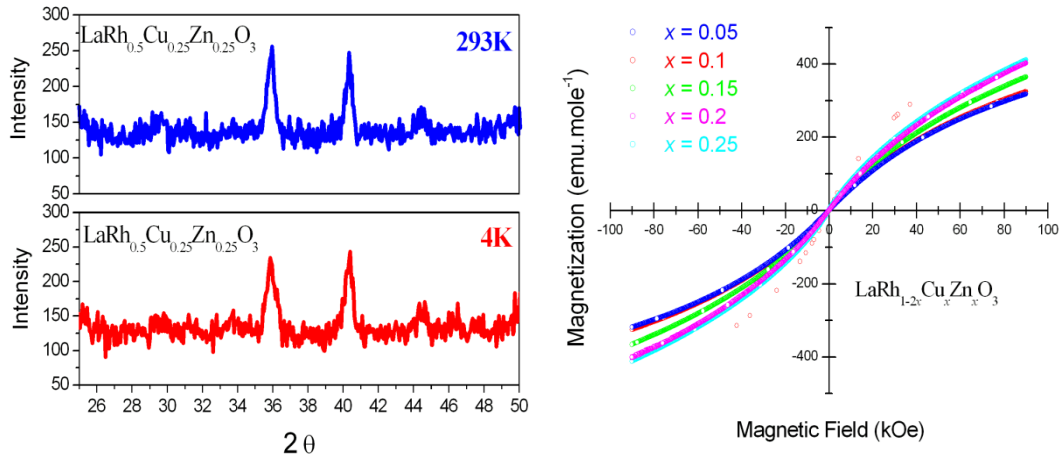

Figure 4.8 Portion of the ND profiles for $LaRh_5Cu_{0.25}Zn_{0.25}O_3$ at 4 and 293K. Magnetization hysteresis loops for $LaRh_{1-2x}Cu_xZn_xO_3$ at 5K are also illustrated.

Figure 4.9 illustrates the temperature dependence of the magnetic susceptibilities for $LaRh_{0.5}Cu_{0.25}Zn_{0.25}O_3$ and $LaRh_{0.5}Cu_{0.25}Sc_{0.25}O_3$ under ZFC and FC cooling conditions in the temperature range 4-300K. The absence of divergence between the ZFC and FC magnetic susceptibilities and magnetic hysteresis in the magnetization-magnetic field curves indicates that these compounds remain paramagnetic to 4 K. A fit of the inverse magnetization curves allows the effective magnetic moments (μ_{eff}) and Weiss constants (Θ) to be estimated. As summarized in Table 4.5, the Zn doped oxides have higher effective magnetic moments and lower negative Weiss temperature than the Sc doped oxides. For instance, $LaRh_{0.5}Cu_{0.25}Zn_{0.25}O_3$ has the highest effective magnetic moment (1.91 μ_B) and lowest negative Weiss temperature (-131.09 K), whereas $LaRh_{0.5}Cu_{0.25}Sc_{0.25}O_3$ has a lower effective magnetic moment (0.93 μ_B) and higher Weiss temperature (-14.6 K). These values are intermediate between those of the weak paramagnetic oxide $LaRhO_3$ (-2.74 K, 0.295 μ_B) [31] and the antiferromagnetic mixed valence oxide

$Eu^{3+/2+}Rh^{3+/4+}O_3$ (-297 K, 4.717 μ_B) [31] and suggests the materials may be weakly antiferromagnetic [32]. The positive Weiss constants (+24.9 and +9.1) for $LaRh_{0.9}Cu_{0.05}Sc_{0.05}O_3$ and $LaRh_{0.8}Cu_{0.1}Sc_{0.1}O_3$ indicate that the materials are weakly ferromagnetic at lower Cu contents. The effective magnetic moments for $LaRh_{1-2x}Cu_xZn_xO_3$ are higher than predicted for a mixture of Rh^{4+} ($4d^5$) and Cu^{2+} ($3d^9$) suggesting Cu^{3+} ($3d^8$) ions may be important.

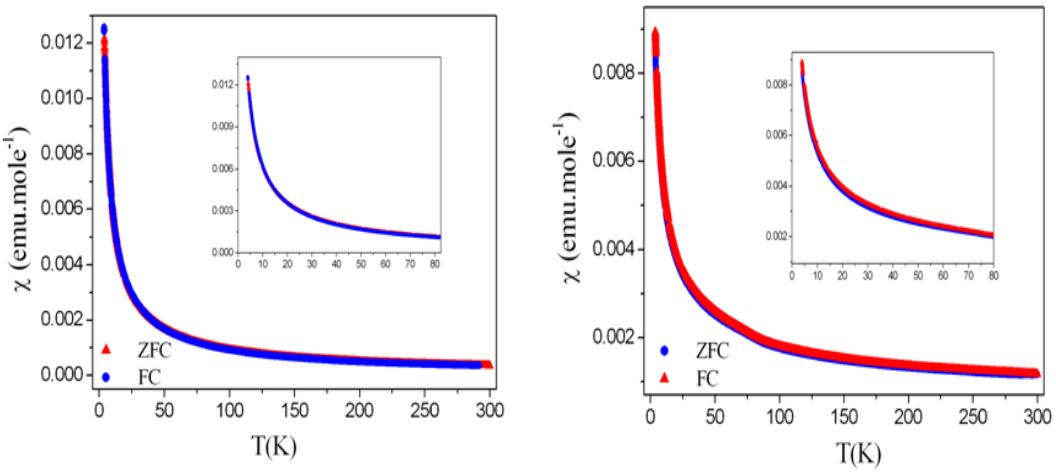

Figure 4.9 The temperature dependence of the molar magnetic susceptibility for $LaRh_{0.5}Cu_{0.25}Zn_{0.25}O_3$ and $LaRh_{0.5}Cu_{0.25}Sc_{0.25}O_3$ recorded under zero field cooling and zero cooling conditions with an applied field of 5 kOe. The inserts are from the low temperature data and demonstrate the lack of any apparent difference between the ZFC and FC curves.

Table 4.5 Curie constant *C*, Weiss constant Θ, magnetic susceptibly coefficient factor χ_o, and effective magnetic moment μ_{eff} for $LaRh_{1-2x}Cu_xB_xO_3$.

x	$LaRh_{1-2x}Cu_xSc_xO_3$				$LaRh_{1-2x}Cu_xZn_xO_3$			
	Θ (K)	χ_o (10^{-3})	C (emu. mole$^-$)	μ_{eff} (μ_B)	Θ (K)	χ_o (10^{-3})	C (emu. mole$^-$)	μ_{eff} (μ_B)
0.05	+24.8	-0.731	-0.450	0.38	-11.1	5.759	0.713	0.71
0.1	+9.1	-5.785	-0.485	0.65	-9.1	7.811	0.652	0.75
0.15	-1.1	54.110	0.077	0.72	-28.5	4.762	3.862	1.04
0.2	-10.9	9.338	1.120	0.90	-99.3	3.193	31.456	1.59
0.25	-14.6	7.412	1.596	0.93	-131.1	3.495	60.077	1.91

The temperature dependence of the inverse susceptibility (Figure 4.10) shows that the magnetization increases as the Cu content increases. The $LaRh_{0.7}Cu_{0.15}B_{0.15}O_3$ oxide exhibits higher magnetic susceptibility than $LaRh_{0.5}Cu_{0.25}B_{0.25}O_3$. The magnetization was also found to be strongly dependent on the Rh^{4+} ($4d^5$) content. $LaRh_{0.7}Cu_{0.3}O_3$ (1.11 μ_B) has a higher magnetic moment than $LaRh_{0.7}Cu_{0.15}Sc_{0.15}O_3$ (0.72 μ_B) and $LaRh_{0.7}Cu_{0.15}Zn_{0.15}O_3$ (1.04 μ_B) whereas the magnetic moment for $LaRh_{0.5}Cu_{0.5}O_3$ (1.17 μ_B) is intermediate between those for $LaRh_{0.5}Cu_{0.25}Sc_{0.25}O_3$ (0.93 μ_B) and $LaRh_{0.5}Cu_{0.25}Zn_{0.25}O_3$ (1.91 μ_B). This reflects that $LaRh_{0.7}Cu_{0.3}O_3$ has higher Rh^{4+} content than $LaRh_{0.5}Cu_{0.5}O_3$. The XANES data (Table 3.2) demonstrate the Rh^{4+} content decreases from 0.252 moles per formula unit for $LaRh_{0.7}Cu_{0.3}O_3$ to 0.236 moles per formula unit for $LaRh_{0.5}Cu_{0.5}O_3$ as a consequence of the gradual increase in the formal valency of the Cu. The addition of the diamagnetic cations Sc^{3+} ($3d^0$) and Zn^{2+} ($3d^{10}$) into the $LaRh_{1-2x}Cu_xB_xO_3$ perovskites system does not directly impact on the magnetization. However, the oxidation of Rh^{3+} to Rh^{4+} due to the addition of Cu and Zn should result in an increase in the magnetic susceptibility.

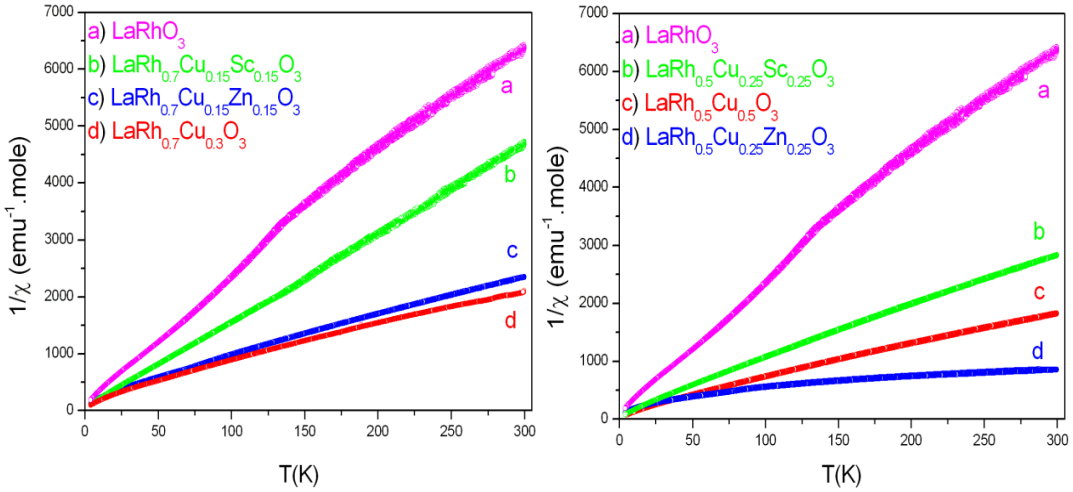

Figure 4.10 The temperature dependence of the inverse susceptibility for $LaRh_{0.7}Cu_{0.15}B_{0.15}O_3$ and $LaRh_{0.5}Cu_{0.25}B_{0.25}O_3$ recorded under zero field cooling conditions with an applied field of 5 kOe.

4.2.4 Electrical conductivity

Electrical conductivity measurements show that doping with Cu increases the conductivity of the oxides, suggesting an increase in carrier mobility occurs as a result of oxidation of Rh^{3+} ($3d^6$) to Rh^{4+} ($3d^5$) which generates holes in the band gap.

This was evident from the electrical conductivity for $LaRh_{0.5}Cu_{0.5}O_3$ (4.35×10^3 $S.m^{-1}$) which is 10 times higher than for $LaRh_{0.5}Cu_{0.25}Zn_{0.25}O_3$ (0.476×10^3 $S.m^{-1}$) and $LaRh_{0.5}Cu_{0.25}Sc_{0.25}O_3$ (0.395×10^3 $S.m^{-1}$) at 300K. Also σ_{300K} for $LaRh_{0.7}Cu_{0.3}O_3$ (17.24×10^3 $S.m^{-1}$) was higher than for $LaRh_{0.7}Cu_{0.15}Zn_{0.15}O_3$ (2.34×10^3 $S.m^{-1}$) and $LaRh_{0.7}Cu_{0.15}Sc_{0.15}O_3$ (0.426×10^3 $S.m^{-1}$) at 300K. The electrical conductivity for $LaRh_{0.7}Cu_{0.3}O_3$ is higher than that of $LaRh_{0.5}Cu_{0.5}O_3$ reflecting the high Rh^{4+} content in the former oxides (see Table 4.2). The Arrhenius plots are shown in Figure 4.11. Doping with Sc^{3+} results in an increase in the activation energy from 0.049 eV 0.088 eV whereas doping with Zn does not change the activation energy (0.046 eV). At x = 0.15, the activation energies slightly increased from 0.040 eV for $LaRh_{0.7}Cu_{0.3}O_3$ to 0.059 and 0.070 eV for the corresponding Zn and Sc doped oxides. This is attributed to differences in the charge delocalization.

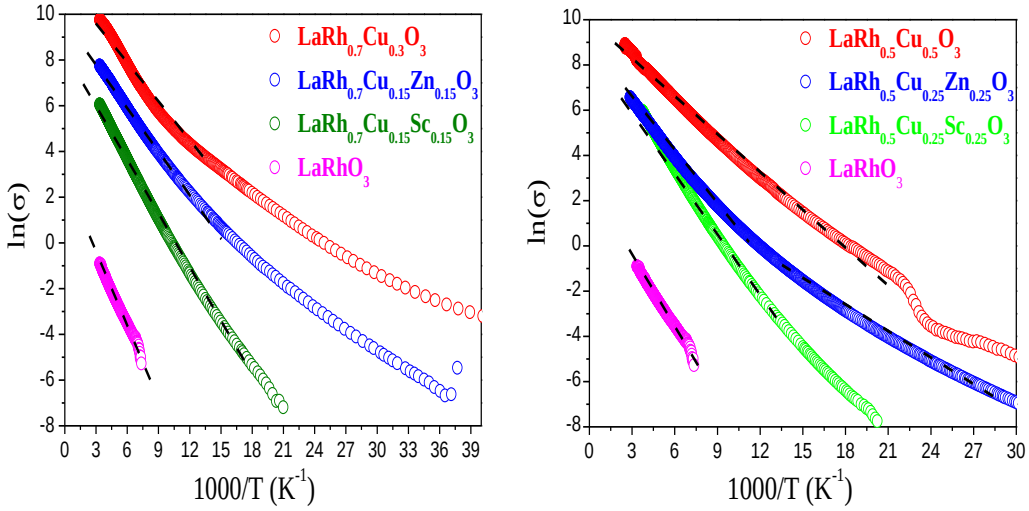

Figure 4.11 The Arrhenius plots of Ln (σ) verses inverse temperature for $LaRh_{0.7}Cu_{0.15}B_{0.15}O_3$ and $LaRh_{0.5}Cu_{0.25}B_{0.25}O_3$ perovskites.

4.2.5 Summary

The structural, magnetic and electrical properties of the $LaRh_{1-2x}Cu_xB_xO_3$ (B = Sc^{3+}, Cu^{2+} and Zn^{2+}) oxides have been investigated. The decrease in the cell volumes and the increase in the magnetic moments of the Cu and Zn doped oxides are indicative of an increase in the formal valency of Cu and Rh ions. The formal valency of the Cu in $LaRh_{1-2x}Cu_{2x}O_3$ apparently increases as x increases. Doping with Sc resulted in higher cell volumes and lower magnetic moments than doping by Zn as a consequence of charge delocalization. A deviation from linear Curie Weiss

behaviour for the Zn doped oxides was observed with increased Zn content. The magnetization curves show negative values for Weiss temperatures indicating short range antiferromagnetic interactions may be present. One exception is $LaRh_{1-2x}Cu_xSc_xO_3$ which demonstrated positive Weiss temperatures at $x = 0.05$ and $x = 0.1$, indicating ferromagnetic correlations. Nevertheless, the oxides lacked long range magnetic ordering and all best described as spin glasses. Additional measurements such as AC-susceptibility analysis is required to confirm this. The electrical conductivity of the oxides increases as the Cu content increases.

4.3 Results and discussion: $La_{0.75}A_{0.25}Rh_{1-2x}Cu_xB_xO_3$

Various oxides of the type $La_{0.75}A_{0.25}Rh_{1-2x}Cu_xB_xO_3$ ($A = Pb^{2+}$ and Bi^{3+}; $B = Sc^{3+}$, Cu^{2+} and Zn^{2+}) were investigated. Except for $La_{0.75}Pb_{0.25}Rh_{1-2x}Cu_xSc_xO_3$ ($x \leq 0.15$) and $La_{0.75}Bi_{0.25}Rh_{1-2x}Cu_xZn_xO_3$ ($x = 0.1$ and 0.25), all the compositions studied gave single phase products with an orthorhombic structure.

4.3.1 Visual Inspection

The $La_{0.75}A_{0.25}Rh_{1-2x}Cu_xB_xO_3$ samples are black powders with different particles sizes. The black colour of the samples appeared at the second heating step at 950 ºC. Figure 4.12 demonstrates that $La_{0.75}Pb_{0.25}Rh_{0.5}Cu_{0.25}Zn_{0.25}O_3$ is more crystalline than $La_{0.75}Bi_{0.25}Rh_{0.5}Cu_{0.25}Zn_{0.25}O_3$ and $La_{0.75}Bi_{0.25}Rh_{0.5}Cu_{0.25}Sc_{0.25}O_3$. Increasing the content of the divalent dopants resulted in an increase in the crystallinity of the samples. SEM measurements (Figure 4.13) demonstrated the particles sizes of $La_{0.75}Pb_{0.25}Rh_{1-2x}Cu_xZn_xO_3$ samples increases as x increased. EDX analysis showed mass ratios consistent with the targeted compositions.

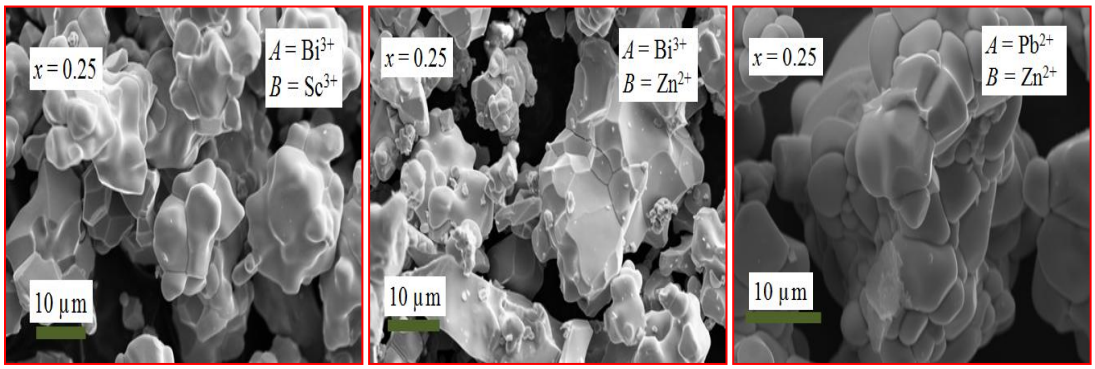

Figure 4.12 Scanning Electron Micrograph image for $La_{0.75}Bi_{0.25}Rh_{0.5}Cu_{0.25}Sc_{0.25}O_3$, $La_{0.75}Bi_{0.25}Rh_{0.5}Cu_{0.25}Zn_{0.25}O_3$ and $La_{0.75}Pb_{0.25}Rh_{0.5}Cu_{0.25}Zn_{0.25}O_3$.

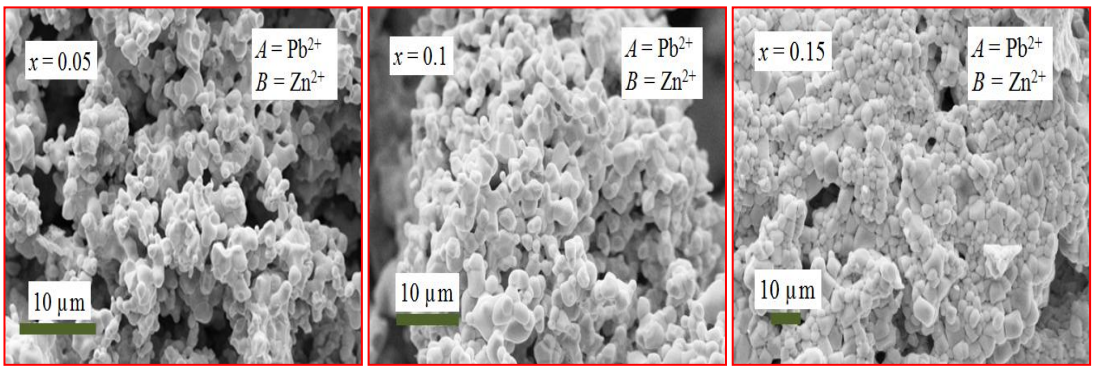

Figure 4.13 Scanning Electron Micrograph images for $La_{0.75}Pb_{0.25}Rh_{1-2x}Cu_xZn_xO_3$.

4.3.2 Crystal Structure

X-ray measurements showed the $La_{0.75}A_{0.25}Rh_{1-2x}Cu_xB_xO_3$ oxides have an orthorhombic *Pbnm* structure. The S-XRD study of $La_{0.75}Pb_{0.25}Rh_{1-2x}Cu_xSc_xO_3$ oxides reveals the presence of additional phases at $x \leq 0.15$. This is attributed to the solubility limit of Pb^{2+}. The amount of the structural impurity decreased as x increased.

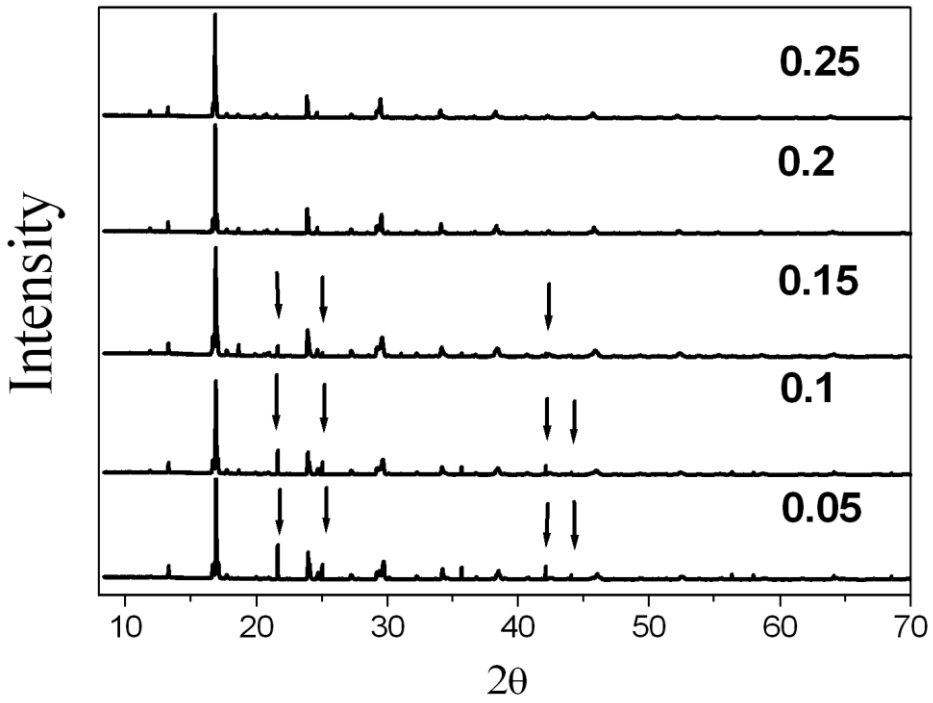

Figure 4.14 Synchrotron X-ray diffraction patterns for different compositions in the $La_{0.75}Pb_{0.25}Rh_{1-2x}Cu_xSc_xO_3$ series. The black arrows indicate the strongest impurity peaks in the patterns.

Attempts to identify the second phase were made using the X' pert high score programme. The search-match algorithm in High Score combines peak and net profile data in a single search step, which usually produces the most reliable results [33]. The impurity peaks observed in the patterns (Figure 4.14) are likely due to Pb_3O_4. The structural impurity peaks were matched with X-ray diffraction patterns for a tetragonal Pb_3O_4 with space group *P42/mbc*. The phase analysis for the sample $x = 0.05$ is shown in Figure 4.15. The reliability factors for the structure refinement using the Rietveld method are $R_p = 5.84$, $R_{wp} = 7.56$ and $\chi^2 = 1.98$. Refined lattice parameters for Pb_3O_4 were $a = 8.830(2)$ and $c = 7.106(3)$ Å. The weight percent of the second phase is ~ 6.84 %. Unlike $La_{0.75}Pb_{0.25}Rh_{1-2x}Cu_xSc_xO_3$, the $La_{0.75}Pb_{0.25}Rh_{1-2x}Cu_xZn_xO_3$ series were all a single phase with an orthorhombic *Pbnm* structure. Figure 4.16 illustrates the Rietveld refinement profiles for $La_{0.75}Pb_{0.25}Rh_{0.5}Cu_{0.25}Zn_{0.25}O_3$.

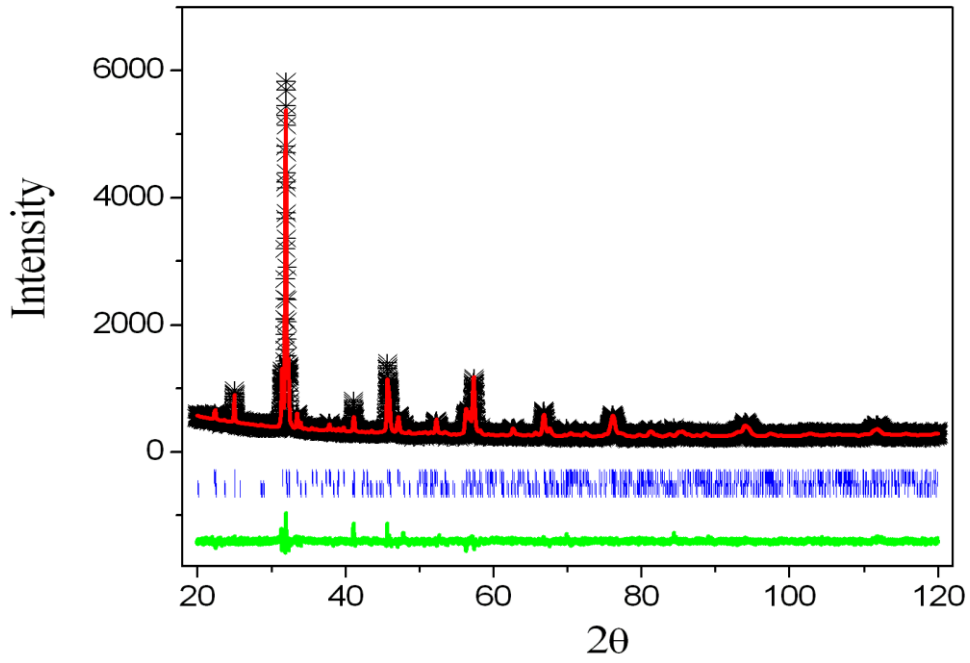

Figure 4.15 X-ray diffraction profiles for $La_{0.75}Pb_{0.25}Rh_{0.9}Cu_{0.05}Sc_{0.05}O_3$. The data are represented by the black crosses and the solid red and green lines are the observed, calculated and difference profiles. The positions of the space group allowed reflections are shown by the markers. The upper markers are for $La_{0.75}Pb_{0.25}Rh_{0.9}Cu_{0.05}Sc_{0.05}O_3$ and lower marks for Pb_3O_4.

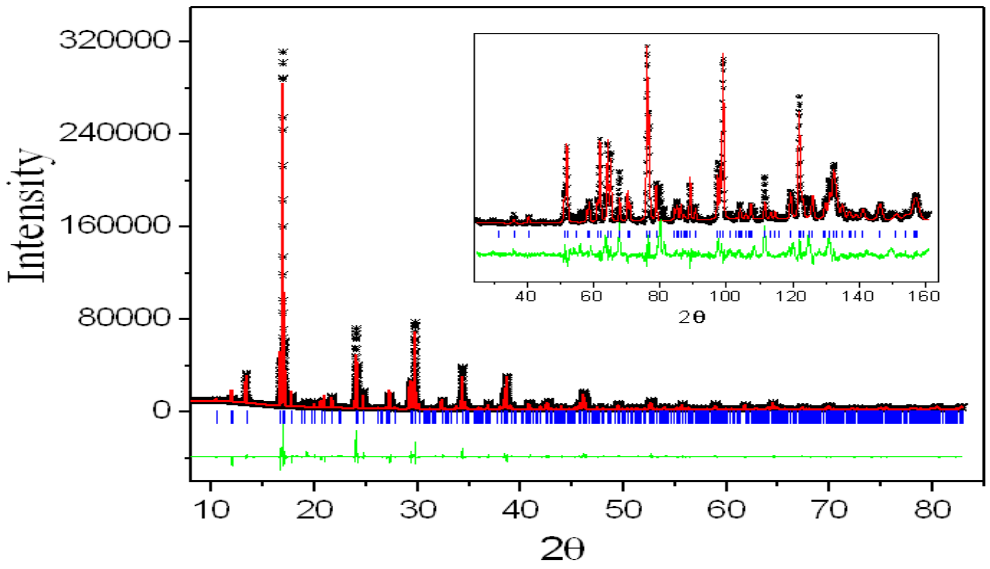

Figure 4.16 Synchrotron X-ray diffraction profiles for $La_{0.75}Pb_{0.25}Rh_{0.5}Cu_{0.25}Zn_{0.25}O_3$. The data are represented by the crosses and the solid lines are the calculated and difference profiles. The positions of the space group allowed reflections are shown by the vertical markers immediately below the observed profile. Neutron diffraction profiles of the oxide are shown in the insert. The observed impurity peaks in ND patterns are due to Pb_3O_4, that were no evident in the smaller sample used in the SXRD measurements.

The fit to the neutron diffraction data for $La_{0.75}Pb_{0.25}Rh_{0.5}Cu_{0.25}Zn_{0.25}O_3$ is summarised in Table 4.6. The data provide no evidence for oxygen vacancies. Cooling the sample to 4 K did not result in any changes to the neutron profiles indicative of no long range magnetic ordering. There is no systematic change in the *M*-O(1)-*M* and *M*-O(2)-*M* angles between 4 and 293 K. Unexpectedly, the tilt angles ψ and φ of $La_{0.75}Pb_{0.25}Rh_{0.5}Cu_{0.25}Zn_{0.25}O_3$ (11.16º, 14.32º) are found to be higher than those of $LaRh_{0.5}Cu_{0.25}Zn_{0.25}O_3$ (10.67º, 14.26º). Assuming Rh and Cu have average oxidation states of +3.5 and +2.5, we estimate the tolerance factors (τ) for $LaRh_{0.5}Cu_{0.25}Zn_{0.25}O_3$ and $La_{0.75}Pb_{0.25}Rh_{0.5}Cu_{0.25}Zn_{0.25}O_3$ to be 0.881 and 0.892 respectively. This suggests that the magnitude of tilt should be higher in $LaRh_{0.5}Cu_{0.25}Zn_{0.25}O_3$ than in $La_{0.75}Pb_{0.25}Rh_{0.5}Cu_{0.25}Zn_{0.25}O_3$. The tilt angles should decrease as tolerance factor increases [34,35]. An increase in octahedra tilting will result in a decrease in the cell volume which can be reflected from the *M*-O-*M* bond angles [36].

Table 4.6 Results of the structural refinements for $La_{0.75}Pb_{0.25}Rh_{0.5}Cu_{0.25}Zn_{0.25}O_3$ using neutron powder diffraction data. The *B* site cations are at (0, 0, 0).

Structural parameters	4K	293K
a (Å)	5.5381(5)	5.5522(4)
b (Å)	5.6641(6)	5.6567(4)
c (Å)	7.8540(6)	7.8720(5)
V ($Å^3$)	246.37(4)	247.28(3)
La/Pb *x*	0.4859(8)	0.4882(9)
La/Pb *y*	-0.0474(7)	-0.0458(7)
La/Pb *z*	1/4	1/4
La/Pb B_{iso} ($Å^2$)	0.12(14)	0.42(15)
B/Rh B_{iso} ($Å^2$)	0.78(16)	1.17(16)
O1 *x*	0.5873(13)	0.5887(13)
O1 *y*	0.5252(11)	0.5235(11)
O1 *z*	1/4	1/4
O1 B_{iso} ($Å^2$)	0.61(15)	0.90(16)
O2 *x*	0.2993(7)	0.2996(8)
O2 *y*	0.2002(7)	0.2010(7)
O2 *z*	0.0462(6)	0.0451(6)
O2 B_{iso} ($Å^2$)	0.02(12)	0.48(12)
M-(O1)-M (º)	151.19(40)	150.93(40)
M-(O2)-M (º)	149.81(21)	150.18(22)
B/ Rh-O1 (Å)	2.0272(2)	2.0331(1)
B/ Rh-O2 (Å)	2.0407(2)	2.0460(1)
B/ Rh-O2 (Å)	2.0617(2)	2.0552(1)
B/ Rh-O(av) (Å)	2.0432	2.0448
R_P (profile) (%)	12.05	11.87
R_{wp}(weighted profile) (%)	16.47	16.53
χ^2	5.54	5.58
Tilt angle (º)		
ψ (in phase)	11.22	11.16
φ (out of phase)	14.65	14.32

The bond angles in $La_{0.75}Pb_{0.25}Rh_{0.5}Cu_{0.25}Zn_{0.25}O_3$ (150.9(4)º, 150.2(2)º) are found to be lower than those in $LaRh_{0.5}Cu_{0.25}Zn_{0.25}O_3$ (151.4(3)º, 150.9(2)º). Also, $La_{0.75}Pb_{0.25}Rh_{0.5}Cu_{0.25}Zn_{0.25}O_3$ (247.30(9) $Å^3$, 293K) has lower cell volume than $LaRh_{0.5}Cu_{0.25}Zn_{0.25}O_3$ (249.08(2) $Å^3$, 293K) reflecting the increase in octahedral tilting. The neutron diffraction patterns of $La_{0.75}Pb_{0.25}Rh_{0.5}Cu_{0.25}Zn_{0.25}O_3$ showed a clear splitting of the (221) reflection indicative of a distorted symmetry. It is believed that doping by Pb^{2+} into the *A* site of $La_{0.75}Pb_{0.25}Rh_{0.5}Cu_{0.25}Zn_{0.25}O_3$ results in an increase in ion-ion repulsions that destabilize the structure as the tilt increases [37]. The increase in the *A* site covalency would also lead to small displacements of the oxygen atoms [38].

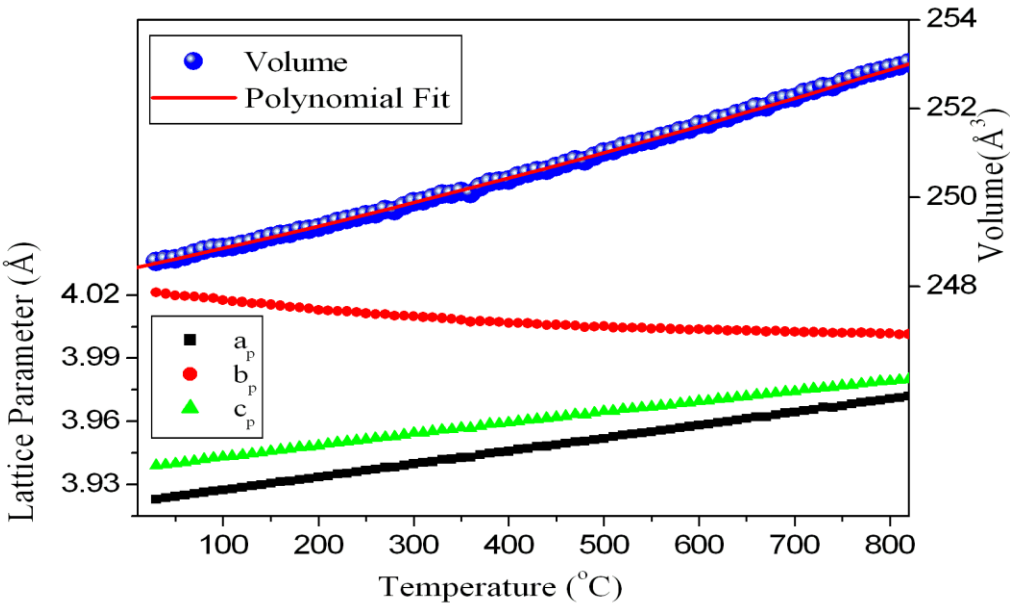

Figure 4.17 The temperature dependence of lattice parameters for $La_{0.75}Pb_{0.25}Rh_{0.5}Cu_{0.25}Zn_{0.25}O_3$ estimated by Rietveld refinement using X-ray diffraction data. The variation of the cell volume is fit by the equation $V_{(t)} = 248.37(2) + 4.67(7)\times10^{-3}\,T + 1.19(1)\times10^{-6}\,T^2$.

The tilt angles ψ and φ of $La_{0.75}Pb_{0.25}Rh_{0.5}Cu_{0.25}Zn_{0.25}O_3$ were found to decrease as temperature increased and these cause an increase in the cell volume [19]. The displacements of oxygen O(2) ($u \cong w \cong 0.050$) are about the same suggesting the octahedra are reasonably rigid. $La_{0.75}Pb_{0.25}Rh_{0.5}Cu_{0.25}Zn_{0.25}O_3$ has $\Delta d = 6.418 \times 10^{-5}$ which is lower than that in $LaRh_{0.5}Cu_{0.25}Zn_{0.25}O_3$ ($\Delta d = 7.345 \times 10^{-5}$). The suppression of the octahedral distortion is believed to be positively correlated with

tilting [34], although variable temperature neutron diffraction analysis would be required to confirm this. The VT-XRD measurements demonstrate the orthorhombic structure of $La_{0.75}Pb_{0.25}Rh_{0.5}Cu_{0.25}Zn_{0.25}O_3$ persists over the temperature range 30 to 800 °C. The temperature dependence of the lattice parameters for $La_{0.75}Pb_{0.25}Rh_{0.5}Cu_{0.25}Zn_{0.25}O_3$ is illustrated in Figure 4.17. There was no evidence for a structural transformation. The observed negative thermal expansion of *b* parameter for $La_{0.75}Pb_{0.25}Rh_{0.5}Cu_{0.25}Zn_{0.25}O_3$ is similar to that found for $La_{0.75}Pb_{0.25}Rh_{0.5}Cu_{0.5}O_3$ (section 3.2.2) and is thought to be a consequence of the reduction in the tilting upon heating.

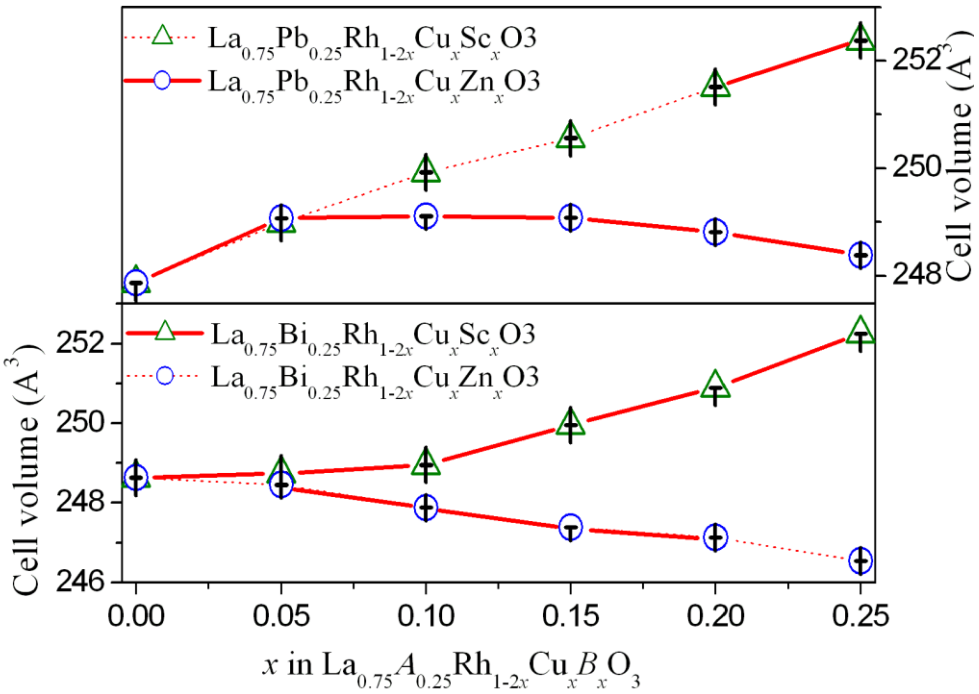

Figure 4.18 Composition dependence of the cell volume in $La_{0.75}A_{0.25}Rh_{1-2x}Cu_xB_xO_3$ estimated by Rietveld refinement using synchrotron X-ray diffraction data. Where not obvious the error bars are smaller than the symbols. The dashed lines cover the samples that contain a second phase.

The S-XRD measurements of $La_{0.75}A_{0.25}Rh_{1-2x}Cu_xB_xO_3$ showed the cell volumes are influenced by both the *A* and *B* site dopings. As found for $LaRh_{1-2x}Cu_xB_xO_3$, in Section 4.2.2, doping Sc^{3+} onto the *B* site results in an increase in the cell volume whereas doping by divalent Zn^{2+} decreases the volume. The composition dependent variation of the cell volume (Figure 4.18) is more linear than that in the

$LaRh_{1-2x}Cu_xB_xO_3$ oxides. This possibly indicates small displacements of the *A* site cations may be enhanced by covalency. The cell volumes of $La_{0.75}Bi_{0.25}Rh_{0.5}Cu_{0.5}O_3$ (246.607(4) $Å^3$) and $La_{0.75}Pb_{0.25}Rh_{0.5}Cu_{0.5}O_3$ (247.868(3) $Å^3$) are found to be either higher, or lower, than those of the $La_{0.75}Bi_{0.25}Rh_{0.5}Cu_{0.25}Zn_{0.25}O_3$ (246.537(3) $Å^3$) and $La_{0.75}Pb_{0.25}Rh_{0.5}Cu_{0.25}Zn_{0.25}O_3$ (248.385(3) $Å^3$), suggesting the average oxidation states of the Rh may be lower than 3.5 + in the Bi doped oxides, but higher in those in the Pb doped oxides. These results correlate with the distortion in $La_{0.75}Bi_{0.25}Rh_{0.5}Cu_{0.25}Zn_{0.25}O_3$, and a significant decrease in the values of thermal parameters B_{iso} of La(Pb) from 1.66(10) $Å^2$ for $La_{0.75}Pb_{0.25}Rh_{0.5}Cu_{0.5}O_3$ to 0.47(01) $Å^2$ for $La_{0.75}Pb_{0.25}Rh_{0.5}Cu_{0.25}Zn_{0.25}O_3$. The large B_{iso} value in the former case may be related to local disorder [39].

Table 4.7 Lattice parameter distortions *D*, octahedral distoration Δd and bond angles *M*-O(1)-*M* and *M*-O(2)-*M* for $La_{0.75}A_{0.25}Rh_{0.5}Cu_{0.25}B_{0.25}O_3$ oxides.

Compound	*D (%)*	$\Delta d \times 10^{-4}$	*M*-O(1)-*M*	*M*-O(2)-*M*
$La_{0.75}Bi_{0.25}Rh_{0.5}Cu_{0.25}Sc_{0.25}O_3$	0.85	0.05	150.5(2) º	151.8(2)º
$La_{0.75}Bi_{0.25}Rh_{0.5}Cu_{0.5}O_3$	0.91	8.76	151.2(6)º	154.7(5)º
$La_{0.75}Bi_{0.25}Rh_{0.5}Cu_{0.25}Zn_{0.25}O_3$	0.92	15.79	148.6(8)º	150.6(5)º
$La_{0.75}Pb_{0.25}Rh_{0.5}Cu_{0.25}Sc_{0.25}O_3$	0.56	15.22	150.3(6)º	152.9(4)º
$La_{0.75}Pb_{0.25}Rh_{0.5}Cu_{0.5}O_3$	1.15	1.67	151.3(3)º	150.6(1)º
$La_{0.75}Pb_{0.25}Rh_{0.5}Cu_{0.25}Zn_{0.25}O_3$	0.95	0.64	151.2(4)º	150.0(2)º

Table 4.7 demonstrates that the distortion of the BO_6 octahedra is negatively correlated with the cell volume of the oxides. Δd for $La_{0.75}Bi_{0.25}Rh_{0.5}Cu_{0.25}Sc_{0.25}O_3$ is less than that for $La_{0.75}Bi_{0.25}Rh_{0.5}Cu_{0.5}O_3$ and $La_{0.75}Bi_{0.25}Rh_{0.5}Cu_{0.25}Zn_{0.25}O_3$, whereas Δd for $La_{0.75}Pb_{0.25}Rh_{0.5}Cu_{0.25}Sc_{0.25}O_3$ is greater than that for $La_{0.75}Pb_{0.25}Rh_{0.5}Cu_{0.5}O_3$ and $La_{0.75}Pb_{0.25}Rh_{0.5}Cu_{0.25}Zn_{0.25}O_3$. This suggest that the oxide system is balanced as a consequence of charge delocalization between $Rh^{3+/4+}$ and $Cu^{2+/3+}$ ions. Doping by isovalent cations such as Pb^{2+} and Zn^{2+} or Bi^{3+} and Sc^{3+} resulted in equivalent magnitudes of distortions. For instance, Δd for $La_{0.75}Bi_{0.25}Rh_{0.5}Cu_{0.25}Zn_{0.25}O_3$ (15.79×10^{-4}) is equivalent to that for $La_{0.75}Pb_{0.25}Rh_{0.5}Cu_{0.25}Sc_{0.25}O_3$ ($\Delta d = 15.22 \times 10^{-4}$). It was found that Δd increases as the bond angles *M*-O(1)-*M* and *M*-O(2)-*M*

decrease in the $La_{0.75}Bi_{0.25}Rh_{0.5}Cu_{0.5}O_3$ and $La_{0.75}Bi_{0.25}Rh_{0.5}Cu_{0.25}Zn_{0.25}O_3$, whereas Δd decreases as the lattice distortion D increases in $La_{0.75}Pb_{0.25}Rh_{0.5}Cu_{0.5}O_3$ and $La_{0.75}Pb_{0.25}Rh_{0.5}Cu_{0.25}Zn_{0.25}O_3$. The anisotropy in bond distances, lattice parameter and bond angles of the oxides are all a consequence of the tilting of the BO_6 octahedra [40].

4.3.3 Magnetization

The inverse susceptibility plots (Figure 4.19) show the magnetic susceptibilities for the $La_{0.75}A_{0.25}Rh_{0.5}Cu_{0.25}Zn_{0.25}O_3$ oxides are approximately 15 times higher than those for the $La_{0.75}A_{0.25}Rh_{0.5}Cu_{0.25}Sc_{0.25}O_3$ oxides. This is because of the partial oxidation of Rh^{3+} ($3d^6$) to Rh^{4+} ($3d^5$). Doping by Bi^{3+} or Pb^{2+} into the A site results in a decrease in the susceptibility which is consistent with the increase in the A site covalency. The electronegativity of both Bi^{3+}(2.02) [41] and Pb^{2+} (1.87) [41] is greater than that of La^{3+}(1.10) [41]. These results are in an agreement with those found for the $LaRh_{1-2x}Cu_xB_xO_3$ oxides (section 4.2.3) and for the $La_{0.75}A_{0.25}Rh_{0.5}Cu_{0.5}O_3$ oxides (section 3.2.3) in which the susceptibility increases as the content of divalent dopant increased, and decreases as the covalency of the A site dopant increased.

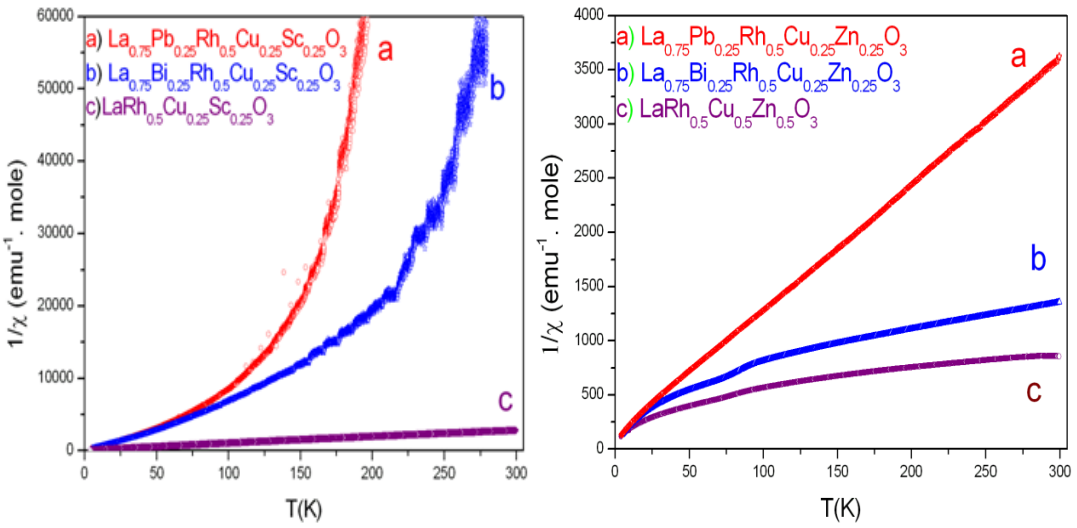

Figure 4.19 The temperature dependence of the inverse susceptibility for $La_{0.75}A_{0.25}Rh_{0.5}Cu_{0.25}Sc_{0.25}O_3$ and $La_{0.75}A_{0.25}Rh_{0.5}Cu_{0.25}Zn_{0.25}O_3$ recorded under zero field cooling conditions with an applied field of 5 kOe. The noisy data for $La_{0.75}A_{0.25}Rh_{0.5}Cu_{0.25}Sc_{0.25}O_3$ at high temperature reflects the sensitivity limits of the instrument at lower susceptibility values.

The best linear fit to the inverse magnetization curves (Table 4.8) provides an estimate for the effective magnetic moments (μ_{eff}) for the oxides and these are negative correlated with the Weiss constant (Θ). Except for $La_{0.75}Bi_{0.25}Rh_{0.5}Cu_{0.25}Sc_{0.25}O_3$ (+60.9 K) and $La_{0.75}Pb_{0.25}Rh_{0.5}Cu_{0.25}Sc_{0.25}O_3$ (+28.4 K), the Weiss constants were negative for the all oxides suggesting weak antiferromagnetic interactions. The magnetic susceptibility measurements for $La_{0.75}Pb_{0.25}Rh_{0.5}Cu_{0.5}O_3$ (0.83 μ_B, -24.4 K) and $La_{0.75}Pb_{0.25}Rh_{0.5}Cu_{0.25}Zn_{0.25}O_3$ (0.83 μ_B, 11.5 K) gave a lower magnetic moment than that for $LaRh_{0.5}Cu_{0.5}O_3$ (1.17 μ_B, -23.5 K) and $LaRh_{0.5}Cu_{0.25}Zn_{0.25}O_3$ (1.91μ_B, -131.1K) indicative of magnetic coupling. It is believed that the spin orientation is influenced by the $6s^2$ electrons of the Pb^{2+} ion resulting in a reduction in magnetization [42,43]. Figure 4.20 shows the temperature dependence of the inverse susceptibility for $LaRh_{0.5}Cu_{0.5}O_3$, $LaRh_{0.5}Cu_{0.25}Zn_{0.25}O_3$, $La_{0.75}Pb_{0.25}Rh_{0.5}Cu_{0.5}O_3$ and $La_{0.75}Pb_{0.25}Rh_{0.5}Cu_{0.25}Zn_{0.25}O_3$. Hysteresis loop measurements show the absence of any long range magnetic ordering. In general, all the studied samples exhibit spin glass magnetic behaviour as was evident from the magnetic susceptibility measurements.

Table 4.8 Curie constant *C*, Weiss constant Θ, magnetic susceptibly coefficient factor χ_o, and effective magnetic moment μ_{eff} for $La_{0.75}A_{0.25}$ $Rh_{0.5}Cu_{0.25}B_{0.25}O_3$.

Compound	Θ (K)	χ_o (10^{-3})	C (emu. mole$^-$)	μ_{eff} (μ_B)
$LaRh_{0.5}Cu_{0.25}Sc_{0.25}O_3$	-14.6	7.412	1.596	0.93
$LaRh_{0.5}Cu_{0.5}O_3$	-23.5	7.337	4.057	1.17
$LaRh_{0.5}Cu_{0.25}Zn_{0.25}O_3$	-131.1	3.495	60.077	1.91
$La_{0.75}Bi_{0.25}Rh_{0.5}Cu_{0.25}Sc_{0.25}O_3$	+60.9	-0.069	4.057	0.18
$La_{0.75}Bi_{0.25}Rh_{0.5}Cu_{0.5}O_3$	-5.9	10.965	0.388	0.72
$La_{0.75}Bi_{0.25}Rh_{0.5}Cu_{0.25}Zn_{0.25}O_3$	-113.4	2.537	32.646	1.51
$La_{0.75}Pb_{0.25}Rh_{0.5}Cu_{0.25}Sc_{0.25}O_3$	+28.4	-3.113	-0.251	0.26
$La_{0.75}Pb_{0.25}Rh_{0.5}Cu_{0.5}O_3$	-24.4	3.550	2.108	0.83
$La_{0.75}Pb_{0.25}Rh_{0.5}Cu_{0.25}Zn_{0.25}O_3$	-11.5	7.491	0.987	0.83

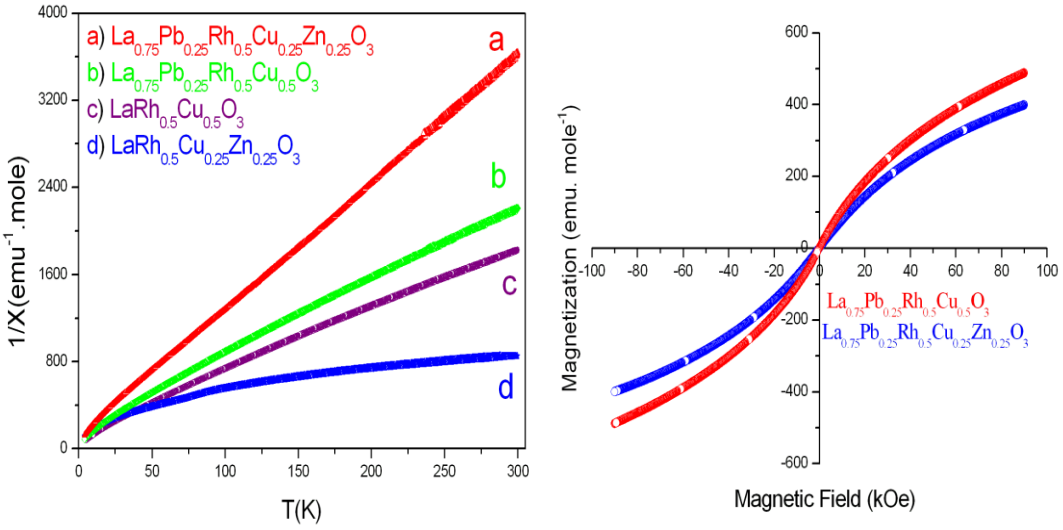

Figure 4.20 The temperature dependence of the inverse susceptibility for $La_{0.75}A_{0.25}Rh_{0.5}Cu_{0.25}B_{0.25}O_3$ oxides (A = La^{3+} and Bi^{3+}; B = Cu^{2+} and Zn^{2+}) recorded under zero field cooling conditions with an applied field of 5 kOe. Magnetization hysteresis loops for $La_{0.75}Pb_{0.25}Rh_{0.5}Cu_{0.5}O_3$ and $La_{0.75}Pb_{0.25}Rh_{0.5}Cu_{0.25}Zn_{0.25}O_3$ at 5K are also illustrated.

4.3.4 Electrical conductivity

Electrical conductivity measurements show that doping $La_{0.75}A_{0.25}Rh_{0.5}Cu_{0.25}B_{0.25}O_3$ with either Pb or Bi lowers the conductivity of the oxides, suggesting an increase in the band gap occurs as a result of the strong interaction between Pb^{2+} and Bi^{3+} 6*s* orbitals and the 3*d* and 4*d* orbitals of the *B* site cations. The conductivity of $LaRh_{0.5}Cu_{0.25}Zn_{0.25}O_3$ (476.86 Ω^{-1}) is around 40 times higher than that of $La_{0.75}Pb_{0.25}Rh_{0.5}Cu_{0.25}Zn_{0.25}O_3$ (12.24 Ω^{-1}) at 300K. Likewise, the conductivity of $LaRh_{0.5}Cu_{0.25}Sc_{0.25}O_3$ (1.66×10^{-1} Ω^{-1}) is ~50 times higher than that of $La_{0.75}Bi_{0.25}Rh_{0.5}Cu_{0.25}Sc_{0.25}O_3$ (3.15×10^{-3} Ω^{-1}) at 300K. The Arrhenius plot (Figure 4.21) gave activation energies for $LaRh_{0.5}Cu_{0.25}Zn_{0.25}O_3$ (0.046 eV), $La_{0.75}Bi_{0.25}Rh_{0.5}Cu_{0.25}Zn_{0.25}O_3$ (0.043 eV) and $La_{0.75}Pb_{0.25}Rh_{0.5}Cu_{0.25}Zn_{0.25}O_3$ (0.036 eV) that are significantly smaller than that found for $LaRh_{0.5}Cu_{0.5}O_3$ (0.055 eV). This is attributed to differences in the charge delocalization. The $La_{0.75}Bi_{0.25}Rh_{0.5}Cu_{0.25}Sc_{0.25}O_3$ (0.110 eV) and $La_{0.75}Pb_{0.25}Rh_{0.5}Cu_{0.25}Zn_{0.25}O_3$ oxides exhibit lower activation energies than $La_{0.75}Bi_{0.25}Rh_{0.7}Cu_{0.15}Sc_{0.15}O_3$ (0.156 eV) and $La_{0.75}Pb_{0.25}Rh_{0.7}Cu_{0.15}Zn_{0.15}O_3$ (0.105 eV), suggesting a decrease in the divalent dopant content lowers the activation energies of the compounds. Doping with

divalent cations introduces holes in the electronic structure as result of the oxidation of Rh^{3+} to Rh^{4+}. The introduction of holes in the band gap semiconductor allows excitation of valence band electrons, leaving mobile holes in the valence band [44].

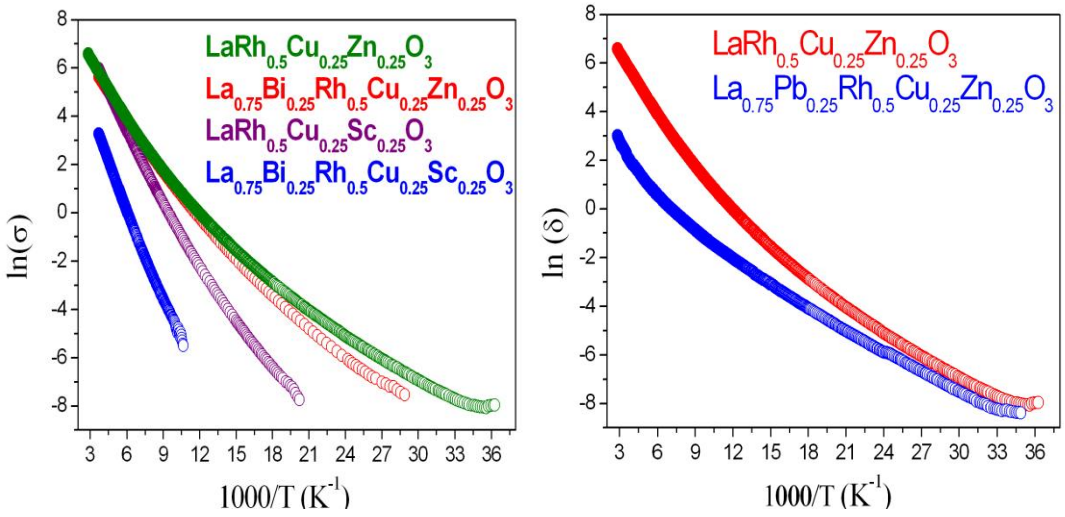

Figure 4.21 The Arrhenius plots of Ln (σ) verses inverse temperature for $La_{0.75}A_{0.25}Rh_{0.5}Cu_{0.25}B_{0.25}O_3$ perovskites.

4.3.5 Summary

Various samples of $La_{0.75}A_{0.25}Rh_{1-2x}Cu_xB_xO_3$ (A = Pb^{2+} and Bi^{3+}; B = Sc^{3+}, Cu^{2+} and Zn^{2+}) were prepared and characterized. Doping either Pb or Bi into the A site did not alter the space group symmetry. $La_{0.75}Pb_{0.25}Rh_{1-2x}Cu_xSc_xO_3$ contained an impurity for $x \leq 0.15$ due to the solubility limit of Pb. Doping Sc^{3+} and Zn^{2+} into the B site of $La_{0.75}A_{0.25}Rh_{1-2x}Cu_xB_xO_3$ alters the cell volumes. The cell volumes of the oxides were found to be negatively correlated with the octahedral distortion. The changes in the cell volumes, octahedral distortion and the bond angles of the oxides are mainly attributed to the effects of the octahedral tilting and the charge delocalization between the Rh and Cu ions. The decrease in the effective magnetic moments and the electrical conductivities of the $La_{0.75}A_{0.25}Rh_{1-2x}Cu_xB_xO_3$ oxides suggests that doping Pb and Bi into the A site results in magnetic coupling and an increase in the band gap.

4.4 References

[1] H. Usui, K. Kuroki, R. Arita, *Journal of Physics: Conference Series*, 150 (2009) 022095.

[2] S. Shibasaki, Y. Takahashi, I. Terasaki, *Journal of Electronic Material*, 38 (2009) 1013-1016.

[3] S. Asai, N. Furuta, R. Okazaki, Y. Yasui, I. Terasaki, *Physical Review B*, 86 (2012) 014421.

[4] K. Knížek, J. Hejtmánek, M. Maryško, Z. Jirák, J. Buršík, *Physical Review B*, 85 (2012) 134401.

[5] M.T. Haque, H. Satoh, N. Kamegashira, *Journal of Alloys and Compounds*, 390 (2005) 115-121.

[6] S. Shibasaki, Y. Takahashi, I. Terasaki, *Journal of Physics: Condensed Matter*, 21 (2009) 115501.

[7] K.S. Kwong, A.E. Smith, M.A. Subramanian, *Materials Research Society*, 1267 (2010) 267.

[8] J. Li, A.E. Smith, K.-S. Kwong, C. Powell, A.W. Sleight, M.A. Subramanian, *Journal of Solid State Chemistry*, 183 (2010) 1388-1393.

[9] J. Ting, B.J. Kennedy, Z. Zhang, M. Avdeev, B. Johannessen, L.Y. Jang, *Chemistry of Materials*, 22 (2010) 1640-1646.

[10] A.E. Smith, A.W. Sleight, M.A. Subramanian, *Materials Research Bulletin*, 45 (2010) 460-463.

[11] Z.L. Gong, X.O. Yin, L.A. Hong, *Journal of the Electrochemical Society*, 157 (2010) 129-134.

[12] R.D. Shannon, *Acta Crystallographica Section A*, 32 (1976) 751-767.

[13] K. Liss, B. Hunter, M. Hagen, T. Noakes, S. Kennedy, *Physica B*, 385–386 (2006) 1010–1012.

[14] K.S. Wallwork, B.J. Kennedy, D.A. Wang, *AIP Conference Proceedings*, 879 (2007) 879-882.

[15] B.A. Hunter, C.J. Howard, RIETICA. A Computer Program for Rietveld Analysis of X-Ray and Neutron Powder Diffraction Patterns, (1998)

[16] T.E. Dann, S.C. Chung, L.J. Huang, J.M. Juang, C.I. Chen, K.L. Tsang, *Journal of Synchrotron Radiation*, 5 (1998) 664-666.

[17] R.B. Macquart, M.D. Smith, H.-C. Zur Loye, *Crystal Growth & Design*, 6 (2006) 1361-1365.

[18] G.A. Gehring, *Journal of Physics C: Solid State Physics*, 7 (1974) L379.

[19] B.J. Kennedy, C.J. Howard, B.C. Chakoumakos, *Journal of Physics: Condensed Matter*, 11 (1999) 1479.

[20] R. Ranjan, A. Senyshyn, V. Vashook, R. Niewa, H. Boysen, F. Frey, *Applied Physics Letters*, 90 (2007) 251913.

[21] R. Ranjan, R. Garg, A. Senyshyn, M.S. Hegde, H. Ehrenberg, H. Boysen, *Journal of Physics: Condensed Matter*, 21 (2009) 326001.

[22] A.N. Salak, O. Prokhnenko, V.M. Ferreira, *Journal of Physics: Condensed Matter*, 20 (2008) 085210.

[23] R. Ubic, Y. Hu, I. Abrahams, *Acta Crystallographica Section B*, 62 (2006) 521-529.

[24] J.M. Zhang, D.N. Ye, C.T. Prewitt, *American Mineralogist*, 76 (1991) 100-105.

[25] D.C. Koningsberger, R. Prins, X-Ray Absorption: Principles, Applications, Techniques of EXAFS, SEXAFS and XANES, 1987, John Wiley and Sons Inc, New York.

[26] P.J. Potts, J.F.W. Bowles, S.J.B. Reed, M. Society, M.R. Cave, Microprobe Techniques in the Earth Sciences, 1995, Chapman & Hall, New York.

[27] T. Burnus, Z. Hu, H. Wu, J.C. Cezar, S. Niitaka, H. Takagi, C.F. Chang, N.B. Brookes, H.J. Lin, L.Y. Jang, A. Tanaka, K.S. Liang, C.T. Chen, L.H. Tjeng, *Physical Review B*, 77 (2008) 205111.

[28] IFEFFIT: Interactive XAFS Analysis, http://cars.uchicago.edu; 2012

[29] M.A. Carpenter, C.J. Howard, *Acta Crystallographica Section B*, 65 (2009) 134-146.

[30] A. Arulraj, R.E. Dinnebier, S. Carlson, M. Hanfland, S. van Smaalen, *Progress in Solid State Chemistry*, 35 (2007) 367-377.

[31] T. Taniguchia, W. Iizukaa, Y. Nagataa, T. Uchidab, H. Samatac, *Journal of Alloys and Compounds*, 350 (2003) 24-29.

[32] T. Ohnishia, T. Taniguchia, A. Ikoshia, S. Mizusakia, Y. Nagataa, S.H. Lai, M.D. Lanb, Y. Noroc, T.C. Ozawad, K. Kindoe, A. Matsuoe, S. Takayanagif, *Journal of Alloys and Compounds*, 506 (2010) 27-32.

[33] HighScore, Panalytical, http://www.panalytical.com; 2012

[34] M.W. Lufaso, P.M. Woodward, *Acta Crystallographica Section B*, 60 (2004) 10-20.

[35] M.W. Lufaso, P.M. Woodward, *Acta Crystallographica Section B*, 57 (2001) 725-738.

[36] P. Woodward, *Acta Crystallographica Section B*, 53 (1997) 32-43.

[37] P. Woodward, *Acta Crystallographica Section B*, 53 (1997) 44-66.

[38] C. Elissalde, A. Villesuzanne, V. Hornebecq, J. Ravez, *Ferroelectrics*, 229 (1999) 1-10.

[39] N.W. Thomas, S.A. Ivanov, S. Ananta, R. Tellgren, H. Rundlof, *Journal of the European Ceramic Society*, 19 (1999) 2667-2675.

[40] Y. Shimakawa, *Inorganic Chemistry*, 47 (2008) 8562-8570.

[41] A.L. Allred, *Journal of Inorganic and Nuclear Chemistry*, 17 (1961) 215-221.

[42] P. Baettig, C. Ederer, N.A. Spaldin, *Physical Review B*, 72 (2005) 214105.

[43] L.M. Volkova, D.V. Marinin, *Journal of Superconductivty and Novel Magnetism*, 24 (2011) 2161-2177.

[44] W. Shockley, Electrons and Holes in Semiconductors: with Applications to Transistor Electronics, 1950, Van Nostrand, New York.

Structural, Electrical and Magnetic Studies of *A* site and *B* Site Doped $TbRh_{1-x}Cu_xO_3$ (*A* = Ca^{2+}, Pb^{2+} and Bi^{3+}; *B* = Sc^{3+} and Zn^{2+})

5.1 Introduction

Like other 4*d* transition metal oxides, orthorhodates have been investigated as potential candidates for use in devices such as metallic conductors, catalysts and anode materials in photoelectrolytic cells [1,2]. The 4*d* electrons have a large spatial distribution, very strong spin orbital coupling and large ligand field effect [3,4]. There are only few studies addressing the behaviour of lanthanoid ions in orthorhodates [5,6]. Lanthanoid oxides exhibit fascinating magnetic properties due to the large spin and orbital angular moment of the lanthanoid ions [7,8]. The magnetic moment of 4*f* electrons is shielded by the outer orbital electrons and, therefore, magnetic dipole interaction between rare-earth cations is often comparable, or superior, to the superexchange interaction in the oxides [7,8].

The lanthanoid rhodium oxides ($LnRhO_3$), containing trivalent rhodium, adopt distorted perovskite structures with orthorhombic symmetry space group *Pbnm* [6]. The crystal lattice of $LnRhO_3$ becomes more distorted as the size of the *Ln* cation decreases and the number of 4*f* electrons increase [5,9]. The tilting of the RhO_6 octahedra increases as the ionic radius of the lanthaniod ion decreases leading to an increase in the orthorhombicity. The orthorhombicity of such compounds is given by $(b-a)/a$ (where a and b are the lattice constants) [5,10]. The magnetic moment of the $LnRhO_3$ compounds are strongly influenced by the 4*f* electrons of the lanthanoid ions. However in some cases, such as $EuRhO_3$, a noticeable contribution of the 4*d* electrons can add to the magnetization. This is due to a charge compensation of Rh^{3+} to Rh^{4+} resulting from the coexistence of mixed valence Eu^{2+} and Eu^{3+} cations [5]. The resistivity of all $LnRhO_3$ oxides has an activation-type (or semiconductor-like) temperature dependence. The changes in the crystal lattice are thought to modify the band structure increasing the activation energy [5,11].

Substitution at the *A*- and *B*- site can significantly alter the properties of $LnRhO_3$. One such example is the perovskite $LaRh_{0.5}Mn_{0.5}O_3$. The compound shows ferromagnetic behaviour at low temperatures [12,13], but the substitution of lanthanoid elements with higher atomic number such as Gd suppresses the ferromagnetic

interaction [13]. The electrical conductivity shows semiconducting behaviour above room temperature and the conductivity decreases as the size of the lanthanoid decreases [13].

5.1.1 Aims and Objectives

In order to understand the role of the *Ln* cation on the properties of mixed metal Rh-Cu perovskites, a series of oxides of the type $TbRh_{1-x}Cu_xO_3$ was synthesized and characterized. Tb was chosen as an alternate to La since this has the possibility of existing as Tb^{3+} or Tb^{4+}. It is postulated that charge delocalization between Rh and Cu would influence the formal valency of the *A* cations resulting in a partial oxidation of Tb^{3+} to Tb^{4+}. In this study, the effects of charge delocalization on the structural, electrical and magnetic properties of both *A* and *B*-site doped $TbRh_{1-x}Cu_xO_3$ (*B* = Sc^{3+}, Cu^{2+} and Zn^{2+}; *A* = Ca^{2+}, Sr^{2+}, Pb^{2+} and Bi^{3+}) is discussed. The aim of this work was to investigate the role of the 4 *f* rare earth cation in controlling the structural and physical properties of these perovskites.

5.1.2 Methodology

Reactants were $Tb(NO_3)_3.5H_2O$ (Aldrich ≥ 99.9 %), Sc_2O_3, Bi_2O_3, PbO (Aldrich ≥ 99.99 %), CuO, ZnO (Merck, ≥ 99%) and Rh (Althaca 99.95 %). The preparation started by mixing the raw materials, and then heating these in several steps. Before each heating step, the materials were finely ground by a mortar and pestle. Samples were heated to 850 $^{\circ}$C for 24 h followed by heating at 950 $^{\circ}$C for 24 h, and then 1000 $^{\circ}$C for 48 h and 1050 $^{\circ}$C for 48 h. The reaction was completed by heating at 1100 $^{\circ}$C for 48 h. Synchrotron X-ray powder diffraction data were collected over the angular range $5 < 2\theta < 85°$, using X-rays of wavelength 0.82554 Å on the powder diffractometer at the Australian Synchrotron [14]. Samples were packed into 0.3 mm diameter capillaries. The structures were refined using the program RIETICA [15]. The peak shapes were modelled using a pseudo Voigt function.

The magnetic measurements were carried out using a Quantum Design, PPMS. The temperature dependence of the magnetic susceptibilities was measured under both zero-field cooled (ZFC) and field cooled (FC) conditions in an applied field of 5 kOe over the temperature range 4-300 K. The temperature dependence of the resistivity was measured using a DC four probe technique with the same

measurement system. The sintered samples were cut into pieces of size approximately 3 × 5 mm. Four contacts were painted onto the samples using silver paste. The microstructure of the powder samples was examined by scanning electron microscopy (SEM) using a Intellection Quemscan**.**

5.2 Results and discussion: $Tb_{1-y}A_yRh_{1-2x}Cu_xB_xO_3$

Various compositions of $TbRh_{1-2x}Cu_xB_xO_3$ (B = Sc^{3+}, Cu^{2+} and Zn^{2+}), $Tb_{0.75}A_{0.25}Rh_{0.7}Cu_{0.3}O_3$ (A = Ca^{2+}, Sr^{2+}, Pb^{2+} and Bi^{3+}), $Tb_{1-y}Pb_yRh_{0.6}Cu_{0.4}O_3$ and $Tb_{0.75}Bi_{0.25}Rh_{1-2x}Cu_xSc_xO_3$ were prepared and characterized. The $TbRh_{1-2x}Cu_{2x}O_3$ samples generally have the same physical properties as the La^{3+} analogous. However, the cell volume and magnetic susceptibility of the oxides were sensitive to the presence of Tb^{3+}. Single phases with an orthorhombic structure were obtained for y = 0.3 and x = 0.2 for the A and B sites respectively.

5.2.1 Visual Inspection

The heating regime described above produced black coloured samples. After heating at 1000 ºC, the colour of the all samples turns from dark yellow to brown. This suggests changes in the electronic structure, involving the redistribution of *d* and *f* electrons via redox reactions. SEM measurements (Figure 5.1) show doping with Cu^{2+} results in particles of larger size and higher apparent crystallinity than in undoped $TbRhO_3$.

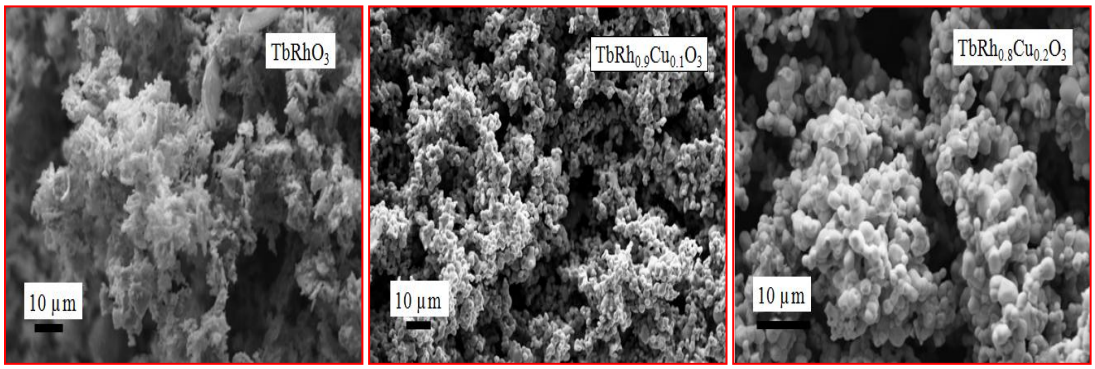

Figure 5.1 Scanning Electron Micrograph images for $TbRhO_3$, $TbRh_{0.9}Cu_{0.1}O_3$ and $TbRh_{0.8}Cu_{0.2}O_3$.

SEM images for some representative examples of the doped $TbRh_{1-x}Cu_xO_3$ oxides are also shown in Figure 5.2. Doping with divalent cations, such as Pb^{2+} and Zn^{2+}, results in more crystalline samples than doping with trivalent cations such as

Bi^{3+} and Sc^{3+}. The sample of $Tb_{0.75}Ca_{0.25}Rh_{0.7}Cu_{0.3}O_3$ has better formed particles (size and shape) than the sample of $Tb_{0.75}Pb_{0.25}Rh_{0.7}Cu_{0.3}O_3$. This possibly reflects the influence of the relative sizes of the *A* dopant cations on the crystal packing. Ca^{2+} (8-coordinate ionic radius, 1.12 Å[16]) has smaller ionic size than Pb^{2+}(1.29 Å)[16]. Elemental analysis showed the oxides have their nominal composition.

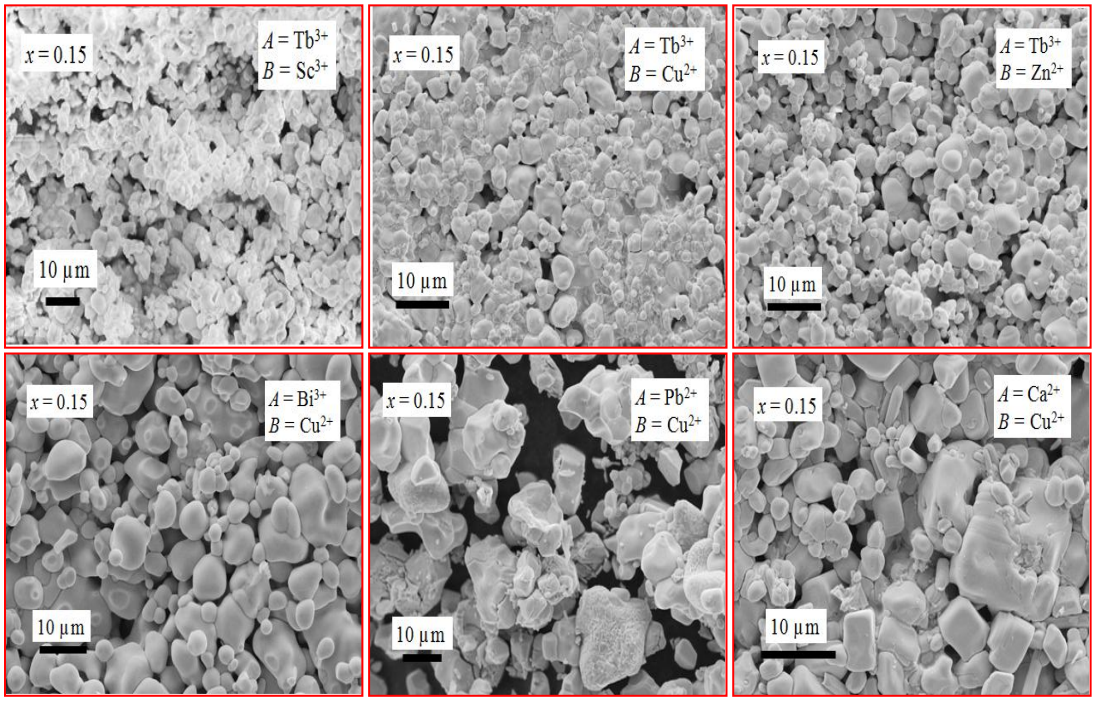

Figure 5.2 Scanning Electron Micrograph images for $TbRh_{0.7}Cu_{0.15}B_{0.15}O_3$ where B = Sc^{3+}, Cu^{2+}, and Zn^{2+} and $Tb_{0.75}A_{0.25}Rh_{0.7}Cu_{0.3}O_3$ where A = Bi^{3+}, Pb^{2+}, and Ca^{2+}.

5.2.2 Crystal Structure

Except for $TbRhO_3$, samples in the four solid solution series were found to be single phase under the preparation conditions described above. The observed peaks from X- ray profiles can be indexed on the basis of an orthorhombic unit cell (space group *Pbnm*). This is one of the most commonly observed distortions of the perovskite structure [17]. The preparation of an extensive solid state solution allows us to study the effects of altering the chemical composition on the physical properties. The results of the structural refinements, obtained from Rietveld analysis against the synchrotron diffraction data, are summarized below. Figure 5.3 illustrates, as a representative example, the Rietveld refinement profiles for $TbRh_{0.6}Cu_{0.4}O_3$.

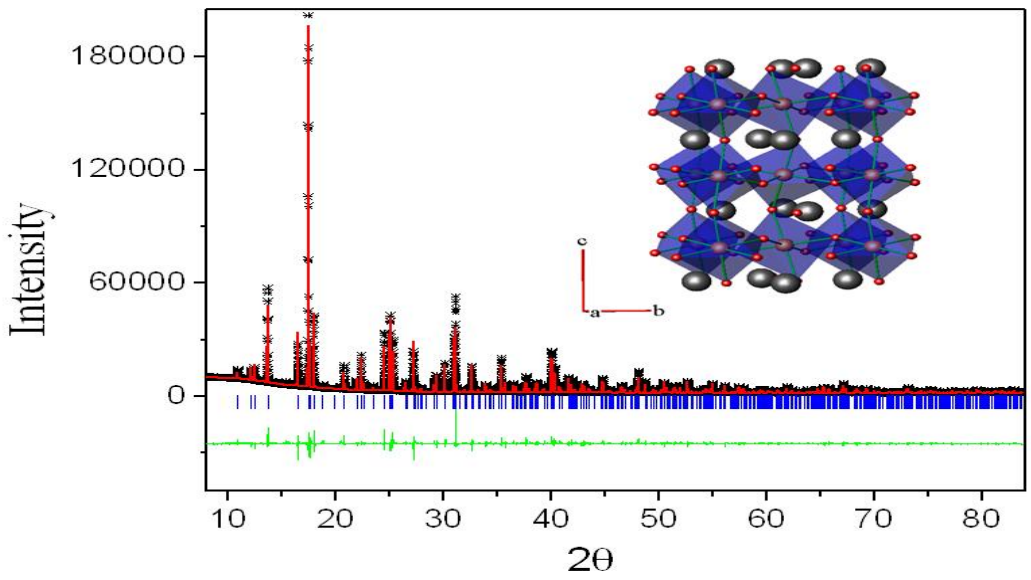

Figure 5.3 Synchrotron X-ray diffraction profiles for $TbRh_{0.6}Cu_{0.4}O_3$. The data are represented by the crosses and the solid lines are the calculated and difference profiles. The positions of the space group allowed reflections are shown by the vertical markers immediately below the observed profile. A representation of the $TbRh_{0.6}Cu_{0.4}O_3$ structure is included.

The crystallographic data for $TbRh_{0.6}Cu_{0.4}O_3$ and $LaRh_{0.6}Cu_{0.4}O_3$ are given in Table 5.1. The diffraction studies demonstrate that the Cu and Rh cations were disordered at the *B*- sites. The O-atom coordinates, obtained from the X-ray Rietveld refinements, are expected to be more poorly determined than those from the neutron diffraction measurements, as the presence of La and Tb cations limits the accuracy of the X-ray refined structures. Compared with $LaRh_{0.6}Cu_{0.4}O_3$ where a = 5.5697(2), b = 5.6697(2), and c = 7.8753(2) Å, the substitution of Tb^{3+} into $LnRh_{0.6}Cu_{0.4}O_3$ drives an elongation of b to 5.7565(1) Å and contraction in the a and c lattice parameters to 5.2713(1) and 7.6036(1) Å respectively. $TbRh_{0.6}Cu_{0.4}O_3$ (230.72(1) $Å^3$) has lower cell volume than $LaRh_{0.6}Cu_{0.4}O_3$ (248.68(1) $Å^3$). The anisotropy in the lattice parameters is a consequence of the tilting of the BO_6 octahedra. The lower cell volume of $TbRh_{0.6}Cu_{0.4}O_3$ corresponds to an increase in tilt, driven by the smaller size of Tb^{3+}. Tb^{3+} (1.04 Å) [18] has a smaller ionic size than La^{3+} (1.16 Å) [16]. The value for B_{iso} of the O2 anion is larger in the Tb compound (1.00(12) $Å^2$) than in the corresponding La compound (0.34(14) $Å^2$) suggesting that if vacancies form in the Tb oxides, they do so preferentially in the O2 position.

Table 5.1 Results of the structural refinements for $TbRh_{0.6}Cu_{0.4}O_3$ and $LaRh_{0.6}Cu_{0.4}O_3$ profiles using synchrotron X-ray powder diffraction data at 300 K.

Structural parameters	$TbRh_{0.6}Cu_{0.4}O_3$	$LaRh_{0.6}Cu_{0.4}O_3$
a (Å)	5.2713(1)	5.5697(2)
b (Å)	5.7565(1)	5.6697(2)
c (Å)	7.6036(1)	7.8753(2)
V ($Å^3$)	230.72(1)	248.68(1)
A x	0.4751(1)	0.4972(9)
A y	-0.0795(1)	-0.0507(2)
A z	1/4	1/4
A B_{iso} ($Å^2$)	1.09(1)	1.30(2)
B/Rh B_{iso} ($Å^2$)	0.49(2)	0.78(2)
O1 *x*	0.627(2)	0.588(3)
O1 *y*	0.556(2)	0.495(2)
O1 *z*	1/4	1/4
O1 B_{iso} ($Å^2$)	0.92(15)	1.09(2)
O2 *x*	0.316(1)	0.275(2)
O2 *y*	0.192(1)	0.226(2)
O2 *z*	0.0545(9)	0.0696(8)
O2 B_{iso} ($Å^2$)	1.00(12)	0.37(14)
R_P (profile) (%)	6.02	4.19
R_{wp}(weighted profile) (%)	9.39	6.18
χ^2	26.49	13.01
Tilt angle (º)		
ψ (in phase)	13.9	5.9
φ (out of phase)	17.2	21.1
Tolerance factor (τ)	0.85	0.89

Selected interatomic bond distances and angles derived from Rietveld refinements for $TbRh_{0.6}Cu_{0.4}O_3$ and $LaRh_{0.6}Cu_{0.4}O_3$ are given in Table 5.2. Tb has an effective nine-fold coordination due to its small ionic size. The average *A*-O bond lengths are generally shorter in $TbRh_{0.6}Cu_{0.4}O_3$ than in $LaRh_{0.6}Cu_{0.4}O_3$ resulting in a

greater orbital overlap between *f* orbitals of Tb^{3+} and sp^2 hybrid orbitals of oxygen[7]. The *A*-O and *B*-O bond lengths, and *B*-O-*B* bond angles and tilting angle along *c* axis are in good agreement with each other. The tilt angles can be estimated from the atomic coordinates [19]. The in-phase and out of phase tilting are estimated to be 13.9º and 17.2º in $TbRh_{0.6}Cu_{0.4}O_3$, and 5.9º and 21.1º in $LaRh_{0.6}Cu_{0.4}O_3$ at room temperature. The in-phase tilt angle is larger for $TbRh_{0.6}Cu_{0.4}O_3$ reflecting the smaller size of Tb but surprisingly the out phase tilting angle is smaller than for $LaRh_{0.6}Cu_{0.4}O_3$.

Table 5.2 Selected interatomic bond distances and angles of $LaRh_{0.6}Cu_{0.4}O_3$ and $TbRh_{0.6}Cu_{0.4}O_3$.

Compound	$TbRh_{0.6}Cu_{0.4}O_3$	$LaRh_{0.6}Cu_{0.4}O_3$
Bond distance (Å)		
A-O_1	2.237(8)	2.334(9)
	2.248(9)	2.632(9)
	3.267(8)	3.141(9)
		3.260(9)
A-O_2 (1)	2.316(7) × 2	2.415(7) × 2
	2.507(6) × 2	2.444(8) × 2
A-O_2 (2)	2.645(6) × 2	3.000 (7) × 2
		3.488(7) × 2
A-*O* (average)	2.521	2.838
Cu/Rh-O_1	2.040(3) × 2	2.032(4) × 2
Cu/Rh-O_2(1)	2.042(7) × 2	2.066(9) × 2
Cu/Rh-O_2(2)	2.061(7) × 2	2.074(8) × 2
B-*O* (average)	2.048	2.057
Bond Angles (º)		
Cu/Rh -O_1-Cu/Rh	137.4(5)	151.2(8)
Cu/Rh -O_2-Cu/Rh	144.0(4)	147.5(3)

The difference between the tilt angles ψ and φ of $LaRh_{0.6}Cu_{0.4}O_3$ (5.9º, 21.1º) appears to be unreasonable reflecting lower accuracy and precision in structural

refinements obtained from X-ray, rather than neutron, diffraction data. The combination of excellent counting statistics, high resolution, and the large number of observed reflections in synchrotron X-ray diffraction patterns usually results in higher accuracy of structural refinements than that can typically be achieved using conventional X-ray diffraction data [20]. In the most favourable cases, the accuracy of these refinements is comparable to the accuracy that could be obtained from high-resolution neutron diffraction data. However, additional factors such as lattice strain and psuedo-cubic symmetry can lead to significant peak overlap, which reduces the precision of the refinement [20]. It was not possible to measure neutron diffraction patterns for the sample due to the instrument availability. The displacements of the O(2) oxygen atoms of $LaRh_{0.6}Cu_{0.4}O_3$ ($u \cong v \cong 0.025$) and $TbRh_{0.6}Cu_{0.4}O_3$ ($u \cong 0.066$ and $v \cong 0.058$) suggest that the BO_6 octahedra are less rigid in $TbRh_{0.6}Cu_{0.4}O_3$ than in $LaRh_{0.6}Cu_{0.4}O_3$.

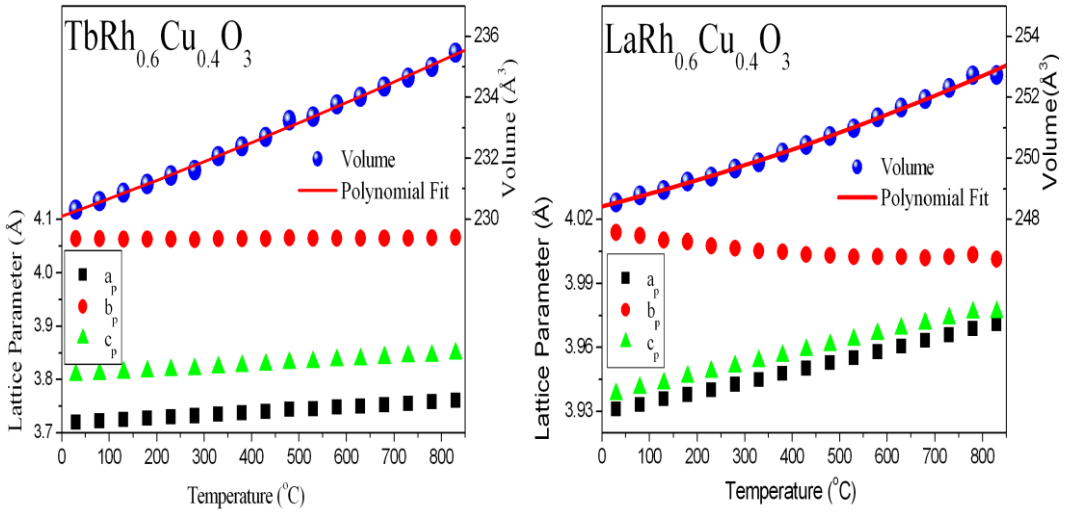

Figure 5.4 The temperature dependence of lattice parameters for $TbRh_{0.6}Cu_{0.4}O_3$ and $LaRh_{0.6}Cu_{0.4}O_3$ estimated by Rietveld refinement using X-ray diffraction data. a_p, b_p and c_p are the individual lattice parameters converted to the length of the equivalent primitive unit cell ($\frac{a}{\sqrt{2}}, \frac{b}{\sqrt{2}}, \frac{c}{2}$). The temperature dependent variation of the cell volume for $TbRh_{0.6}Cu_{0.4}O_3$ is fitted by $V_{(t)} = 230.09(6) + 5.57(3)\times10^{-3}\,T + 8(3)\times10^{-7}\,T^2$, and for $LaRh_{0.6}Cu_{0.4}O_3$ by $V_{(t)} = 248.38(2) + 4.46(9)\times10^{-3}\,T + 2.1(1)\times10^{-6}\,T^2$.

X-ray diffraction measurements showed that the orthorhombic structure persisted over a wide temperature range, 30 to 830 ºC, for the various oxides. The

temperature dependences of the lattice parameters for representative samples are illustrated in Figure 5.4. The failure to observe any structural phase transitions below 830°C in the XRD studies is consistent with the tolerance factor estimated to be 0.85 and 0.89 for $TbRh_{0.6}Cu_{0.4}O_3$ and $LaRh_{0.6}Cu_{0.4}O_3$ respectively. Both $LaRh_{1-x}Cu_xO_3$ and $TbRh_{1-x}Cu_xO_3$ oxides show conventional positive thermal expansion of *a* and *c* axis. However, the *b* parameter in $TbRh_{0.6}Cu_{0.4}O_3$ is essentially independent of temperature whereas that in $LaRh_{0.6}Cu_{0.4}O_3$ shows weak negative thermal expansion. This can be attributed to the tilting of the BO_6 octahedra which acts to maintain a constant variation in the cell volume [21]. A similar effect has been reported for $TbMnO_3$ [21] and was seen elsewhere in this thesis.

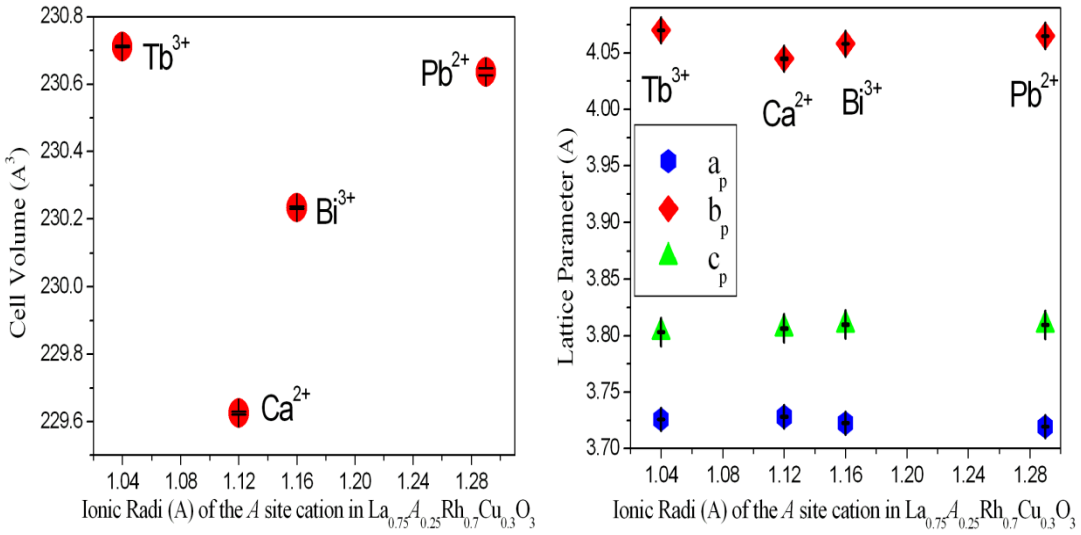

Figure 5.5 Composition dependence of the cell volume and the lattice parameter indices for $Tb_{0.75}A_{0.25}Rh_{0.7}Cu_{0.3}O_3$ estimated by Rietveld refinement using synchrotron X-ray diffraction data. Where not obvious the error bars are smaller than the symbols.

The influence of the *A* site doping on $Tb_{0.75}A_{0.25}Rh_{0.7}Cu_{0.3}O_3$ (A = Ca^{2+}, Pb^{2+} and Bi^{3+}) and $Tb_{1-x}Pb_xRh_{0.6}Cu_{0.4}O_3$ was investigated. As illustrated in Figure 5.5, doping Ca^{2+} (8 coordinate ionic radius, 1.12 Å) into $Tb_{0.75}A_{0.25}Rh_{0.7}Cu_{0.3}O_3$ reduces the cell volume from 230.711(2) $Å^3$ to 229.625(4) $Å^3$. This is likely driven by the partial oxidation of Rh^{3+} (0.67 Å) to Rh^{4+} (0.60 Å),[18] necessary to maintain charge neutrality. Despite the impact of such oxidation, the Pb doped oxide exhibits an increase in the cell volume, from 229.625(4) $Å^3$ to 230.407(2) $Å^3$ due to the large

ionic size of the Pb^{2+} cation (1.29 Å). Surprisingly, the addition of Bi into $Tb_{0.75}A_{0.25}Rh_{0.7}Cu_{0.3}O_3$ results in a smaller cell volume, from 230.711(2) $Å^3$ to 230.234 (4) $Å^3$, despite Bi^{3+} having a similar formal valency and larger ionic radii (1.17 Å) [18] than Tb^{3+} (1.04 Å) [18]. This can be attributed to the high covalent character of the Bi ions, with small displacement of the *A* site cations on the 4*a* site, at 0.525(1), 0.079(1), 0.25 in $TbRh_{0.7}Cu_{0.3}O_3$ to 0.524(1), 0.078(1), 0.25 in $Tb_{0.75}Bi_{0.25}Rh_{0.7}Cu_{0.3}O_3$ enhanced by the covalency [22,23]. It was established that Sr has a lower solubility in $TbRh_{0.7}Cu_{0.3}O_3$ compared to $LaRh_{0.7}Cu_{0.3}O_3$. It was not possible to prepare single phase samples with a Sr content of $x \geq 0.25$. The composition dependence of the cell volume and the lattice parameter for $Tb_{0.75}A_{0.25}Rh_{0.7}Cu_{0.3}O_3$ is illustrated in Figure 5.5. The anisotropy in lattice parameters seems to be independent of the ionic radii of the *A* site cation.

An interesting question, and one we are addressing here, is what causes Pb^{2+} to be incorporated in $Tb_{0.75}A_{0.25}Rh_{1-x}Cu_xO_3$ at a greater dopant level than possible with Sr^{2+}. These two cations have identical formal valencies and similar ionic radii. A striking feature of Pb^{2+} is that the cation has potentially stereochemically active lone pair electrons and strong covalent character. To improve the understanding of Pb behaviour in these oxides, the series $Tb_{1-x}Pb_xRh_{0.6}Cu_{0.4}O_3$ ($x \leq 0.3$) was also examined. Unexpectedly, Pb was less soluble in $Tb_{1-x}Pb_xRh_{0.6}Cu_{0.4}O_3$ than in $La_{1-x}Pb_xRh_{0.6}Cu_{0.4}O_3$, at range $0 \leq x \leq 0.2$. Additional peaks indicative of a second phase were observed in the synchrotron X-ray diffraction profiles for $Tb_{1-x}Pb_xRh_{0.6}Cu_{0.4}O_3$ (Figure 5.6) showing incomplete incorporation of the Pb. The solubility of Pb is possibly limited by the large size mismatch of Pb^{2+} (1.29Å) and Tb^{3+} (1.04Å). It is postulated that an internal chemical pressure was generated within the lattice due this size difference thus destabilising the structures. The impact of the *A*-site ionic size mismatch on the solubility, structure and physical properties of perovskites has been previously reported in many papers [24,25]. For instance, the single-phase region of $(Ba_{1-y}Pb_y)_{6-x}Ln_{8+2x/3}Ti_{18}O_{54}$ (where *Ln* = La^{3+} or Nd^{3+}) was determined to exist within the Pb^{2+} concentration range corresponding to $0 < y < 0.70$ ($x = 0$), $0 < y < 0.60$ ($x = 0.75$) and $0 < y < 0.4$ ($x = 1.5$). For all compositions outside the single phase region secondary phases emerge as result of size mismatch [26,27]. The Rietveld refinement profiles for $Tb_{0.7}Pb_{0.3}Rh_{0.6}Cu_{0.4}O_3$ and the observed synchrotron X-ray diffraction profiles for $La_{1-x}Pb_xRh_{0.6}Cu_{0.4}O_3$ oxides are shown in Figure 5.6.

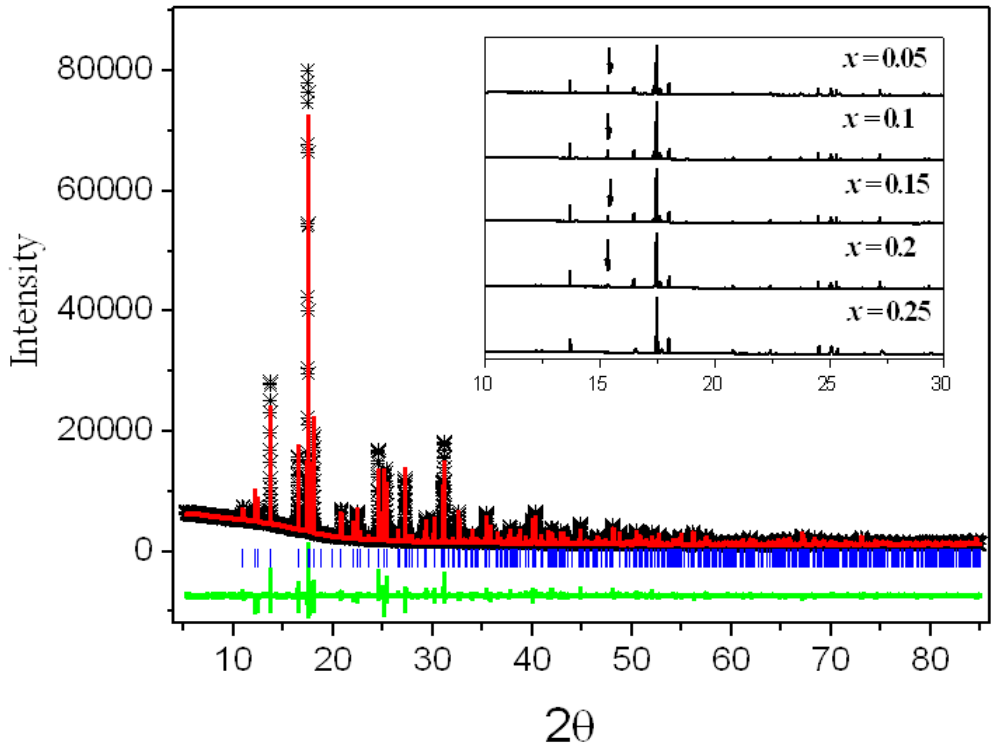

Figure 5.6 Synchrotron X-ray diffraction profiles for $Tb_{0.7}Pb_{0.3}Rh_{0.6}Cu_{0.4}O_3$. The data are represented by the crosses and the solid lines are the calculated (red line) and difference profiles (green line). The positions of the space group allowed reflections are shown by the vertical markers immediately below the observed profile. Synchrotron X-ray diffraction patterns for different $Tb_{1-x}Pb_xRh_{0.6}Cu_{0.4}O_3$ compositions are also included. The black arrows indicate a structural impurity peak on the patterns.

The refined structural parameters for $Tb_{0.7}Pb_{0.3}Rh_{0.6}Cu_{0.4}O_3$ are given in Table 5.3. $Tb_{0.75}Pb_{0.25}Rh_{0.6}Cu_{0.4}O_3$ and $Tb_{0.7}Pb_{0.3}Rh_{0.6}Cu_{0.4}O_3$ both form single phase orthorhombic structures. Changes in the *A*–O covalent bonding are thought to play a role in determining the structure [28]. Pb^{2+} with strong covalent character attracts three of the twelve surrounding oxygens, whereas the remaining anions are further away. This has the effect of increasing the *B*-O bond interactions. Although, Pb^{2+} (1.87) [29] has higher electronegativity than Tb^{3+}(1.10) [29], the electronic 'lone pairs' are stereochemically active, pointing toward empty spaces in the structure and inducing cationic shifts. One consequence of this is the local structure of the Pb^{2+} and Tb^{3+} cations may be different.

Table 5.3 Structural parameters for $Tb_{0.7}Pb_{0.3}Rh_{0.6}Cu_{0.4}O_3$ as obtained from the Rietveld refinement against powder synchrotron diffraction data.

Atom	*Site*	*x*	*y*	*z*	B_{iso} (Å^2)	*Occ*
Tb/Pb	4(*c*)	0.5254(1)	-0.0784(1)	0.25	1.13(01)	0.75/0.25
Cu/Rh	4(*b*)	0	0	0	0.11(01)	0.5/0.5
O(1)	4(*c*)	0.372(1)	0.442(1)	0.25	0.87(14)	1.0
O(2)	8(*d*)	0.3064(9)	0.2029(9)	0.0590(8)	1.00(10)	1.0
Parameters	*a* = 5.26469(3), *b* = 5.74974(3) and *c* = 7.60661(5) Å					
R- factors	R_p = 4.82 %, R_{wp} = 7.00 % and χ^2 = 8.71					

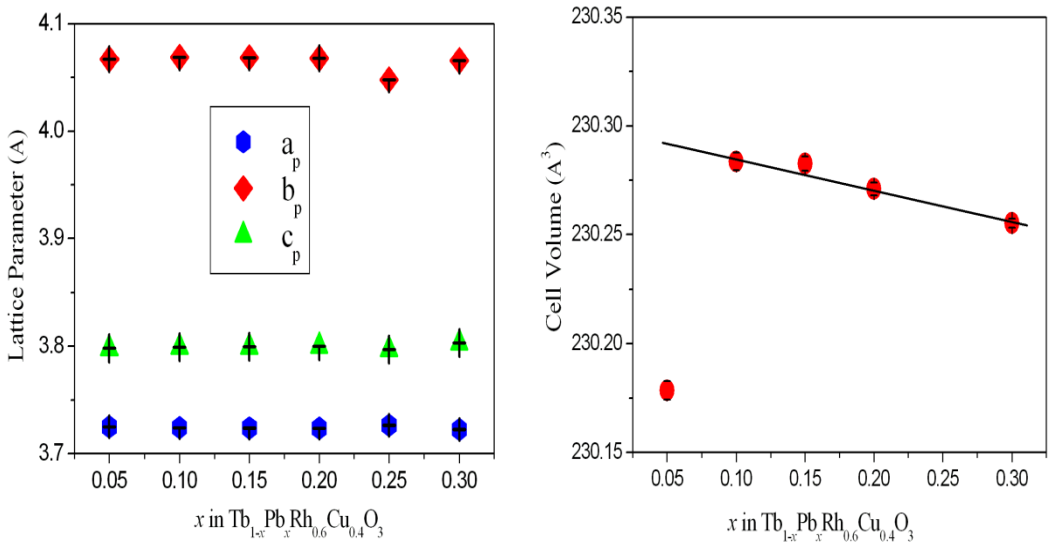

Figure 5.7 Composition dependence of the cell volume and the lattice parameters for $Tb_{1-x}Pb_xRh_{0.6}Cu_{0.4}O_3$ estimated by Rietveld refinement using synchrotron X-ray diffraction data. The cell volume at x = 0.25 was excluded from the plot as it was found to be anomalously low.

Figure 5.7 shows the effect of Pb doping on the cell volumes of $Tb_{1-x}Pb_xRh_{0.6}Cu_{0.4}O_3$. This differs from the behaviour observed for $La_{1-x}Pb_xRh_{0.5}Cu_{0.5}O_3$ in chapter 3.3.2 suggesting the 4*f* electrons may moderate the influence of the Pb^{2+} cation. The cell volume increases rapidly at low doping levels $x < 0.1$ as anticipated from the larger size of the Pb^{2+} cation. At higher contents, the volume actually decreases, possibly as a consequence of charge delocalization. The absence of any

superlattice reflections in the S-XRD patterns indicated that the Cu and Rh cations were randomly distributed over the perovskite *B*-sites. A number of the *B* site doped oxide were also prepared and described here. These were all single phase with an orthorhombic structure. There were no obvious structural impurities observed in the synchrotron X-ray diffraction profiles for $TbRh_{1-2x}Cu_xSc_xO_3$ (Figure 5.8) and $TbRh_{1-2x}Cu_xZn_xO_3$ (Figure 5.9).

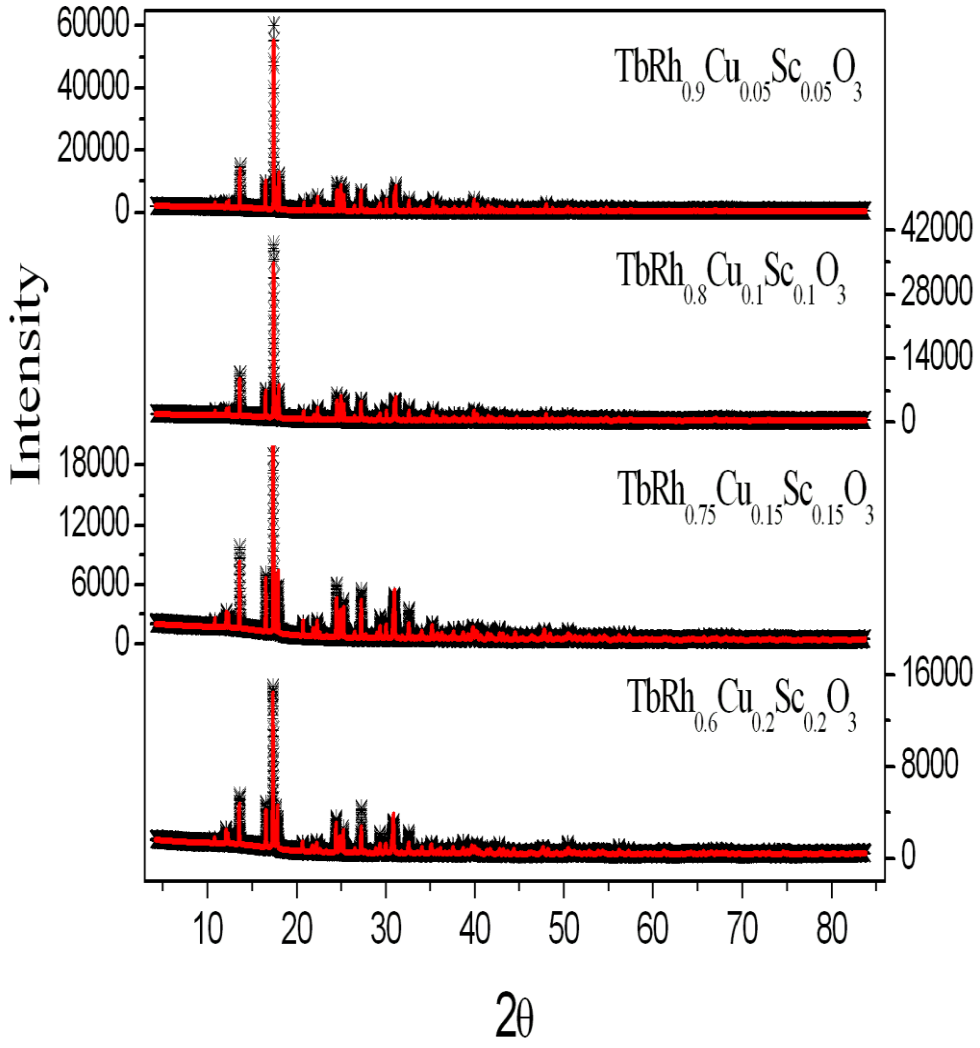

Figure 5.8 The observed and calculated synchrotron X-ray diffraction profiles for $TbRh_{1-2x}Cu_xSc_xO_3$. R_p= 6.23, 6.56, 6.25 and 6.67; and R_{wp} = 8.85, 9.21, 9.20 and 9.72 for x = 0.05, 0.1, 0.15 and 0.2 respectively.

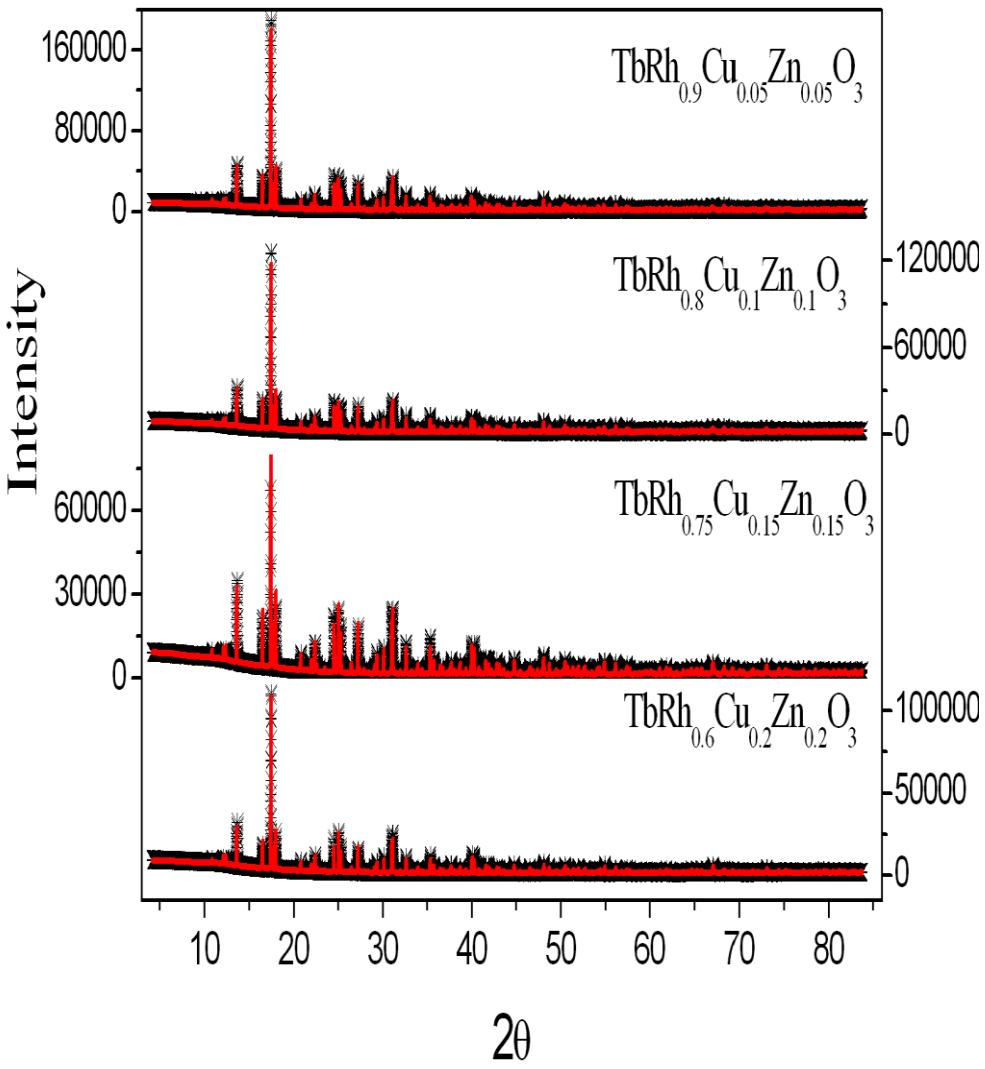

Figure 5.9 The observed and calculated synchrotron X-ray diffraction profiles for $TbRh_{1-2x}Cu_xZn_xO_3$. R_p= 5.85, 5.22, 5.11 and 5.67; and R_{wp} = 8.68, 7.48, 7.31 and 8.03 for x = 0.05, 0.1, 0.15 and 0.2 respectively.

The composition dependence of the unit cell volumes estimated from Rietveld refinement against synchrotron diffraction data for the series $TbRh_{1-2x}Cu_xB_xO_3$ are illustrated in Figure 5.10. The unit cell volumes of $TbRh_{1-2x}Cu_xB_xO_3$ show a similar trend to that observed for $LaRh_{1-2x}Cu_xB_xO_3$, suggesting the presence of trivalent Tb. The cell volumes for terbium oxides are approximately 17-19 $Å^3$ smaller than those for lanthanum oxides due to the smaller ionic radii of Tb^{3+} (1.04 Å) [18] compared to La^{3+} (1.16 Å) [18]. The addition of divalent cations such as Cu^{2+} (6-coordinate ionic radius, 0.73 Å) [18] and Zn^{2+} (0.74 Å) [18] into $TbRh_{1-2x}Cu_xB_xO_3$ decreases the cell volumes, presumably as a consequence of partial oxidation of the Rh^{3+} (0.665 Å) to

Rh^{4+} (0.60 Å) [18]. Partial oxidation of Tb^{3+} to Tb^{4+} (0.88 Å) [18] may also occur. Doping with equal quantities of Sc^{3+} and Cu^{2+} initially results in a rapid decrease in the cell volumes suggesting the coexistence of charge delocalization between the Rh and Cu cations. As described previously, partial change transfer involving Rh^{4+} to Rh^{3+} and Cu^{2+} to Cu^{3+} (0.53 Å) [18] is possible [30]. $TbRh_{0.9}Cu_{0.05}Sc_{0.05}O_3$ has a lower cell volume than $TbRh_{0.9}Cu_{0.1}O_3$ and $TbRh_{0.9}Cu_{0.05}Zn_{0.05}O_3$ although the former oxide has lower divalent dopant content, suggesting greater oxidation of Cu^{2+} to Cu^{3+}. The increase in cell volume of $TbRh_{1-2x}Cu_xSc_xO_3$ at $x > 0.1$ reflects the increase in the Sc^{3+} content since the Sc^{3+} (0.745 Å) [18] ion is larger than Rh^{3+}. The substitution of Sc^{3+} is not expected to drive a change in the overall charge of the system, since it has the same formal valence as Rh^{3+}.

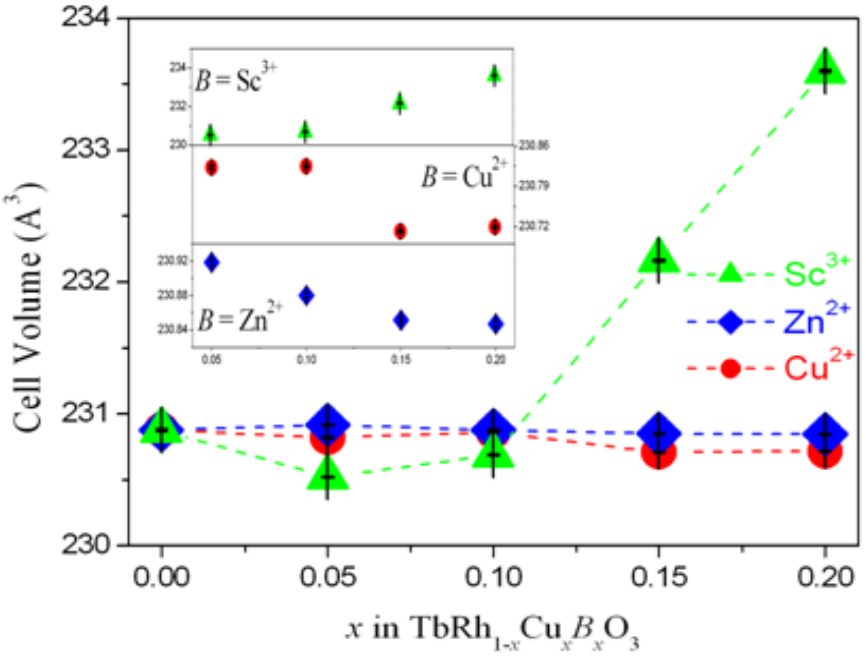

Figure 5.10 Composition dependence of the cell volume for the individual and combined $TbRh_{1-2x}Cu_xB_xO_3$ series estimated by Rietveld refinement using synchrotron X-ray diffraction data.

The external structural distortion, D, the internal structural distortion, Δd, and M-O(1)-M and M-O(2)-M bond angles for the $TbRh_{1-2x}Cu_xB_xO_3$ series are summarised in Table 5.4. The trends in these show that the reduction in tolerance factor induces tilting which distorts the lattice. The $TbRh_{1-2x}Cu_xB_xO_3$ series exhibited three times higher lattice parameter distortions (lower symmetrical arrangements)

than the $LaRh_{1-2x}Cu_xB_xO_3$ oxides. This is a manifestation of the substitution of the smaller Tb^{3+} cation. The impact of the changed tolerance factor on the lattice metric can be monitored by the correlation between *D* and composition. *D* decreases with *x* in the two series $TbRh_{1-2x}Cu_xSc_xO_3$ and $TbRh_{1-2x}Cu_xZn_xO_3$, but increases as *x* increased in $TbRh_{1-2x}Cu_{2x}O_3$. The changes in *D* are consistent with the small differences in the ionic radii of Sc^{3+} (0.745Å) [18], Zn^{2+} (0.74Å) [18] and Cu^{2+} (0.73Å) [18]. The tolerance factor increases as the size of *B* dopant decreases whereas *D* decreases with the size of *B* dopant [28,31]. In the double perovskite Ca_2MnMO_6 (*M* = Sb, Ta, Nb and Ru), the increase in the tolerance factor results in a decrease in the lattice parameter distortions [28]. Except for the Sc doped oxides, there were no obvious correlations between the octahedral distortions and other structural parameters in $TbRh_{1-2x}Cu_xB_xO_3$. The increase in Δd for $TbRh_{1-2x}Cu_xSc_xO_3$ is in good agreement with the rapid increase in the cell volumes. Since Cu^{2+} ($3d^9$) ions are Jahn-Teller (JT) active [28], the increase in Δd can be attributed to this effect. The partial oxidation of Cu^{2+} to Cu^{3+} and the tilting of the octahedron are a means of reducing the JT distortion.

Table 5.4 Lattice parameter distortion *D*, octahedral distortion Δd , *M*-O(1)-*M* and *M*-O(2)-*M* bond angles for $TbRh_{1-2x}Cu_xB_xO_3$.

X	$TbRh_{1-2x}Cu_xSc_xO_3$		$TbRh_{1-2x}Cu_{2x}O_3$		$TbRh_{1-2x}Cu_xZn_xO_3$	
	D (%)	$\Delta d\times10^{-5}$	*D (%)*	$\Delta d\times10^{-5}$	*D (%)*	$\Delta d\times10^{-5}$
0.05	3.40	3.89	3.44	108	3.44	8.60
0.10	3.35	0.05	3.46	3.62	3.43	0.72
0.15	3.11	174	3.51	16. 3	3.43	1.74
0.20	2.90	365	3.52	14.5	3.43	19.7
X	M(O1)M°	M(O2)M°	M(O1)M°	M(O2)M°	M(O1)M°	M(O2)M°
0.05	138.3(4)	143.8(3)	138.1(6)	145.8(4)	139.2(4)	143.7(3)
0.10	137.9(5)	145.3(4)	140.1(6)	145.8(5)	137.3(4)	143.6(3)
0.15	136.4(6)	144.7(4)	139.8(4)	143.1(3)	138.0(4)	144.6(3)
0.20	136.9(7)	143.2(5)	136.8(6)	142.8(4)	138.3(5)	143.3(4)

The structural properties of the *A* site doped oxides were further investigated by doping Zn^{2+} and Sc^{3+} into $Tb_{0.75}Pb_{0.25}Rh_{1-2x}Cu_xB_xO_3$ and $Tb_{0.75}Bi_{0.25}Rh_{1-2x}Cu_xB_xO_3$ respectively. Neither $Tb_{0.75}Pb_{0.25}Rh_{1-2x}Cu_xZn_xO_3$ nor $Tb_{0.75}Bi_{0.25}Rh_{1-2x}Cu_xSc_xO_3$ gave single phase samples at $x \leq 0.2$. One exception is $Tb_{0.75}Bi_{0.25}Rh_{0.6}Cu_{0.2}Sc_{0.2}O_3$. The Rietveld profiles for $Tb_{0.75}Bi_{0.25}Rh_{0.6}Cu_{0.2}Sc_{0.2}O_3$ and the observed synchrotron X-ray diffraction data for $Tb_{0.75}Bi_{0.25}Rh_{1-2x}Cu_xSc_xO_3$ are illustrated in Figure 5.11. Table 5.5 shows the structural parameters for $Tb_{0.75}Bi_{0.25}Rh_{0.6}Cu_{0.2}Sc_{0.2}O_3$ as obtained from the Rietveld refinement. The temperature dependence of the lattice parameter (Figure 5.12) is similar to that observed for $TbRh_{0.6}Cu_{0.4}O_3$. The distorted structure of the $Tb_{0.75}Pb_{0.25}Rh_{1-2x}Cu_xZn_xO_3$ and $Tb_{0.75}Bi_{0.25}Rh_{1-2x}Cu_xSc_xO_3$ oxides could be attributed to the impact of the tolerance factor and a large ionic size mismatch between the *A* and *B* sites. The possible partial oxidation of Tb^{3+} (1.04 Å) to Tb^{4+} (0.88 Å) [16], may also result in the partial occupancy of Tb^{4+} onto the *B* site. Terbium is known to adopt the mixed valence state Tb^{3+}/Tb^{4+} in several compounds [32] such as $TbBaCoO_{5-\delta}$ [33]. The tetravalent terbium ions can be stabilized at the *B* sites of perovskites such as $BaTbO_3$ [34] and Sr_2TbIrO_6 [35].

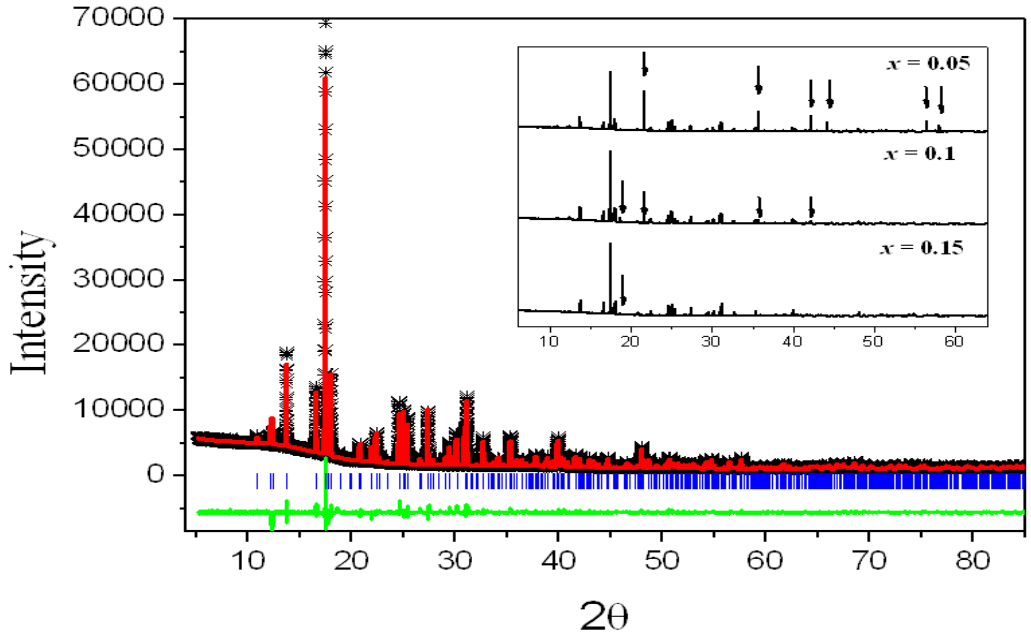

Figure 5.11 Synchrotron X-ray diffraction profiles for $Tb_{0.75}Bi_{0.25}Rh_{0.6}Cu_{0.2}Sc_{0.2}O_3$ included the observed profiles for different compositions in $Tb_{0.75}Bi_{0.25}Rh_{1-2x}Cu_xSc_xO_3$. The black arrows indicate on the strongest peaks from an impurity phase.

Table 5.5 Structural parameters for $Tb_{0.75}Bi_{0.25}Rh_{0.6}Cu_{0.2}Sc_{0.2}O_3$ as obtained from the Rietveld refinement against powder synchrotron diffraction data.

Atom	*Site*	*x*	*y*	*z*	B_{iso} (Å^2)	*Occ*
Tb/Bi	4(*c*)	0.5211(3)	0.0728(2)	0.25	0.55(2)	0.75/0.25
Rh/*B*	4(*b*)	0	0	0	1.73(2)	0.6/0.2
O(1)	4(*c*)	0.381(2)	0.450(1)	0.25	0.62(2)	1.0
O(2)	8(*d*)	0.320(2)	0.216(1)	-0.0548(10)	0.43(10)	1.0
Parameter	*a* = 5.2792(2), *b* = 5.7145(2) and *c* = 7.6430(2) Å					
R-factors	R_p = 6.34 %, R_{wp} = 9.60 % and χ^2 = 18.62					

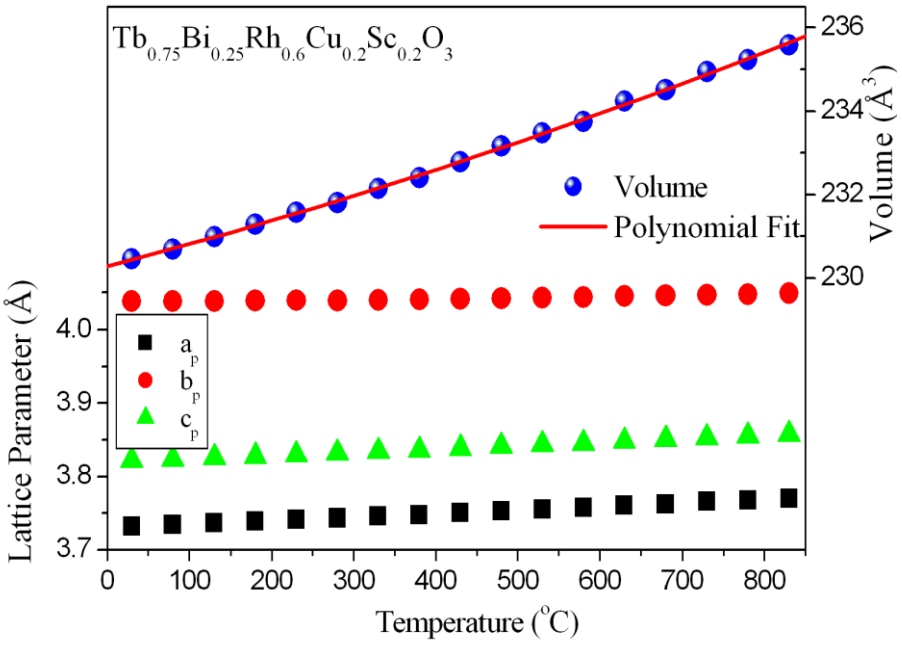

Figure 5.12 Temperature dependence of the lattice parameters for $Tb_{0.75}Bi_{0.25}Rh_{0.6}Cu_{0.2}Sc_{0.2}O_3$ estimated by Rietveld refinement using X-ray diffraction data. The temperature dependent variation of the cell volume is fitted to $V_{(t)} = 230.27(3) + 5.1(3)\times10^{-3}\,T + 1.5(2)\times10^{-6}\,T^2$.

The lattice parameter distortion, *D*, octahedral distortion, *Δd*, and the bond angles *M-O1-M°* and *M-O2-M°* for different $Tb_{0.75}A_{0.25}Rh_{0.7}Cu_{0.3}O_3$ and $Tb_{1-x}A_xRh_{0.6}Cu_{0.4}O_3$ compositions are given in Table 5.6. There is a negative correlation between the octahedral distortion and lattice parameter distortion for the oxides. The decrease in Δd for $Tb_{0.75}Ca_{0.25}Rh_{0.7}Cu_{0.3}O_3$ ($\Delta d = 0.52 \times 10^{-3}$) and

$Tb_{0.75}Pb_{0.25}Rh_{0.7}Cu_{0.3}O_3$ ($\Delta d = 0.12 \times 10^{-3}$), that both have an equivalent content of divalent type dopants, is indicative of a suppression of the JT distortions due to octahedral tilting. The decrease in Δd is consistent with the decrease in the *M*-O-*M* bond angles of $Tb_{0.75}Ca_{0.25}Rh_{0.7}Cu_{0.3}O_3$, 141.0(6)º and 145.8(4)º compared to $Tb_{0.75}Pb_{0.25}Rh_{0.7}Cu_{0.3}O_3$, 137.7(5)º and 144.5(4)º. Doping $Tb_{0.75}Bi_{0.25}Rh_{0.7}Cu_{0.3}O_3$ with a trivalent cation such as Bi^{3+}, results in higher octahedral distortion compared to divalent doped oxides such as $Tb_{0.75}Ca_{0.25}Rh_{0.7}Cu_{0.3}O_3$ and $Tb_{0.75}Pb_{0.25}Rh_{0.7}Cu_{0.3}O_3$, possibly due to charge delocalization. Examination of the structures, refined from synchrotron X-ray diffraction data, show that increasing the Cu content from 0.15 to 0.2 in $Tb_{0.75}Bi_{0.25}Rh_{1-2x}Cu_xSc_xO_3$ significantly increases the octahedral distortion. For example, the octahedral distortion in $Tb_{0.75}Bi_{0.25}Rh_{0.6}Cu_{0.2}Sc_{0.2}O_3$, $\Delta d = 1.71 \times 10^{-3}$, is larger than in $Tb_{0.75}Bi_{0.25}Rh_{1-2x}Cu_xSc_xO_3$ ($\Delta d = 5.34 \times 10^{-3}$). On the other hand, increasing in the Pb content from 0.25 to 0.3 in $Tb_{1-x}Pb_xRh_{0.6}Cu_{0.4}O_3$ significantly decreases octahedral distortion. Since no systematic changes in the *M*-O-*M* bond angles were evident for the two oxides, the decrease in Δd is believed to result from partial oxidation of the Cu^{2+} to Cu^{3+}.

Table 5.6 Lattice parameter distortions *D*, octahedral distortions Δd and bond angles *M(O1)M º* and *M(O2)M º* for $Tb_{0.75}A_{0.25}Rh_{0.7}Cu_{0.3}O_3$ and $Tb_{1-x}A_xRh_{0.6}Cu_{0.4}O_3$.

Compound	*D (%)*	$\Delta d \times 10^{-3}$	*M*(O1)*M* º	*M*(O2)*M* º
$Tb_{0.75}Ca_{0.25}Rh_{0.7}Cu_{0.3}O_3$	3.20	0.52	141.0(6)	145.8(4)
$Tb_{0.75}Pb_{0.25}Rh_{0.7}Cu_{0.3}O_3$	3.45	0.12	137.7(5)	144.5(4)
$Tb_{0.75}Bi_{0.25}Rh_{0.7}Cu_{0.3}O_3$	3.36	1.11	140.6(3)	141.9(5)
$Tb_{0.75}Pb_{0.25}Rh_{0.6}Cu_{0.4}O_3$	3.30	0.52	138.5(7)	145.4(5)
$Tb_{0.7}Pb_{0.3}Rh_{0.6}Cu_{0.4}O_3$	3.48	0.04	136.8(4)	146.3(4)
$Tb_{0.75}Bi_{0.25}Rh_{0.7}Cu_{0.15}Sc_{0.15}O_3$	3.11	1.71	139.3(6)	143.9(4)
$Tb_{0.75}Bi_{0.25}Rh_{0.6}Cu_{0.2}Sc_{0.2}O_3$	3.03	5.34	140.2(5)	146.6(4)

5.2.3 Magnetization

Since the magnetic susceptibilities of the Rh^{4+} and Cu^{2+} ions are both smaller than that of the Tb^{3+} ion, the observed magnetic susceptibilities of the $TbRh_{1-}$

$_{2x}Cu_{2x}O_3$ oxides are dominated by the contribution from Tb^{3+}. However, the co-existence of three magnetic ions in a single lattice commonly results in complicated magnetic interactions that can be difficult to explain. The magnetization curves of both the *A* and *B* site doped $TbRh_{1-2x}Cu_{2x}O_3$ series are shown in Figures 5.12 and 5.13 respectively. The magnetic susceptibilities did not show a defined maximum, and the inverse susceptibilities of all the oxides display Curie–Weiss type behaviour. Hysteresis loop measurements point towards the absence of any long range magnetic ordering in the various oxides. The inverse susceptibility plots for the $Tb_{0.75}A_{0.25}Rh_{0.7}Cu_{0.3}O_3$ (Figure 5.13) demonstrate that susceptibility decreases by doping this system with Ca^{2+} and Pb^{2+}, but increases by doping with Bi^{3+}. The magnetic susceptibilities of $Tb_{1-x}Pb_xRh_{0.6}Cu_{0.4}O_3$ decreases systematically upon doping, suggesting partial oxidation of Rh^{3+} ($4d^6$) to Rh^{4+} ($4d^5$).

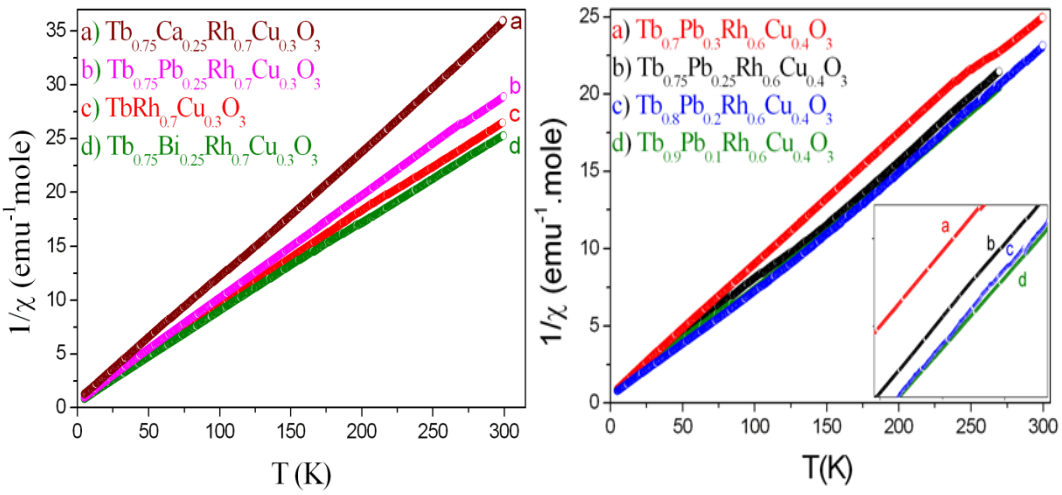

Figure 5.13 The temperature dependence of the inverse susceptibility for $Tb_{0.75}A_{0.25}Rh_{0.7}Cu_{0.3}O_3$ and $Tb_{1-x}A_xRh_{0.6}Cu_{0.4}O_3$ recorded under zero field cooling conditions with an applied field of 5 KOe.

The magnetic susceptibilities for $TbRh_{0.7}Cu_{0.3}O_3$ (Figure 5.14) are generally higher than those for $TbRh_{0.7}Cu_{0.15}Sc_{0.15}O_3$ and $TbRh_{0.7}Cu_{0.15}Zn_{0.15}O_3$, possibly because of the larger Cu content in the former. The effective charge of the cations and the strong overlap of 3*d* orbitals with sp^2 oxygen orbitals [36] are expected to affect on the formal valency of 4*d* ions, leading to changes in the magnetic and electronic properties [37,38]. Thus, the relatively small decrease in the magnetic susceptibility for $TbRh_{0.7}Cu_{0.15}Zn_{0.15}O_3$ may be the result of partial oxidation of Tb^{3+}

($4f^8$) to Tb^{4+} ($4f^7$) [39]. In general, all the *A* and *B* site doped $TbRh_{1-2x}Cu_{2x}O_3$ oxides have higher susceptibilities than those for the La oxides due to the strong contribution of Tb 4*f* electrons.

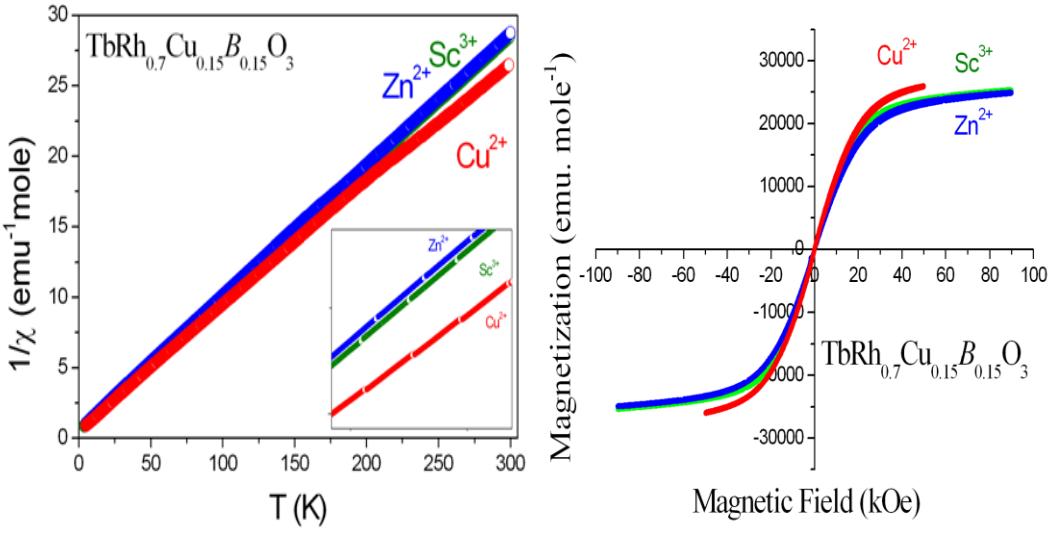

Figure 5.14 The temperature dependence of the inverse susceptibility for $TbRh_{0.7}Cu_{0.15}B_{0.15}O_3$ recorded under zero field cooling conditions with an applied field of 5 kOe. Magnetization hysteresis loops for the oxides at 5K are also illustrated.

Linear regression fits to the inverse magnetization curves (Table 5.7) showed Curie constant (*C*), susceptibility (χ_o) and effective magnetic moment (μ_{eff}) for the Tb containing oxides are higher than those for the corresponding La oxides, reflecting the change in the number of the *f* electrons. The negative Weiss constant of all oxides is indicative of very weak antiferromagnetism. However, an antiferromagnetic transition was not observed at temperature above 4 K. It is believed that the superexchange interaction between the lanthanoid ions is a dominant interaction for the formation of antiferromagnetic order in such system [5]. Hence, a transition from paramagnetism to antiferromagnetism is expected to occur at very low temperatures [5]. $TbRhO_3$ exhibits an antiferromagnetic transition below 2 K [5]. The magnetic susceptibility is affected by the thermally populated excited states because of the spin-orbit coupling [40]. The effective magnetic moments for $Tb_{0.75}A_{0.25}Rh_{0.7}Cu_{0.3}O_3$ and $Tb_{1-x}Pb_xRh_{0.6}Cu_{0.4}O_3$ are higher than calculated for the appropriate mixtures of Tb^{3+} ($4f^8$, S = 3), Rh^{4+} ($4d^5$, S = 1/2) and Cu^{2+} ($3d^9$, S = 1/2),

suggesting spin orbit coupling may be important. The theoretical effective moments (μ_{cal}) can be calculated from the equation $\mu_{cal} = \sqrt{\sum n\mu_i^2}$ where *n* and μ_i are the mole ratio and the independent magnetic moment of each ion in the compound [41]. The larger magnetic moments of $Tb_{0.75}Pb_{0.25}Rh_{0.7}Cu_{0.3}O_3$ (9.15 μ_B) and $Tb_{0.75}Bi_{0.25}Rh_{0.7}Cu_{0.3}O_3$ (9.82 μ_B) compared to $Tb_{0.75}Ca_{0.25}Rh_{0.7}Cu_{0.3}O_3$ (8.26 μ_B) and $TbRh_{0.7}Cu_{0.3}O_3$ (9.57 μ_B) is attributed to spin orbit coupling. The impact of the lone pair $6s^2$ electrons of the Pb^{2+} and Bi^{3+} on the alignments of the magnetic moments of the cations may also be important.

Table 5.7 Curie constant (*C*), Weiss constant (Θ), magnetic susceptibly coefficient factor (χ_o), effective magnetic moment (μ_{eff}) and theoretical magnetic moment (μ_T) for oxides of the type $Tb_{1-y}A_yRh_{1-2x}Cu_xB_xO_3$.

Compound	Θ (K)	χ_o (emu.mole$^-$)	C (emu. mole$^-$)	μ_{eff} (μ_B)	μ_T (μ_B)
$TbRh_{0.7}Cu_{0.15}Sc_{0.15}O_3$	-7.3	1.472	79.02	9.26	9.75
$TbRh_{0.7}Cu_{0.3}O_3$	-8.8	1.315	101.0	9.57	9.79
$TbRh_{0.7}Cu_{0.15}Zn_{0.15}O_3$	-8.3	1.289	89.07	9.23	9.79
$Tb_{0.75}Ca_{0.25}Rh_{0.7}Cu_{0.3}O_3$	-4.7	1.841	39.92	8.26	8.55
$Tb_{0.75}Pb_{0.25}Rh_{0.7}Cu_{0.3}O_3$	-7.2	1.456	76.24	9.15	8.55
$Tb_{0.75}Bi_{0.25}Rh_{0.7}Cu_{0.3}O_3$	-8.2	1.476	99.54	9.82	8.51
$Tb_{0.9}Pb_{0.1}Rh_{0.6}Cu_{0.4}O_3$	-3.6	3.820	48.55	10.4	9.35
$Tb_{0.8}Pb_{0.2}Rh_{0.6}Cu_{0.4}O_3$	-7.2	1.670	86.45	9.77	8.85
$Tb_{0.75}Pb_{0.25}Rh_{0.6}Cu_{0.4}O_3$	-5.1	2.574	66.08	10.2	8.79
$Tb_{0.7}Pb_{0.3}Rh_{0.6}Cu_{0.4}O_3$	-9.1	1.334	109.7	9.81	8.74

Unlike the *A* site doped $TbRh_{1-x}Cu_xO_3$ oxides, the effective magnetic moments of the *B* site doped oxides $TbRh_{0.7}Cu_{0.15}B_{0.15}O_3$ (~ 9.23 to 9.57 μ_B) were lower than expected for a mixture of Tb^{3+}, Rh^{4+} and Cu^{2+} cations. The magnetic moments of $TbRh_{0.7}Cu_{0.15}Zn_{0.15}O_3$ (9.23 μ_B) and $TbRh_{0.7}Cu_{0.15}Sc_{0.15}O_3$ (9.26 μ_B) suggest that doping with divalent cation does not have any impact on the oxidation state of Tb^{3+}. It is well known that Tb^{3+} has a considerably larger magnetic moment (9.72 μ_B) [35] than Tb^{4+}(~ 7.94 μ_B) [35]. The magnetization of the $TbRh_{0.7}Cu_{0.15}B_{0.15}O_3$ oxides

suggests that the spins of the Rh cations are, weakly, aligned antiparallel to the Tb ions at low magnetic fields. Previous studies on the magnetic properties of rare earth rhodium oxides $LnRhO_3$ [5] showed the magnetization of $TbRhO_3$, 8.870 μ_B is considerably smaller than the theoretical moments μ_{eff} = 9.05 μ_B and almost completely saturates at 70 kOe. This means a magnetic transition at higher magnetic fields is required to attain saturation magnetization [5]. The hysteresis loops measurements (Figure 5.14) show that the magnetization of the $TbRh_{0.7}Cu_{0.15}B_{0.15}O_3$ oxides is enhanced at high magnetic field. In $EuTiO_3$, the spin state can also be controlled by an applied magnetic field, changing from antiferromagnetic ordering to ferromagnetic ordering [42].

5.2.4 Electrical conductivity

The temperature dependence of the conductivity, in the absence of an applied magnetic field, shows that all the samples exhibit semiconductor-like behaviour. Doping with divalent cations generally increases the conductivity, suggesting an increase in carrier mobility due to the introduction of holes in the band gap as a result of oxidation of Rh^{3+} ($3d^6$) to Rh^{4+} ($3d^5$). The electrical conductivity for $Tb_{0.75}Pb_{0.25}Rh_{0.7}Cu_{0.3}O_3$ (1.26×10^2 $S.m^{-1}$) is around 6 times higher than $Tb_{0.75}Bi_{0.25}Rh_{0.7}Cu_{0.3}O_3$ (16.15 $S.m^{-1}$) at 300K. Also σ_{300K} for $TbRh_{0.7}Cu_{0.15}Zn_{0.15}O_3$ (5.57×10^2 $S.m^{-1}$) was 4 times higher than $TbRh_{0.7}Cu_{0.15}Sc_{0.15}O_3$ (1.40×10^2 $S.m^{-1}$). The electrical conductivity for $TbRh_{0.7}Cu_{0.15}Zn_{0.15}O_3$ is higher than $TbRh_{0.7}Cu_{0.3}O_3$ (1.28×10^2 $S.m^{-1}$) indicative of a larger Rh^{4+} content in the former, which suggests the coexistence of Cu^{3+} in the system. The electrical conductivity for $Tb_{1-x}Pb_xRh_{0.6}Cu_{0.4}O_3$ is generally higher than that observed for $TbRh_{0.6}Cu_{0.4}O_3$. $Tb_{0.8}Pb_{0.2}Rh_{0.6}Cu_{0.4}O_3$ has the highest electrical conductivity and $Tb_{0.7}Pb_{0.3}Rh_{0.6}Cu_{0.4}O_3$ has the lowest electrical conductivity among the series. This possibly reflects either changes in the structure [43], or the presence of vacancies [44]. Electrical resistance measurements of $La_{1-x}Pb_xFeO_3$ showed that, with increasing x, the conductance increased to a maximum at x = 0.2, then decreases to a minimum at x = 0.32. It is speculated that these trends are a consequences of oxygen vacancies clustering and electron localization in the structure [44]. In general, the magnetic moment of the oxides does not appear to influence the transport properties of the oxides.

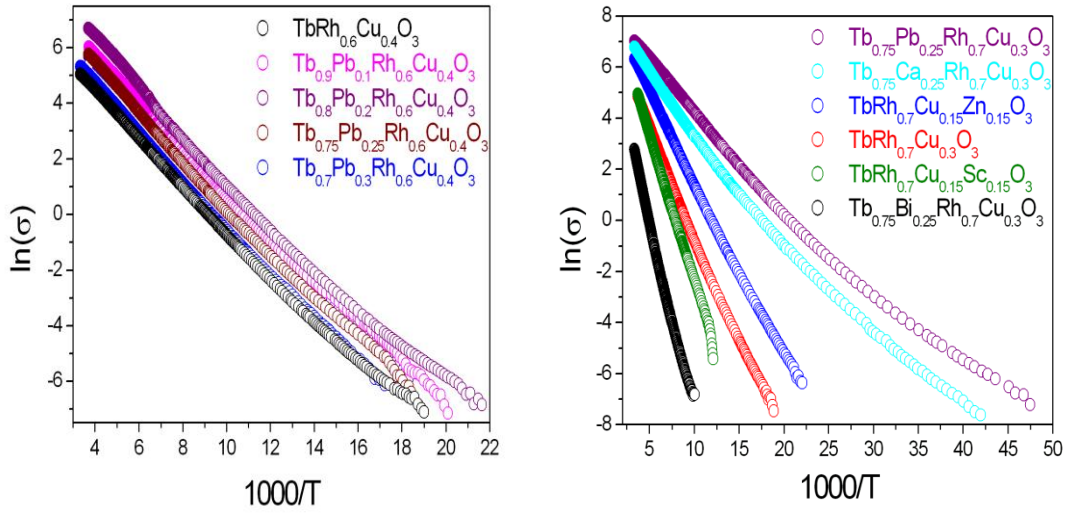

Figure 5.15 The Arrhenius plots of ln (σ) verses inverse temperature for $Tb_{0.75}A_{0.25}Rh_{0.7}Cu_{0.3}O_3$ and $Tb_{1-x}A_xRh_{0.5}Cu_{0.5}O_3$ series.

The Arrenhius plot shown in Figure (5.15) gave activation energy for $TbRh_{0.7}Cu_{0.3}O_3$ of 0.072 eV, which is 75 % higher than that observed for $LaRh_{0.7}Cu_{0.3}O_3$, 0.041 eV. This is likely the result of an increase in the band gap due to the interactions between the valence shell of the *A* cations and the *nd* orbitals of the *B* cations. It was found that doping with Bi^{3+} or Sc^{3+} results in an increase in the activation energy from 0.072 eV to 0.131 and 0.100 eV, respectively, whereas doping with Ca^{2+}, Pb^{2+} or Zn^{2+} results in a decrease in the activation energy from 0.072 eV to 0.036, 0.031 and 0.060 eV, respectively. Doping by similar cations generally has a similar effect on the activation energy. Surprisingly, all the members of $Tb_{1-x}Pb_xRh_{0.6}Cu_{0.4}O_3$ series exhibited similar activation energies (0.070± 0.001 eV), suggesting to Rh^{4+} content is independent of the Pb amount. The fact that these oxides present a similar activation energy suggests that the structural strains caused by the size misfit of the cations is of the same order of magnitude as the strains present in the orthorhombic unit cell of $Tb_{1-x}Pb_xRh_{0.6}Cu_{0.4}O_3$ [45]. This agrees with reports in literature concerning the electrical properties of the defect mixed oxides $Ce_{1-x}Zr_xO_{2-\sigma}$ [46].

5.3.5 Summary

The structural, electrical and magnetic properties of the *A* and *B* sites doped $TbRh_{1-2x}Cu_{2x}O_3$ oxides (*A* = Pb^{2+} and Bi^{3+}; *B*= Sc^{3+}, Cu^{2+} and Zn^{2+}) were investigated. Compared to $LaRh_{1-2x}Cu_{2x}O_3$, Tb^{3+} does not significantly change the

structural and physical properties. The oxides exhibit an orthorhombic perovskite structure with space group *Pbnm*, in addition to semiconductor and paramagnetic behaviours. The X-ray measurements showed the structures of $Tb_{1-x}Pb_xRh_{0.6}Cu_{0.4}O_3$ and $Tb_{0.75}Bi_{0.25}Rh_{1-2x}Cu_xSc_xO_3$ are distorted at $x \leq 0.15$ due to the large ionic size mismatch into *A* and *B* sites and possible oxidation of Tb^{3+}. The unit cell volumes for the oxides are somewhat smaller than the analogous lanthanum oxides because the small ionic size of Tb^{3+}. Doping divalent cations into the *A* or *B* site generally resulted in a decrease in the cell volumes. The increase in the cell volumes of the $Tb_{1-x}Pb_xRh_{0.6}Cu_{0.4}O_3$ series is consistent with the doping *A* site with the larger Pb^{2+} cation.

Compared with the analogous lanthanum oxides, the magnetic susceptibly was larger because of the contribution of Tb^{3+} $4f^8$ electrons. The substitution of Bi^{3+} and Pb^{2+} into the *A* site increases the magnetic moments due to the impact of the lone pair 6*s* electrons of the two cations on the magnetic moment alignments of Rh and Cu cations. Doping with divalent cation increases the conductivity, suggesting an increase in carrier mobility occurs from the oxidation of Rh^{3+} ($3d^6$) to Rh^{4+} ($3d^5$) which induces holes in the band. The activation energy is generally dependent on the electron configuration of the ions. The electrical conductivity measurements of $Tb_{1-x}Pb_xRh_{0.6}Cu_{0.4}O_3$ oxides suggest the presence of vacancies in their structure. In general, the magnetic moments of the oxides are irrelevant to their transport properties of the oxides where Rh ions make the major contribution to the semiconductor-like transport properties.

5.3 References

[1] G. Korotcenkov, Chemical Sensors, Vol. 1, 2010, Momentum Press, New York.

[2] B.Z. Jang, Photo-Electrolytic Catalyst Systems and Method for Hydrogen Production From Water, 2003, U.S. Patent Application 10/657, 037.

[3] H.P.J. Wijn, Magnetic Properties of Metals, 1991, Springer-Verlag, US.

[4] J.H. Van Vleck, The Theory of Electric and Magnetic Susceptibilities, 1944, Oxford University Press, UK.

[5] T. Ohnishi, T. Taniguchi, A. Ikoshi, S. Mizusaki, Y. Nagata, S.H. Lai, M.D. Lan, Y. Noro, T.C. Ozawa, K. Kindo, A. Matsuo, S. Takayanagi, *Journal of Alloys and Compounds*, 506 (2010) 27-32.

[6] R.B. Macquart, M.D. Smith, H.-C. Zur Loye, *Crystal Growth & Design*, 6 (2006) 1361-1365.

[7] Caro, Rare Earths, 1998, Editorial Complutense, Spain.

[8] F. Edgar, J. Westrum, *Advances in Chemistry*, 71 (1967) 380.

[9] A. Wold, R.J. Arnott, W.J. Croft, The Reaction of Rare Earth Oxides with a High Temperature Form of Rhodium (iii) Oxide, 1963, Defense Technical Information Center, US.

[10] I.M. Tang, S. Leelaprute, T. Osotchan, *Solid State Communications*, 103 (1997) 577-580.

[11] T. Taniguchi, W. Iizuka, Y. Nagata, T. Uchida, H. Samata, *Journal of Alloys and Compounds*, 350 (2003) 24-29.

[12] M.T. Haque, H. Satoh, N. Kamegashira, *Journal of Alloys and Compounds*, 390 (2005) 115-121.

[13] M.T. Haque, N. Kamegashira, *Journal of Alloys and Compounds*, 395 (2005) 220-226.

[14] K.S. Wallwork, B.J. Kennedy, D.A. Wang, *AIP Conference Proceedings*, 879 (2007) 879-882.

[15] B.A. Hunter, C.J. Howard, RIETICA. A Computer Program for Rietveld Analysis of X-Ray and Neutron Powder Diffraction Patterns, (1998)

[16] R.D. Shannon, *Acta Crystallographica Section B*, 26 (1970) 447-449.

[17] P. Woodward, *Acta Crystallographica Section B*, 53 (1997) 32-43.

[18] R.D. Shannon, *Acta Crystallographica Section A*, 32 (1976) 751-767.

[19] B.J. Kennedy, C.J. Howard, B.C. Chakoumakos, *Journal of Physics: Condensed Matter*, 11 (1999) 1479.

[20] P.M. Woodward, T. Vogt, D.E. Cox, A. Arulraj, C.N.R. Rao, P. Karen, A.K. Cheetham, *Chemistry of Materials*, 10 (1998) 3652-3665.

[21] T.S. Chan, R.S. Liu, C.C. Yang, W.H. Li, Y.H. Lien, C.Y. Huang, J.F. Lee, *The Journal of Physical Chemistry B*, 111 (2007) 2262-2267.

[22] S. Takagi, A. Subedi, V.R. Cooper, D.J. Singh, *Physical Review B*, 82 (2010) 134108.

[23] D.L. Corker, A.M. Glazer, W. Kaminsky, R.W. Whatmore, J. Dec, K. Roleder, *Acta Crystallographica Section B*, 54 (1998) 18-28.

[24] R. Mahesh, M. Itoh, *Physical Review B*, 60 (1999) 2994-2997.

[25] A. Sundaresan, A. Maignan, B. Raveau, *Physical Review B*, 56 (1997) 5092-5095.

[26] S. Yun, X. Wang, J. Shi, D. Xu, *Journal of Materials Research*, 24 (2009) 3073-3077.

[27] A.G. Belous, O.V. Ovchar, M. Valant, D. Suvorov, D. Kolar, *Journal of the European Ceramic Society*, 21 (2001) 2723-2730.

[28] M.W. Lufaso, P.M. Woodward, *Acta Crystallographica Section B*, 60 (2004) 10-20.

[29] A.L. Allred, *Journal of Inorganic and Nuclear Chemistry*, 17 (1961) 215-221.

[30] J. Ting, B.J. Kennedy, Z. Zhang, M. Avdeev, B. Johannessen, L.Y. Jang, *Chemistry of Materials*, 22 (2010) 1640-1646.

[31] V.M. Goldschmidt, *Naturwissenschaften*, 14 (1926) 477-485.

[32] E. Largeau, M. El-Ghozzi, D. Avignant, *Journal of Solid State Chemistry*, 139 (1998) 248-258.

[33] S. Roy, I.S. Dubenko, M. Khan, E.M. Condon, J. Craig, N. Ali, W. Liu, B.S. Mitchell, *Physical Review B*, 71 (2005) 024419.

[34] K. Tezuka, Y. Hinatsu, Y. Shimojo, Y. Morii, *Journal of Physics: Condensed Matter*, 10 (1998) 11703.

[35] D. Harada, M. Wakeshima, Y. Hinatsu, K. Ohoyama, Y. Yamaguchi, *Journal of Physics: Condensed Matter*, 12 (2000) 3229.

[36] Z.L. Gong, X.O. Yin, L.A. Hong, *Journal of the Electrochemical Society*, 157 (2010) 129-134.

[37] X. Wan, J. Zhou, J. Dong, *Europhysics Letters*, 92 (2010) 57007.

[38] J.E. Greedan, *Journal of the Less Common Metals*, 111 (1985) 335-345.

[39] L. Soderholm, U. Staubt, The Role of Selected F Ions in the Suppression of High-Tc Superconductivity, 1999, Springer US.

[40] I.B. Bersuker, Electronic Structure and Properties of Transition Metal Compounds: Introduction to the Theory, 2010, Wiley, New Jersy.

[41] Y. Shimoda, Y. Doi, M. Wakeshima, Y. Hinatsu, *Journal of Solid State Chemistry*, 182 (2009) 2873-2879.

[42] H. Wu, W.Z. Shen, *Solid State Communications*, 133 (2005) 487-491.

[43] M.E. Melo Jorge, A. Correia dos Santos, M.R. Nunes, *International Journal of Inorganic Materials*, 3 (2001) 915-921.

[44] L. Zhang, J. Hu, P. Song, H. Qin, M. Jiang, *Sensors and Actuators B: Chemical*, 114 (2006) 836-840.

[45] G. Adachi, N. Imanaka, Z.C. Kang, Binary Rare Earth Oxides, 2004, Kluwer Academic Publishers.

[46] M. Boaro, A. Trovarelli, J.-H. Hwang, T.O. Mason, *Solid State Ionics*, 147 (2002) 85-95.

Influence of water on the structure of anion deficient perovskites $AA^*(BB^*)O_{5.5-\delta}$ (A & A^* = Sr^{2+} and Ba^{2+}, B^* = Sr^{2+}, B = Nb^{5+} and Ta^{5+})

6.1 Introduction

The structure of ordered defect double perovskites of the type $A_2B^*BO_{5.5}$ where A and B^* = Ca^{2+}, Sr^{2+} or Ba^{2+} and B = Sb^{5+}, Nb^{5+} or Ta^{5+} are of current interest, since the mechanism of water interaction and the proton diffusion in the structure are critical in determining the electrical properties of such systems [1, 2]. The title double perovskites exhibit ionic conductivity [3] and can absorb significant amounts of water to become proton conductors [4, 5]. Unlike stoichiometric ABO_3 perovskites, in which all the B- type cations are six coordinate, the effective coordination number of the cations in anion-deficient $A_2B^*BO_{5.5}$ perovskites is reduced from six, so that locally some B- type cations will be five, or even four, coordinate [6]. Water can be incorporated into the lattice by occupying either the vacancies or nearby interstitial sites. The site which the incorporated water occupies will be dependent on the differences in the coordination tendencies of the B^* and B cations [6].

The typical crystal chemical effects observed in the $A_2B^*BO_{5.5}$ oxides include B-cation ordering [7] and/or structural distortions approximated by rotation of the nearly rigid BO_6 octahedra [8]; both effects are known to substantially influence the properties of these oxides [7, 9]. A common approach to tune the structure of perovskites is substitution of the cation at the octahedral site forming oxides of the type, $AB_{1-x}B^*_xO_3$. In situations where $x \sim 0.5$ and when the size and/or charge of these two cations are sufficiently different the materials exhibit a 1:1 ordering of the two B-site cations, with alternating layers of the BO_6 and B^*O_6 octahedra along the [111] axis of the cubic cell, leading to a doubling of the unit cell lattice parameter [10, 11]. The A site cations occupy every void that exist between 4 BO_6 and 4 B^*O_6 octahedra resulting in a three-dimensional arrangement that has the same topology as that of the anions and cations in the rock-salt structure [11, 12]. In the non stoichiometric $A_2B^*BO_{5.5}$ oxides, B-site ordering has been reported where the two nominally octahedrally coordinated cations display a rock-salt like ordering [13-15].

Recently, the average and local crystal structures of the perovskites $Sr_2MSbO_{5.5}$ (M = Ca^{2+}, Sr^{2+} and Ba^{2+}) have been reported [15, 16]. These adopt a faced

centred cubic double perovskite structure with space group $Fm\bar{3}m$ and exhibit 1:1 cation ordering. An unusual feature of these oxides is the presence of a displacive disorder of both the *A* site cations and oxygen anions [15]. Representation of the structure of $Sr_2MSbO_{5.5}$ is shown in Figure 6.1.

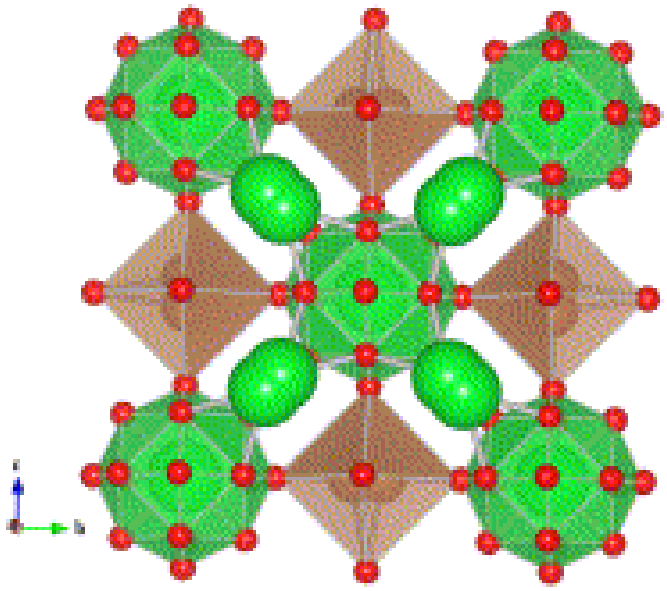

Figure 6.1 Representation of the structure of $Sr_3SbO_{5.5}$ obtained from the refinements against neutron diffraction data[15]. The small red spheres are the oxygen anions, and the tan octahedra are the SbO_6 groups. The large green spheres represent the Sr cations, and the associated disordered SrO_6 groups. The unusual shape of the overlapping spheres is a consequence of the displacive disorder.

In addition these oxides display anomalous thermal expansion of the lattice parameters as a consequence of local clustering of the vacancies and/or the anions with absorbed water molecules [15]. Studies of the local structure using pair distribution function (PDF) analysis of the neutron diffraction data showed that the SbO_x polyhedra adopt distorted trigonal bipyramids as a consequence of movement of oxygen into interstitial positions. This increases the coordination number of the *B* site cation from 5 or 6, to 6 or 7, and decrease the *A* site coordination number from 12 to 11. It is postulated that the movement of the oxygen into the interstitial sites is coupled with large displacements of the *A* and *B* site cations and, for $M = Sr^{2+}$, 45° rotations of the SbO_x polyhedra [16]. The two previous neutron diffraction studies

provided no evidence for long range ordering of the oxygen vacancies in the structure but clearly a considerable amount of short range ordering does exist [15, 16].

6.1.1 Aims and Objectives

In the present work, a new method for creating oxygen vacancies in the perovskites structure was investigated. The methods studied were based on solid state reactions but used different slurry medium, namely acetone and water. The purpose of the solvents is to enhance the homogeneity of the mixtures, and to create dry and wet media for the initial reaction. The main aim of the study is to investigate the impact of an aqueous slurry medium on the structural characteristics of the $Ba_{2-x}Sr_{1+x}BO_{5.5}$ (B = Nb^{5+} and Ta^{5+}, x = 0, 1 or 2) perovskites.

6.1.2 Methodology

The preparation of samples involved different stoichiometric compositions of Nb_2O_5 or Ta_2O_5 (Aldrich, 99.99 %) and $SrCO_3$ or $BaCO_3$ (Aithaca, 99.98 - 99.99 %). The mixtures were initially ground, as either an acetone or aqueous slurry, and preheated at 850 °C for 12 h, and then reground and heated at 1100 °C for 48 h. The crystallography of the samples was monitored by X-ray powder diffraction. Variable temperature powder X-ray diffraction data were collected on a PANalytical X'Pert X-ray diffractometer using Cu Kα radiation and a PIXcel solid-state detector. Temperature control was achieved using an XRK 900 reactor chamber, operating under a vacuum of 10^{-3} Torr.

Room temperature synchrotron X-ray powder diffraction data were collected over the angular range $5 < 2\theta < 85°$, using X-rays of wavelength 0.82518 Å on the powder diffractometer at the Australian Synchrotron [17]. For these measurements each sample was housed in a 0.3 mm diameter capillary. The structures were refined using the program RIETICA [18]. The peak shapes were modelled using a pseudo Voigt function. Neutron powder diffraction data were measured at 293 K using the high resolution powder diffractometer, Echidna [19], at the OPAL facility (Australian Nuclear Science and Technology Organization) at a wavelength of 1.6220 Å.

Thermal gravimetric analysis was conducted using a TGA 2950. The data were recorded under atmosphere of pure N_2 in order to examine weight loss under inert condition. Samples were analysed up to a maximum temperature of 800 °C using a heating rate of 10 °C per minute and purge rate of between 40 and 60

mL/min. The microstructure of the powder samples was examined by scanning electron microscopy using a Intellection Quemscan**.**

6.2 Results and discussion: $AA^*(B\,B^*)O_{5.5}$

Attempts were made to prepare eight compounds of the type $AA^*(BB^*)O_{5.5}$ where *A, A** and $B^* = Sr^{2+}$ or Ba^{2+} and $B = Nb^{5+}$ or Ta^{5+} using both acetone and water during the mixing stages. Only four oxides were successfully obtained as single phases namely $Ba_2SrNbO_{5.5}$, $BaSr_2NbO_{5.5}$, $Sr_3NbO_{5.5}$ and $BaSr_2TaO_{5.5}$ and those all had a faced cubic structure. Other compositions yielded either impure samples, e.g. "$Ba_2SrTaO_{5.5}$" or they were disordered in an orthorhombic structure e.g. $Ba_3TaO_{5.5}$. These structures were possibly distorted due to hydration of the samples [20]. The oxides could be described as $AA^*(BB^*)O_{5.5}.n.H_2O$ to reflect the presence of water in the lattice. For simplicity, the lattice water is neglected when writing the chemical formula. In general, the tolerance factor (τ) of the studied perovskites was found to be less than unity indicating a significant underbonding of the *A*-site cation. The tolerance factor of a perovskite is defined as $\tau = \frac{R_A+R_O}{\sqrt{2}(R_B+R_O)}$ [21] where R_A, R_B and R_x are the ionic radii of the 12-coordinate *A* site and 6-coordinate *B* site cations and the oxygen ion. Accordingly, and assuming random occupancy of the *B* sites by Sr and Nb(Ta), τ was estimated to be 0.926, 0.900 and 0.873 for $Ba_2(SrNb)O_{5.5}$, $BaSr(SrNb)O_{5.5}$, $Sr_2(SrNb)O_{5.5}$ respectively, and for $BaSr(SrTa)O_{5.5}$ τ = 0.900. The decrease in the tolerance factor from 0.926 to 0.873 can be associated with formation of highly strained structures, where the local, coordination environment is different from the average crystal structure of the oxides [16].

6.2.1 Visual Inspection

Visually, it was observed that the colour of the powdered compounds obtained using either acetone or water during the mixing is slightly different. For example, powders of $Ba_2SrNbO_{5.5}$ are dark yellow when prepared using acetone whereas it is light yellow if water is used in the initial mixing. The hardness of the powders was found to be dissimilar; generally samples are much smoother after mixing with water. SEM analysis also revealed that the particle sizes were not equal. These surprising observations indicate that the presence of water in the initial stage of the reaction leads to larger crystallites and this is probably the basis for the differences in appearance and texture. Figure 6.2 demonstrates, as an example, SEM images for

$BaSr_2NbO_{5.5}$ and $BaSr_2TaO_{5.5}$. The grains are monophasic and apparently free of impurities, as confirmed by EDX analysis. The quantitative element analysis indicated that a chemical composition is consistent with the expected stoichiometry.

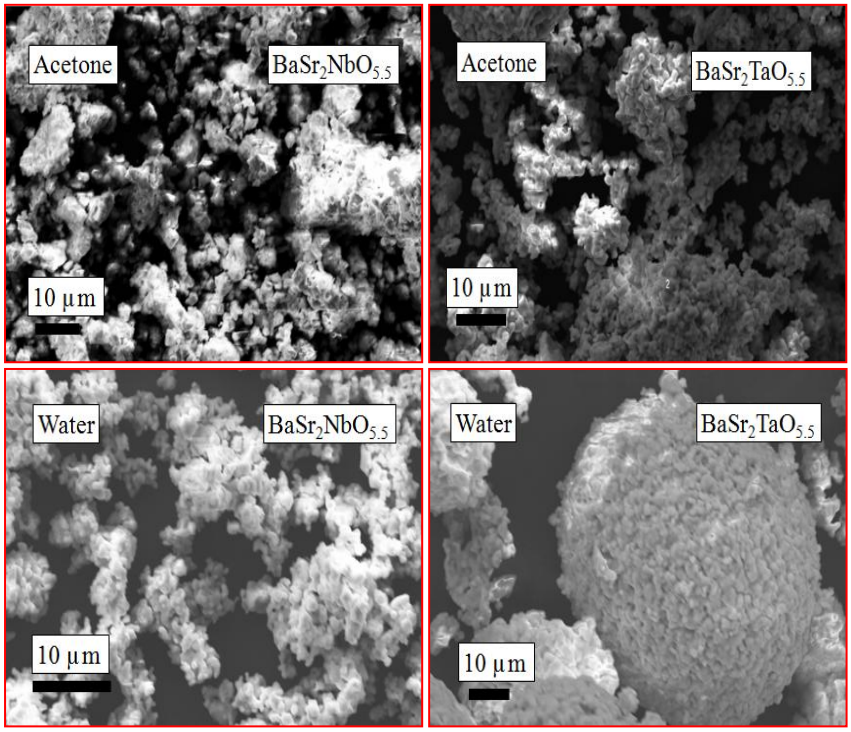

Figure 6.2 Scanning Electron Micrograph images for $BaSr_2NbO_{5.5}$ and $BaSr_2TaO_{5.5}$ obtained using either acetone or water during the mixing.

6.2.2 Crystal Structure

The synchrotron X-ray powder diffraction patterns of the oxides exhibited strong (111) reflections indicative of 1:1 ordering of the *B*-site cations. The (111) reflections were stronger in $Sr_3NbO_{5.5}$ and $BaSr_2TaO_{5.5}$ than in $Ba_2SrNbO_{5.5}$ and $BaSr_2NbO_{5.5}$ oxides, suggesting a high degree of order in the former oxides. The solid state chemistry of Ta^{5+} and Nb^{5+} are generally believed to be similar, so it is reasonable to expect $BaSr_2TaO_{5.5}$ will display similar behaviour to $BaSr_2NbO_{5.5}$. In X-ray diffraction, the former has the advantage that there is significant X-ray contrast between Sr (Z = 38) and Ta (Z = 73) and this will allow the two cations to be distinguished by XRD. The same cannot be claimed for Sr^{2+} and Nb^{5+} (Z = 41), which are isoelectronic. The higher degree of 1:1 ordering for $Sr_3NbO_{5.5}$ and $BaSr_2TaO_{5.5}$ can be attributed to the size mismatch between the *A* and *B* site cations [12] moderated by the time and temperature of annealing. $BaSr_2TaO_{5.5}$ was annealed

for 72 h at 1100 ºC in order to obtain a single phase sample. The effect of the time and temperature of annealing on cation ordering has been extensively investigated in many studies. For example, studies of the evolution of ordering in the $(0.85)Ba(Zn_{1/3}Ta_{2/3})O_3$–$(0.15)BaZrO_3$ and $Pb(Mg_{1/3}Ta_{2/3})O_3$–$PbZrO_3$ solid state solutions showed that the supercell peaks strengthen and sharpen with the anneal time and temperature reflecting the growth of the ordered domains [22, 23]. A recent study of Ba_2YTaO_6 showed heating the oxide for 100 h at 1400 ºC results in the growth of the various reflections such as (111) reflections in the XRD patterns demonstrating the onset of long range ordering of the Y and Ta cations [24]. It has been observed that the structure of Ba_2YTaO_6 is very sensitive to the preparative method employed with prolonged heating necessary to induce long range ordering of the *B* site cations [24].

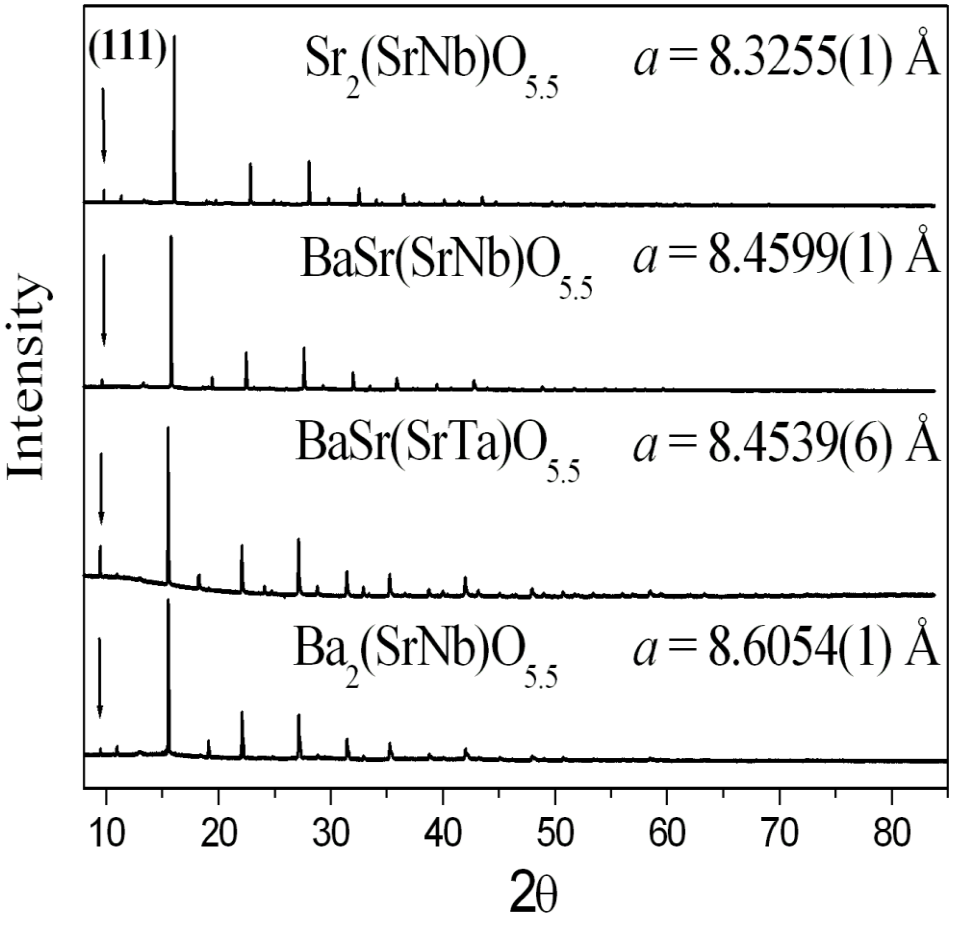

Figure 6.3 The observed synchrotron X-ray diffraction profiles for the $AA^*(BB^*)O_{5.5}$ samples obtained using acetone during the mixing. The arrow shows the position of the (111) reflections.

Figure 6.3 illustrates the observed synchrotron X-ray diffraction profiles for the four $AA^*(BB^*)O_{5.5}$ samples obtained using acetone during the mixing. No splitting or asymmetry of the cubic reflections was detected in the diffraction patterns indicating the structures were all cubic, and the appropriate space group was $Fm\bar{3}m$. As expected, the cell size increases as the size of the *A*- type cation increases from 8.3255(1) Å for $Sr_3NbO_{5.5}$ to 8.4599(1) Å for $BaSr_2NbO_{5.5}$ and 8.6054(1) Å for $Ba_2SrNbO_{5.5}$. Ba^{2+} (12 coordinate ionic radius, 1.61 Å) [25] has a larger ionic size than Sr^{2+}(1.44 Å) [25]. The lattice parameter for $Sr_3NbO_{5.5}$ is similar to that reported by Animitsa *et al* (a = 8.3123 Å) [26], who demonstrated the Nb cations to be pentavalent. The small differences in the values can be attributed to the differences in the preparation method of the samples and/or the incorporation of water. The cell edge of the $BaSr_2TaO_{5.5}$, 8.4539(6) Å, is similar to that of the $Ba_2SrNbO_{5.5}$ reflecting the similarity in the ionic radii of Nb^{5+} (6 coordinate ionic radius. 0.64 Å) and Ta^{5+} (0.64 Å) [25]. The materials are formulated as above in order to emphasize the ordering at the *B* site between the Sr and (Nb, Ta) cations. In the double perovskite structure, it is anticipated that the two smallest cations will order in the octahedral sites, this ordering being a consequence of the differences in the size and/or charge between the two cations [27]. The largest cation will then occupy the 12-coordinate (cuboctahedral) site. The corresponding ionic radii of Ba^{2+} (12 coordinate ionic radius, 1.61 Å and 6 coordinate ionic radius. 1.35 Å) [25]; Sr^{2+} (1.44 and 1.18 Å), Nb^{5+} (6 coordinate ionic radius. 0.64 Å) [25] and Ta^{5+} (0.64 Å) [25] cations suggest that the (Nb^{5+}, Ta^{5+}) and one Sr^{2+} cation will occupy the 6-coordinate sites whereas the Ba^{2+} or a mixture of Sr^{2+} and Ba^{2+} will occupy the cuboctahedral sites.

The Rietveld refinements, using synchrotron X-ray powder diffraction data, confirmed the ordering of the two *B*- site cations and established the distribution of these. Refinement of the structure of $BaSr_2TaO_{5.5}$ (acetone), assuming Sr only occupies the octahedral sites gave R_p = 3.21 % and R_{wp} = 4.77 %. The fractional positions were *A* ($\frac{1}{4}$, $\frac{1}{4}$, $\frac{1}{4}$), B^* (0, 0, 0), *B* ($\frac{1}{2}$, $\frac{1}{2}$, $\frac{1}{2}$) and O (x, 0, 0) with $x \sim 0.25$. Refinements where the Sr and Ta were allowed to disorder over the two appropriate sites (anti-site disorder) did not significantly alter the quality of the fits R_p = 3.15 % and R_{wp} = 4.63 % and indicated less than 3 % of the Ba was mixed in the octahedral site. Figure 6.4 illustrates the Rietveld refinement profiles for the ordered model of $BaSr_2TaO_{5.5}$. The pattern contains a number of weak and somewhat broadened

reflections that are more pronounced at low angles originating from traces of a second perovskite phase. Consequently, a two phase model was utilized where the major phase was in $Fm\bar{3}m$ and the minor phase in $Pm\bar{3}m$ where the cations were disordered over the two sites appropriate to the stoichiometry. The refinements of the structure of $Sr_3NbO_{5.5}$, $BaSr_2NbO_{5.5}$ and $Ba_2SrNbO_{5.5}$ yielded comparable fits, and gave R_p = 5.50, 6.91 and 3.66 % and R_{wp} = 9.55, 13.15 and 5.45 % respectively. The refinements also suggest that less than 4-6 % of Sr and Nb cations were mixed over the two 6 coordinate sites. The refined oxygen occupancies in the all structures provide evidence for the non stoichiometry. The oxides obtained using water during the mixing were found to have similar atom distributions to those made by using acetone suggesting that, as expected, the reaction media had a little impact on ordering. Table 6.1 presents the results of the structure refinement of the $BaSr_2TaO_{5.5}$.

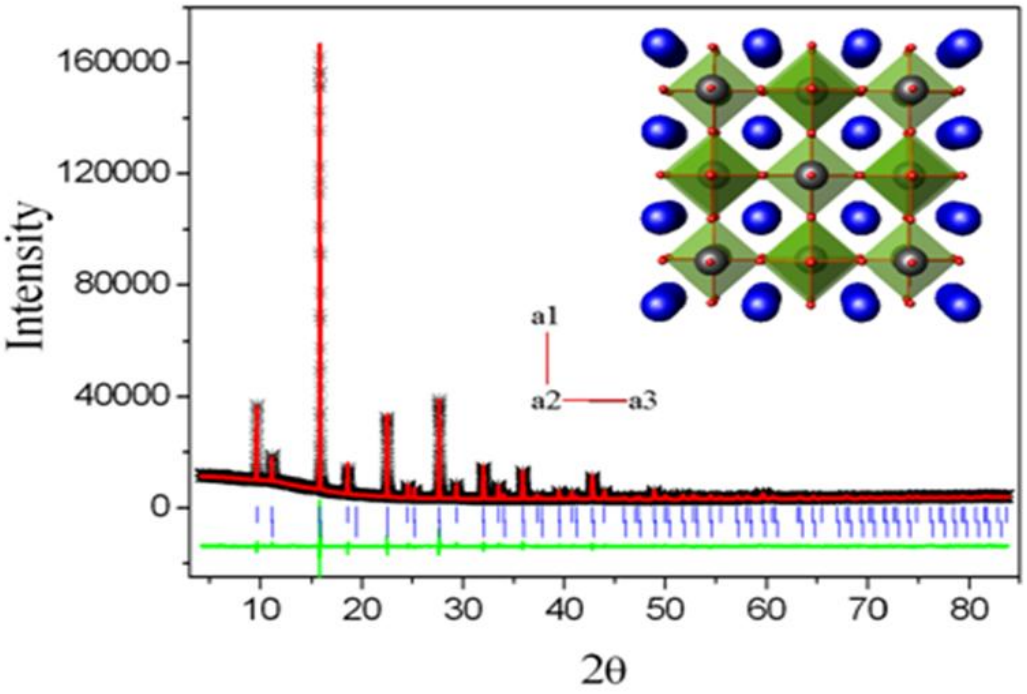

Figure 6.4 Synchrotron X-ray diffraction profiles for $BaSr_2TaO_{5.5}$ (acetone). The data are represented by the crosses and the solid lines are the calculated and difference profiles. The positions of the space group allowed reflections are shown by the vertical markers immediately below the observed profile. Upper marks are from the major phase and lower marks for the minor $Pm\bar{3}m$ phase. A representation of the ordered $BaSr_2TaO_{5.5}$ structure is also included.

Table 6.1 Structural parameters for $BaSr_2TaO_{5.5}$ as obtained from the Rietveld refinement against powder synchrotron diffraction data.

Atom	*site*	*x*	*y*	*z*	B_{iso} ($Å^2$)	*Occupancy*
Major Phase		$Fm\bar{3}m$	*a* = 8.4539(6) Å			Z = 8
Ba/ Sr	8(*c*)	0.25	0.25	0.25	3.97(3)	0.5/0.5
Sr	4(*a*)	0	0	0	4.90(5)	1
Nb	4(*b*)	0.5	0.5	0.5	0.30(1)	1
O	24(*e*)	0.2741(5)	0	0	5.74(2)	0.92(2)
Minor Phase		$Pm\bar{3}m$	*a* = 4.2154(1) Å			Z = 1
Ba	1(*b*)	0.5	0.5	0.5	0.33(16)	1
Nb	1(*a*)	0	0	0	0.10(11)	1
O	3(*b*)	0.5	0	0	7.53(15)	0.71(3)
R- factor		R_p = 3.15 %, R_{wp} = 4.63 %, χ^2 = 8.93.				

The lattice parameters of the oxides were found to be slightly dependent on the synthetic methods. Table 6.3 provides the values of lattice parameters, unit cell volumes and *x* coordinate of the oxygen for the different compositions. The cell volumes are slightly higher where water was employed in the reaction than in the acetone treated samples. This result corresponds to the effect of water on the oxides texture (see Section 6.2.1) where the grain sizes and the cell volumes increased by adding water to the initial reaction. It is thought that in these samples the absorbed water interacted with the framework oxygen resulting in small displacements of the atoms. Water has often had a strong influence on the physical and chemical properties of alkaline earth perovskites [28]. In many cases such as $MgSiO_3$ [29], water can be used to produce samples with large grain sizes and allows homogeneous crystal growth for the oxide [30]. Water content is known also to influence the transformation boundary of $MgSiO_3$ [31, 32].

Table 6.2 Lattice parameters (*a*), unit cell volumes (V) and *x* coordinate of the oxygen for different compositions of $AA^*(BB^*)O_{5.5}$ as obtained from the Rietveld refinement against powder synchrotron diffraction data.

Formula	*a* (Å)	V (Å^3)	*x*
$Ba_2SrNbO_{5.5}$ (acetone)	8.6054(1)	637.263(1)	0.2773(5)
$Ba_2SrNbO_{5.5}$ (water)	8.6060(1)	637.381(1)	0.2806(6)
$BaSr_2NbO_{5.5}$ (acetone)	8.4599(1)	605.476(2)	0.2706(8)
$BaSr_2NbO_{5.5}$ (water)	8.4733(5)	608.554(7)	0.2725(5)
$Sr_3NbO_{5.5}$ (acetone)	8.3255(1)	577.341(1)	0.2897(4)
$Sr_3NbO_{5.5}$ (water)	8.3289(4)	577.784(5)	0.2892(4)
$BaSr_2TaO_{5.5}$ (acetone)	8.4539(6)	604.186(1)	0.2729(6)
$BaSr_2TaO_{5.5}$ (water)	8.4803(4)	609.955(6)	0.2708(5)

Since the structural refinement using the XRD data did not locate the light oxygen atoms with certainty, neutron diffraction was employed to better describe the position of oxygen atoms and to aid in the refinement of any non-stoichiometry. Neutron diffraction data were collected for the two samples $BaSr_2NbO_{5.5}$ (water) and $BaSr_2TaO_{5.5}$ (water). Compared to other oxides studied this pair, displayed a significant difference in the cell volume between the two synthetic methods. A striking feature of the neutron diffraction profiles for $BaSr_2NbO_{5.5}$ and $BaSr_2TaO_{5.5}$ is the presence of diffuse intensity in the form of a modulated background (Figure 6.5). Since there is only one anion site in the ideal structure it is not possible to have an ordered arrangement of the anion vacancies. The diffuse structure was not apparent in the X-rays profiles suggesting that the modulated background is associated with disorder of the lighter atoms. The disordered phase evident in the synchrotron profiles of $BaSr_2NbO_{5.5}$ and $BaSr_2TaO_{5.5}$ was not observed in the corresponding neutron profile, presumably as a result of the lower peak width resolution of the neutron profiles.

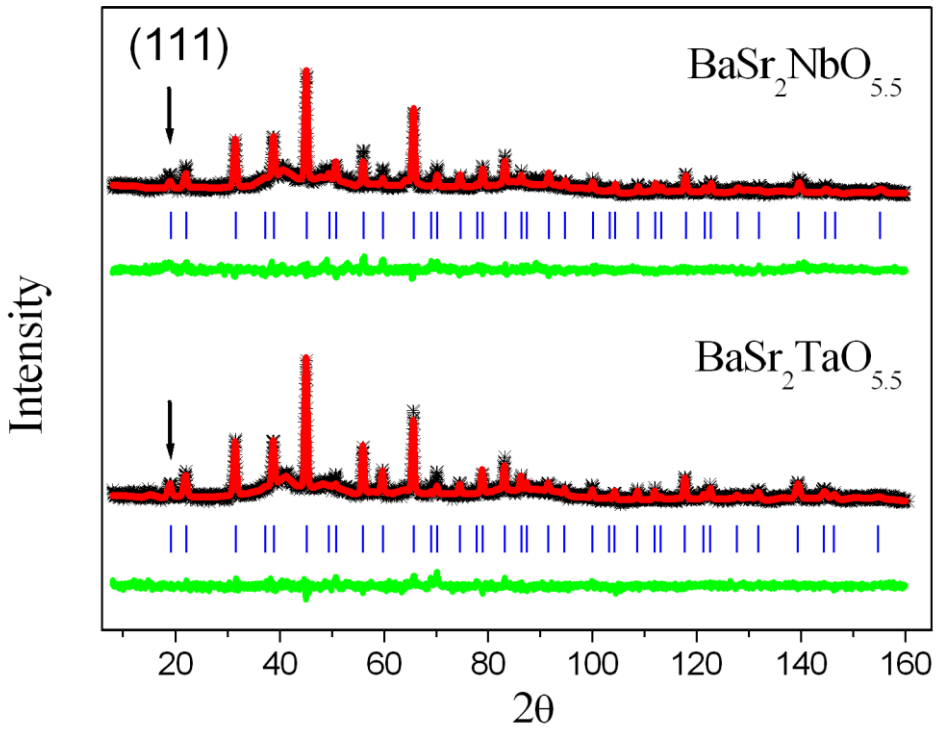

Figure 6.5 Neutron diffraction profiles for $Ba_2SrNbO_{5.5}$ (water) and $BaSr_2TaO_{5.5}$ (water). The data are represented by the crosses and the solid lines are the calculated and difference profiles. The positions of the space group allowed reflections are shown by the vertical markers immediately below the observed profile.

The observed backgrounds are similar to that reported by Zhou *et al*. for $BaSr_2SbO_{5.5}$ [15], who established, from neutron diffraction measurements, that such background has no obvious correlations with the presence of adsorbed water or non stoichiometry in the structure, but were a consequence of disorder of the lighter atoms. A similar observation was also reported by King *et al*. for the same compound [16]. King and co-workers concluded that such modulation must be related to the presence of disorder in the oxygen anion sites. Short-range correlations between atoms displacements can give rise to the modulated diffuse background [16]. Accordingly, the refinements of the structure of $BaSr_2NbO_{5.5}$ and $BaSr_2TaO_{5.5}$ against the neutron diffraction data were performed using the same model suggested by Zhou *et al.* [15] where the Ba(1), Sr (1) and oxygen were disordered at the cuboctahedral and anion sites respectively. As found by Zhou *et al*., the refinements showed evidence for *A* cation and anion displacive disorder in the two oxides

structures. Neutron diffraction studies of the corresponding dehydrated materials may be of interest.

Table 6.3 Results of the structural refinements for $BaSr_2NbO_{5.5}$ (water) and $BaSr_2TaO_{5.5}$ (water) using neutron powder diffraction data.

	Atom	*x*	*y*	*z*	B_{iso} (Å^2)	*Occ*
$BaSr_2NbO_{5.5}$	Ba/Sr(1)	0.264(5)	0.264(5)	0.264(5)	4.91(89)	1
	Sr(2)	0	0.028(3)	-0.028(3)	0.13(99)	0.76(1)
	Nb	0.5	0.5	0.5	3.48(15)	1
	O(1)	0.2725(4)	0	0	3.76(10)	0.71(1)
	O(2)	0	0.164(1)	0.164(1)	0.60(40)	0.08(1)
	R- factors	R_p = 3.82 %, R_{wp} = 4.87 %, χ^2 = 1.51				
$BaSr_2TaO_{5.5}$	Ba/Sr(1)	0.2736(8)	0.2736(8)	0.2736(8)	3.20(29)	1
	Sr(2)	0	0.033(2)	-0.033(2)	1.76(74)	0.77(1)
	Ta	0.5	0.5	0.5	1.97(08)	1
	O(1)	0.2708(5)	0	0	3.90(10)	0.67(1)
	O(2)	0	0.169(1)	0.169(1)	3.88(54)	0.09(1)
	R- factors	R_p = 3.41 %, R_{wp} = 4.46 %, χ^2 = 1.45				

As summarised in Table 6.3, a $\langle 01\bar{1} \rangle$ displacement of the 4*a* cation at (0, 0, 0) onto a 48*i* site at (0, *y*, -*y*) with $y \sim 0$ was evident and such displacement gave an optimal fit to the neutron data. The occupancy of the 48*i* site was refined and gave the required stoichiometry. Examination of the Fourier maps generated by Rietica revealed the presence of nuclear density near 0 1/6 1/6, corresponding to a 48*h* site in $Fm\bar{3}m$. The Fourier transform is a useful probe in the crystallography since the difference map can be used to locate missing atoms in a crystal structure [33]. The Fourier difference maps provided evidence for the presence of the protons (water) in the structure as suggested by TGA analysis (see below). The anion disorder observed in $Ba_2SrNbO_{5.5}$ and $BaSr_2TaO_{5.5}$ is similar to that described for $BaSr_2SbO_{5.5}$ [15] and $Sr_4Nb_2O_9$ [34]. In the $BaSr_2NbO_{5.5}$ and $BaSr_2TaO_{5.5}$, the displacement of the *A*-cations occurs in the absence of long-range tilting of the BO_6 octahedra. The measured neutron and synchrotron X-ray diffraction profiles show no evidence for superlattice

peaks associated with tilts. The absence of tilting in some related anion deficient perovskites was previously described by Levin and co-workers for $Sr_3NbO_{5.5}$ [34] and by Zhou *et al*. for $BaSr_2SbO_{5.5}$ [15] who concluded that the bonding instabilities of the *A*-site cation can be sufficiently relieved by both, displacive disorder of the cations and the anion vacancies, effectively removing the need for tilting. The refined occupancies (*Occ*) of the O(1) and O(2) site correspond to the stoichiometry of $Ba_2SrNbO_{5.23(1)}$ and $Ba_2SrTaO_{5.14(1)}$. The occupancies of oxygen are smaller than expected because oxygen mobility evident by the modulated background impacts on the effective nuclear density of the corresponding site. Oxygen anions in defect perovskites can be mobile, giving rise to oxide ion conductivity [35].

The calculated bond distances of Nb-O (1.9275(1), 3.1671(1) Å) and Ta-O (1.9438 (1), 3.1535 (1) Å) are similar to that reported for Sb-O in $BaSr_2SbO_{5.5}$ (1.966(1) and 3.161(3) Å) [16] suggesting these oxides may have a similar local structure to $BaSr_2SbO_{5.5}$. The PDF study of King *et al*. showed that in $BaSr_2SbO_{5.5}$, the SbO_5 polyhedra form distorted trigonal bipyramids as a result of two of the oxygen atoms moving into interstitial sites. This results in an increase in the local coordination environment of the *B* - site from 5 or 6 to 6 or 7 and a decrease in the coordination number of the *A* - site cation from 11 to 10 [16]. The pair distribution function (PDF) analysis method is a powerful tool for the study of local structure in both crystalline and non-crystalline materials [36]. It involves the direct model free Fourier transformation of X-ray or neutron powder diffraction data and gives the probability of finding any two atoms at a given interatomic distance [36]. In an atomic PDF that distribution appears as a sequence of peaks starting at the shortest and continuing up to the longest distinct atomic pair distance a material shows [36]. The areas under the PDF peaks are proportional to the number of atomic pairs occurring at the respective distances and the widths of the peaks to the root mean square scatter, U_{ij}, about those distances. In particular, the full width at half maximum of a PDF peak equals 2 U_{ij} $\sqrt{2ln2}$ where i and j denote the particular atomic pair type. The atomic root mean square scatter amplitudes may be dynamic (e.g., thermal) or static (e.g., due to strain) in nature reflecting correlated or uncorrelated atomic motion [36]. The average *A*-O1 and *A*-O2 bond distances of $BaSr_2NbO_{5.5}$ (3.0927(1) and 2.5039(1) Å) and $BaSr_2TaO_{5.5}$ (3.1582(1) and 2.4876(1) Å) are higher than those reported for $BaSr_2SbO_{5.5}$ (2.991 and 2.311 Ǻ) which is consistent with the increase in

the relative ionic radii of the *B* site cation. The displacements of the cations from their ideal positions plays an important role in determining their electrochemical properties [37].

6.2.3 Thermal analysis

Thermal analysis measurements (TGA and VT-XRD) demonstrate a weight loss and an unusual thermal expansion upon heating for the oxides prepared using water during the mixing. Figure 6.6 shows the thermal decomposition curves of $BaSr_2NbO_{5.5}.nH_2O$ and $BaSr_2TaO_{5.5}.nH_2O$ in the temperature range 30-600 °C and under a nitrogen atmosphere. These measurements were performed immediately after sample preparation.

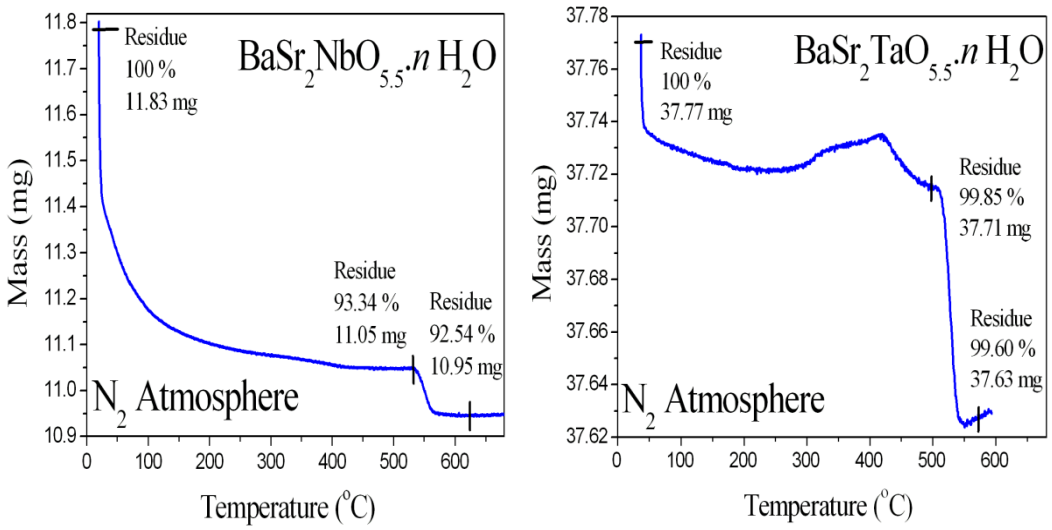

Figure 6.6 Thermogravimetic curves for $BaSr_2NbO_{5.5}.nH_2O$ and $BaSr_2TaO_{5.5}.nH_2O$ under a nitrogen atmosphere.

The initial weight loss for both samples at temperatures of ≤ 100 °C is believed to be due to the loss of chemisorbed water. That this occurs below 100 °C reflects the use of a dry N_2 atmosphere in the measurements. The observed weight loss near 550 °C is indicative of the removal of the water molecules that occupied the nominally vacant anion sites. At higher temperature, the sample weight is essentially constant demonstrating that all the water is lost from the lattice by ~ 600 °C. From the TGA measurements, *n* in $BaSr_2NbO_{5.5}.nH_2O$ and $BaSr_2TaO_{5.5}.nH_2O$ were found to be 0.30 and 0.10 moles per formula unit respectively. The inclusion of water in the oxides suggests the possibility of proton conduction, which might be lost at high temperatures as consequence of the loss of water. $BaSr_2TaO_{5.5}.0.1H_2O$

has a smaller water content than $BaSr_2NbO_{5.5}.0.3H_2O$ possibly due to differences in the annealing time used in the preparing of the two samples or differences in the samples morphology that enable more rapid incorporation of water.

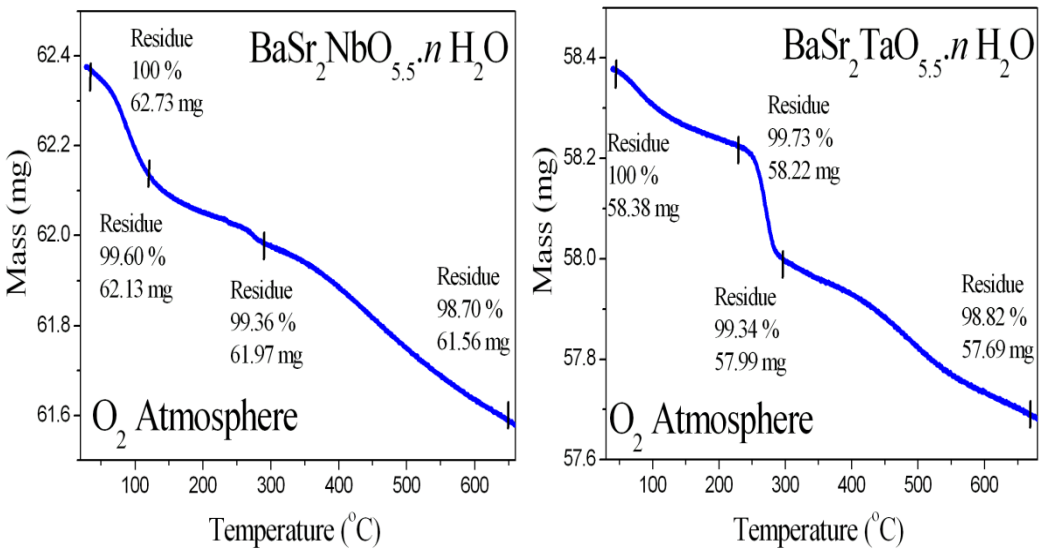

Figure 6.7 Thermogravimetic curves for $BaSr_2NbO_{5.5}.nH_2O$ and $BaSr_2TaO_{5.5}.nH_2O$ under an oxygen atmosphere.

Heating the samples under oxygen (see Figure 6.7) after the samples had been stored for several days showed at least three events are present and these appear different to that observed under nitrogen atmosphere for the freshly prepared samples. In particular, it was found that heating the samples under oxygen decreases the main event corresponding to the removal of water temperature from ~550 to 250 °C suggesting that the mechanism of water release from the structure is very sensitive to the surrounding atmosphere. At temperatures > 250 °C, the samples display gradual weight loss suggesting a considerable amount of CO_2 may be present in structure. This is a consequence of the reaction of the CO_2 from the atmosphere with the sample during storage. IR measurements of the samples showed evidence of the growth of 1500-1400 cm^{-1} peak with the storage time indicative of the formation of CO_3^{2-} in the structure. The presence of CO_2 in the sample may disrupt the H-bonding between the absorbed water and lattice anions. The changes evident upon storage are likely to preclude use of the materials in practical devices. Perovskite oxides of composition $A_2B^*BO_{5.5}$ such as $Sr_{1-x}Ca_xFe_{0.5}Co_{0.5}O_{3-\delta}$ were extensively investigated for CO_2 absorption properties and were proved to be useful as materials

for CO_2 absorption in wide temperature range [38, 39]. During the absorption of CO_2, a spinel compound can be formed according to the following reaction: $2(Sr,Ca)(Fe,Co)O_{2.5} + CO_2 \rightarrow (Sr,Ca)CO_3 + (Sr,Ca)(Fe,Co)_2O_4$ [38]. It is stated that perovskite oxides with lattice oxygen vacancies, which are produced at high temperature, easily absorbed CO_2 [39].

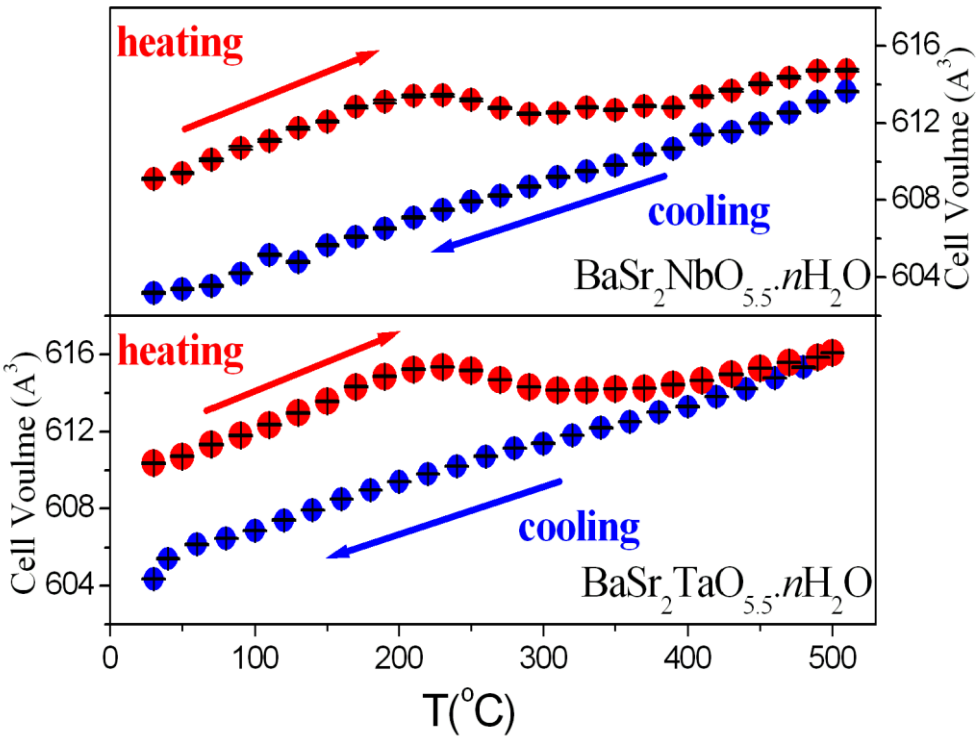

Figure 6.8 Temperature dependence of the cell volume for $BaSr_2NbO_{5.5}.nH_2O$ and $BaSr_2TaO_{5.5}.nH_2O$. The red circles are the results obtained during the heating cycle and the blue circles those during cooling. The sample vacuum was 1 × 10^{-3} Torr during the measurements.

Variable temperature XRD (VT-XRD) data reveals a possible mechanism of the water interaction with the material. As shown in Figure 6.8, initial heating results in normal thermal expansion of the unit cell volumes of $BaSr_2NbO_{5.5}.nH_2O$ and $BaSr_2TaO_{5.5}.nH_2O$ in which both the *A*-O and *B*-O distances increase. Between 250 and 350 ºC, the cell volumes decreases as a result of water loss. Above 350 ºC, the heating, again, results in normal thermal expansion suggesting total removal of the lattice water. Recall that the XRD measurements were performed under vacuum whereas the TGA analysis was under a N_2 atmosphere. The importance of water is reflected in linear thermal contraction upon cooling. A similar observation has been

reported for the $Sr_2MSbO_{5.5}$ (M = Ca^{2+}, Sr^{2+} and Ba^{2+}) system [15]. In this earlier work it was stated that a combination of local clustering of the anions and vacancies together with water–water and water–host hydrogen bonds plays a role in defining the volume of the encapsulated water clusters and that changes in the local structure upon heating result in the anomalous thermal expansion observed in variable temperature diffraction measurements [15]. In that work, the temperature at which the cell size begins to decrease upon heating was found to be dependent on the size of the cation and increases in the order Ca < Sr < Ba [15]. The movement of the oxygen into the interstitial sites is also thought to be important since this is coupled with large displacements of the *A*- and *B*-site cations and gives a broad distribution in bond lengths [16]. Figure 6.9 demonstrates the variation of *A*-O, *B*-O and O-O bond distances of $BaSr_2NbO_{5.5}.nH_2O$ and $BaSr_2TaO_{5.5}.nH_2O$ during the heating process. The anomalous thermal expansion of the bond distances observed in temperature range 200-300 K is correlated with the loss of water lattice. The use of X-ray diffraction methods in determining metal-oxygen bond distances limits the precision of the results and it is not practical to establish if both the AO_x and BO_x polyhedral expand continuously.

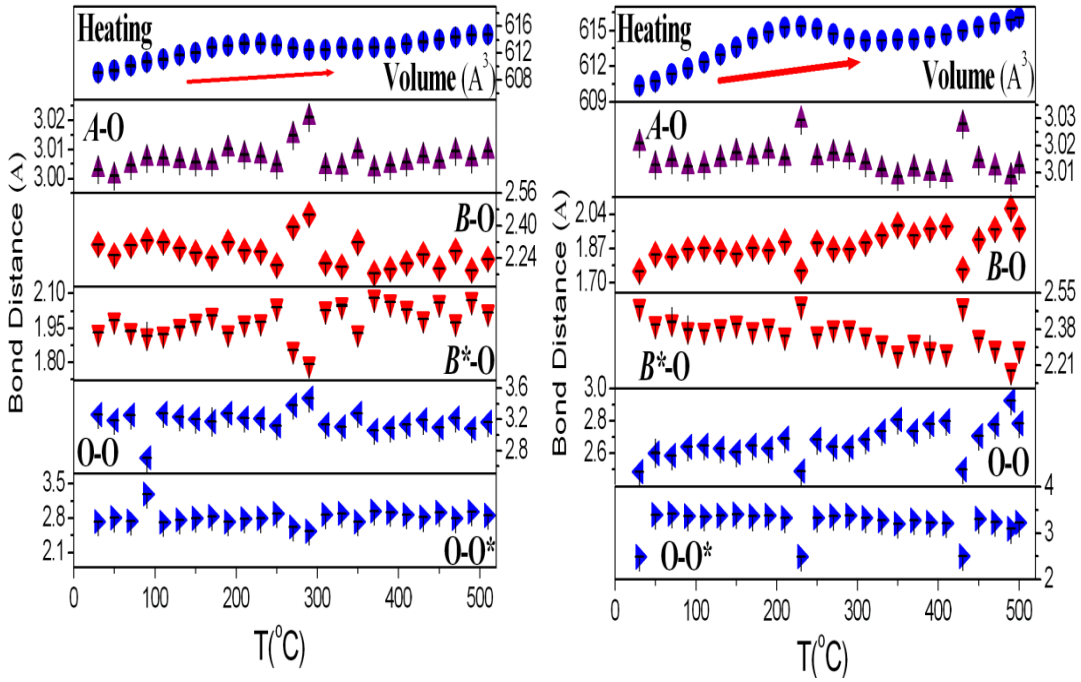

Figure 6.9 The variation of A-O, B-O and O-O bond distances of the $BaSr_2NbO_{5.5}.nH_2O$ and $BaSr_2TaO_{5.5}.nH_2O$ with temperature estimated by X-ray diffraction data.

6.2.4 Summery

The impact of changing the conditions used to prepare some perovskites of the type $AA^*(BB^*)O_{5.5}$ was investigated. The oxides were prepared using acetone and aqueous solvents as media of the reactions. The two synthetic methods produce monophasic powders that differ in color, particle size, and hardness. It is found that mixing water with reactants influences the morphology and the texture of the oxides resulting in yellowish color, larger grain size and rougher surfaces. All the oxides form a cation ordered double perovskite structure and have a $Fm\bar{3}m$ cubic lattice arrangement. There is no evidence for cation mixing between the *A* and *B* sites. The compounds obtained by reaction with water have larger cell volumes than those obtained by reaction with acetone. This suggests a role of hydrogen bondings of water with the oxygen lattice. The neutron diffraction profiles for $Ba_2SrNbO_{5.5}$ (water) and $BaSr_2TaO_{5.5}$ (water) showed the presence of diffuse structure as a consequence of disorder of oxygen atoms. The structural refinements provide evidences for anion deficiency and a displacive disorder of *A* cations into the structures. The oxides demonstrate a weight loss upon heating due to the presence of water within the structures. TGA analysis and IR measurement suggest a trace amount of CO_2 atmosphere can be absorbed during storage. The observation of unusual thermal expansion of the unit cells is explained by the presence of water and vacancies in the structure. It is believed that the movement of the oxygen into the interstitial sites results in large displacements of the *A*- and *B*-site cations and broad bond length distribution. There is the possibility of proton conduction which would be reduced at elevated temperatures as consequence of the loss of water.

6.3 References

[1] K. W. Browall, O. Muller and R. H. Doremus, *Materials Research Bulletin*, 11 (1976) 1475-1481.

[2] N. L. Ross, R. J. Angel, L. W. Finger, R. M. Hazen and C. T. Prewitt, *Journal of American Chemical Society*, 351 (1987) 164-172.

[3] J. Lecomte, J. P. Loup, M. Hervieu and B. Raveau, *Physica Status Solidi*, 65 (1981) 743-752.

[4] A. S. Nowick and Y. Du, *Solid State Ionics*, 77 (1995) 137-146.

[5] R. Glöckner, A. Neiman, Y. Larring and T. Norby, *Solid State Ionics*, 125 (1999) 369-376.

[6] I. Animitsa, A. Neiman, A. Sharafutdinov and S. Nochrin, *Solid State Ionics*, 136–137 (2000) 265-271.

[7] I. Levin, J. Y. Chan, R. G. Geyer, J. E. Maslar and T. A. Vanderah, *Journal of Solid State Chemistry*, 156 (2001) 122-134.

[8] I. Levin, L. A. Bendersky, J. P. Cline, R. S. Roth and T. A. Vanderah, *Journal of Solid State Chemistry*, 150 (2000) 43-61.

[9] E. L. Colla, I. M. Reaney and N. Setter, *Journal of Applied Physics*, 74 (1993) 3414-3425.

[10] C. J. Howard, B. J. Kennedy and P. M. Woodward, *Acta Crystallographica Section B*, 59 (2003) 463-471.

[11] Q. Zhou, B. J. Kennedy and M. Avdeev, *Journal of Solid State Chemistry*, 183 (2010) 1741-1746.

[12] G. King and P. M. Woodward, *Journal of Materials Chemistry*, 20 (2010) 5785-5796.

[13] T. Norby, *Journal of Materials Chemistry*, 11 (2001) 11-18.

[14] I. Animitsa, T. Norby, S. Marion, R. Glöckner and A. Neiman, *Solid State Ionics*, 145 (2001) 357-364.

[15] Q. Zhou, B. J. Kennedy and M. Avdeev, *Journal of Solid State Chemistry*, 184 (2011) 2559-2565.

[16] G. King, K. J. Thomas and A. Llobet, *Inorganic Chemistry*, 51 (2012) 13060-13068.

[17] K. S. Wallwork, B. J. Kennedy and D. A. Wang, *AIP Conference Proceedings*, 879 (2007) 879-882.

[18] B. A. Hunter and C. J. Howard, RIETICA. A Computer Program for Rietveld Analysis of X-Ray and Neutron Powder Diffraction Patterns, 1998, Lucas Heights Research Laboratories Sydney.

[19] K. Liss, B. Hunter, M. Hagen, T. Noakes and S. Kennedy, *Physica B*, 385–386 (2006) 1010–1012.

[20] I. Animitsa, A. Nieman, S. Titova, N. Kochetova, E. Isaeva, A. Sharafutdinov, N. Timofeeva and P. Colomban, *Solid State Ionics*, 156 (2003) 95-102.

[21] V. M. Goldschmidt, *Naturwissenschaften*, 14 (1926) 477-485.

[22] L. Chai and P. K. Davies, *Journal of the American Ceramic Society*, 80 (1997) 3193-3198.

[23] W. Dmowski, M. K. Akbas, T. Egami and P. K. Davies, *Journal of Physics and Chemistry of Solids*, 63 (2002) 15-22.

[24] Q. Zhou, B. J. Kennedy and J. A. Kimpton, *Journal of Solid State Chemistry*, 184 (2011) 729-734.

[25] R. D. Shannon, *Acta Crystallographica Section B*, 26 (1970) 447-449.

[26] I. Animitsa, T. Denisova, A. Neiman, A. Nepryahin, N. Kochetova, N. Zhuravlev and P. Colomban, *Solid State Ionics*, 162–163 (2003) 73-81.

[27] F. Galasso, L. Katz and R. Ward, *Journal of the American Chemical Society*, 81 (1959) 820-823.

[28] M. Murakami, K. Hirose, H. Yurimoto, S. Nakashima and N. Takafuji, *Science*, 295 (2002) 1885-1887.

[29] M. Alfredsson, J. P. Brodholt, D. P. Dobson, A. R. Oganov, C. R. A. Catlow, S. C. Parker and G. D. Price, *Physics and Chemistry of Mineral*, 31 (2005) 671-682.

[30] A. Shatskiy, H. Fukui, T. Matsuzaki, K. Shinoda, A. Yoneda, D. Yamazaki, E. Ito and T. Katsura, *American Mineralogist*, 92 1744-1749.

[31] A. Yeganeh-Haeri, D. J. Weidner and E. Ito, *Science*, 243 (1989) 787-789.

[32] S. D. Jacobsen, Z. Liu, T. B. Ballaran, E. F. Littlefield, L. Ehm and R. J. Hemley, *Physics of the Earth and Planetary Interiors*, 183 (2010) 234-244.

[33] E. J. Mittemeijer and P. Scardi, Diffraction Analysis of the Microstructure of Materials, 2004, Springer, New York, .

[34] I. Levin, J. Y. Chan, J. H. Scott, L. Farber, T. A. Vanderah and J. E. Maslar, *Journal of Solid State Chemistry*, 166 (2002) 24-41.

[35] E. Chinarro, G. C. Mather, A. Caballero, M. Saidi and E. Moran, *Solid State Sciences*, 10 (2008) 645-650.

[36] V. Petkov, Pair Distribution Functions Analysis, 2002, John Wiley & Sons, Inc., US.

[37] W. Dmowski and K. E. Swider-Lyons, *Crystalline Materials*, 219 (2004) 136-142.

[38] K. Nomura, K. Tokumistu, T. Hayakawa and Z. Homonnay, *Journal of Radioanalytical and Nuclear Chemistry*, 246 (2000) 69-77.

[39] K. Nomura, Y. Ujihira, T. Hayakawa and K. Takehira, *Applied Catalysis A: General*, 137 (1996) 25-36.

APPENDIX

The data presented in this appendix is contained on the compact disc on the inside back cover of this thesis. That includes all the data and input files for the X-ray, synchrotron X-ray and neutron powder diffraction patterns utilized during this thesis. These can be read using the programme Rietica. The data of the XANES magnetic and electrical measurements are also included. These can be accessed using Athena programme or commonly available programme Origin. The folders and subfolders containing the data are classified according to the technique used and the chemical compositions of the oxides. The data contained on this compact disc represents a record of the majority of the work presented in this thesis and every attempt has been made to ensure it is presented in a consistent and clear manner.

Chapter 1

Chapter 2

Chapter 3

Chapter 4

Chapter 5

Chapter 6

Appendix